2014

Thermal and Microstructural Analysis of the A356 Alloy Subjected to High Pressure in the Squeeze Casting (SC) UMSA Technology Platform

Mohammad Khurshed-Ul Alam
University of Windsor

Thermal and Microstructural Analysis of the A356 Alloy Subjected to High Pressure in the Squeeze Casting (SC) UMSA Technology Platform

By

Mohammad Khurshed-Ul Alam

A Thesis
Submitted to the Faculty of Graduate Studies
through the Department of
Mechanical, Automotive & Materials Engineering
in Partial Fulfillment of the Requirements for the Degree of
Master of Applied Science in Engineering Materials
at the
University of Windsor

Windsor, Ontario, Canada

2014

Thermal and Microstructural Analysis of the A356 Alloy Subjected to High Pressure in the Squeeze Casting (SC) UMSA Technology Platform

By

Mohammad Khurshed-Ul Alam

APPROVED BY:

_____

S. Das
Department of Civil and Environmental Engineering

_____

D. O. Northwood
Department of Mechanical, Automotive and Materials Engineering

_____

A. Conle
Department of Mechanical, Automotive and Materials Engineering

_____

F. Ghrib
Department of Civil and Environmental Engineering

_____

J. H. Sokolowski, Advisor
Department of Mechanical, Automotive and Materials Engineering

April 30, 2014

DECLARATION OF CO-AUTHORSHIP

Co-Authorship Declaration

I hereby declare that this thesis incorporates material that is a result of joint research, as follows:

This thesis incorporates the outcome of research performed in the field of SEM/EDS Elemental Analysis in collaboration with Dr. Adam Gesing under the supervision of Dr. Jerry H. Sokolowski and Dr. Al Conle. The collaboration is covered in some portions of Sections 4.7-4.8 of Chapter 4 of the thesis. Contributions by the collaborators were primarily through the provision of calculations of micro chemical compositions in SEM/EDS Analysis.

I am aware of the University of Windsor Senate Policy on Authorship and I certify that I have properly acknowledged the contribution of other researcher to my thesis, and have obtained written permission from the co-author to include the above material(s) in my thesis.

I certify that, with the above qualification, this thesis, and the research to which it refers, is the product of my own work. I also certify that the above material describes work completed during my registration as a graduate student at the University of Windsor.

I declare that, to the best of my knowledge, my thesis does not infringe upon anyone's copyright nor violate any proprietary rights and that any ideas, techniques, quotations, or any other material from the work of other people included in my thesis, published or otherwise, are fully acknowledged in accordance with the standard referencing practices.

I declare that this is a true copy of my thesis, including any final revisions, as approved by my Thesis Committee and the Graduate Studies office, and that this thesis has not been submitted for a higher degree to any other University or Institution.

ABSTRACT

The effect of cyclic pressure on the thermal and microstructural behaviour of the A356 alloy and the addition of commercial Al-Sr Master Alloy, Nano Alumina Master Alloy and a combination of both Master Alloys during the squeeze casting was investigated in this study. The results show that the α-dendrite growth temperature was increased and the Al-Si eutectic growth temperature was decreased substantially, resulting in a super refined, as-cast, equiaxed α-Al cells and ultra fine dendritic eutectic Si in the modified and unmodified A356 aluminum alloy. Moreover, very rapid spheroidization of the Si particles was observed within a very short Solution Treatment time (15min) of the squeeze cast unmodified and Sr modified A356 alloy. It is expected that the results of this study will lead to a number of further fundamental and applied research rendering new alloys and technology.

DEDICATION

I dedicate this thesis to my beloved parents whom I lost long ago and who were my first teachers in this world. I pray for their departed souls.

ACKNOWLEDGEMENTS

I would like to express my heartfelt gratitude to the Almighty Allah who has created me and who has given me the ability and strength to carry out my research and the writing of this thesis.

I would like to acknowledge my supervisor Dr. Jerry H. Sokolowski and thank him for giving me the opportunity to conduct my MASc research project under his supervision and for providing me with his scientific and technical support. I am also thankful to the AUTO21 Network of Centres of Excellence for the financial support provided during my MASc project.

I would like to thank Drs. F. Ghrib, D. Northwood and S. Das for consenting to be a part of my Advisory Committee as well as for their continued guidance. Their help and feedback is highly appreciated.

My sincere thanks go to Dr. Al Conle, a Special Member of my Committee, who has been instrumental in the success of my experiments. His continuous assistance and support in carrying out my experiments, and in writing my thesis, is very much appreciated. I would also like to thank to Dr. Adam Gesing and Dr. Marcin Kasprzak for their scientific and technical support on my project. Dr. Gesing's collaborative work has enhanced my research and enriched this thesis.

Thanks to Dr. T. Troczynski (University of British Columbia) for providing the nano Al_2O_3 Master Alloy and thanks to Professor L. Dobrzanski and Professor Z. Rdzawski, from the Silesian University of Technology, Poland, for the further processing of this Master Alloy, for access to their analytical facilities and for providing the author with comprehensive characterization of the experimental test samples.

I wish to express my thanks to Ms. Ellen Moosberger for her invaluable assistance with the editing of this thesis. Special thanks go to my colleagues, Israel Aguilera, Brandon Hooper, Peter Guba, Paul Marchwica, Bruce Durfy, Andrew Jenner, Sharon Lackie and Steve Budinsky for their valuable help in my daily activities.

Most of all, I would like to express my deepest gratitude to my wife Kashfia Nehrin and to my son Ahmad Tashfeen for their absolute love and understanding. It would have been impossible to complete this master's thesis without their unlimited support.

TABLE OF CONTENTS

LIST OF TABLES

LIST OF FIGURES

LIST OF APPENDICES

LIST OF ABBREVIATIONS/SYMBOLS

A/D, D/A	Analogue to Digital, Digital to Analogue
DAP	Data Acquisition Processor
DAQ	Data Acquisition
HPDC	High Pressure Die Casting
HSR	High Solidification Rate
HT/ST	Heat Treatment/Solution Treatment
HT UMSA	High Temperature Universal Metallurgical Simulator and Analyzer
LOM	Light Optical Microscopy
LPDC	Low Pressure Die Casting
LVDT	Linear Variable Differential Transformer
MA	Master Alloy (Al-Sr)
MCPT	Metal Casting and Post-Processing Technology
NAMA	Nano Alumina Master Alloy ($MgAl_2O_3$)
NIST	National Institute of Standards and Technology
SC	Squeeze Casting
SEM	Scanning Electron Microscopy
SDAS	Secondary Dendrite Arm Spacing
SR [ºC/s]	Solidification Rate - Average rate of temperature change in the semi-solid region
SC UMSA	Squeeze Casting Universal Metallurgical Simulator and Analyzer
TA	Thermal Analysis
$T^{\alpha DEN}_{NUC}$ [ºC]	α- Al Dendrite Nucleation Temperature
$T^{\alpha DEN}_{MIN}$ [ºC]	α- Al Dendrite Minimum (Undercooling) Temperature
$T^{\alpha DEN}_{G}$ [ºC]	α- Al Dendrite Growth Temperature
$T^{AlSi}_{E,G}$ [ºC]	Al-Si Eutectic Growth Temperature
T_s [ºC]	Solidus Temperature
$t^{\alpha DEN}_{G}$	α- Al Dendrite Growth Time
t_S	Solidus Time
UBC	University of British Columbia
UM	Unmodified
UMSA TP	Universal Metallurgical Simulator and Analyzer Technology Platform

CHAPTER ONE - INTRODUCTION

1.0. Background

In this competitive automotive industry there is a continuing demand for materials with improved strength and durability for achievement of weight and cost savings. The aluminum casting industry responds to these goals through the use of novel technologies and development of semi-solid processing that result in significant refinement and modification of microstructural features (phases) including eutectic Si, SDAS and α-dendrite cell size for the improvement of components' functional. Alcoa, a leader in the production of A356 aluminum wheels, which are 35 - 44% lighter compared to the conventional steel wheels, uses the Low Pressure Die Casting (LPDC) process [1]. The Metal Casting and Post-processing Technology (MCPT) Group of University of Windsor collaborated with Alcoa on LPDC technology.

The ALCOA Collingwood Aluminum Wheel Plant used the following processing parameters for making A356 aluminum wheels with the LPDC process [2]:

- Induction melting: maximum temperature 780°C
- Degassing and skimming in the temperature range from 760 to 735°C
- Sr master alloy (Al-15wt%Sr) for Si modification: 130 to 150 ppm Sr
- TiB master alloy (Al-5wt%Ti, 1wt%B) for grain refining: 0.12 to 0.13 wt%Ti; 10 to 30 ppm B
- Melt transfer temperature (to the LPDC machine) range from 735 to 705°C
- Casting temperature range: 705 to 695°C

- Wheel ejection temperature: 470°C
- Solution Treatment: temperature range (set point in various zones): 540 to 545°C, time: 297 minutes, 70°C water quenching; Artificial aging: temperature 150°C, time 148 min

There are ample publications on the utilization of Squeeze casting (SC), High Pressure Die Casting (HPDC) and Low Pressure Die Casting (LPDC) technologies for automotive cast components, e.g.: transmission cases and road wheels, radiator support, dash panels etc. However, exploring a novel approach in this area, MCPT group found the SC UMSA to be a potential process for wheel production, which is very similar to the Die Casting process as high pressure is applied on the liquid melt in both processes.

The current study shows that commercial LPDC as-cast and heat treated structures of A356 Al wheels can be significantly improved by using the following methodologies in SC UMSA Technology Platform keeping similar process parameters [2]:

- Melt treatment using commercial Al-10wt.%Sr master alloy and the novel Nano Alumina Master Alloy, $MgAl_2O_3$ (NAMA) individually and combined.
- Various pressure profiles (cyclic pressure up to 115 MPa with 1-50 No. of cycles, amplitude, timing etc.)
- Solution treatment (at 540 ^oC, 15- 30 min) including Quenching at 70^oC water and natural aging, no artificial aging.

MCPT Group is involved in the further developing of SC-UMSA Technology Platform's physical simulation capabilities for possible merging of the SC and LPDC processes rendering ultrafine Si, α-dendrite cell and SDAS. A number of further Master thesis and

Ph.D dissertations will cover the new technology for the development of new Magnesium alloy, hypoeutectic and hypereutectic aluminum alloys. Depending on the research outcome, the new SC technology may be used as an alternative stand alone production process for advanced, cost effective mass production of low weight components. SC UMSA Technology Platform including a novel squeeze pin has been being considered for patenting. The new scientific and applied engineering knowledge needed for rapid progress in the understanding of the metallurgical phenomena governing SC technological processes of new class A356 material(s) and cast components is generated in the scope of this research project.

This thesis will concentrate on the analysis and quantification of the solidification of squeezed cast A356 Aluminum alloy subjected to high pressure applied in a cyclic manner between the liquidus and solidus temperature. Applied Pressure on a solidifying semi solid melt has a great impact on the thermal and microstructural characteristics of the resulting cast component. The pressure can be applied in a number of ways, such as high pressure die casting, hot isostatic pressing or squeeze casting. Squeeze casting (SC) is held to provide the highest mechanical properties of the three. In commercial SC, pressure is applied in static manner and produces large dendrites. Cyclic pressure disintegrates the primary phase (long dendrite arm) as well as the secondary phases (Coarse Si, AlSiFeMg) and produces almost equiaxed α-aluminum cell and ultrafine dendritic eutectic Si. Solution treatment of this structure goes into spheroidization of Si particles within a very short soaking time. Therefore, the innovative cyclic pressure was chosen for the research as per the direction of Dr. Jerry Sokolowski.

In addition, A356 alloy has high demand in the auto industry due to its excellent castability and good weldability. It is currently the most popular alloy used in squeeze casting and semi solid metal processing. A356 has long been the material of choice for cast aluminum automobile wheels in North America and has become the standard for most automotive chassis and suspension castings as well. This alloy is used by Alcoa, Toyota and GKN plc for making automotive wheels through squeeze casting. In other applications where pressure tightness, and good resistance to corrosion are required, A356 alloy is also the right candidate [3].

1.2. Scope of Research

The research is outlined as per the flow chart shown in Fig. 1.

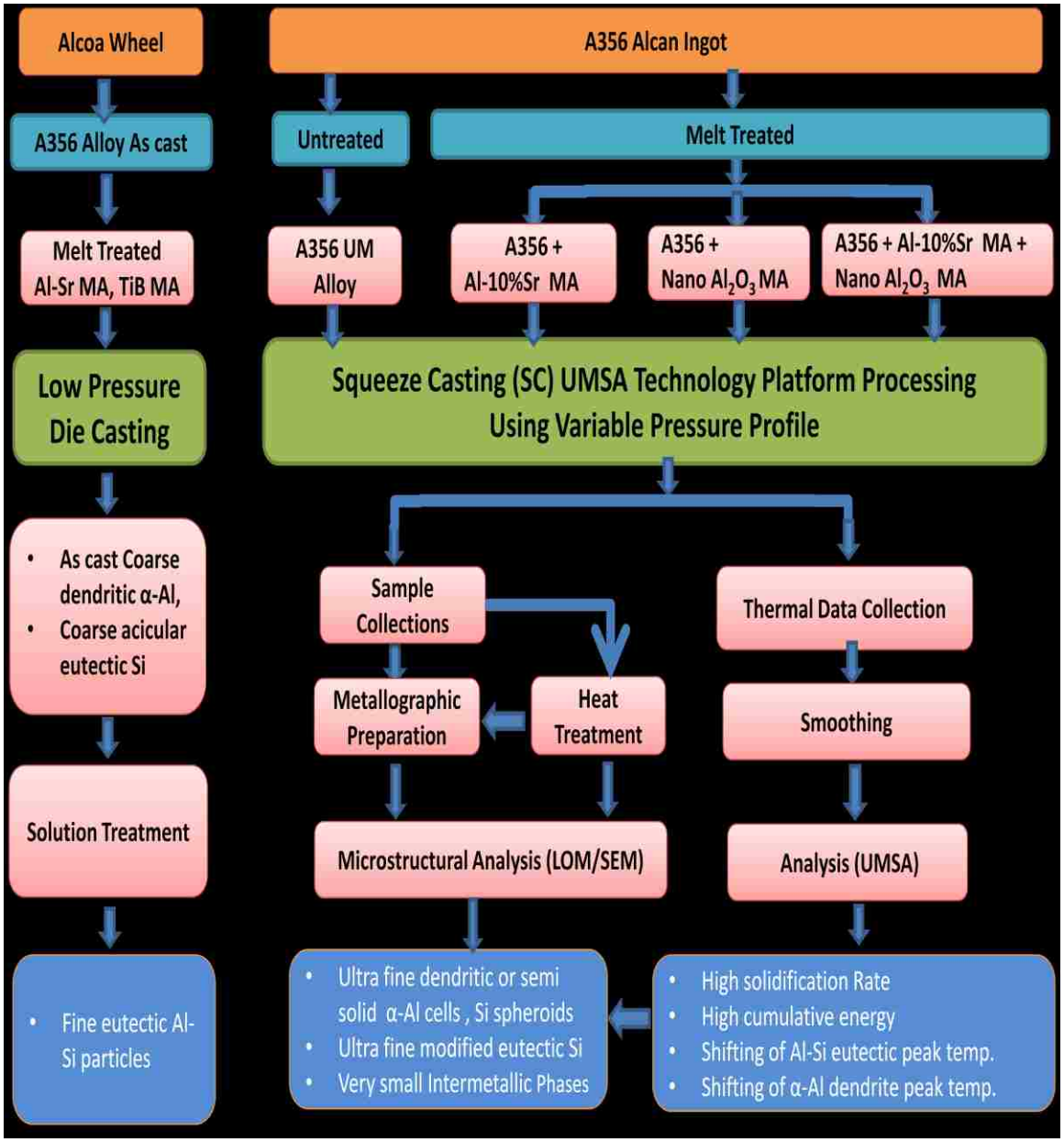

Figure 1 – Flow chart for the scope of research.

1.3. Objectives

1. To perform a worldwide, comprehensive literature review regarding the A356 alloy; its processing technologies including Squeeze casting (SC); the effect of pressure profiles during solidification; master alloys; thermal and metallurgical analysis for material and process characterization.

2. To determine the methodologies and the calibration scope of thermocouples and the Data Acquisition System used in SC UMSA Platform.

    2.1. HT UMSA Calibration at a very low Solidification Rate (SR) against National Institute of Standards and Technology (NIST) calibrated data.

    2.2. SC UMSA Calibration at a high SR against HT UMSA calibrated data.

3. To design and execute SC UMSA experiments for the development of novel materials and technology as well as characterization of the solidification process for untreated and treated A356 melts/samples subjected to variable pressure profiles (Pressure up to 115 MPa, 1-50 cycles).

    3.1. To determine a suitable pressure profile for the untreated and the melt-treated A356 using nano-Al_2O_3 and Sr Master Alloys as well as combined (Sr and Nano Alumina) Master Alloys rendering semi-solid α-Al cells and ultra fine Si in the as-cast SC test samples.

    3.2. To determine Solution Treatment (ST) parameters rendering a significantly improved Si structure in comparison with the LPDC technology.

4. To understand the effect of experimental conditions on the solidified structure and thermal data as well as solution treated microstructures.

CHAPTER TWO - LITERATURE REVIEW

2.1. Aluminum and Aluminum Alloys

2.1.1. Aluminum

Pure aluminum is a soft, lightweight metallic element. It is the second most plentiful metallic element on earth. It became an economic competitor in engineering applications at the end of the 19th century [4]. The properties of aluminum that make this metal and its alloys the most economical and attractive for a wide variety of uses are appearance, light weight, fabricability, physical properties, mechanical properties, and corrosion resistance. Aluminum has a density of only 2.7 g/cm^3, which is approximately one-third of steel (7.83 g/cm^3), copper (8.93 g/cm^3), or brass (8.53 g/cm^3). It can display excellent corrosion resistance in most environments, including atmosphere, water (including salt water), petrochemicals, and many chemical systems if optimized in terms of chemical composition and heat treatment [7-9].

2.1.2. Aluminum Alloys

Aluminum alloys are divided into two major categories based on the processing technology and the primary mechanism of property development: Cast Aluminum and wrought aluminum alloys [7-9]. Wrought alloys are those obtained by working on ingots of particular forms, which can be affected by rolling, extruding, drawing or forging. Cast alloys are those for which ingots are melted and poured into moulds having the shape of the final product [7-9].

2.1.3. Alloy Designation of Cast Aluminum Alloys

A system for designating aluminum and aluminum alloys that incorporate the product form (wrought, casting, or foundry ingot), are covered by American National Standards Institute (ANSI) standard H35.1. The Aluminum Association is the registrar under ANSI H35.1 with respect to the designation and composition of aluminum alloys in the United States [4]. The Aluminum Association has established a system of nomenclatures to divide the alloys according to a number of criteria, including chemistry and processing (i.e. cast vs. wrought alloys). This thesis will discuss only the cast aluminum alloys. The cast aluminum alloys families are shown in Table 1 [4].

Table 1 - Cast Aluminum Alloy Families [4].

Code	Description
1xx.x	Controlled unalloyed (pure) compositions
2xx.x	Copper as major alloying element, other elements may be included
3xx.x	Silicon as major alloying element, other elements (e.g. Cu or Mg) included
4xx.x	Silicon as principal alloying element
5xx.x	Magnesium as principal alloying element
6xx.x	Currently unused
7xx.x	Zinc as principal alloying element, other elements (e.g. Cu, Cr, Mn or Mg) included
8xx.x	Tin as majorly alloying element
9xx.x	Currently unused

Cast alloys are described by a three digit system followed by a decimal value. In this nomenclature, 'xx' is a unique code that identifies a specific alloy composition within the

family of alloys. The ‘x’ following the decimal point refers to alloy composition limits and indicates either cast composition limits (.0) or ingot composition limits (e.g. .1 or .2). Furthermore, a letter added as a prefix to a code indicates a specific restriction to the alloy such as a limitation on impurity elements between primary and secondary alloys [3]. For an instance, differences between designations and the alloys are compared in Table 2 between two alloys, 356.0 and A356.0. Also, some common industrial aluminum alloys are shown in Table 3.

2.1.4. Importance of Al-Si Alloys

Among all commercial aluminum casting alloys, Al-Si alloys are the most important ones mainly because of their excellent casting characteristics. The most attractive reasons for which Al-Si alloys are widely used are their inexpensiveness and availability. Addition of Si to pure aluminum imparts high fluidity, good feeding characteristics, low shrinkage and good hot cracking resistance [4]. The high strength to weight ratio is another important characteristic. While the volume of most metals (including Al) shrinks substantially on solidification, two phase Al-Si alloys contract relatively less. These are the only Al alloys that are not prone to hot-tearing during solidification. Silicon has a density of 2.3 g/cc, which is very close to that of aluminum, and thus is one of the few elements which may be added to aluminum without affecting the light weight of the alloy. For a specific application, the selection of an alloy depends on its castability, the casting process, the required mechanical and physical properties and the end use of the casting. The properties of Al-Si alloys make them very popular in various applications including the automotive, aerospace and defense industries.

Table 2 - Comparison of Two Alloy Designations and Their Chemistries [3].

Code	Composition (Trace elements excluded)
356.0	6.5-7.5 Si, 0.25 Cu max, 0.20-0.45 Mg, 0.35 Mn max, 0.60 Fe max, 0.35 Zn max, 0.25 Ti max
A356.0	6.5-7.5 Si, 0.20 Cu max, 0.25-0.45 Mg, 0.10 Mn max, 0.20 Fe max, 0.10 Zn max, 0.20 Ti max

Table 3 - Some Common Industrial Alloys of Aluminum [8].

Alloy types	Alloy Characteristics
Hypoeutectic Al-Si casting alloys (less than 10% Si)	Standard automotive grades of A356 and 359 Aerospace and structural alloys: C355 and 357 High-purity alloys: B356, C356 and E357, F357 Low strength, high ductility, binary alloys: 443 and 444 Die-casting alloys: 360 and
Eutectic Al-Si casting alloys (greater than 10% and less than 12.6% Si)	High-purity near-eutectic Al-Si alloys: 413.X and A413.x For thin wall intricate, high integrity die-cast parts requiring ductility and consistent castability and pressure tightness A365, Aural™-2 and Aural™-3
Hypereutectic Al-Si casting alloys (greater than 12.6 % Si)	For wear resistance castings: A390.1
Al-Cu alloys	High strength and ductility alloy with fracture toughness: A206, B206. High temperature alloy 242
Al-Si-Cu alloys	Automotive and Aerospace alloys: 319, 354, A355, and C355. Specialty diesel engine cylinder head alloys by inquiry only.

2.1.5. Al-Si Alloy System

Al-Si binary alloy is a eutectic system with the eutectic composition at 12.6 wt. % Si and eutectic temperature at 577 C. The Al-Si binary phase diagram is shown in Figures 2-3.

The two phases in equilibrium below the eutectic temperature will be Al solid solution (solid solution of Si in Al) and pure Si. The solid solubility of Si in Al at 577 ^{o}C is 1.65%. However, rapid quenching from the liquid in non-equilibrium stage raises the solubility up to 16% Si and shifts the eutectic point up to 17% Si [9]. Silicon reduces the thermal expansion coefficient, increases corrosion and wear resistance and improves casting and machining characteristics of the alloy. As the Al-Si alloy solidifies, the primary alpha aluminum forms and grows in dendrites. When the eutectic point is reached, the eutectic Al-Si phases nucleate and grow until the end of solidification. The alloys to the left of the eutectic composition are referred to as hypoeutectic alloys and those to the right as hypereutectic alloys [12-13].

At room temperature, hypoeutectic alloys consist of a soft and ductile primary aluminum phase and a hard brittle eutectic silicon phase. In hypoeutectic alloys, the silicon varies between 5.5 and 10.5%, and primary aluminum is the first phase to solidify. The microstructure consists of primary aluminum dendrites, eutectic Si and AlSiFe intermetallic phases. Eutectic alloys contain 10.5 to 12.5% silicon and have microstructures consisting mainly of aluminum - silicon eutectic. In hypereutectic alloys containing more than 12.6% silicon, the first phase to solidify is the primary silicon phase. Hypereutectic alloy usually contains coarse, primary silicon cuboids as well as angular eutectic silicon phase. These alloys having a distribution of coarse silicon cuboids provide excellent wear resistance [11].

Although binary Al-Si alloys show excellent casting characteristics, the addition of Mg, Cu and Zn makes the alloys heat treatable, providing the means to enhance their properties with the use of appropriate heat treatments. Magnesium contents are typically

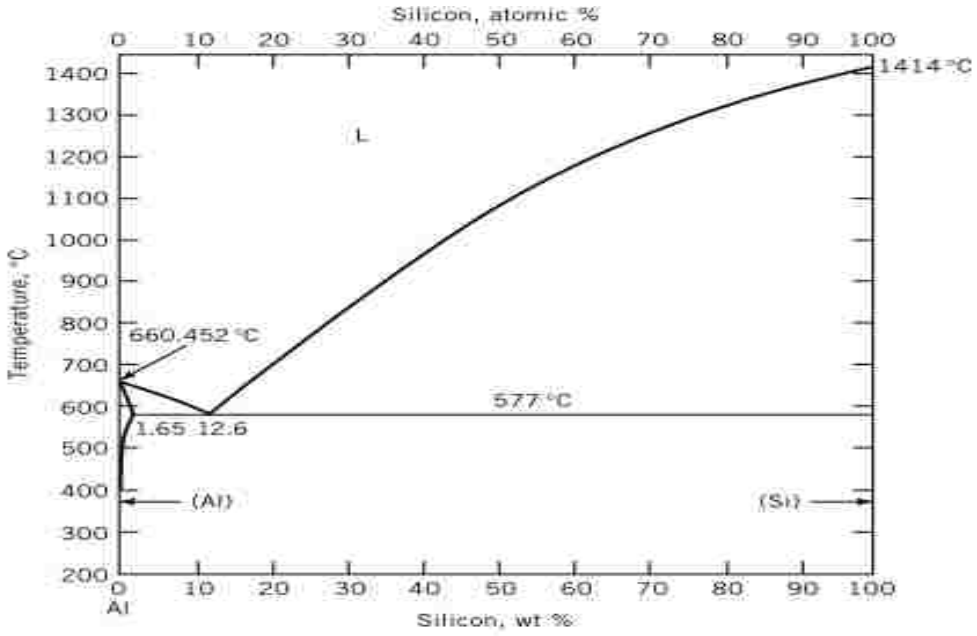

Figure 2 - Al-Si Binary phase diagram [4], [6].

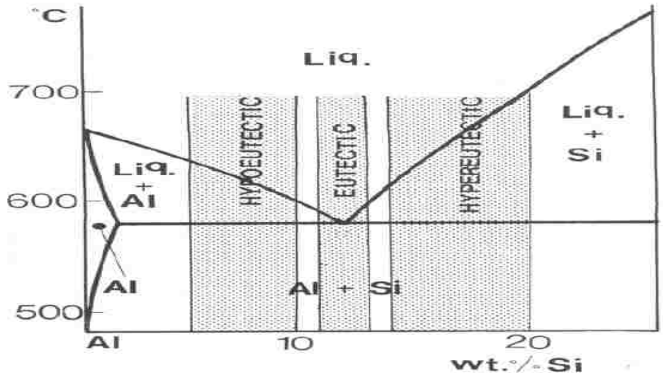

Figure 3 - Part of the Al-Si Binary phase diagram [10].

less than about 0.75%, because increased additions impair fluidity and feeding. The most common primary aluminum casting alloys in the Al-Si-Mg family are Al-7Si-0.3Mg (A356) and Al-7Si-0.6Mg (A357) [10-14]. Alloy A357 is similar to A356 but has higher strength. Alloys 360 and A360 are in the same family as A356, but were designed

specifically for die casting and, as such, contain more silicon and higher iron and allow more impurities than A356 [13].

2.1.6. Mechanical Properties of Al-Si Alloys

The mechanical properties of an Al-Si cast alloy are mainly governed by the grain size, secondary dendrite arm spacing (SDAS), α-dendrite cell size and the size, shape and distribution of the eutectic silicon particles, as well as the morphologies and amounts of intermetallic phases present [3, 6, 16]. The amount of aluminum dendrites in hypoeutectic Al-Si alloys is mainly dependant on solidification parameters like applied pressure, cooling rate, casting process etc., and its control can improve mechanical properties of the finished products. Further, the desirable mechanical properties in these alloys can also be obtained by controlling chemical composition and process parameters during melting, casting and heat treatment [13, 17].

The amount of silicon added can depend on the casting process being used. Slow cooling processes such as sand and investment casting can use alloys with silicon compositions of 5% to 7%, while fast cooling processes, such as squeeze casting and die casting, silicon contents are used from 8% to 12%. The latter alloy has a higher fluidity and lower melting point than the former. The higher silicon content, approaching the eutectic composition of 12.6%, decreases the solidification range of the alloy, reducing the chance of cold shuts and incomplete filling in the faster cooling processes, when cast at the same temperature [3, 13-14, 16]. These advantages result in most common commercial casting alloys containing a significant proportion of silicon. Other alloying additions are made to improve the mechanical properties of the casting, or are present as impurities, either arising from the casting process or are present in the raw material.

2.1.7. Effect of Minor Common Elements Present in Al-Si Alloys

Alloying elements are selected based on their effects and suitability. The alloying elements may be classified as major and minor elements, microstructure modifiers or impurities; however the impurity elements in some alloys could be major elements in others. Apart from the silicon, there are some common minor elements (e.g. Copper, Magnesium, Manganese) added to the alloy that also have significant effect on the mechanical properties of Al-Si alloys, while iron is treated as common impurity. A summary of those element and their effects are discussed below [3-4, 11, 13]. Silicon modifying elements (Strontium, Sodium, and Antimony) will be discussed in section 2.1.8.

Copper

Generally copper increases the mechanical properties of the as-cast and heat-treated alloy through solution strengthening and precipitation strengthening. Copper additions also reduce corrosion resistance, decrease castability and slightly reduce ductility [4].

Magnesium

A small addition (up to 0.1%) of magnesium causes increases in tensile and fatigue strength, and large decreases in ductility and impact strength. The reduction in ductility and impact properties is due to the formation of Mg_2Si precipitates in the bulk metal. In addition, Shilvock [15] found that the presence of magnesium could detrimentally affect Si modification of Al12Si alloy.

Iron

Iron is usually present in aluminium alloys as an impurity. If the level of iron concentration is more than 0.6%, intermetallic compounds such as FeAl3 and βAlFeSi

are formed [15]. The β phase is associated with plate-like precipitates containing aluminium, silicon and iron, which are detrimental to the mechanical properties. Iron increases hot tear resistance and reduces die soldering but decreases flowability and feeding characteristics [15].

Manganese

Manganese is reported to have a little effect on the mechanical properties of cast aluminium silicon alloys [14]. However, Shilvock [16] reports a number of conflicting studies which show that, in the absence of iron, manganese will either slightly increase or decrease tensile strength and decrease ductility. Shilvock concludes that tensile strength gains from manganese are only seen when strontium is used as a silicon modifier, and the presence of manganese is detrimental to ductility in all cases [16]. In the presence of significant iron (>0.5%) manganese is added to create αAl(Mn,Fe)Si "Chinese script" precipitates instead of more embrittling βAlFeSi plates [15].

2.1.8. The A356 Alloy and Silicon Modification

Aluminum A356 alloy is a hypo-eutectic alloy. It is one of the most widely used casting aluminum alloys in the automotive and aerospace industries due to its excellent mechanical strength, ductility, hardness, fatigue strength, pressure tightness, fluidity, and machinability [3]. The nominal chemical composition [3] of A356 alloy is (6.5-7.5)wt% Si, (0.25-0.45)wt.% Mg, 0.10wt.% Mn max, 0.20wt.% Fe max, 0.10 wt.% Zn max, 0.20wt.% Ti max. The designation of this alloy is different in other countries, and it is known as LM25 in the Great Britain, AC4C in, Japan, L-2651 in Spain and A19 in Russia. In unmodified A356 alloy, the main eutectic reaction occurs at 577 ºC as a binary

reaction. It has about 50 vol. % eutectic phases. The final microstructure is mainly determined by the eutectic reaction [17].

The role of silicon in this alloy is to improve castability, resistance to hot tearing, and reduce the casting's susceptibility to shrinkage defects, as silicon increases in volume on solidification [18]. Though Si needles strengthen the α-aluminum matrix, Si lowers the ductility [19] of the material significantly. At low solidification rates, silicon appears as coarse acicular flakes that serve as crack initiators, causing the material susceptible to fracture in a brittle mode and reduce its fatigue life [20-21]. These needles work as major stress raisers in Al-Si alloys and need to be converted to a fibrous form to minimize the stress risk [20, 22].

In unmodified A356 alloys, the eutectic silicones are found in the form of large plates with sharp ends as acicular type. Silicon crystals in eutectic mixture grow in a fetched manner as shown in Fig. 4. Lamellar silicon is a finer version of the coarse, acicular structure, while fibrous silicon has a fine, apparently globular, morphology. "Silicon modification" is a method in which inoculants are added in the form of master alloys to A356 melt in order to promote the formation of a fine and fibrous eutectic silicon structure during the solidification process. Eutectic modification refers to the transition from acicular to fibrous or lamellar silicon. The modification of the eutectic silicon to a finer and more rounded structure improves the mechanical properties of A356 alloy considerably [20-21, 23] including a slight increase in UTS and a large increase in ductility [21-22, 24-28]. According to the widely accepted impurity induced twinning theory proposed by Lu and Hellawell [29-30], Na or Sr (modifier) is adsorbed on the growing Si crystal surfaces and thus the crystal growth is restricted. This leads to the

forced twinning of the silicon crystal and thus resulting in enhanced branching and a fibrous microstructure (Figure 5).

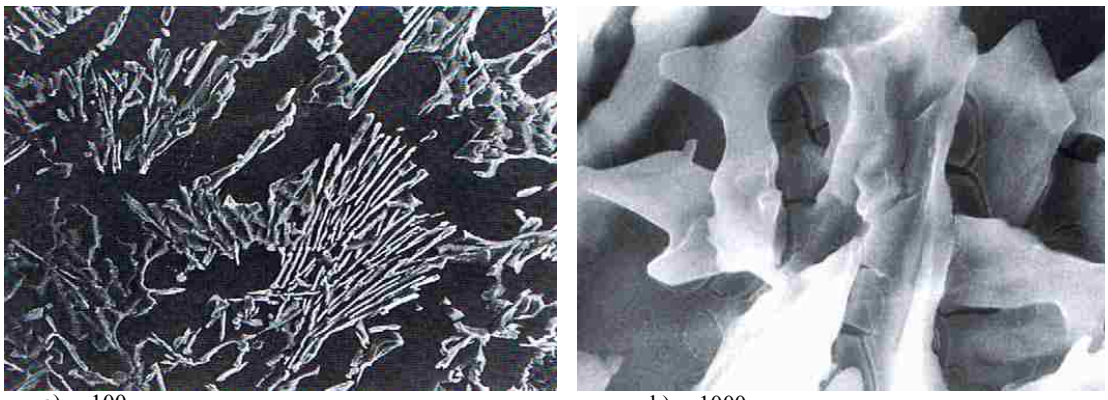

a) 100x b) 1000x

Figure 4 - Silicon crystals in a unmodified A356 alloy sample, SEM pictures after deep etching [10].

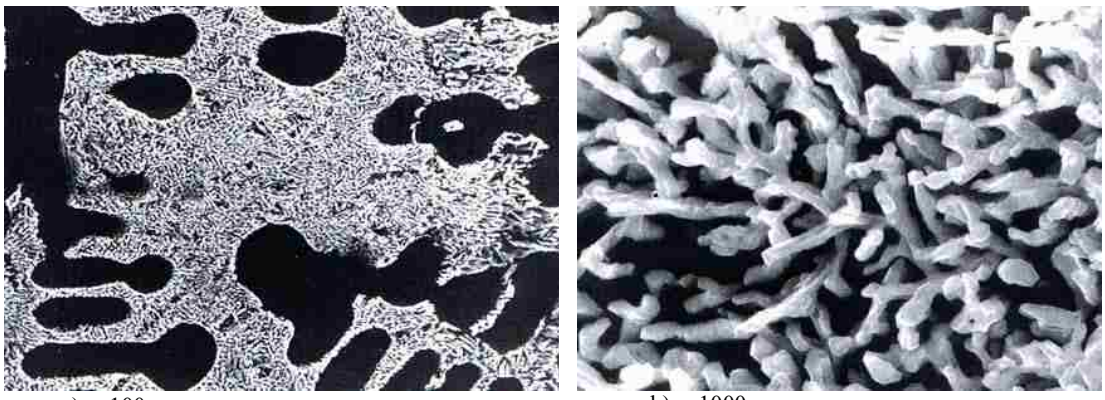

a) 100x b) 1000x

Figure 5 - Silicon crystals in a modified A356 alloy sample, SEM pictures after deep etching [10].

Three well-known eutectic modification methods were found in the literature namely, chemical modification [26, 30-38], quench modification [38-41], and super-heating modification [40]. Recent additional modification methods mentioned in the literature are namely, melt thermal treatment [41], ultrasonic vibration of melt [17] and mould vibration during solidification. A significant modification in eutectic silicon was also claimed by users of those methods [42].

Among all of the methods, chemical modification is most popular in the industry with the addition of trace-levels of several elements, such as sodium, antimony, potassium,

calcium, strontium, and barium. The addition of strontium is most widely used due to long lasting effect in the melt [45-46]. A comparison of silicon morphology in unmodified, Sr modified and Antimony modified hypoeutectic Al-Si alloy is shown in Figure 6 [44].

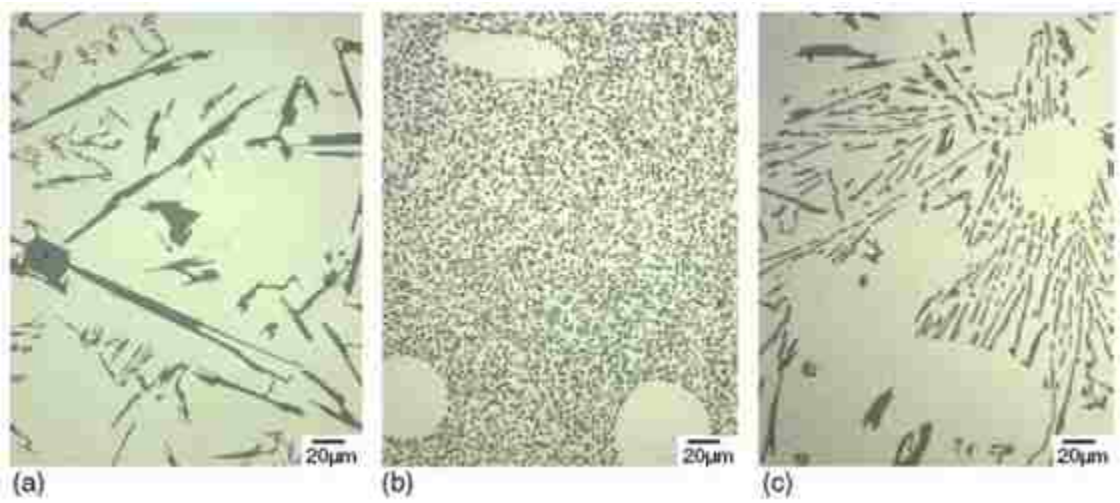

Figure 6 - Comparison of the silicon morphology in (a) unmodified, (b) Sr-modified (300ppm Sr) and (c) Sb-modified (2400ppm Sb), hypoeutectic Aluminum–Silicon alloys [44].

2.1.9. Chemical Modification and Mechanical Characteristics

2.1.9.1. Strontium

Strontium has become very prominent as a major Si modifier in the foundry industry. Pure strontium can be used as a modifier, but is commonly added in the form of Al-10wt%Sr master alloy to minimize reactions with air and water vapor [25, 47-48]. Backerud et al. [10], reported that strontium addition in a A356 alloy changed the morphology of the eutectic silicon crystals from large flakes into a fibrous structure resembling a seaweed type morphology (Fig. 5). This morphological change influenced

the nucleation and growth process of eutectic Si by lowering the nucleation and α-dendrite growth temperature of the alloy by approximately 10 ^{o}C [10].

A superior modification of the silicon eutectic phase in Al-Si alloys was found in the range of 0.007% [35], to 0.017% strontium [45, 49] despite a wider range of concentrations found in industry from 0.015 to 0.050% and beyond. However, it is usually accepted that modification of the eutectic Si phase occurs at strontium levels higher than 150 ppm (0.015%) [48]. As the amount of strontium in the melt increases, the level of modification also increases [51-52]. The optimum modification level depends mainly on the cooling rate of the casting [18] and on its chemistry [51].

Over addition of strontium may negatively affect castability of the alloy [23]. Two discrete effects are associated with the strontium over modification [46]. The first one is coarsening of the silicon structure and the reversion of the fine fibrous silicon to an interconnected plate form. The second one is the presence of strontium containing intermetallic phases in the microstructure, such as Al_2SrSi_2 or Al_4SrSi_2 [25, 48] . Both of these effects can reduce the mechanical properties of the alloy, causing them to revert to values more typical of unmodified alloys. Surplus strontium in the melt, can also form Al_2Si_2Sr particles and reduce the modification properties [50].

2.1.9.2. Sodium

Sodium could be used in aluminium silicon alloys as a modifier of the eutectic phase. Addition of small quantities of Sodium could greatly improve mechanical properties of cast aluminium silicon alloys by refining the coarse plates of eutectic silicon into a finely dispersed fibrous structure [54-55]. Excess sodium modification results in over-

modification, reducing the gains in strength and ductility achieved from the eutectic refinement [14]. Over-addition of sodium has been shown to decrease tensile strength and elongation from the peak values. Sodium has a high rate of loss in the melt due to the high vapour pressure of liquid sodium. The time interval window for an acceptable level of modification of a eutectic aluminium-silicon alloy by sodium is short compared to strontium, e.g. approximately 20 minutes to 50 minutes [14].

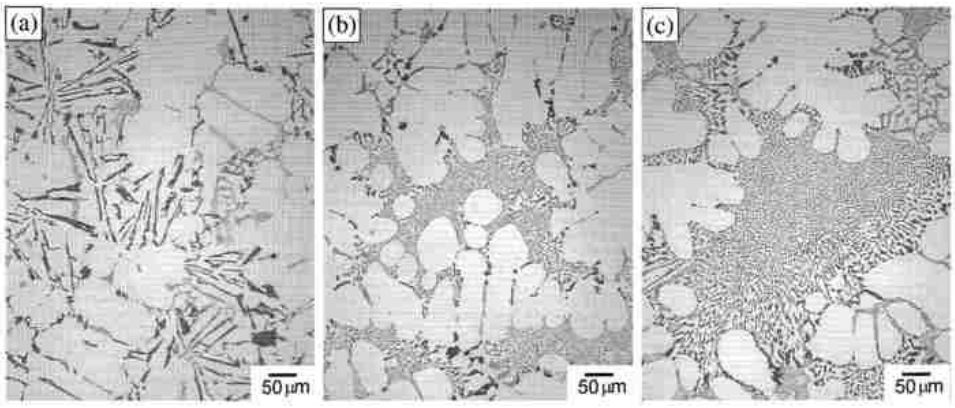

Figure 7 - Microstructure at the end of solidification (unquenched): a) unmodified, b) 0.008% Na and c) 0.017% Na [52]**.**

Na produces the finest modified structures at the lowest Na concentration, so it might be expected that sodium is the ideal modifier, but factors such as ease of dissolution, vapor pressure, and stability in the melt can limit its use [46]. The addition of sodium is accompanied by a violent reaction which can result in increased hydrogen levels. Typical retained sodium levels for effective modification are in the range 0.005-0.01% [47-48]; additions of Na over 0.02%. As shown in Figure 7 over modification with Na leads to a coarsening of the Si [52] and is associated with bands of primary aluminum [46]. Sodium levels in the melt are difficult to control, as it is difficult to accurately add it to the melt, and it fades rapidly. Re-modification is performed as required to maintain the desired weight % level.

2.1.9.4. Antimony

Antimony is very stable in the melt with virtually no losses (even after re-melting), so extra additions are not required. Sb is effective in amounts of 0.1-0.4% [46]. Although it was once used fairly extensively for commercial applications in Europe and Japan, it is now used less, primarily because recycling metal containing Sb is difficult. In addition, Sb can react with hydrogen dissolved in the liquid aluminum to form deadly stibine gas (SbH_3) [46].

2.1.10. Levels of Si Morphology Modification

The level of Si modification of an A356 alloy appear to have a strong reliance not only on the strontium content, but mainly on the applied pressure during solidification, solidification rates and post solidification solution heat treatments [19]. The modified microstructures contain fine fibrous silicon. These fibres appear to be small individual particles on a conventional polished surface, but etching away the aluminum shows that they are connected in a coral or a sea weed like structure [10].

Two standards to determine the level of modification of silicon particles have been suggested in the literature, namely: the AFS Si Modification Standard and MCPT Quantitative Si Modification Level [18], [54]. The first method can only be used for Al-Si hypoeutectic alloys and the second one for both hypo and hypereutectic alloys. In the first method, the determination of the level of modification of silicon is carried out by comparing micrographs of the test sample with the AFS wall chart by visual observation. These results could be biased and could have observational error. It does not take advantage of the analytical accuracy made possible by modern image analysis techniques.

In the second method quantitative assessment of SiML is introduced by MCPT group at the University of Windsor. Jiang and Sokolowski [56] developed a quantitative methodology of assessing AFS Si partic1e modification using a Leica Q550IW Image Analysis system. Later on Bhowmik and Alam expanded the quantitative Image analysis of Si under the supervision of Dr. J.H. Sokolowski [59-60]. Six candidate criteria (length, width, perimeter, equivalent diameter, area and aspect ratio) were assessed, based on their ability to differentiate between the Si modification levels [56].

2.1.11. The Nano Alumina Master Alloy (NAMA)

Despite having traditional individual master alloy for grain refinement and silicon modification, materials scientists have been working to develop a master alloy that will serve the purpose of both grain refinement and modification of secondary phases including eutectic Si. The University of British Columbia (UBC) developed the Magnesium Matrix Composite (MMC) by using Baikowski polishing nano Alumina powder (40 nanometer particle size) as reinforcement materials known as Nano Alumina Master Alloy (NAMA). This master alloy contains 93% pure magnesium and 7% nano Alumina powder. It was fabricated by using a unique method for dispersion of nano Alumina ceramic particles, throughout the volume of liquid alloy melt, to induce heterogeneous nucleation sites. These particles are wettable by the melt due to the unique method of their surface modification [57].

Fig. 8 shows the particles remain suspended in the melt for an extended period of time due to nano particle size and a negligible sedimentation force while Fig. 9 shows an improved structure with the addition of some cold work. As the ceramic nano alumina are

thermodynamically stable in the melt, this novel technology provides much needed time flexibility during melt holding, processing and casting operations. S. Bhowmik [57] reported a 15% reduction in SDAS of Al-Si-Cu alloy after adding 2% Nano alumina MA. He also reported that NAMA alloy has a high ability to modify silicon particles of 328 aluminum alloy. A. Alam [58] reported that using 1.0-2.0 wt.% Nano Alumina MA in A356 alloy showed (Figures 10 - 11) a high level of Silicon Modification and Grain Refinement with 2.0wt% being the most effective level.

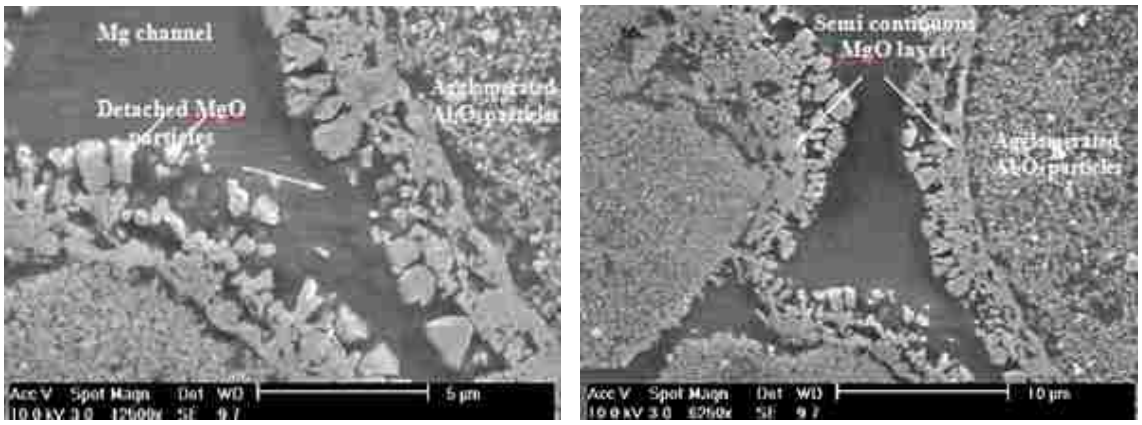

Figure 8 - Higher magnified SEM micrographs showing the typical microstructure of (a) the semi continuous MgO layer (b) Detached MgO particles and the Mg channel in the NAMA [57].

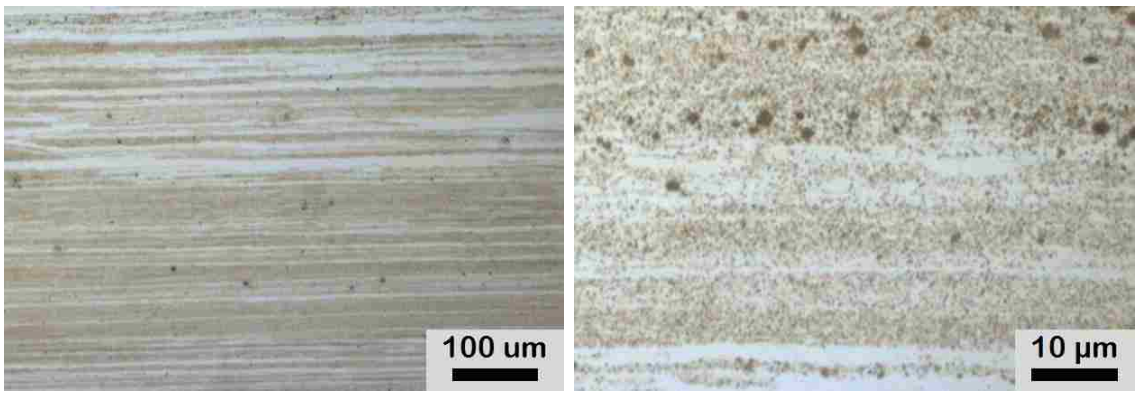

Figure 9 – LOM Micrographs shows improved structure of Nano Alumina Master Alloy developed by University of Windsor [57].

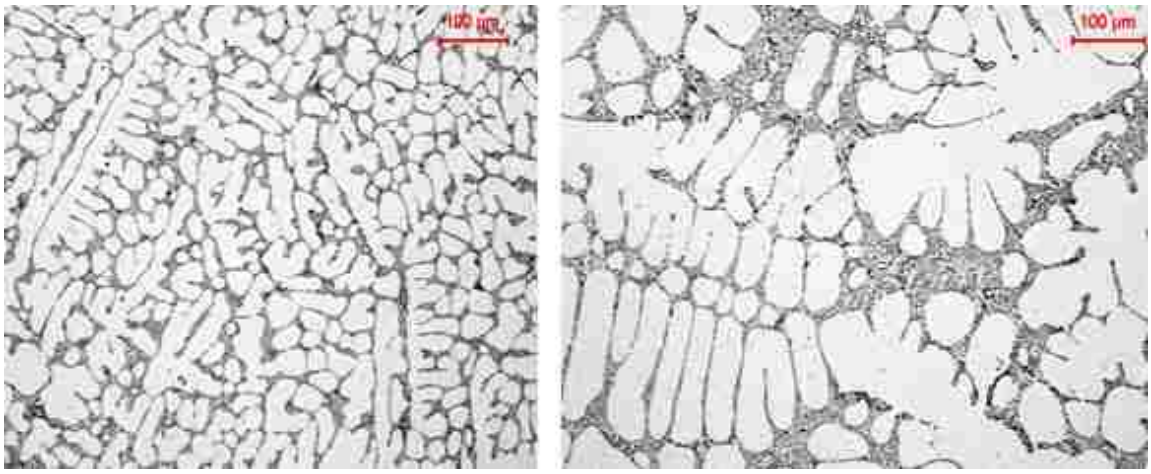

Figure 10 - LOM micrographs of As-Cast A356 test sample at two different locations from the chilling end after addition of 1.0 wt. % NAMA (a) 20 mm (b) 50 mm [58].

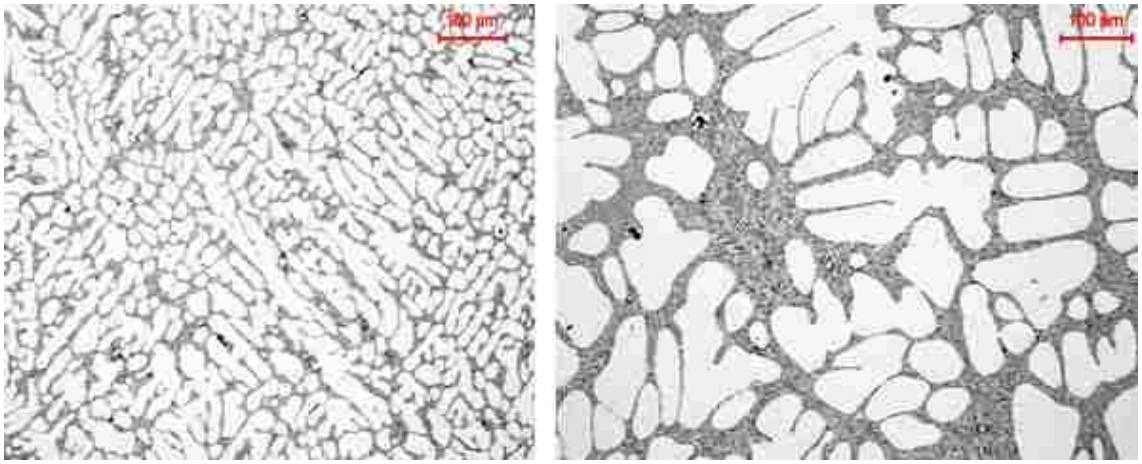

Figure 11- LOM micrographs of As-Cast A356 test sample at two different locations from the chilling end after addition of 2.0 wt. % NAMA (a) 20 mm (b) 50 mm [58].

As reported by A. Alam in his master thesis, the preliminary results indicated an unprecedented high level of refinement and modification of the primary and secondary phase. Metallurgical analysis of the melt treated with the new master alloy indicated that during the cast test sample solidification process, the ceramic particles did serve as heterogeneous nucleation sites for all the phases including eutectics that were formed at different temperatures. The resulting morphology of grains, major and minor phases, and

eutectics as well as micro porosity cavities were significantly improved in comparison to any melt treatment using commercial master alloys [58].

2.1.12. Secondary Dendrite Arm Spacing (SDAS)

Solidification of a hypoeutectic aluminum silicon alloy commences with the growth of a primary α-Al dendritic network [20, 56]. The distances between the secondary arms of these dendrites, are known as Secondary Dendrite Arm Spacing (SDAS). The SDAS and also where dendritic structure is broken into α-dendrite equiaxed cell, dendrite cell size has great influence over the mechanical properties of the alloy. As the SDAS or dendrite cell size is reduced, the cast structure becomes finer and more sound, resulting in higher mechanical properties [20, 56].

SDAS or dendrite cell size is exclusively controlled by solidification rate as shown in Fig.12. There are at least three measurements used to describe dendrite refinement [11]:

• Secondary Dendrite arm spacing: The distance between the secondary dendrite arms

• Dendrite cell interval: The distance between centerlines of adjacent dendrite cells

• Dendrite cell size: The width of individual dendrite cells

The larger the dendrite arm spacing, the coarser the micro constituents and the more pronounced their effects on properties. Finer dendrite arm spacing is desirable for improved mechanical property performance [11]. Cooling rates directly control dendrite arm spacing, which influences property development and substantially improves ductility. The relationship between solidification rates and the SDAS is inverse; the higher the solidification rate, the lower the SDAS [56, 61].

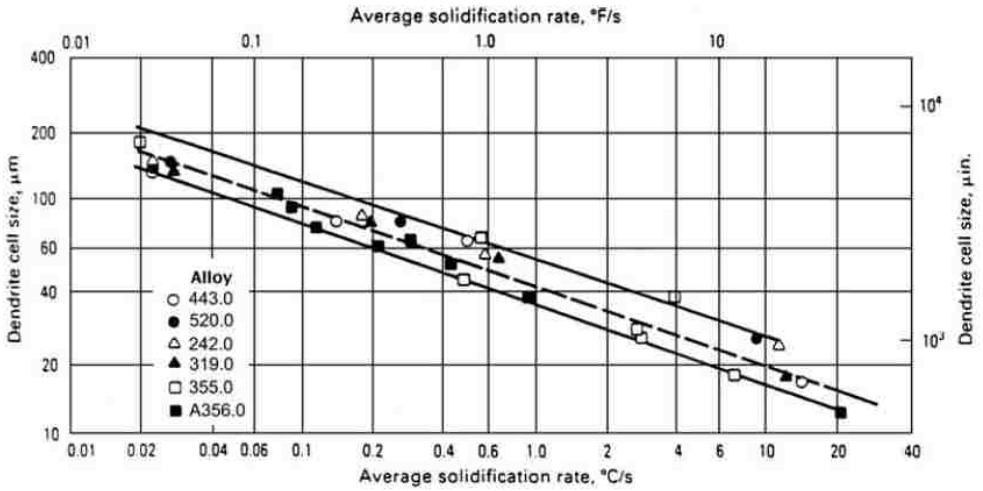

Figure 12 - Dendrite arm spacing and dendrite cell size as a function of local solidification rate [11].

As well as refining the SDAS, a high solidification rate also refines the dendrite cell size [56]. The solidification time of the casting should be as short as possible, to ensure the smallest SDAS [59]. For optimum grain size, the temperature gradient in the casting should also be very steep [59].

SDAS have a great effect on the microstructure of A356. The secondary SDAS controls the size and distribution of porosity and intermetallic particles in casting, therefore as the SDAS decreases, porosity and secondary phase constituents are smaller, and are distributed more finely and evenly resulting in substantially better mechanical properties [18]. Also as the SDAS is reduced, the speed of homogenization is increased, allowing more complete homogenization, giving more solute in solution and so greater strength from the subsequent precipitation reaction. The rate of solution is also increased, allowing a greater proportion of the non-equilibrium phase to be taken into solution. The smaller numbers and sizes of remaining particles, if any, and the extra solute usefully available in solution, will once again bring benefits to strength and toughness.

2.1.13. Heat Treatment

The term “Heat Treatment” is generally used to describe the steps required to achieve maximum strength in any suitable casting composition through the sequence of solution heat treatment, quenching and natural aging or artificial aging. Heat treatment comprises all thermal practices intended to modify the metallurgical structure of a casting in such a way that the physical and mechanical characteristics are controllably altered to meet specific engineering criteria [7, 16].

Solution treatment changes the cast structure depending on the status of the alloy whether or not it was modified [25, 48]. It is agreed between investigators that heat treated microstructures reveal a globular eutectic structure regardless of the amount of Sr present, making it difficult to correlate the degree of modification with Sr after heat treatment. Figure 13 shows the effect of heat treatment on the microstructure of unmodified and Sr modified A356 alloy [46].

On the other hand, Vanko et al [25] reported that at 100 MPa pressure squeezed cast unmodified A356 alloy showed a tendency of spheroidization of lamellar Si with a 10 minutes soaking time in a solution treatment at 540°C followed by water quenching at 20^{o}C and 4 hours artificial aging. However, as can be seen in Fig. 14, it didn’t fully spheroidized as claimed by him either in 3, 5 or 10 minutes soaking times [25]. Shivkumar et al. [18] reported that rapid spheroidization on heat treatment occurred in strontium modified melts as they experienced fragmentation rapidly. During solution treatment, the modified eutectic becomes more spherical. It has therefore been suggested [18] that chemical modification can be used to reduce heat treatment soaking time and overall costs.

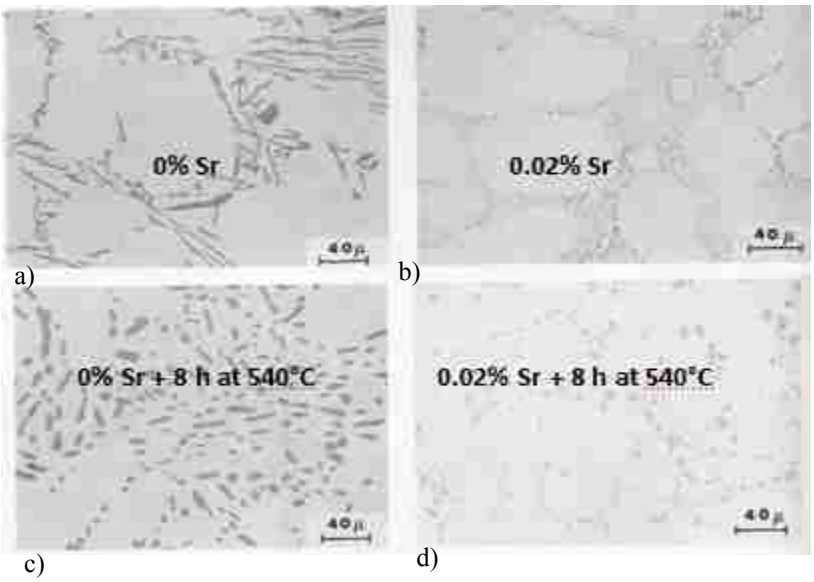

Figure 13 - Microstructures of the A356 alloy before and after solution heat treatment a) unmodified, b) 0.02% strontium modified, c) unmodified heat treated, d) Sr modified solution treated [46].

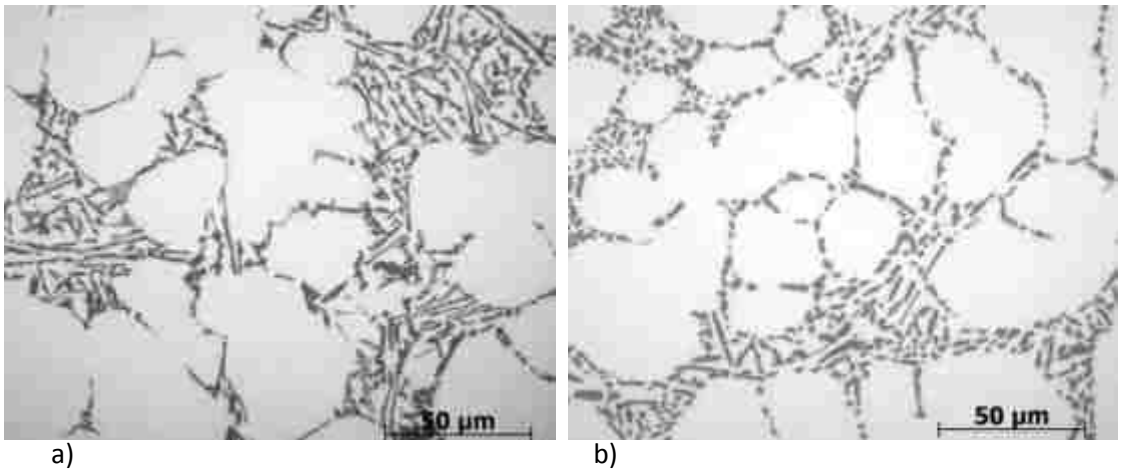

Figure 14 - Microstructures of the Squeeze cast unmodified A356 alloy before and after solution heat treatment a) Eutectic silicon angular lamellas are short and relatively coarse or longer and thinner, b) Eutectic silicon lamellas are shorter and rounded, but also coarser [25].

Microstructural changes of the eutectic Si due to modification and heat treatment both have a considerable effect on the mechanical properties of the A356 alloy, while the effect of heat treatment on the mechanical properties is more significant than that of chemical modification [60]. Beumler et al [48] reported that the tensile strengths of as-cast or heat treated structures are not significantly influenced by increasing the strontium content. However, modification of the melt with strontium does contribute to big

changes in % elongation for both as-cast and heat treated structures [48]. Investigators have found [48] that at equivalent strontium levels, the tensile data after heat treatment are higher than those for as-cast [48].

Paray et al [60] found that a longer solution heat treatment increases the ductility of the unmodified alloy, whereas when strontium is present, the greatest improvement is observed for yield strength [60]. The greatest advantages of chemical modification are evident for the slower solidification rates associated with sand casting. The coarseness of the original eutectic structure of the unmodified sand casting explains the beneficial effect of strontium which persists with heat treatment [60]. It was suggested that the best mechanical properties are reached when strontium is used in combination with heat treatment, although more work is necessary to define the optimum solution treatment time for the best properties [60].

2.2. Squeeze Casting

Squeeze casting is a specialized permanent mould process in which pressure is applied through a hydraulically operated ram during the freezing stage of casting [61]. It is used to obtain near net shape castings with better mechanical properties. It has been considered a high-integrity process and has emerged as an alternative to conventional casting techniques e.g. gravity permanent mould, low-pressure permanent mould or sand casting [62]. It has been widely used to manufacture automotive components (mainly aluminium) requiring high impact strength, high fatigue strength, and pressure tightness or wear resistance. Today, many automotive components are squeeze cast, with aluminium wheels being one of the largest products of this process as shown in Figures 15-16.

Squeeze casting involves the slow, direct application of pressure to a volume of liquid metal before or during solidification. The pressure applied during the process increases heat transfer between the casting and the die, reduces or eliminates porosity in the final casting and also ensures complete filling of the die [14].

2.2.1. History of Squeeze Casting

Squeeze casting was first originated in Russia in 1878 where steam pressure was applied to the molten metal during its solidification in a mould as suggested by D. K. Chernov [63]. However, the first recorded experiment on the effect of pressure on Al-Si alloys in a squeeze casting was carried out by Welter in 1931 [63]. Casting on an industrial scale was underway in the U.S.S.R. in the 1960s, with commercial development in the West being established about the same period. As reported by Rajagopal [83], the earliest American study on pressurized solidification of metals was carried out by Reiss and Kron in the 1960s on a U. S. Air Force sponsored research project, which outlined a cautious examination of the effect of solidification pressure, pour temperature, and tooling temperature on the microstructures and mechanical properties of A356 aluminum alloy. However, the pressure level studied was in the range of 350 - 700 MPa, which was too high for the process to be directly implemented [83]. The most notable application of the process was in the production of alloy wheels by Toyota, starting from 1979, using squeeze casting machines developed by UBE Industries as shown in Fig. 15. The casting process was used to produce a low porosity aluminium wheel. The squeeze cast wheel was lighter, stronger and more durable than the previous component [15].

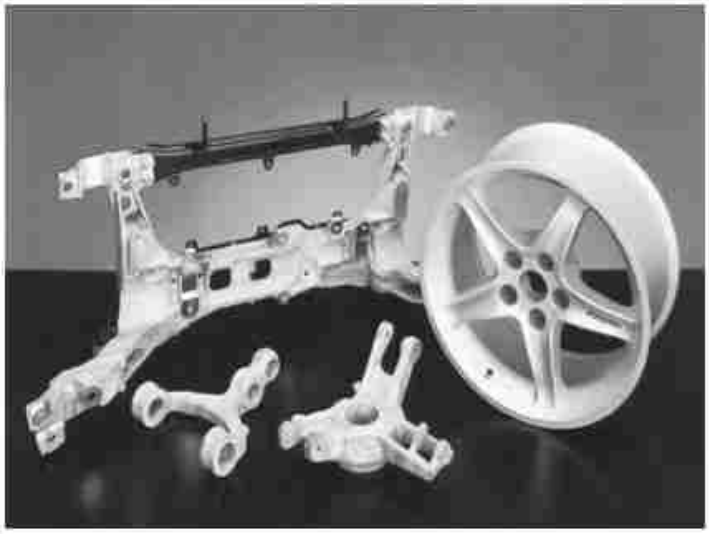

Figure 15 - Automotive parts produced by the squeeze casting process. Courtesy of UBE Industries [11].

Squeeze casting is now used for a wide range of products, including heavy duty diesel engine pistons, light alloy gears and pulleys, light alloy connecting rods, mortar shell cases and other general engineering components. Squeeze casting is also a major method in the manufacture of metal matrix composites (MMC's).

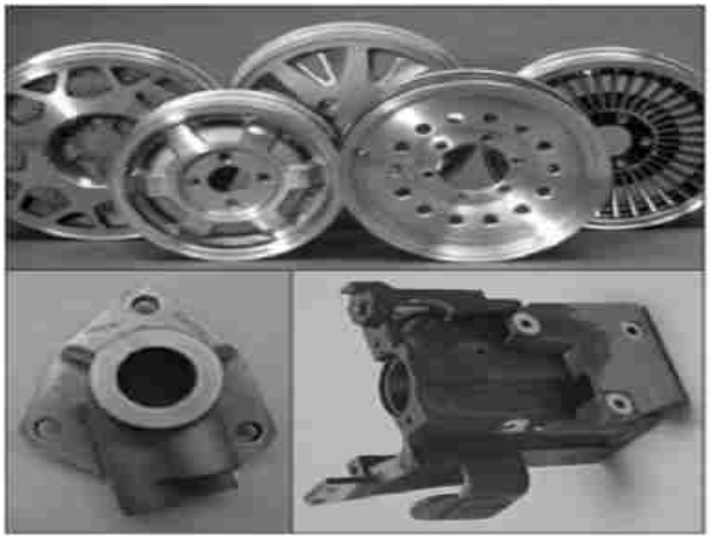

Figure 16 - Squeeze cast automotive components produced by SPX Contech Corporation (upper - wheels, lower left - valve housing, lower right - steering column housing) [64].

2.2.2. Squeeze Casting Processes

The process of squeeze casting involves the following steps [65]:

1. A pre-specified amount of molten metal is poured into a preheated die cavity, located on the bed of a hydraulic press.

2. The press is activated to close off the die cavity and to pressurize the liquid metal. This is carried out very quickly, rendering solidification of the molten metal under pressure.

3. The pressure is held on the metal until complete solidification. This not only increases the rate of heat flow, but also most importantly may eliminate macro/micro shrinkage porosity.

4. Finally the punch is withdrawn and the component is ejected.

2.2.3. Mechanics of Squeeze Casting

2.2.3.1. The die

A most crucial aspect in permanent mould castings such as die-casting or squeeze casting is the die itself and, most importantly, the design of the die including the selection of a suitable die material, the manufacturing process, appropriate heat treatment and the maintenance practice. Squeeze casting dies are exposed to severe thermal and mechanical cyclic loading, which may cause thermal fatigue, cracking, erosion, corrosion, and indentation. The nature and features of a die are greatly influenced by the particular alloy to be cast. Currently H13 tool steel is a widely used material for die constructions as it has good hot hardness, high temper resistance, adequate toughness and especially a high degree of cleanliness and uniform microstructure [66].

2.2.3.2. *The Casting Process: Key Features*

Two basic forms of the process may be distinguished, depending on whether the pressure is applied directly on to the solidifying cast product via an upper or male die (punch) or the applied pressure is exerted through an intermediate feeding system as schematically shown in Fig. 17: (i) the direct squeeze casting mode, and (ii) the indirect squeeze casting mode. For an instance, Metal Matrix composites (MMC's) are produced by using the direct squeeze casting method as shown in Fig. 18.

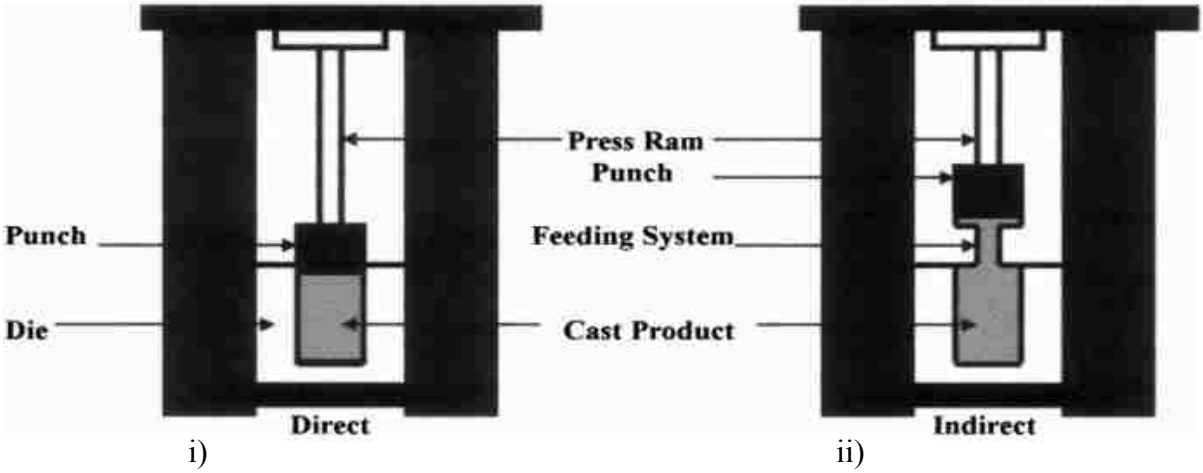

Figure 17 - Schematic diagram to illustrate the direct and indirect modes of the squeeze casting [65].

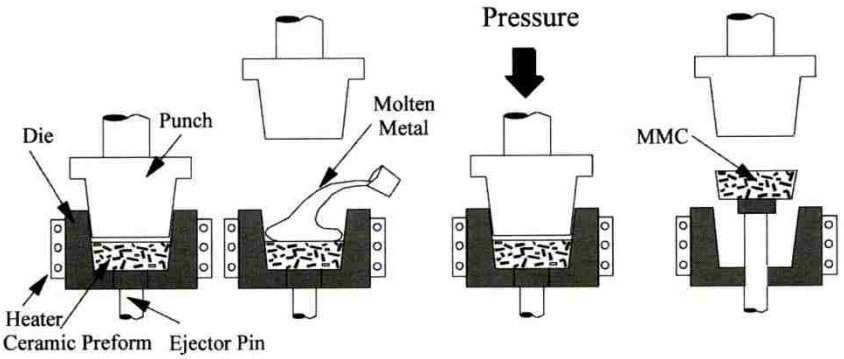

Figure 18 - Schematic diagram of the stages of squeeze casting to manufacture metal matrix composites (MMC) [61].

2.2.4. Application of Pressure and its Effect on Solidification

J. J. Sobczak reported [67] that pressure could affect casting solidification and structure formation in two ways, namely (1) mechanical effects and (2) thermodynamic effects. Mechanical effects related to the physical phenomena at macro-level like elastic and/or plastic deformation, intensification of heat exchange between casting and mould, variation of cooling rate, control of mould filling, etc. On the other hand, thermodynamic effects are related to transport phenomena at micro-level like changes in phase diagrams, physical properties, Gibbs free energy, chemical potentials, specific heat, surface tension, diffusion coefficients, etc. The physical phenomena at both macro- and micro scales alter some basic thermodynamic and kinetic parameters of systems and, thus, influence phase transformations in the system [67]. The main parameters in pressure application are magnitude of pressure, manner of its application to the solidifying melt, duration of pressure influence and physical or thermal status of melt before application of the pressure. Higher than atmospheric pressures can be applied to solidifying melts using either gas or specific mechanical systems through piston or plunger mechanisms [67].

Conventional autoclaves or their variants are usually used for solidification under elevated gas pressure. Units with one or more plungers are designed for direct application of pressure on solidifying melt [67]. Pressure can be applied during melt preparation (melting and alloying), melt transfer (die filling), at the commencement of casting solidification, just before the end of solidification, or after solidification of entire casting but before its complete cooling (i.e. when casting temperature is less than but close to solidus temperature). On the other hand, the melt can be overheated or cooled below the liquidus to form semisolid slurry before pressurization. Conventional casting

technologies that make use of pressure are often based on purely empirical knowledge rather than sound design criteria that originate in an understanding of the physical changes caused by pressure. Understanding the entire complex of physical phenomena that accompany solidification under high pressure is facilitated by the thermodynamic and kinetic descriptions of the solidification process [67].

Applying high pressure during solidification can increase the solidification rate by increasing the heat transfer at the metal/mold interface and consequently changing the thermodynamic properties such as solid-liquid transition temperature [68]. From a theoretical point of view, the effect of the pressure application is related to the alloy phase diagram modification whereby thermodynamic equilibrium curves shift toward higher temperatures as pressure increases [69].

The application of pressure during solidification would be expected to affect phase relationships in an alloy system [65]. This may be deduced by considering the Clausius - Clapeyron equation,

$\Delta T_s/\Delta P = T_s (V_l - V_s)/ \Delta H_f$ **……Equation 1**

Where, T_s is the equilibrium solidification temperature, V_l and V_s are the specific volumes of the liquid and solid, respectively, and ΔH_f is the latent heat of fusion.

Substituting the appropriate thermodynamic equation for volume, the effect of pressure on solidification point may roughly be estimated as follows:

$P = P_0 \exp(-\Delta H_f/RT_s)$……Equation 2

Where, P_0, ΔH_f and R are constants. Therefore, T_s should increase with increasing pressure. On a mechanistic approach, such change in solidification temperature is

expected due to the reduction in interatomic distance with increasing pressure and thus restriction of atomic movement, which is the prerequisite for melting/solidification. The inter-solubility of constituent elements together with the solubility of impurity and trace elements is also expected to increase with pressure. The above mentioned theoretical predictions have been proven experimentally where a liquidus temperature rise of up to 9°C has been reported for pure Al/Si binary alloys at a pressure of 150 MPa [70]. Furthermore, the eutectic point moves to the right, i.e., to higher Si contents as shown in Fig. 19 [71]. The consequences of such changes in the phase diagrams are a significant improvement in the microstructure and mechanical properties of SC-fabricated components.

Another indirect effect of pressure is related to the solidification rate. Allowing the better contact between the die and the cast part during solidification and thereby enhances heat transfer, and increased solidification rate. As a consequence, a refined grain size is observed [69].

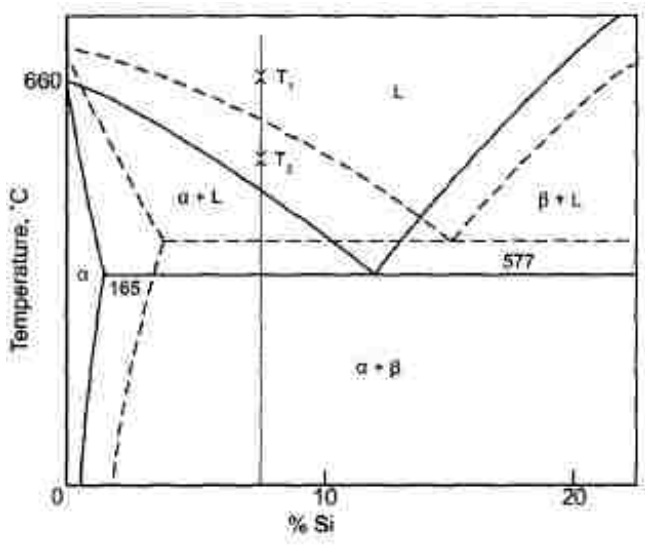

Figure 19 - Change of Liquidus and solidus lines in the binary Al-Si phase diagram following rapid solidification under high squeezed pressure [64, 73].

Based upon these advantages of high pressure solidification, various investigators have reported substantial refinement of microstructures and improvement of mechanical properties. In many articles [65, 67, 71, 74-88], it has been reported that applied pressure during solidification in squeeze casting has a tremendous effect on the overall quality of the casting. The quality of the squeeze cast components in terms of fine microstructure, grain refinement, porosity reduction and improved mechanical properties increases with increasing applied pressure during solidification.

Hu et. al [80] reported the effect of applied pressure on the tensile properties and microstructure of squeeze cast Mg- 5wt%- 1wt%Ca (AX51) alloy. They found that the fraction of 2^{nd} phases and porosity level reduced with an increase in applied pressure from 3-90 MPa. Also, Ultimate Tensile Strength, Yield Strength and elongation of AX51 alloy increased with increasing pressure.

In another investigation, Yu et al. [87] found that the application of external pressures on the solidifying magnesium alloy AM50A affected its solidification behavior; the Liquidus Temperatures of the alloy increased by 1.85, 2.62 and 5.40◦C under the applied pressure levels of 35, 70 and 105MPa, respectively.

A considerable microstructural refinement was observed by Han et al. [68] in an investigation of an hypoeutectic Al-Cu alloy during the solidification under very high pressure in the range of up to 1.7 GPa. He found that the average dendrite cell size changed from 30 μm, without applied pressure, to 5 μm at 1.7 GPa.

Similarly, Stefanos et. al. [82] reported the effect of applied pressure on the microstructure and mechanical properties of squeeze cast AA 6061 alloy. They observed

that squeezed casting decreased the volume fraction of porosity and microspores size as well as the size of dendrites and of the interdendritic areas. The ultimate tensile strength and elongation were increased accordingly with the increase of applied pressure.

In another study, MT. Abou-El-Khair [88] reported that the application of a squeeze pressure of 70 MPa resulted in a structure of α-Al of about 50 μm size with fine eutectic Si in a Al6Si0.3Mg alloy. He also found that increasing the applied pressure from 100 to 160 MPa reduced the grain size of the primary phase from 30 μm to 20 μm with formation of a very fine eutectic Si. However, he didn't observe any modification in eutectic Si at high pressure [88]. He also reported that in a solution treatment, the Si particles of squeeze cast alloy have spheroidized and coarsened to some extent compared to as-cast alloy despite having longitudinal shape in some particles as shown in Fig. 20, and that prolonged solution treatment led to coarsening of the particles [88].

For an Al-Si alloy (designated as B390) a substantial microstructure refinement was also observed as a consequence of the pressure application (up to 100 MPa) and higher mechanical properties were measured in terms of hardness and tensile strength [78].

Other studies showed that in direct and indirect squeeze casting, apart from the pressure, other process parameters such as melt and die temperature strongly affect microstructure and mechanical properties [80-81, 85-86]. Also for aluminum matrix composites, a positive effect of the applied pressure was observed on the mechanical properties of the cast composites [63].

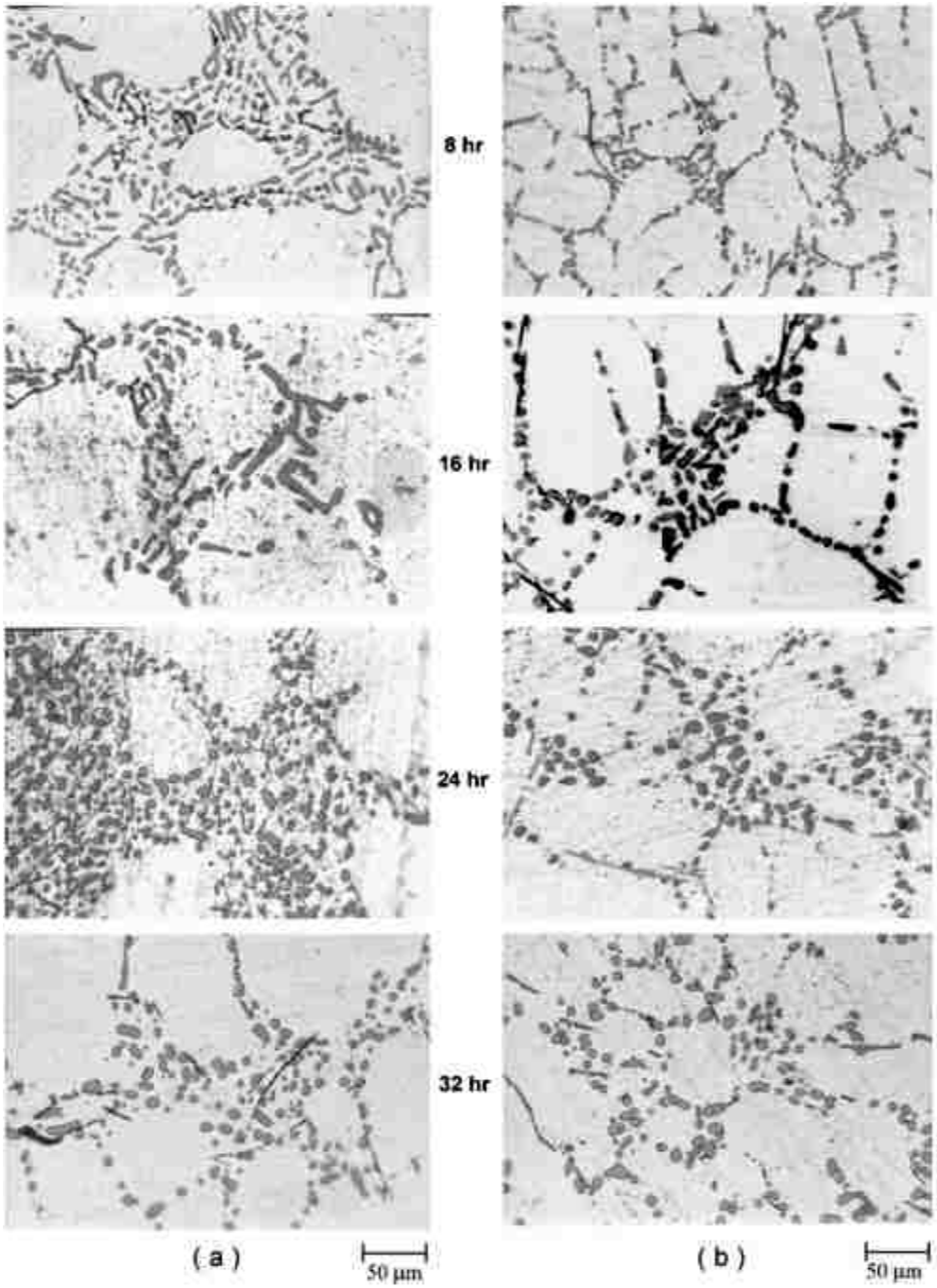

Figure 20 - Microstructure of solution-treated alloys (a) as-cast (b) squeeze cast at 70 MPa [88].

2.3. Thermal Analysis (TA)

Thermal analysis technique has been used for seven decades in both ferrous and nonferrous industries for evaluating the metallurgical quality of the liquid metal before

casting. TA principles of solidification processes are recognized as the high potential powerful scientific and applied engineering tool for making rapid manufacturing and R&D decisions. Most commercial TA systems lack the technical capabilities for comprehensive and automated assessment of the melt's metallurgical characteristics.

In addition, simplification and/or analytical errors in both software and hardware design result in inherent discrepancies between TA results and the test sample structure. For example, ATAS, Foseco and Heraeus utilize a thermal sensor located in a large rectangular solidifying test sample that is held in a Very High Thermal Mass (VHTM) sand test cup(s). VHTM tall rectangular test cups induce complex multi-directional heat transfer and melt convection resulting in a "smeared and convoluted" TA signal that is not ideal for high resolution heating/cooling curve analysis.

The University of Windsor developed a custom made novel High Temperature (HT) UMSA Technology Platform that guarantees unbiased physical simulations representing selected sections of industrial cast components. Simulated processes include heating, heat treatment, homogenization alloying, inoculation, casting, solidification with average and instantaneous heating/cooling rates. Universal Metallurgical Analyzer and Simulator (UMSA) Technology Platform is the state of the art technology for the modern thermal analysis. It uses low thermal mass that produce high resolution heating- cooling curves. In chapter three detail descriptions are provided on UMSA [89].

There are several methods for thermal analysis which include Differential Scanning Calorimetry (DSC), Differential Thermal Analysis (DTA) and Cooling Curve Analysis (CCA). All of these methods are mainly based on the similar principle. However, Cooling Curve Analysis (CCA) is the most widely used method. It measures the changes in

temperature in a sample that occur as it is heated or solidified through phase transformations. The record of these temperatures can be analyzed in order to derive metallurgical characteristics of the sample.

Cooling Curve Analysis (CCA) has been used in this study. It deals with temperature measurements using one or more thermocouple(s) inserted within the bulk of a sample during a heating/cooling cycle. The heating and cooling curves can be described as the "metallurgical DNA" of the melting and solidification processes [89]. Major and minor thermal events called metallurgical reactions that are thermodynamically strong enough in terms of the latent heat evolution that manifest themselves on the heating and cooling curves as inflection points and slope changes etc. can be determined. These changes are proportional to the volume fraction of the phases undergoing transformation. Unfortunately, phases appearing in small amounts are harder to detect on a cooling curve. By examining the first derivative of the cooling curve it is possible to increase the resolution of the thermal events. These thermal curves and their derivatives can be used to identify key metallurgical characteristic points [90]. Many researchers [91-102] have tried to correlate parameters of the cooling curves with microstructure features. However, using the UMSA solidification methodology, the test sample structure and the mechanical properties can be analyzed at any point between the liquidus and solidus or after completion of the solidification process in relation to the metallurgical reaction characteristics [89].

The Metal Casting and Post-processing Group at the University of Windsor has carried out an extensive thermal analysis on Alcoa A356 cast wheel and related ingot bar samples using UMSA Technology Platform [2]. In Table 4, the metallurgical reactions

are stated corresponding to temperature for the as cast wheel material. A comparison of cooling curves and their first derivatives for different cooling rates are shown in Figures 21-22. The respective metallurgical reactions are identified at listed in Table 5 as per different cooling rates.

Table 4 - UMSA Cooling Cycle Thermal Characteristic for the Alcoa 356 Cast Wheel [2].

Points	Thermal Characteristic	Solidification Rate 0.3°C/s Temperature, °C/ Standard Dev.
1	Nucleation of α Al dendrite network (Liquidus Temperature)	616.7±1.1
2	Nucleation of Al-Si eutectic	563±1.7
3	Nucleation of Mg_2Si phase	550.9±1.4
4	Finish of the alloy solidification (Solidus Temperature)	530.4±1.2
5	Solidification Range	86.3

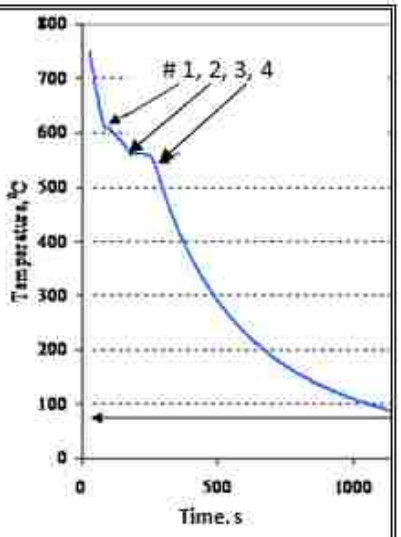

In another study, Bäckerud et al. [10] reported the common solidification reactions from a thermal analysis on A356 as shown in Table 6. Metallurgical reactions occur at different temperature based on the solidification rates. Solidification events may shift considerably in response to changes in the solidification rate. Some phase changes, such as $Al_8Mg_3FeSi_6$ in Table 6, will not even be resolvable at low cooling rates.

A comparison is made in Table 7 based on the selected properties of A356 as found on the literature of Bäckerud [10].

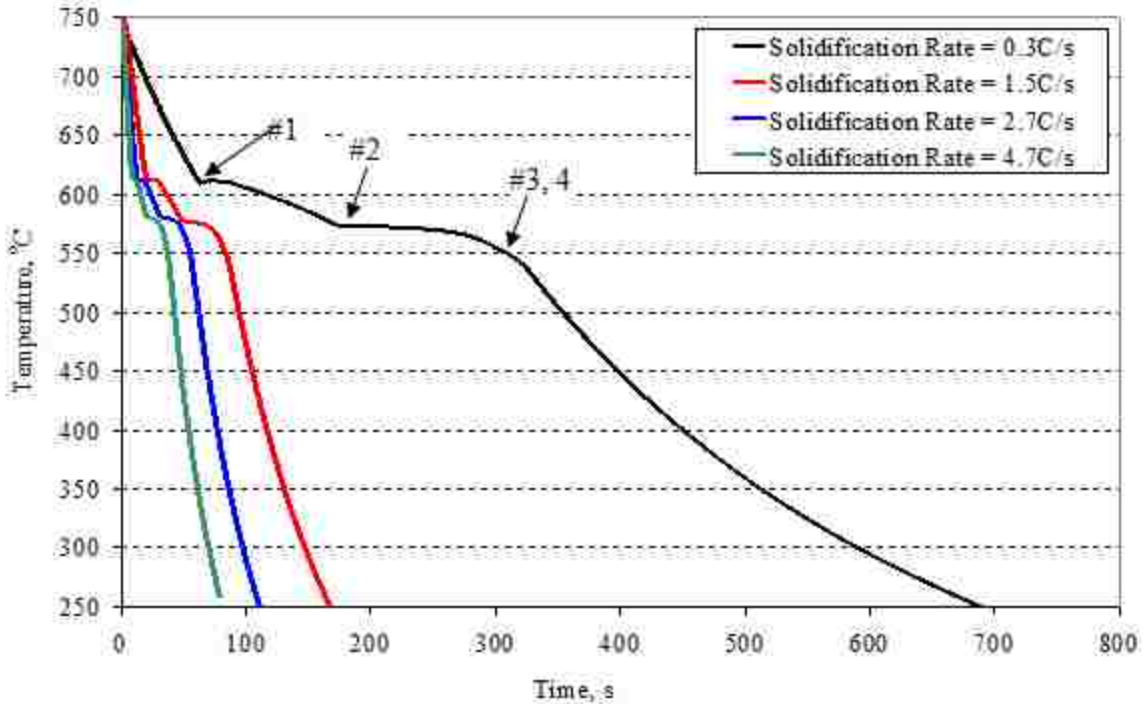

Figure 21 - Comparisons of different cooling curves obtained from A356 ingot samples [2].

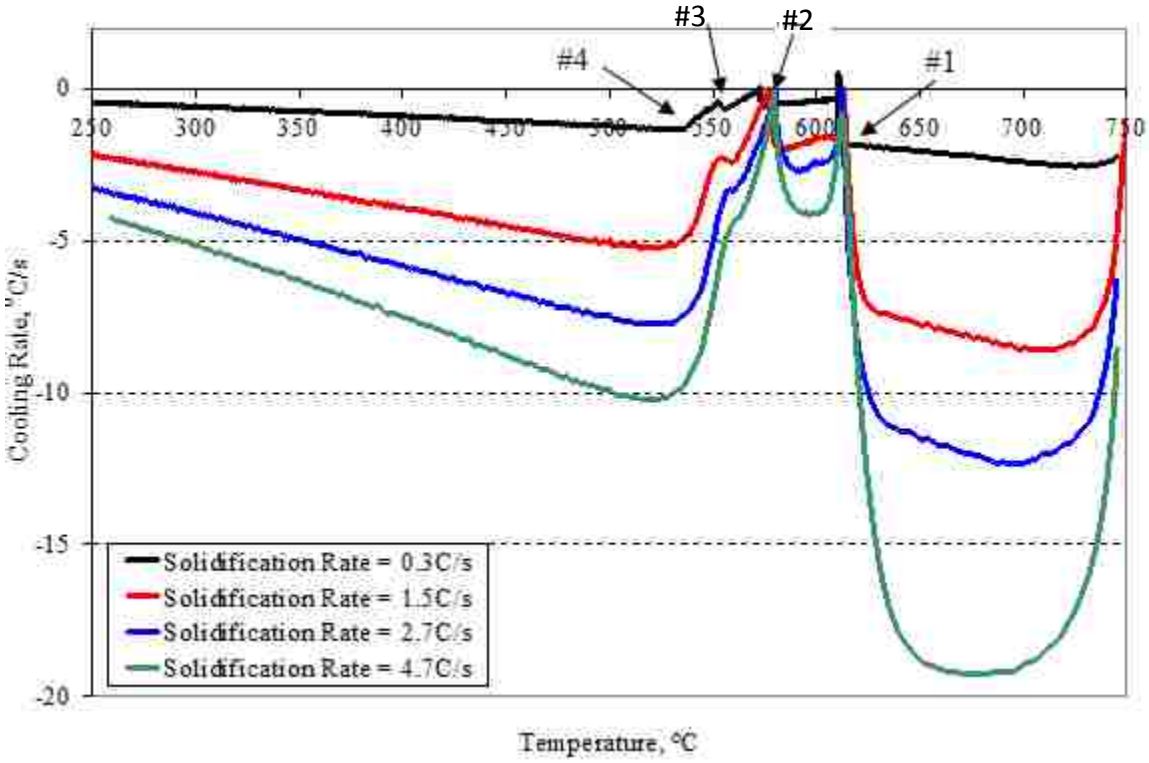

Figure 22 - Comparison of the first derivative of the cooling curves obtained from A356 ingot samples [2].

Table 5 - Comparison of Metallurgical Reactions of A356 Alloy at Different Solidification Rates [2].

Points	Thermal Characteristics	Average Solidification Rates, °C/s			
		0.3	1.5	2.7	4.7
1	Nucleation of α Al dendrite network (Liquidus Temperature)	613.6	625.2	630.1	652.2
2	Nucleation of Al-Si eutectic	574.7	583.5	591.9	595.7
3	Nucleation of Mg_2Si phase	555.5	559.1	558.6	562.5
4	Finish of the Alloy Solidification (Solidus Temperature)	535.8	523.6	520.8	517
Solidification Range		77.8	101.6	109.3	135.2

Table 6 - Reactions during Solidification of A356 Aluminum Alloy [10].

Reaction No.	Reaction	Suggested Temperature (°C)
1	Development of dendritic network	614
2a	Liq. → $Al + Al_{15}(Mn,Fe)_3Si_2$	594
2b	Liq. → $Al + Al_5FeSi + Al_{15}(Mn,Fe)_3Si_2$	594
3	Liq. → $Al + Si + Al_5FeSi$	575
4	Liq. → $Al + Si + Mg_2Si$	555
5*	Liq. → $Al + Si + Mg_2Si + Al_8Mg_3FeSi_6$	554
* Detected only at higher cooling rates		

In all of the above mentioned studies in the literature, thermal analysis was done at atmospheric pressure. However, no thermal analysis of A356 Alloy was found done

under high pressure. In the results and discussion section the behavior of A356 at high pressure will be elaborated in greater detail.

Table 7 - Comparison of Selected Characteristics of A356 in Relation to Solidification Rate [10]**.**

Characteristics	Average Solidification Rate (°C/s)		
	0.2	**0.6**	**5**
Temp. of Reaction 1 (°C)	612-610	613-608	614-611
Temp. of Reaction 2 (°C)	594-571	592-570	590-574
Temp. of Reaction 3 (°C)	569-568	563-561	565-562
Temp. of Reaction 4 (°C)	553-559	552-542	548-541
Temp. of Reaction 5 (°C)	-	-	541-505
f_s of Reaction 1 (%)	12	23	32
f_s of Reaction 2 (%)	19	20	11
f_s of Reaction 3 (%)	25	28	22
f_s of Reaction 4 (%)	3	3	7
f_s of Reaction 5 (%)	-	-	9
Dendrite Arm Spacing (μm)	95	69	33
Solidification Temp. Range (°C)	73	71	109
Solidification time(s)	785	274	49
End temperature (°C)	539	542	505

2.4. Silicon Equivalency and Liquidus Temperature

Silicon Equivalency (SiEQ) is a means of equating quantities of alloying and impurity elements in aluminum to an equivalent amount of alloying silicon, based on the effect

they have on the melting temperature [97]. When dealing with multi-component aluminum alloys, sometimes there is a lack of accurate liquidus temperature information in a ternary or high-order phase diagram. This difficulty can be addressed by using Si_{EQ}. In the Si_{EQ} system, for elements other than silicon , the wt.% of major or minor alloying elements are numerically converted to an 'equivalent' silicon value [90]. 'Equivalent' in this case means that x wt.% of those elements will have the same effect on the solidus/liquidus temperatures as y wt.% of silicon (where x and y are variables). Silicon was chosen as the base element for this method since it is common in all 3XX alloys [92, 103-104].

Si_{EQ} uses information from binary phase diagrams between Al and others elements (denoted ***Xi***). The slopes of the liquidus lines of Al-Xi phase diagrams can be expressed using second order polynomials. Equation 3 below contains an example polynomial for the liquidus line in the Al-Si phase diagram (where 660.452°C is the melting point of pure aluminum).

$$T^{AlSi}_{LIQ} = 660.452 - 6.11 \cdot Si - 0.057 \cdot Si^2 \ [^oC] \quad \text{.....Equation 3}$$

Taking into consideration the whole temperature range between the melting temperature of pure aluminum and the eutectic temperature of the binary alloy the following relationship can be established between $\boldsymbol{Si^{Xi}_{EQ}}$ and the concentration of the element Xi as shown in Equation 4:

$$Si^{Xi}_{EQ} = a_0^{Xi} + b_0^{Xi} \cdot Xi + c_0^{Xi} \cdot Xi^2 \ [wt.\%] \quad \text{.....Equation 4}$$

Where, $\boldsymbol{a_0^{Xi}}$, $\boldsymbol{b_0^{Xi}}$ and $\boldsymbol{c_0^{Xi}}$ are polynomial coefficients, ***Xi*** is concentration of alloying element in wt.% shows calculated polynomial coefficients for various common alloying elements.

Table 8 - Polynomial Coefficients for Binary Al-Xi alloys [58].

Al-Xi Alloy	a_o	b_o	c_o
Al-Cu		0.350	-0.027
Al-Mg		0.0258	-0.0088
Al-Mn		0.8221	-0.0349
Al-Fe		0.6495	0.0003
Al-Zn		0.1227	-0.0002
Al-Sn		0.7849	-0.0313
Al-Bi	0	0.9076	-0.0092
Al-Pb	0	0.859	0.02976
Al-Ca	0	0.0594	0.00685
Al-Sb	0	0.8255	-0.0327
Al-Ni	0	0.5644	-0.0285
Al-Sr	0	0.7854	-0.0157
Al-Ti	0	-0.8159	0.009927
Al-B	0	-0.9977	0.00007506

With the silicon equivalents for all component alloys calculated, the overall silicon equivalency value can be expressed using Equation 5 below. Substituting this Si_{EQ} value into equation 6, allows the characteristic liquidus temperatures of A356 alloy to be calculated for this project.

$$Si_{EQ} = Si + \Sigma Si^{Xi}_{EQ} \ [wt.\ \%] \quad \text{Equation 5}$$

$$T^{Al\text{-}Si\text{-}\Sigma i}_{LIQ} = 660.452 - 6.11 \cdot Si_{EQ} - 0.057 \cdot Si_{EQ}^{2} \ [^{o}C] \quad \text{Equation 6}$$

CHAPTER THREE - EXPERIMENTAL METHODOLOGIES

3.1. Material Chemistry of A356 Alloy for Squeeze Casting

In this investigation "as-received and unmodified" A356 alloy was used as the primary base alloy, the basic properties of which have already been outlined in the literature review. The test samples' material was taken from an Alcan supplied ingot of Aluminum Association designated A356 cast alloy and the unmodified A356 samples were directly machined from the ingot. Ingot chemistry was supplied by Rio Tinto Alcan and the chemical composition is shown in Table 9. Using the equations 5 and 6, the equilibrium liquidus temperature was calculated as 614.4°C, which is very close to 615°C found in the literature [4]. The equilibrium solidus temperatures is approximately 555°C [4].

Table 9 - Chemical Composition (wt %) of the A356 Ingot.

Si	**Fe**	**Cu**	**Mn**	**Mg**	**Ni**	**Zn**	**Ti**	**Pb**
6.956	0.096	0.005	<0.01	0.208	0.005	0.002	0.0003	0.01
B	**Be**	**Na**	**Ca**	**Li**	**Sr**	**Sb**	**Si_{EQ}**	
<0.0001	<0.0001	<0.0001	0.0002	<0.0001	<0.001	<0.001	7.03	

Apart from the unmodified alloy, three melt treated modified A356 alloys were also prepared and examined in this study. The first modified A356 alloy used the same A356 ingot with the addition of Strontium (Sr). These modified samples were made by re-melting part of the ingot in a Lindbergh furnace in a small crucible. During re-melting, the liquid metal was allowed to reach a target temperature of 730°C in the furnace. When it reached to the target temperature, a 0.015wt% of Sr (150 ppm) was added in a form of Al-10%Sr master alloy and stirred. The melt was then held for 10 minutes at 730°C, and subsequently poured into a dried Ø25mm tubular graphite crucible coated with boron nitride.

Similarly, the second and third modified samples also used the same A356 ingot material as its base, but with the addition of 1% Nano alumina and combination of both 0.015 wt. % Sr and 1 wt% Nano Alumina Master Alloys respectively and were prepared in the same way.

3.1.1 Calculations for Sr and Nano Alumina Master Alloy Additives

In this investigation, 0.04 wt. % and 0.015 wt. % Strontium were used in the form of Al-10%Sr master alloy. Test Sample weight was 24gm. For this test sample, in the first category, 0.0096gm strontium was used in the form of 0.096gm Master Alloy, while in the second category, 0.0036gm Sr was used in the form of 0.036gm Master Alloy.

Similarly for the 24gm test sample, 1 wt. % Nano Alumina Master Alloy (NAMA) was used. NAMA consists of 7 wt. % Nano Alumina powder with 93 wt. % Magnesium. Therefore, 0.0168gm (0.07 wt. %) of Nano Alumina was used in the form of 0.24 gm

Nano alumina master alloy, that is, 0.2232gm (0.93 wt. %) of Magnesium (contributed from the master alloy) was added as well.

3.1.2. A356 Ingot Segregation

Al-Si ingots are prone to the micro and macro-segregation of alloying and impurity elements. The main contribution to as-cast macro-segregation is the melt's thermo-solute convection in the semi-solid state and, prior to the Dendrite Coherency Point (DCP), movement of the free solid dendrites which is also influenced by gravity.

In order to minimize the difference between the bulk SC UMSA test samples' chemical composition, ingot(s) should be re-melted in the induction furnace and rapidly solidified. However, Metal Casting and Post-Processing Technology Group lost some of its technical capabilities including induction furnace and therefore, this processing step cannot be performed.

In addition due to the lack of access to the Optical Emission Spectrometer (OES) for a bulk chemical analysis of the individual test samples, A356 ingots' certified nominal composition provided by the supplier Rio Tinto Alcan was utilized (Table 9) and the novel SEM/EDS analytical methodologies were developed (Table 18-20).

3.1.3. SEM/EDS Analysis of SC UMSA Test Sample Phases and Bulk Chemical Analysis

In order to compensate for the lack of OES bulk chemistry data of the SC UMSA test samples and inability of simultaneous SEM/EDS analysis of phases smaller than electron beam diameter and lack of analytical procedures from equipment manufacturer and to-date users, the novel procedures were developed by one of the Auto21 Network

Researchers Dr. Adam Gesing. His paper "Quantitative X-Ray Fluorescence Determination of Elemental Composition of Micro-Constituents Smaller than the Electron Probe" was published in TMS and won the TMS 2013 award. The same methodology was utilized in this thesis with Dr. Gesing's permission.

The EDS micro-chemical composition of various phases presented in Tables 18-20 and can be directly compared, while the difference in bulk chemical composition between test samples (termed: alloy) indicates the magnitude of macro-segregation.

3.2. Squeeze Casting (SC) – UMSA Technology Platform

3.2.1. Background

The Universal Metallurgical Simulator and Analyzer (UMSA) Technology Platform has unique capabilities for physical simulation and thermal interpretation of the metallurgical processes. It allows researchers to rapidly develop new alloys and improve existing alloys, their processing and post-processing technologies leading to better in-service cast components. Recently addition of High Temperature capability in the new HT UMSA extended its functional characteristics to cover a wide range of research and development on the Ferrous and Non-Ferrous alloys. However, to cover High Pressure Technology parameters including the cyclic pressure and high solidification rates, the idea of developing the squeeze casting and high pressure die casting platform was initiated by Dr. J. H. Sokolowski of Metal Casting and Post-processing Technology Group at the University Windsor as part of the patented UMSA through incorporation of a tool steel die into the Instron Mechanical Testing Frame. Initially two students namely Joe Giovanatto and Rahul Kapoor started working on the development of the die in the frame

of integrated AUTO21 and Capstone Projects. Then the author, Brandon Hooper, Dr. Al Conle and Peter Guba worked together under the supervision of Dr. J. Sokolowski on the modification and up-gradation of the die setting, new plunger design, slide gating, thermocouple setting and improvement in data collection as well as software development for successful operation of the Platform. In addition, Dr. Adam Gesing and Dr. Marcin Kasprzak are also involved on the automation of the overall SC UMSA Technology Platform. A patent of squeeze pin with various pressure profiles is going to be commercialized by the University of Windsor.

3.2.2. SC UMSA Technology Platform's Functional Design

The SC-UMSA Technology Platform is integrated with an Instron Mechanical Testing Frame including an environmental chamber as shown in Figures 23-24. The environmental chamber can achieve temperatures of 350^{o}C and provides the necessary protection to allow experiments to be completed safely. The applied pressure ranges from the ambient to 115 MPa in a static or cyclic manner on the samples having a diameter of 20.5 mm and height of 26 mm. The maximum instantaneous cooling rate achieved is of approximately 100 °C/sec with an average solidification rate of 40 °C/sec. The present squeeze casting technology can address a quantitative assessment of the cumulative and individual effects of the solidification rate not limited to the average rate.

3.2.3. SC Die

The design of the squeeze casting die and corresponding assembly for producing a cylindrical test sample is illustrated in Figures 25-26. The Die assembly is composed of

the main die block, melting chamber, associated thermocouples, die pre-heating systems, and die cooling system.

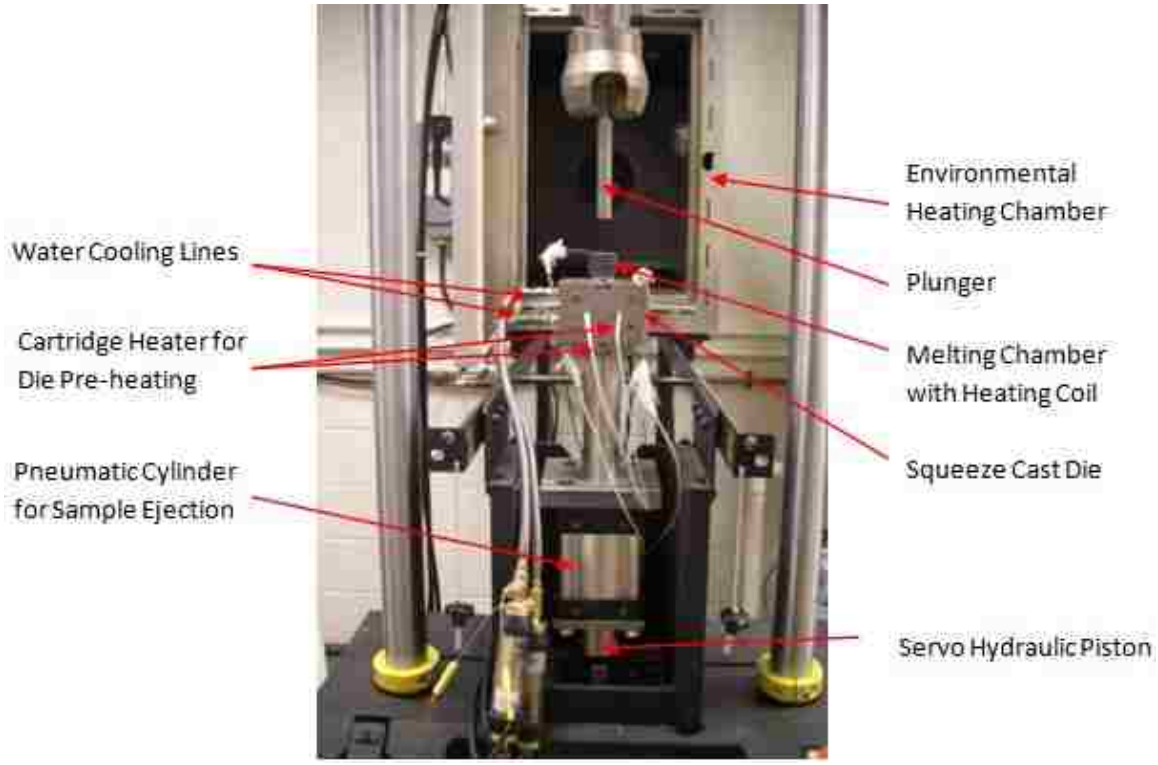

Figure 23 - Overall view of the SC-UMSA frame.

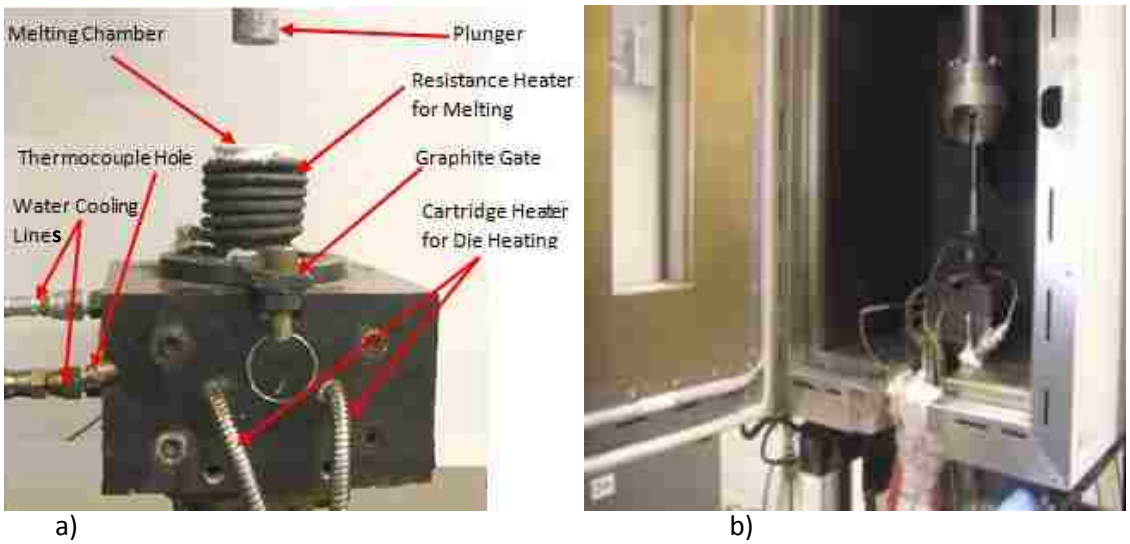

Figure 24 - a) Details of die assembly, b) Environmental chamber.

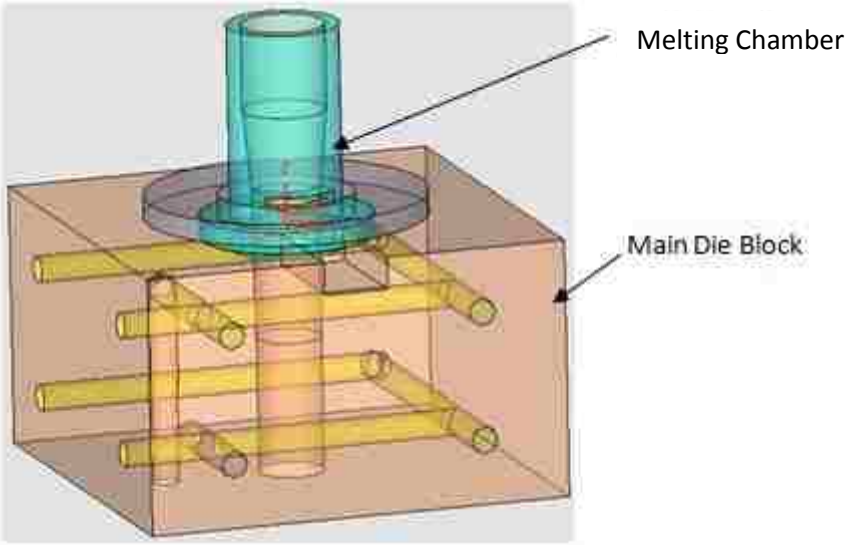

Figure 25 - Schematic drawing of 3D SC Die.

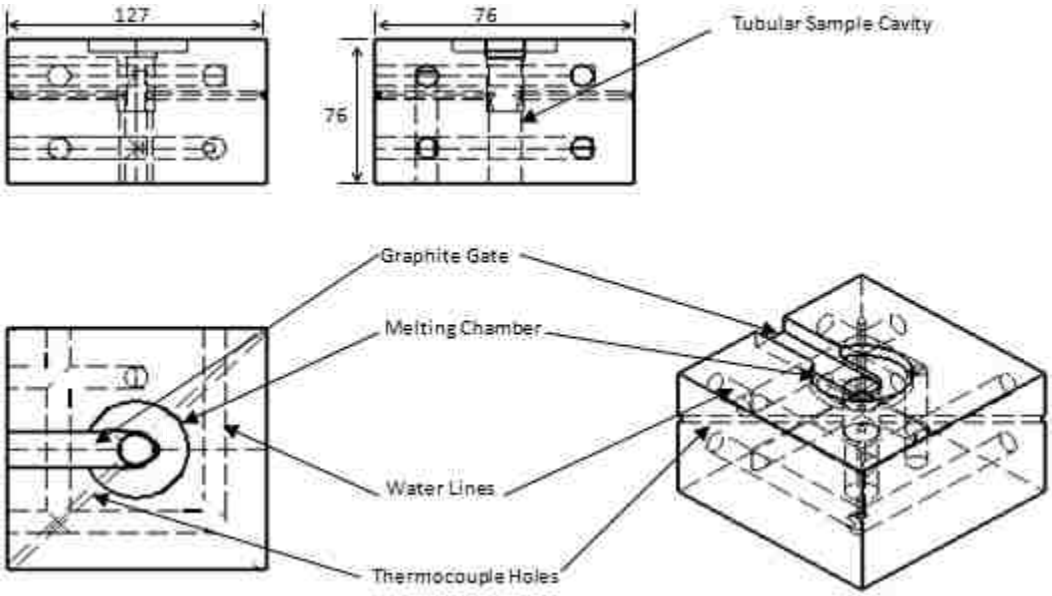

Figure 26 - Schematic drawing of the squeeze cast die.

Figures 25-26 show the schematic view and design of the die which has water lines (1/8" or 3.18mm) drilled through the die block, and two levels of cooling passages within the die. Two holes (1/16" or 1.59mm) were also drilled diagonally in the die, opposite to each other for inserting thermocouples. One is through hole for the temperature measurement of the test sample and the other one is a blind hole for measuring die temperature during experiments. A passage for graphite gate and melting chamber are engraved on the top part of the die.

The melt chamber is made of stainless steel (G304), is capable of handling temperatures of up to 1100°C. However, 850°C is a maximum sheath temperature of the coil can be generated using a tubular heater.

3.2.4. Test Sample

As shown in Fig. 27 all samples for melting in the Squeeze Cast experiment were machined into truncated cone shape at the University of Windsor Technical Support center.

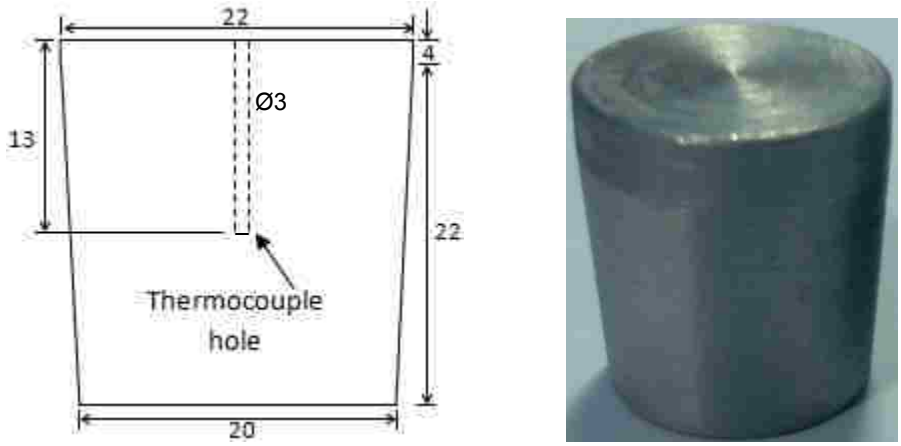

a) b)

Figure 27 - Samples of squeeze cast experiment, a) Plain drawing (dimensions are in mm), b) Picture

3.2.5. Processing Parameters for Programmable Squeeze Casting Experiments

3.2.5.1. Casting Pressure (Solidification Pressure)

Pressure is a thermodynamic function. Genereally it is treated as a constant in the thermodynamic reactions. However; it can be used as a variable parameter in many forms and processing characteristics. Commercially pressure is applied in a static manner in the squeeze casting. In the SC UMSA Platform, pressure can be applied in a cyclic manner as shown in Figures 29, which is a new method of applying pressure during solidification of A356 alloy in squeeze casting. As discussed in Section 2.2, experimental evidence indicates that the minimum required pressures to eliminate shrinkage and gas porosity are within the range of 70 to 108 MPa for all non ferrous alloys. In this investigation up to 115 MPa pressure with 1-50 cycles are applied to see its effective role on the microstructural and thermal changes in A356 Alloy.

The casting pressure was calculated by Pascal Law. If casting pressure P is:

$$P = F/A \quad \text{.....Equation 7}$$

Where, F is force applied by the Instron Machine, A is area of the plunger tip.

The maximum force of the SC UMSA Platform is 50kN that is determined by the Instron Load Cell. The applied force was controlled by automatic control panel.

Calculation of Casting Pressure

The applied pressure was calculated by using equation 7.

For example: F= 20 kN, Diameter of plunger (D) is 20.3mm =0.0203m

Area of the plunger is $A = \pi (D^2)/4 = 3.24e^{-4}\ m^2$

P = 61794246.15 Pa = 61.79 MPa

3.2.5.2. *Stroke and Plunger Speed*

If the distance between the die and plunger is large, a two-speed action may be used, with a rapid approach to the melt surface followed by a slower impact speed.

In this investigation, initially plunger moved with a fast speed of 0.15m/s followed by the slow speeds between 0.004m/s and 0.015m/s and then the plunger moved in a cyclic manner when the cyclic pressure was applied as shown in Figure 28.

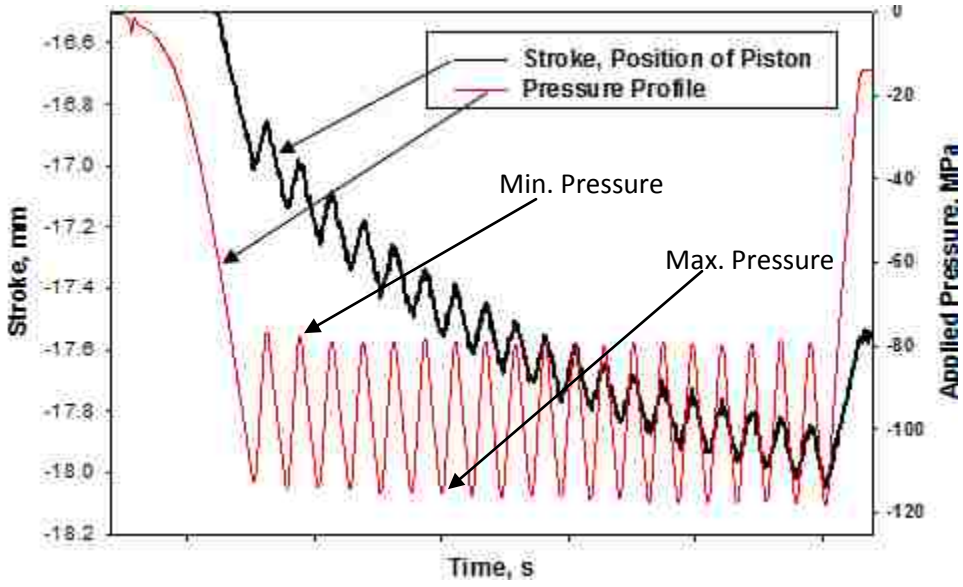

Figure 28 - Relationship between stroke and pressure vs. time.

3.2.5.3. *Melt Superheating Temperature*

Melt superheating temperature is a temperature when liquid melt is heated to higher than its liquidus temperature and homogenized for few minutes before melt delivery. In this investigation 750 ± 10^{o}C was used as melt superheating temperature.

3.2.5.4. Metal Casting Temperature

The temperature at which the molten metal is delivered into the die cavity has a significant effect on the quality of the casting and the die life. Too low a pouring temperature was avoided, as it can cause incomplete die fills and cold laps. Too high a casting temperature was also avoided as it may cause excessive porosity in the cast sample and adversely affect the die life. In this investigation, pouring temperature was measured at 0mm from the bottom of the cavity. Since liquid melt was delivered through a manual gating system (Fig. 29), the pouring temperature varied in a wide range between 635°C and 715°C, which are above the liquidus temperature of A356 alloy.

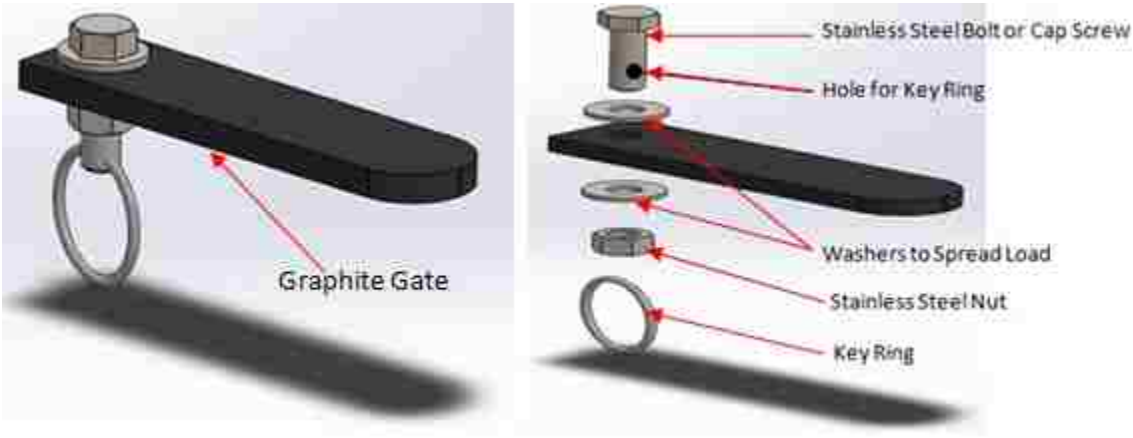

Figure 29 – Gating System, a) Graphite Gate, b) Components of gating system.

3.2.5.5. Die Temperature

The initial die temperature was monitored within close limits. Too low a die temperature may result in premature solidification affecting ability of melt treatment. Too high a die temperature may cause surface defects and welding of the casting to the die in general. A die temperature of 250 ± 10°C was generally maintained for all of the experiments.

3.2.5.6. Die Coating and Lubrication

Some release agents used in pressure die casting work reasonably well in squeeze casting applications. A commonly used lubricant is Boron Nitride that was sprayed onto the die and the plunger between each cycle. Limiting the thickness of the coating/lubricant under 50 microns can prevent surface contamination of the parts with coating residues stripped from the die surface. This lubricant was used in all of the SC Experiments to lubricate the die cavity. The coating needs to be dried well before delivering the melt into die cavity as it creates gas porosity inside the casting.

3.2.6. Test Control Software and Data Collection Procedure for Squeeze Casting Experiments

A special computer software was developed by Dr. Al Conle as part of an Open Source Fatigue Test Control Software servo hydraulic test control project. The software is a combination of C++, FORTRAN and Linux scripts and run on a specially designed PC computer with a Microstar 840/103 analog to digital(A/D) and digital to analog(D/A) control processor board installed on the PCI bus.

As shown in Fig. 31, Data Acquisition (DAQ), Data Acquisition Processor (DAP) boards at PC, Bayonet Nut Coupling (BNC) Connectors and Instron Control Panels are the data collecting devices that transmit experiments generated data to the software.

Data collection and control signals for stroke command (D/A) (plunger position), applied load (A/D) are managed by the Instron 8800 servo control system and temperatures(A/D) are conditioned by a Nat. Instruments SCXI-1000, which are illustrated in Figure 32.

Figure 30 - SC-UMSA test set-up, data recording and data collection devices: main test and data control computer monitor on left, SCXI-1000 at center, and HP system for monitoring temperature of thermocouples at the right.

The control computer software records six Data Channels:

Channel 1 Position of the plunger (stroke): ±10V

Channel 2 Load: ±10V

Channel 3 Liquid melt temperature: ±5V

Channel 4 Solidification temperature of the sample: ±5V

Channel 5 Outlet temperature of the waterlines: ±5V

Channel 6 Die temperature near sample chamber: ±5V

The Instron test controller and the PC test controller measure the conditioned signals, such as stroke, load or temperature, in voltage units. Ram, stroke and load are amplified to be in a range of +/-10Volts. The NI SCXI - thermocouple conditioner amplifies the temperature generated millivolt signal from the thermocouple to a range of +/-5V.

Data for each channel was recorded in the form of a digital +/-32767 numbering system which was then scaled for the range of +/-10.000 volts prior to storage on the disk. Since the computer program reads everything in voltages, it was necessary to develop a relationship, through "calibration" between device's voltage output and the actual signal or variable of interest.

The Instron mechanical testing machine was calibrated by Instron standard such that

(a) Stroke or ram displacement: +/-10.000V is +/-75mm

(b) Load on +/-10.000V is +/-50.0kN

3.2.7. Calibration of Thermocouple and Data Acquisition System

3.2.7.1. Thermocouple and Selection Criteria

Apart from Data Acquisition System as discussed earlier, another important sensor utilized to collect data is the thermocouple. In this research, thermocouples are widely used to measure temperature of die, melt and characterize of the solidification process. Hence the accuracy of thermocouples was established through calibration procedure before carrying out the experiments. Before going into details of calibration, some explanation will be given on the type and selection of thermocouples for a clear understanding of its significant performance.

A thermocouple is a sensor for measuring temperature. The working principle of thermocouple is the Seebeck effect, which states that when two dissimilar metal wires are connected with each other in a loop to form two junctions that are maintained at two different temperatures, a voltage potential or electro-motive force (emf) will be generated

and current will flow through the loop circuit. The current will be proportional to the difference in temperature between the junctions and the metals used.

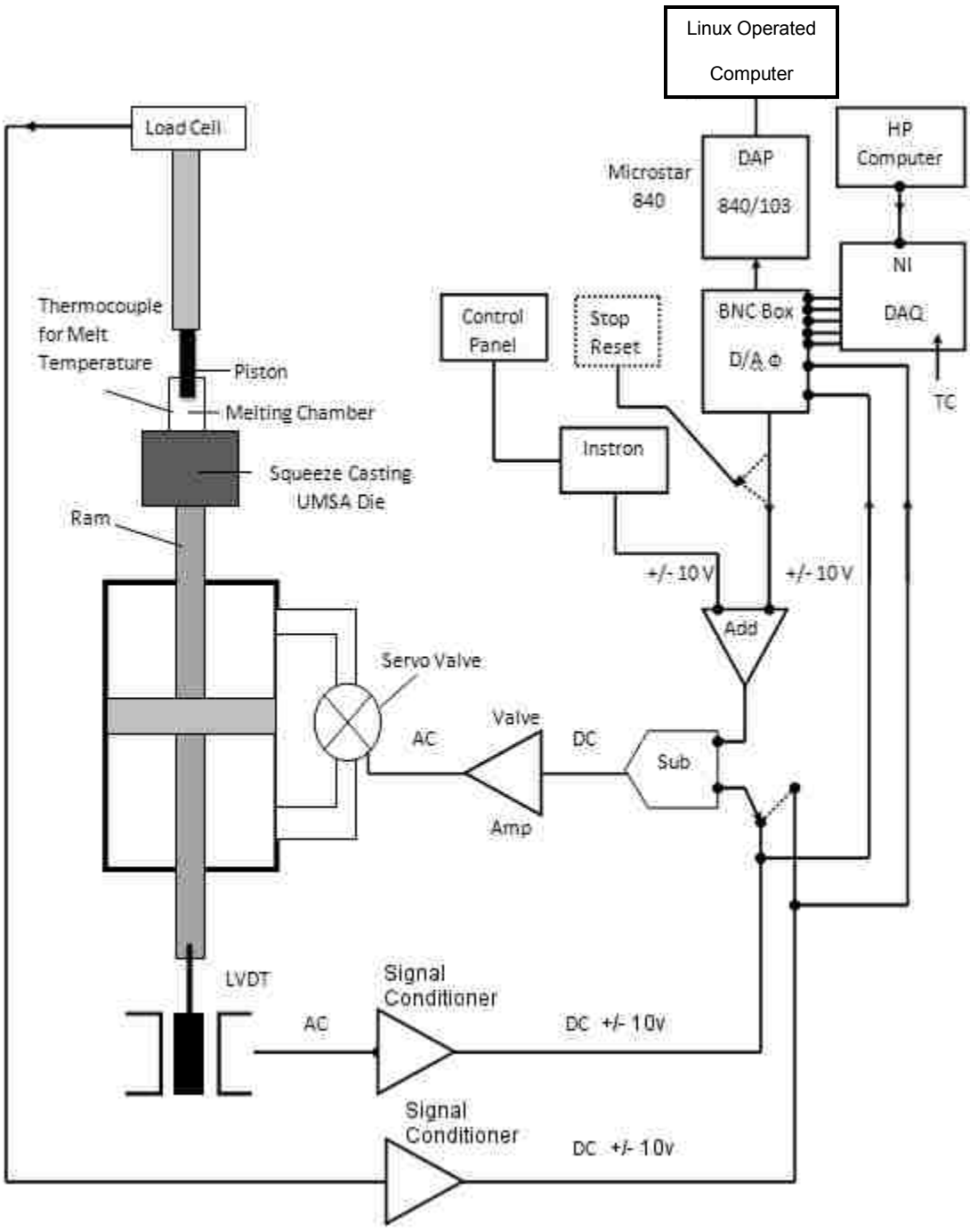

Figure 31 - Schematic diagram of SC-UMSA data collection.

The first task was to select the most suitable thermocouple for recoding temperature of solidification sequence of A356 Alloy in SC UMSA Platform. Thermocouples are available in different combination of metals. The four most common types of thermocouples are J, K, T, and E. Each type has a different temperature range of operation, although the maximum temperature varies with the diameter of the wire used in the thermocouple. The most common thermocouple types and their temperature ranges are given in the Table 10.

Sheathed thermocouple probes are available with one of the three junction types: grounded, ungrounded, or exposed. At the tip of the grounded junction probe, thermocouple wires are physically attached to the inside of the probe wall. This results in good heat transfer from the outside, through the probe wall to the thermocouple junction. In an ungrounded probe the thermocouple junction is detached from the probe wall. The response time is slower compared to the grounded style but this offers electrical isolation. The ungrounded junction is excellent for applications where stray EMFs would affect the reading and for frequent or rapid temperature cycling. In the exposed junction style, the thermocouple protrudes out of the tip of the sheath and is exposed to the surrounding environment. This type offers the best response time but is limited in use to non-corrosive and non-pressurized applications [103]. Figure 33 illustrates the three junction types discussed above.

The K-type ungrounded thermocouples are used in all of the experiments conducted for this research project and thesis. The chromel-alumel K-type thermocouple is produced by OMEGA with a 304 stainless steel sheath. The OMEGA specifications used are

"KMQSS-020U- 6" that stand for a 6″ length probe, 0.020″ or 20 thou (0.508mm) diameter and U-for ungrounded.

Table 10 - Thermocouple Types and Temperature Ranges.

Thermo-couple Type	Thermocouple Alloy	Temperature Range °C	Standard Limit of Error	Comments
J	Iron– Constantan	0-750	Greater of 2.2°C or 0.75%	Suitable for reducing atmospheres
K	Chromel - Alumel	-200-1250	Greater of 2.2°C or 0.75%	Recommended for use in clean oxidizing atmospheres.
E	Chromel - Constantan	-200-900	Greater of 1.7°C or 0.5%	This thermocouple has the highest emf output of any standard metallic thermocouple.
T	Copper - Constantan	-250-350	Greater of 1°C or 0.75%	Recommended for mildly oxidizing and reducing atmospheres. Suitable for applications where moisture is present.

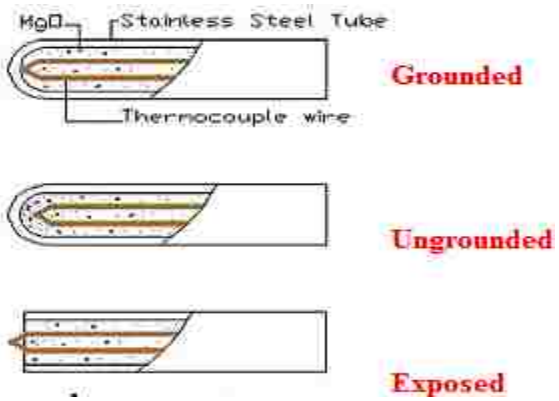

Figure 32 Three Junctions of Thermocouples [103]

Ungrounded thermocouples were chosen in order to have less interference from the surrounding Electromagnetic Force (EMF). Moreover, for a better response time, 20 thou (0.508mm) diameter is selected, as the lower the diameter of thermocouple, the better the response time [103]. It is estimated that for the same thermocouple, the response time could be approximately 0.25s in water environment [90]. Other sources indicate values of less than 0.13s [104]. However, there was found no available response time in high temperature and high pressure environment.

3.2.7.2. Calibration Requirements

Calibration is the process of standardizing a temperature monitoring instrument to ensure that it will measure within a specific temperature range in which the instrument is designed to operate [105]. It is also a process to verify and validate the thermocouple at its working condition. Accuracy of a thermocouple is its ability to measure temperature correctly without error. Generally thermocouples are designed to work at certain conditions. However, due to necessity of experimental condition thermocouples are used in different environments, e.g. slow solidification environment to high solidification environment as well as atmospheric pressure to high pressure environments. Investigators found that pressure has an effect of less than 5^{o}C on the Chromel - Alumel Thermocouples at 4GPa pressure in the temperature up to 1000^{o}C, while for Pt-Pt Rh thermocouples the correction factor is 35^{o}C in the same range of pressure and temperature [106]. By contrast, Ivan C. Getting and George C. Kennedy from the University of California found that at 3GPa and for temperature up to 600^{o}C, the corrections for Chromel- Alumel Thermocouples are less than 2^{o}C [106]. In contrast to those high pressure experiments, in this investigation we have used only 50-115 MPa

pressure. Therefore, it is expected that there will less effect of pressure on the Chromel-Alumel Thermocouples. Apart from the pressure effect, there might be also effect for high solidification rate and effect of cyclic pressure as well as combined effect on the thermocouples data.

3.2.7.3. Calibration Procedures

Thermocouples are calibrated by measurement either at a series of fixed point temperatures, e.g. melting/solidification points or, by comparison with reference or standard thermometers, in thermally stabilized baths or furnaces suitable for the calibration, or by a combination of techniques, e.g. comparisons and fixed-point temperatures [107, 109]. Fixed-point(s) and standard thermometer(s) shall be traceable to national standards. Generally, fixed point calibrations are only required for the calibration of platinum-rhodium thermocouples at the highest accuracy. However, it could be used for Chromel –Alumel thermocouples as well.

In this investigation K-type thermocouples (Chromel-Alumel) were used to measure solidification sequence of A356 alloy whose liquidus and solidus temperature are 614.4^{o}C and 555^{o}C respectively and the melt temperature was in the range of 700 - 750^{o}C. Therefore, equivalent procedure of fixed points temperatures e.g. solidification temperature of pure (99.99) Al and Zn are used for the calibration as their solidification temperatures (as per NIST) are 660.32^{o}C and 419.6^{o}C respectively.

In order to perform the calibration the following factors need to be considered:

1. Effect of slow heating/cooling rates on the thermocouple and data acquisition system's temperature characteristics.

2. Effect of high heating/cooling rates on the thermocouple and data acquisition system's temperature characteristics.
3. Effect of static pressure on the thermocouple and data acquisition system's temperature characteristics.
4. Effect of cyclic pressure on the thermocouple and data acquisition system's temperature characteristics.
5. Combined effects of high cooling rate and cyclic pressure on the thermocouple and data acquisition system's temperature characteristics.

However, due to severe time constraints the calibration procedures are kept limited to the following procedures:

1. Calibration to convert voltage into degree C at SC UMSA.
2. HT UMSA Calibration against NIST calibrated data for slow solidification rate.
3. SC UMSA Calibration against HT UMSA calibrated data for high solidification rate at atmospheric pressure.

1. Calibration to Convert Voltage to Degree (^{o}C) at SC UMSA.

Thermocouples produce a voltage output that can be correlated to the temperature that the thermocouple is measuring. To convert the voltage into temperature and to determine a relationship between temperature and voltage, the first calibration was done through carrying out experiments for pure aluminum and pure zinc at atmospheric pressure in SC-UMSA Platform. During the experiments, temperatures were recorded separately in degree Celsius converted from voltages in Windows (HP) and Linux operated computer respectively. The solidification temperature of pure aluminum and zinc were determined through thermal analysis and tabulated in Table-11, in both degree Celsius and voltage

and plotted in Fig. 33. A linear regression analysis provided a linear relationship between voltage and temperature that was used in the automated program to convert the temperature from voltage to degree C. The relationship is: y = 240x+25, where y = temperature in ^{o}C, x = voltage

Table 11 - Calibration Between Voltage and Temperature.

Tested Materials	Temperature(ºC)	Voltage(v)
Pure Al	652.15	2.604
Pure Zn	410.29	1.599

2. **HT UMSA Calibration against NIST Calibrated Data for Slow Solidification Rate at Atmospheric Pressure**

The Second calibration was done in HT UMSA Platform at atmospheric pressure and in a very slow solidification rate. The solidification temperature of pure Al and Zn were determined through thermal analysis using UMSA Tai software. Experimental data are plotted against NIST Calibrated solidification temperature of pure Al and Zn. Using the regression equation **y** = 0.9988x + 0.0227, (where x and y represent uncalibrated and calibrated temperature respectively) solidification temperature of pure Al and Zn are recalculated and found that the new calibrated temperature is almost equal to the NIST calibrated data (Table 12) as ΔT is 0.01 and 0.02^{o}C respectively.

3. **SC UMSA Calibration against HT UMSA Calibrated Data for High Solidification Rate at Atmospheric Pressure.**

The third calibration was done in SC UMSA at atmospheric pressure and at a high solidification rate (e.g. 6.5^{o}C/s). As shown in Fig. 35, experimental solidification temperature of pure Zn and Al are plotted against the HT UMSA calibrated data. The

high SR regression equation, **y** = 1.0x + 11.0 (where x and y represent uncalibrated and calibrated temperature respectively) showed that experimental temperature is 11°C lower than the calibrated temperature. Data Acquisition was adjusted accordance with the correction factor of 11°C. All data were recorded and listed in Table 12.

Sincere there was no calibrated data available at high pressure environment for pure Zn and Al, all experimental data produced at cyclic pressure were corrected against the calibrated data of atmospheric pressure at high SR in SC UMSA Platform. For instance, the correction factor was incorporated for the experimental data produced at 90 MPa with 10 pressure cycles as shown in Figure 36. However, it is recommended to incorporate pressure effect in future studies.

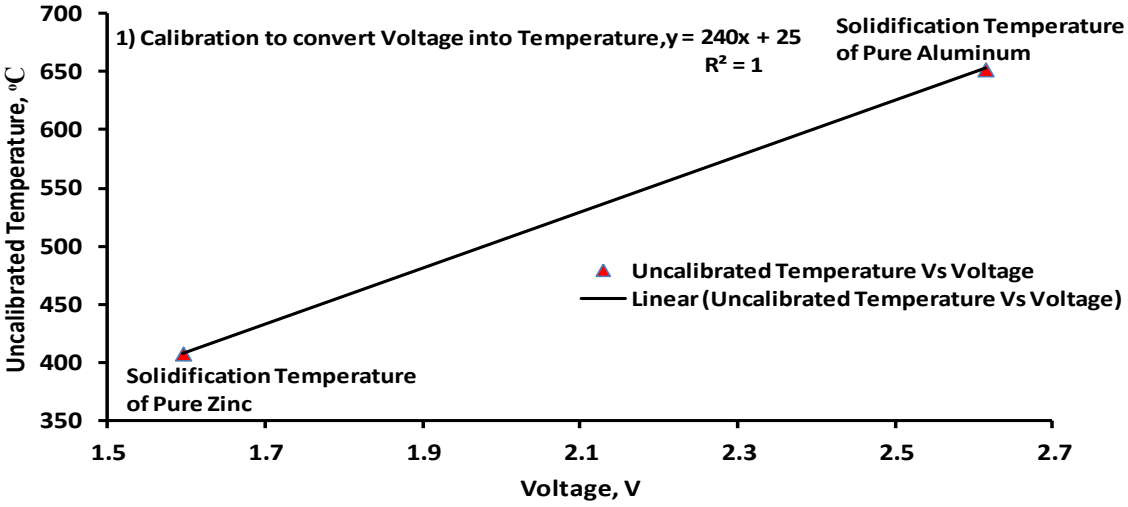

Figure 33 - Relationship between voltages and uncalibrated temperature.

Table 12 - Calibration Data Summary.

Experi-mental Materials	NIST Calibrated Solidification Temperature (°C)	HT UMSA Uncalibrated Solidification Temperature (°C)	HT UMSA Calibrated Solidification Temperature (°C)	SC UMSA Uncalibrated Solidification Temperature (°C)	SC UMSA Calibrated Solidification Temperature (°C)
Zinc	419.572	420.03	419.55	410.29	421.29
Aluminum	660.32	661.1	660.33	652.15	663.15

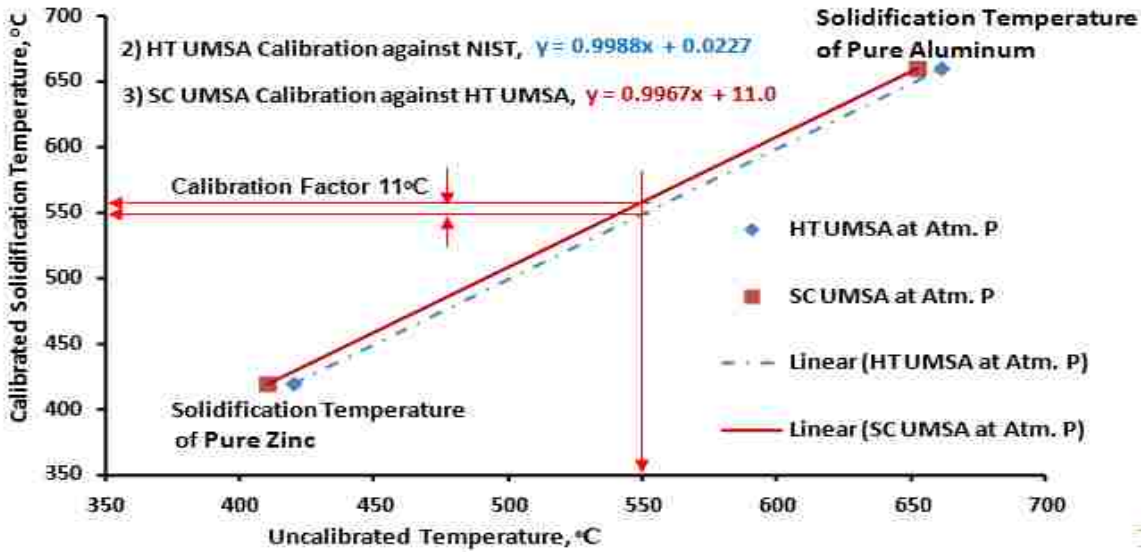

Figure 34 - Relationship between calibrated data and uncalibrated data.

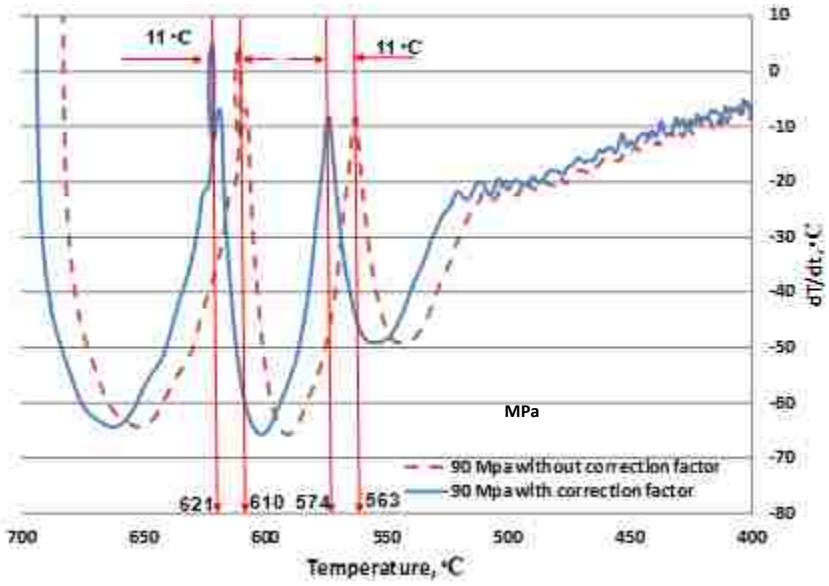

Figure 35 - Incorporation of calibration factor in the first derivative of cooling curve of unmodified A356 at 90 MPa for 10 pressure cycles.

3.2.8. Experimental Procedure for the Squeeze Casting

Before starting the squeeze casting experiments, the die cavity was cleaned with small tools to break off any loose residual metal left from a previous experiment. A vacuum

cleaner was used to remove all tiny particles. A layer of boron nitride die release was then sprayed onto the melt and mold chamber walls.

The thermocouple for measuring solidification temperature of the squeeze cast sample was also coated or thin filmed with boron nitride to minimize the thermocouples sticking in the sample or in the die and then inserted into the access hole at the corner of the die such that the tip was at the center of the die cavity. Any extra vapor or moisture inside the die cavity was evaporated during die warm up to a temperature of 250 ^{o}C using the two cartridge heaters. The graphite gate was then inserted into its position just beneath the melting chamber in the die and it too was sprayed with boron nitride.

The test sample was placed inside the melting chamber on top of the gate. A thermocouple was inserted into a small hole previously drilled into the top of the sample for measuring and recording the melt temperature. Another thermocouple was inserted diagonally into a blind hole at the side of the die such that the tip measured the die temperature close to the die cavity chamber. An additional thermocouple was inserted into a small hole located near the bottom of the melt chamber to measure the external temperature of the melt chamber and its output was connected to the temperature controller of the melt chamber. The melt chamber that was coiled with one high temperature tubular heater was able to heat up the melts up to 800 ^{o}C. It was energized with 110 VAC from the controller.

When all thermocouples were placed in their respective positions, four channels Labview software was started in the HP computer to see whether all thermocouples were working

properly and to observe and record the heating/cooling of the melt. The desktop view of the four channel software is shown in Fig. 36.

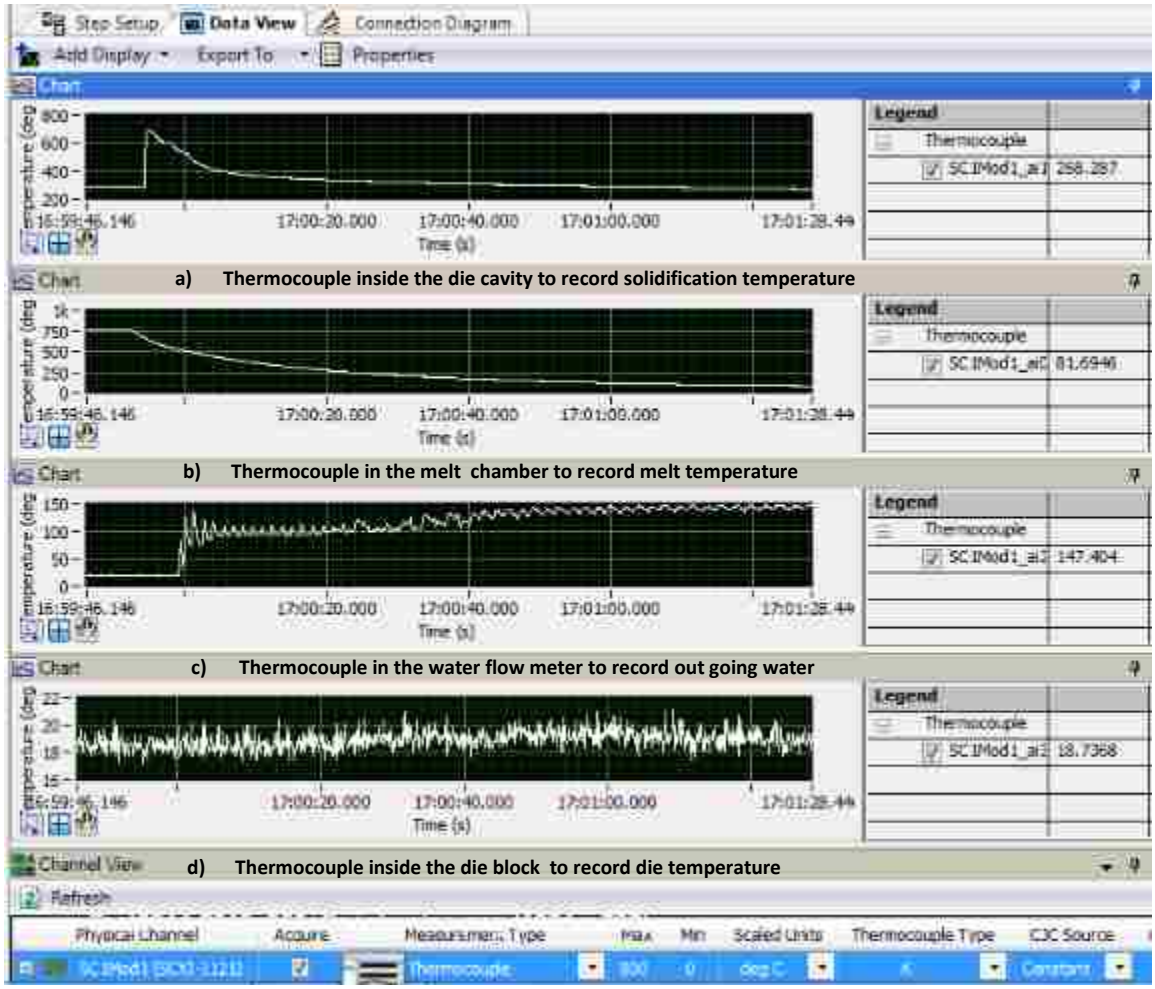

Figure 36 - Desktop view of four channels labview software for monitoring and recording temperatures of thermocouples in HP computer as shown in a), b), c), and d).

The Instron piston was set at a position so that the plunger was just above the melting chamber. The environmental and safety chamber was then closed to contain any melted aluminum splash during the test. The cartridge heaters were controlled manually using a 110 VAC dimmer switch and allowed the die temperature to stabilize at 250 °C with a ± 10 °C. When the die temperature reached 180 ° C, the tubular heater surrounding the melting chamber was switched on.

As the alloy temperature approached to test sample's melting point, the automated software in the main data control computer for SC-UMSA was started to collect the data through six channel sensors as described earlier. When the liquid metal temperature reached 750°C, a targeted temperature for the liquid metal of A356 Al alloy, the melt was held at that temperature for 5 minutes to homogenize the liquid phase. After the hold the slide gate was opened to deliver the molten metal into the die cavity below. From this part of the experiment to the end of solidification, the process was automatically controlled by the Squeeze Casting Test Control Software.

The squeeze casting test control program works in six stages, and in each stage all 6 channels of data are recorded to the hard disk at 333 data points/second/channel. The six control stages are:

Stage 1: The program monitors the die cavity thermocouple to see when the melt has been delivered to the die cavity. When the thermocouple exceeds 1.5 volts the program concludes that the cavity is filled with melt and stage 2 begins.

Stage 2: The program monitors the die cavity thermocouple's signal to see when a peak temperature is achieved. The computer tracks the voltage on the way up and when a specified voltage drop (0.50) occurs the program concludes that the peak temperature has been achieved. The volt window is required because the thermocouple signal has inherent noise which, if the window is too small, could trigger an incorrect "peak detected" state. When a peak temperature has been observed stage 3 begins.

Stage 3: The program monitors the die cavity thermocouple as the temperatures decrease to see when a user defined post peak temperature trigger has occurred. Then it goes to stage 4.

Stage 4: The program gives instruction to move the ram (via outputs onto the D/A) into a predefined position just above the dropped melt at a high ram speed. The ram speed needs to be determined iteratively as overshoot of the target position above the melt is possible. As the ram gets close to the target position the voltage step size is decreased by a factor of 2, to slow the ram. When the stage 4 ram position is reached, stage 5 starts.

Stage 5: The program selects a target load voltage from the program list and change stoke (ram position) in very small voltage steps to minimize overshoot of the target load. As each of the programmed loads is achieved, select the next target load in the list. When the load list is completed go to stage 6.

Stage 6: The program monitors and records all 6 channels data until the stop signal is received and shut down eventually.

The die cavity thermocouple recorded data of the solidification process to verify the solidification/cooling rate of the test sample. Just after dropping the melt into die cavity, the water flow is on. The water lines inside the die block helped cooling the die block and the cast sample. However, the heavy die block absorbed the heat so fast that the subsequent water cooling had negligible effect on the solidification process as by the time the water started cooling the block the solidification process usually did finish. The outlet water temperature was recorded as one of the data channels.

The experimental data was processed by the PC Data Acquisition System (DAS). Final outputs were recorded in a large data log file for computation purposes, which was then truncated to required set of data. Using a Linux Bash script a set of data files with important variables including time, temperature, stroke and cyclic pressure were created for data analysis. All data channels were converted from volts to their respective units (e.g. time in seconds, stroke in mm, temperature in ^{o}C etc.).

The Savitzky-Golay algorithm was applied twice, each time with a window of 60 points on both sides of each smoothed point. The point window size was larger than that of used in the standard UMSA program because the number of samples per second was larger. Savitzky-Golay code was also used to compute the first derivative of the cooling curves. In parallel to the PC control and record system, the HP computer and its UMSA software was used to obtain heating/cooling curve and 1st derivatives.

Once the solidification process was completed, the subsequent step was to eject the test sample (see Fig. 37) from the die. This was done through the pneumatic ejection cylinder activated by way of a detent control valve. The maximum capacity of the air regulator was between 80-90 psi which ejected the test sample from out of the die cavity. Prior to the ejection of the sample, an attempt was made to remove the specimen thermocouple from the die though it was not usually successful. Then the test sample was prepared for the metallographic observations through LOM & SEM/EDS.

Figure 37 – SC test samples.

3.3. High Temperature Universal Metallurgical Simulator and Analyzer (HT UMSA)

Part of the calibration (slow SR) and initial thermal analysis of UM A356 alloy as well as the heat treatment of the squeezed cast A356 samples were done in the High Temperature Universal Metallurgical Simulator and Analyzer Technology Platform (HT UMSA), a unique platform for thermal analysis jointly developed by the researchers at the University of Windsor and the Silesian University of Technology in Gliwice, Poland (Fig. 38). It has been patented as Canadian Patent No: 2,470,127 and US Patent No: 7,354,491.

3.3.1. Hardware Platform

The HT UMSA consists of several components, including:

A) Melting and Environmental Chamber

The melting chamber is a four sided uncovered stainless steel container, where the testing is performed. Inside the melting chamber is the induction coil, inside which heating and melting of the test samples takes place. During operation at high temperatures, the induction coil is protected from the heated test sample by the cement insulation and the insulating sheath. The induction coil is also cooled by circulating cold water flowing through the cooling coil and heat exchanging system.

Figure 38 - Photograph of the HT UMSA Technology Platform. A – Melting and environmental chamber, B - heat exchanging systems, C – Power supply, D – Data acquisition system, E –Desktop computer, X – Water cooling pump.

B) Heat Exchanging Systems

The heat exchanging system consists of a water pump and controller capable of cycling 220 liters per hour of water from the cooling coil to the heat exchanger.

C) Power Supply

The UMSA is powered by a 5 kW power supply with options for altering the output amperage and frequency.

D) Data Acquisition Unit

The data acquisition unit is a 16-bit system capable of logging temperature/time measurements on two channels simultaneously and has a scan rate of up to 100Hz per channel. However, 5Hz scan rate was used during the current experiments.

E) Desktop Computer

A desktop computer interfaces with the HT-UMSA platform via a National Instruments data acquisition system. Live control of the platform through the computer software allows the operator to specify detailed process parameters, make in-process input changes, if necessary, and complete post-process analysis using custom designed thermal analysis software. This thermal analysis software allows for calculation of various data of metallurgical importance, including derivatives, temperature of metallurgical reactions, fraction solid curves, etc.

3.3.2. Software Platform

The software components of the UMSA consist primarily of [90] two front-end programs namely UMSA-TAI and UMSA-CA, which were designed for use with the UMSA and handle all end-user thermal analysis operations. These programs were written in C++ by the developers of the hardware system.

UMSA-CA is used for control and data logging during experiments conducted on the UMSA platform. It accepts user input in the form of settings, temperature settings, heat treatment paths, etc. and regulates the power supply accordingly. If cooling is required it may also release gas coolants via the integrated cooling coil.

UMSA-TAI is a post-processing software used to analyze data logged by UMSA-CA. Using the temperature/time data as input; the program is capable of efficiently calculating

information of metallurgical importance, including derivatives, baselines and fraction solid curves. The program is well-suited to the visualization and comparison of multiple graphs and also has curve smoothing capabilities (following the Savitzky-Golay algorithm). The data is also easily exportable to any standard spreadsheet program for further analysis [90].

3.3.3. Solution Treatment Procedure

One fourth of squeezed cast samples were cut longitudinally for the heat treatment. A 10mm deep thermocouple hole was made at the top center of the quarter sample and then cleaned by ultrasound cleaning. The sample was placed inside the induction coil of UMSA. A K type thermocouple coated with boron nitride was inserted into the hole at the top of the sample.

The UMSA-CA software, described in the previous section, was used to run the heat treatment by using 20% power to heat up the sample to 540 $^{\circ}$ C, where the temperature was held for a certain period e.g.(15-30 minutes) for both as-cast A356 alloy, and the Sr modified A356 alloy as shown in Fig. 39. The sample was then quenched into the warm water of 70 $^{\circ}$ C. No artificial aging was done for any of the samples except natural aging.

3.4. Metallographic Sample Preparation

Metallographic samples were prepared at the MCPT lab in the University of Windsor. Squeezed cast samples were cut using a saw along the longitudinal axis and one half samples was cut in transverse section. The sample pieces were then mounted in blue epoxy using the Buehler Mounting Press. Grinding and polishing were done in Buehler Ecomet ll Grinding, Lapping, Polishing Machine at a single speed of 300rpm or lower.

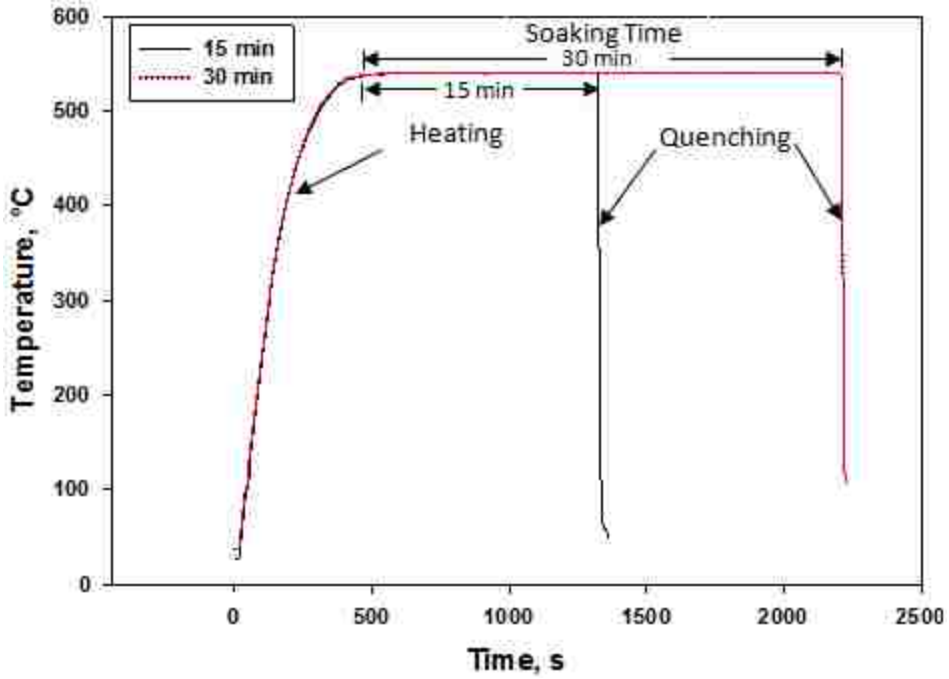

Figure 39 - Solution Treatment heating- quenching curve.

Samples were ground manually using Silicon Carbide 320 grit paper in a magnetic disc with an adaptor followed by polishing using Struers diamond solution MD Largo (9µm for 4 min), MD Mol (3µm for 3 min) and final polishing by OP-Chem (OP-S, 0.04µm for 1 min). Final cleaning was done with ethyl alcohol (95%).

3.5. Light Optical Microscopy (LOM) Analysis

The LOM observations were made using a Leica Q5501W microscope connected with an OPTIXCAM camera and a desktop computer along with OCVIEW Image processing software. The microscope has five objective lenses (5x, 10x, 20x, 50x and 100x) which are in series with a 10x lens, resulting in a maximum of 1000x magnification. The imaging system was calibrated for all objective lenses to obtain accurate pixel: micron ratios. A calibrated scale of 2 mm is shown in the Figure 40 at different magnification.

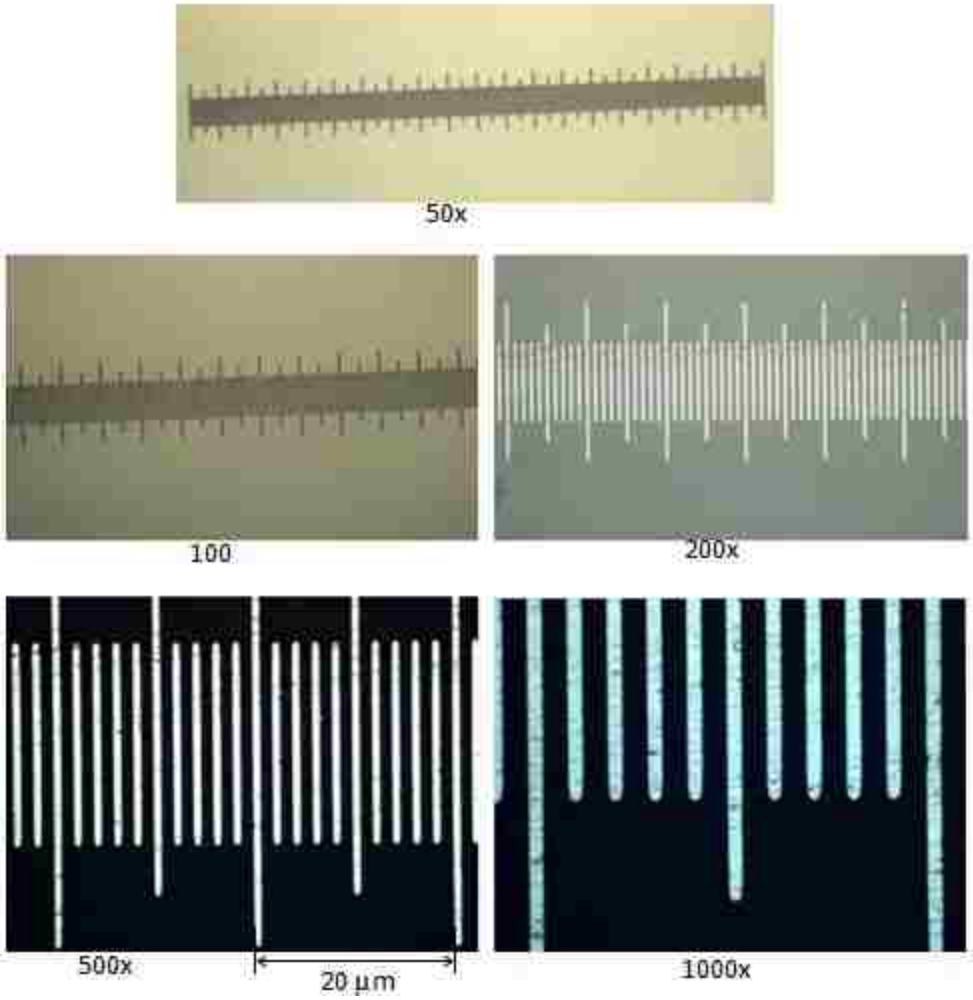

Figure 40 - Calibration scale at different LOM magnification.

3.6. Measurement of Dendrite Refinements - Secondary Dendrite Arm Spacing (SDAS) and Dendrite Cell Size

Secondary Dendrite Arm Spacing (SDAS) is the distance between the two adjacent Secondary Dendrite Arms. Dendrite cell size is the width of individual dendrite cells. As both measurements procedures are similar, here only the SDAS measurements procedure is described as per the Ford Material Specification WSE-M2A151-A3 (also ASTM E-3).

The LOM micrograph of the as-cast A356 sample solidified at atmospheric pressure is shown in Fig.41. The intersection method was utilized to calculate the SDAS. Several lines were drawn over the Secondary Dendrite Arms in a perpendicular direction. The length of the intersect lines and the number of intersecting secondary dendrite arms were measured and the average SDAS was calculated as shown in the following paragraphs.

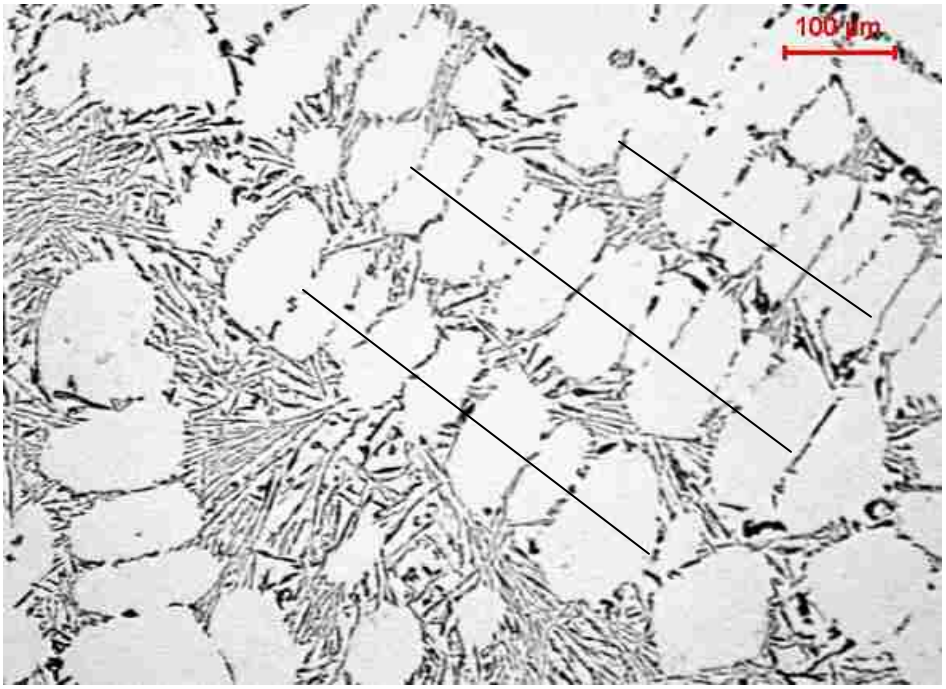

Figure 41 - The As-Cast microstructure showing the dendrite structure and superimposed intersect lines according to the ASTM R-1(Al. 100X) [58]

Measuring procedure of the SDAS is:

SDAS = (Total width of the secondary dendrite arms/Number of secondary dendrite arms);

The average SDAS = (L1 + L2 + L3)/(N1 + N2 + N3)…….Equation 8

Where, L1, L2, L3 stands for the lines of dendrite width and N1, N2, N3 stands for number of dendrites in the respective lines.

In order to obtain statistical reliability and repeatable results, numerous measurements had to be taken. The SDAS and dendrite cell size measurements were based on 20 fields, and 5 measurements were taken in each field.

3.7. Experimental Design

A summary of the squeeze casting experiment and testing conditions used during experimentation is shown in the Table 13 while the solution treatment matrix is stated in the Table 14.

Table 13 - Matrix of SC- UMSA Tests.

Runs#	Sample Reference	Alloy	Applied Pressure(MPa)		No of Pressure Cycle	Temperature of Applied Pressure (°C)	
			Min.	Max.		Start	End
1	31513	Unmodified	0	0	-	-	-
2	31813	″	0	0	-	-	-
3	32513	″	0	0	-	-	-
4	32713	″	0	45	1	-	-
5	32813	″	0	50	1	615	614
6	40113	″	0	55	10	618	614
7	40213	″	0	60	10	615	608
8	50613	″	0	60	1	-	-
9	41913	″	30	80	10	619	613
10	41713	″	20	90	10	622	619
11	60513	″	60	100	10	-	-
14	62513	″	80	115	20	620	537
12	61013	″	20	115	40	615	362
13	61213A	″	20	115	50	622	348
15	51313	0.04%Sr +	0	100	1	591	568
16	51513	″	75	100	10	614	593
17	72413B	0.015%Sr + A356	0	0	-	-	-
18	61913	″	20	115	7	619	565
19	71613	″	20	115	50	619	360
20	72413A	1%Al_2O_3 +	0	0	-	-	-
21	61213B	″	20	115	2	615	602
22	62013	″	80	115	20	615	538
23	71513	″	80	115	50	614	430
24	72413C	0.015%Sr+ 1%Al_2O_3 +	0	0	-	-	-
25	81413	″	20	115	12	623	534
26	62413	″	80	115	20	617	523
27	61713	″	20	115	50	623	366

Table 14 - Matrix of Solution Treatment Experiments.

Runs #	Test reference	Alloy	Holding Temperature, (°C)	Holding Time, (s)
1.	62513	Unmodified A356	540	30
2.	62513	Unmodified A356	540	15
3.	71613	Sr modified A356	540	30
4.	71613	Sr modified A356	540	15

CHAPTER FOUR - RESULTS AND DISCUSSION

4.1. Determination of Thermal Characteristics of A356 Alloy

As mentioned in section 2.3, a lot of research has been done on the thermal analysis of A356 at slow cooling rates and solidification characteristics were identified. The MCPT Group using a low thermal mass crucible produced high resolution thermal data as shown in Figures 21-22. However, no thermal data was found for the experimental high pressure profile of the A356 alloy or other.

In this investigation, the thermal behavior of unmodified A356 alloy was characterized with an experiment done under slow solidification using the HT UMSA Platform. The cooling curve and its first derivation are shown in Fig. 42. Another experiment was done under relatively high solidification rate in SC UMSA Platform and the cooling curve and its first derivatives are illustrated in Fig. 43. Both experiments were done under atmospheric pressure. A number of other experiments were done under high pressure and high solidification on SC UMSA Platform. An example of the cooling curves and first derivative of UM A356 alloy under 115 MPa with 20 pressure cycles is shown in Fig. 44. In all cases thermal characteristics of A356 were determined using UMSA Thermal Analysis (TA) methodologies and procedures.

The thermal characteristic points are briefly discussed here to show the readers how the points have been determined.

The α-Al Dendrite Nucleation Temperature, ($T^{\alpha DEN}_{NUC}$) – Non Equilibrium Liquidus Temperature (NT_L)

The α-Al Dendrite Nucleation Temperature, ($T^{\alpha DEN}_{NUC}$) characterizes the point at which primary α dendrites start to nucleate from the melt. This event is exhibited by the change in the slope of the cooling curve and determined by the first derivative inflection point (point#1 in figure 42-44). However, FDs in Figures 43 and 44 (SC UMSA – atmospheric pressure and SC UMSA – cyclic pressure respectively) with increased SR and cyclic pressure show progressively worsened spatial resolution to the point that the precise determination of the T_L (point # 1) is not feasible.

The α-Al Dendrite Minimum (Undercooling) Temperature, ($T^{\alpha DEN}_{MIN}$)

The α-Al Dendrite Minimum Temperature, **(**$T^{\alpha DEN}_{MIN}$**)** exemplifies a state (point#2 in Fig. 43) where the nucleated dendrites have grown to such an extent that the liberated latent heat of fusion stabilizes the heat extracted from the test sample. After this point, the melt temperature increases to a steady state growth temperature ($T^{\alpha DEN}_{G}$, point#3 in Fig. 43). The $T^{\alpha DEN}_{MIN}$ as the local minimum is determined by the point (point#2) at which the first derivative intersects the zero line (dT/dt=0). If the first derivative does not intersect the zero line, point#2 does not exist as in Fig. 42 and Fig 44.

The α-Al Dendrite Growth Temperature, ($T^{\alpha DEN}_{G}$)

The α-Al Dendrite Growth Temperature, ($T^{\alpha DEN}_{G}$ see Fig. 43) denotes the local maximum temperature of this reaction. It is also called the "steady state growth temperature". It corresponds to the second zero point (point#3 in Fig. 43) on the first

derivative curve (dT/dt=0) following the start of nucleation. If the first derivative curve in this region does not intersect the zero line as in Fig. 42 and Fig. 44, the $T\alpha^{DEN}{}_{MIN}$ and the $T^{\alpha DEN}{}_{G}$ both temperatures are identical and correspond to the maximum point on the first derivative curve.

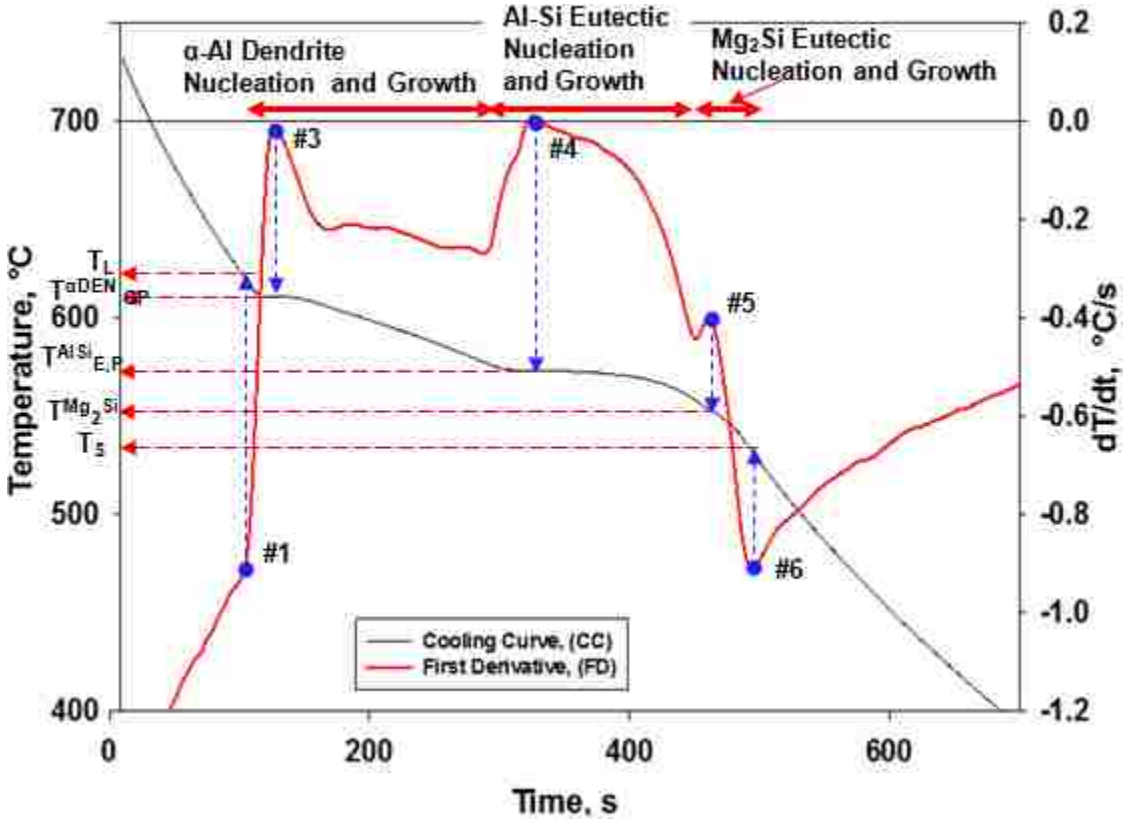

Figure 42 - Cooling curve and its first derivative of unmodified A356 at atmospheric pressure in HT UMSA Platform.

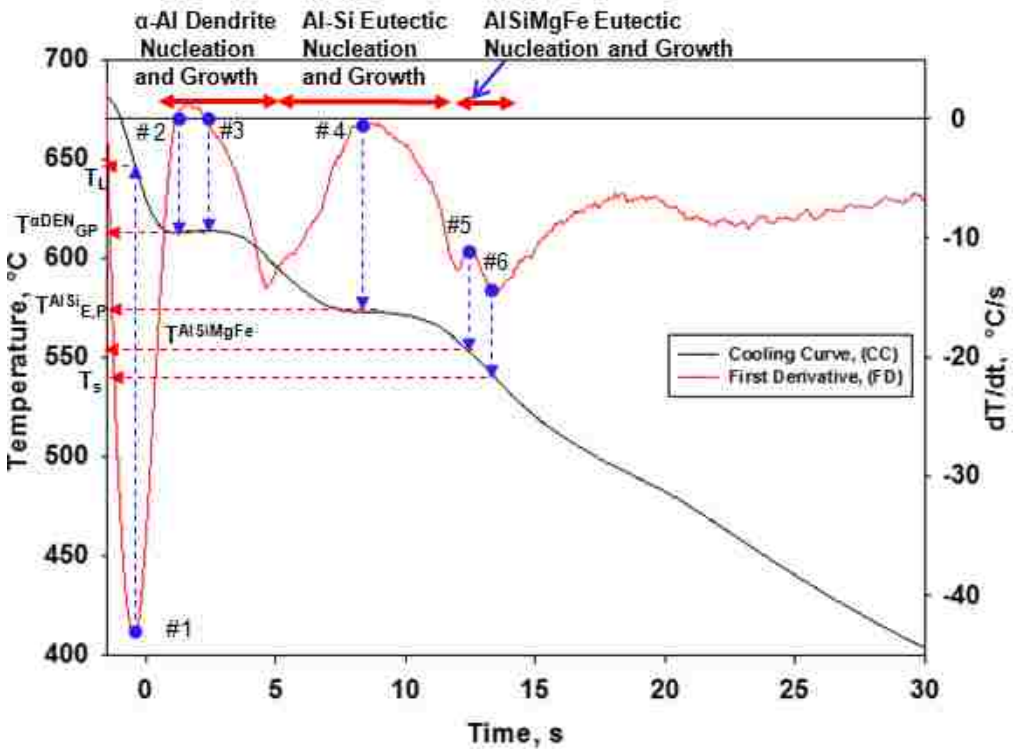

Figure 43 - Cooling curve and its first derivative of unmodified **A356** at atmospheric pressure in SC UMSA Platform.

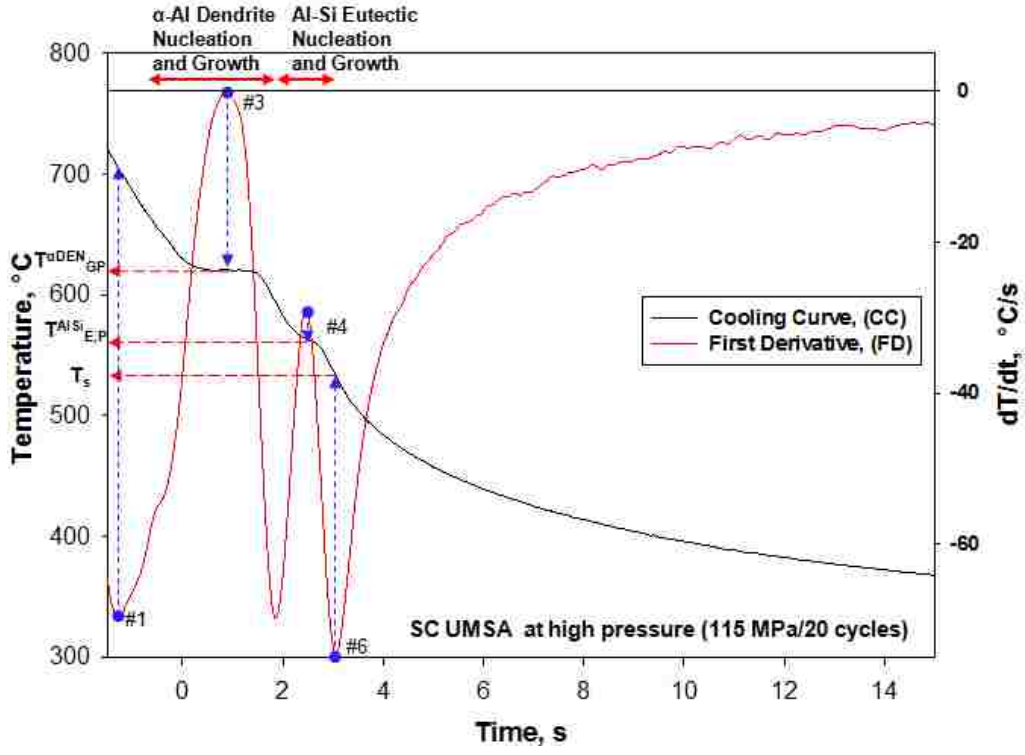

Figure 44 - Cooling curve and its first derivative of unmodified A356 alloy at 115 MPa pressure with 20 cycles.

The Al-Si Eutectic Growth Temperature, ($T^{AlSi}_{E,G}$)

Al-Si Eutectic Growth Temperature, ($T^{AlSi}_{E,G}$) represents the temperature at which considerable Al-Si eutectic growth occurs. This point (point #4 in Figures 42-44) generally corresponds to the maximum point on the first derivative curve, if the first derivative curve does not intersect the zero line. In this study the first derivative curve didn't intersect the zero line for any of the experiments.

Al- Mg- Fe-Si Eutectic Nucleation and Growth Temperature

According to the literature and to the University of Windsor's experimental 3XX alloy data, the Al-Si eutectic formation leads to a further localized increase in Mg and other remaining elements (e.g. Fe) contained in the liquid and will represent these phases by separate dT/dt peak(s). In figures 42-43, a third peak (point # 5) is formed in the first derivative curve that corresponds to the phases of either Mg_2Si or AlMgFeSi phase. At slow solidification rates less than 5°C/s, this peak is considered as the peak of Mg_2Si (Fig. 42). At moderate high cooling rates between 5-7°C/s, the Mg_2Si peak does not show up, instead the peak of AlMgFeSi appeared at approximately 554°C (Figure 43). However, at the high solidification rates above 7°C/s achieved during high pressure solidification, the first derivative curve neither show Mg_2Si nor AlMgFeSi as a separate peak (Fig. 44).

Solidus Temperature (T_S)

The solidus temperature is the temperature below which the melt is completely solidified and is the end of the solidification process. The corresponding temperature of point # 6 in

Figures 42-44 is considered to be the apparent solidus temperature as it is not feasible to determine T_S precisely due to the effect of high thermal mass die on the TA data.

4.2. Determination of Solidification Rate (SR)

The rationale of determining Solidification Rate (SR) for highly non-equilibrium solidification is discussed here. The solidification process is involved with the liquidus and solidus temperature range. The SR is defined as the temperature change divided by the time difference between the liquidus and solidus points. During slow solidification with low thermal mass at very slow SR, liquidus and solidus temperatures are easy to identify using UMSA high resolution thermal analysis as shown in Figure 42. However, a high thermal mass die in SC UMSA and high SR, precise determination of the T_L and T_S temperature is not feasible in all of squeeze casting experiments.

Hence, it was decided to use the α-Al Dendrite Growth Temperature ($T^{\alpha DEN}_{G,}$ point#3) as apparent liquidus temperature, and point #6 as apparent solidus temperature. Considering all of the above points, it was decided to calculate the apparent Solidification Rate (SR) based on $T^{\alpha DEN}_{G,}$ (point#3) and T_S (Point#6) for all highly non-equilibrium solidification tests on the SC UMSA platform.

Based on the above definitions and discussions in section 4.1 and 4.2, the characteristic points associated with individual non-equilibrium metallurgical events taking place during solidification processes in HT UMSA and SC UMSA are summarized and compared in Table 15. Also, a summary of squeeze casting test results and thermal characteristics points of unmodified and modified A356 alloy is tabulated in Table 16 and Table 17. Note that all experimental data are calibrated as discussed in section 3.2.7.

Table 15 - Thermal Characteristics of Unmodified A356 alloy.

Thermal Characteristics	Atmospheric Pressure		115 MPa /20cycles
	HT UMSA	SC UMSA	SC UMSA
Av. Solidification Rate, ^{o}C/s	0.3	6.5	40.1
α- Al Dendrite Growth Temperature, ($T^{\alpha DEN}_{G}$), ^{o}C	611.0	613.9	621.0
Al-Si Eutectic Growth Temperature, ($T^{AlSi}_{E,G}$), ^{o}C	573.0	573.0	564.0
Growth Temperature of Mg enriched phases, Mg_2Si or AlFeMgSi ($T^{AlSiMgFe}_{G}$), ^{o}C	553.0	552.0	-

4.3. Effect of Cyclic Pressure on the Unmodified A356 Alloy in the SC UMSA Platform

As has been discussed in Chapter Two, applying pressure on the solidifying melt in the water cooled steel die creates non-equilibrium solidification. Moreover, high pressure promotes better contact between the steel die and the test sample that enhanced the solidification rate. In the entire squeeze casting experiments, melt temperature and initial die temperature have been kept constant at 750^{o}C and 250^{o}C respectively with ± 10^{o}C. Pressure profiles are varied in terms of number of cycles and magnitude. Since pressure has been applied in a cyclic manner on the solidifying melt, it was found that the thermal and microstructural behavior of A356 alloy has been greatly influenced by the cyclic pressure in comparison to static and atmospheric pressure. All thermal characteristics of the unmodified alloy are tabulated in Table 16. Comparisons of cooling curves and their first derivatives are depicted in Figures 45 - 46 and individual graphs are shown in

Appendix A (Figures 114 – 137). All experimental data have been incorporated with the calibration as discussed in Chapter Three.

4.3.1. Changes in the Thermal Characteristics of Unmodified A356 Alloy

The first experiment in the squeeze casting platform was done by applying 50 MPa with 1 cycle pressure. As can be seen in Table 16 and Figures 45-46, the α-Al Dendrite Growth Temperature ($T^{\alpha DEN}{}_{G}$) was increased from 613.9°C (at atmospheric pressure) to 615.5°C together with a decrease in the Al-Si Eutectic Growth Temperature ($T^{AlSi}{}_{E,G}$) from 573°C (at atmospheric pressure) to 566°C at 50 MPa pressure. In later experiments the pressure was increased to 55 MPa and 60 MPa respectively for 10 cycles each. The combined effect of pressure and increasing number of cycles increases the $T^{\alpha DEN}{}_{G}$ to 618.1°C and 615.1°C respectively with further reduction in the $T^{AlSi}{}_{E,G}$ to 565°C and 563°C respectively. Two more experiments done at the pressure range of 80 MPa and 90 MPa for the same number of cycles showed that both the $T^{\alpha DEN}{}_{G}$ and $T^{AlSi}{}_{E,G}$ were increased simultaneously in the range of (619.1-622.3)°C and (572-578)°C. A high pressure test of 20 cycles at 115 MPa was performed in the seventh experiment and showed (Fig. 47) that the $T^{\alpha DEN}{}_{G}$ and $T^{AlSi}{}_{E,G}$ reached 620.8°C and 564°C respectively. Keeping the same level of pressure, two more experiments were carried out with further increasing number of cycles to 40 and 50 respectively (Fig. 47). However, it was found that in these latter experiments the α-Al Dendrite Growth Temperature ($T^{\alpha DEN}{}_{G}$) were reduced to 615.2°C and 613.1°C along with the $T^{AlSi}{}_{E,G}$ increase to 573°C and 568°C respectively.

Table 16 - Summary of Test Results and Thermal Characteristics of Unmodified A356 under Variable Pressure and Cycles.

Ref. #	Melt Drop Temp. °C	Pressure MPa		No. of Cycles	Temperature of Applied Press.°C		Cum. Energy Joule	$T^{\alpha DEN}{}_{G}$ °C	$t^{\alpha DEN}{}_{G}$ s	T_s °C	t_s s	$T^{ALS}{}_{EG}$ °C	Sol. Time s	SR °C/s	SDAS (D. Cell) µm
		Min.	Max.		Start	End									
31513	681	0	0	0	-	-	0	613.9	2.2	540.6	13.4	573	11.2	6.5	23.8
32813	643	0	50	1	615	614	8.6	615.5	2.6	547.8	5.5	566	2.9	23.2	15.2
40113	709	0	55	10	618	614	16.9	618.1	2.1	542.3	4.5	565	2.4	31.8	11.3
40213	666	0	60	10	615	608	18.4	615.1	1.1	542.2	3.5	563	2.4	30.7	9.9
41913	657	40	80	10	619	613	19.5	619.1	0.8	557.0	3.1	572	2.3	27.3	11.9
41713	693	20	90	10	622	619	20.3	622.3	0.8	551.9	3.5	574	2.6	26.6	12.5
62513	736	80	115	20	620	537	53.9	620.8	0.9	533.3	3.1	564	2.2	40.1	8.1
61013	658	20	115	40	615	362	59.2	615.2	1.0	535.1	3.4	573	2.5	32.7	11.5
61213	716	20	115	50	622	348	67.5	613.1	0.8	532.2	3.1	568	2.3	35.4	10.9

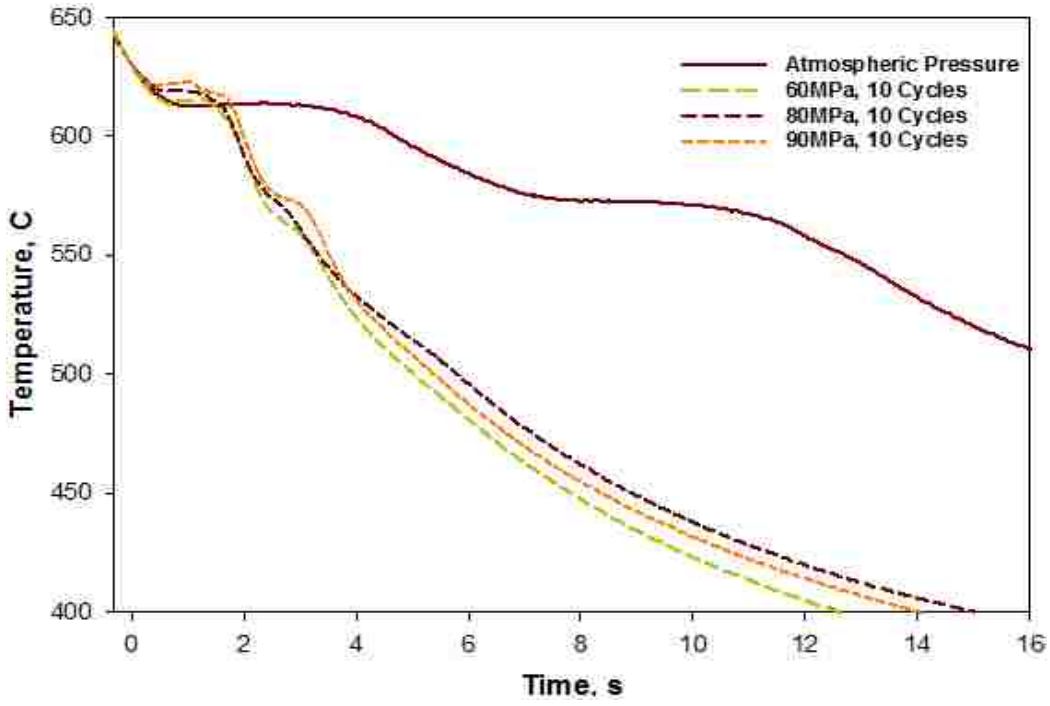

Figure 45 – Comparison of cooling curves of unmodified A356 at different pressure profiles.

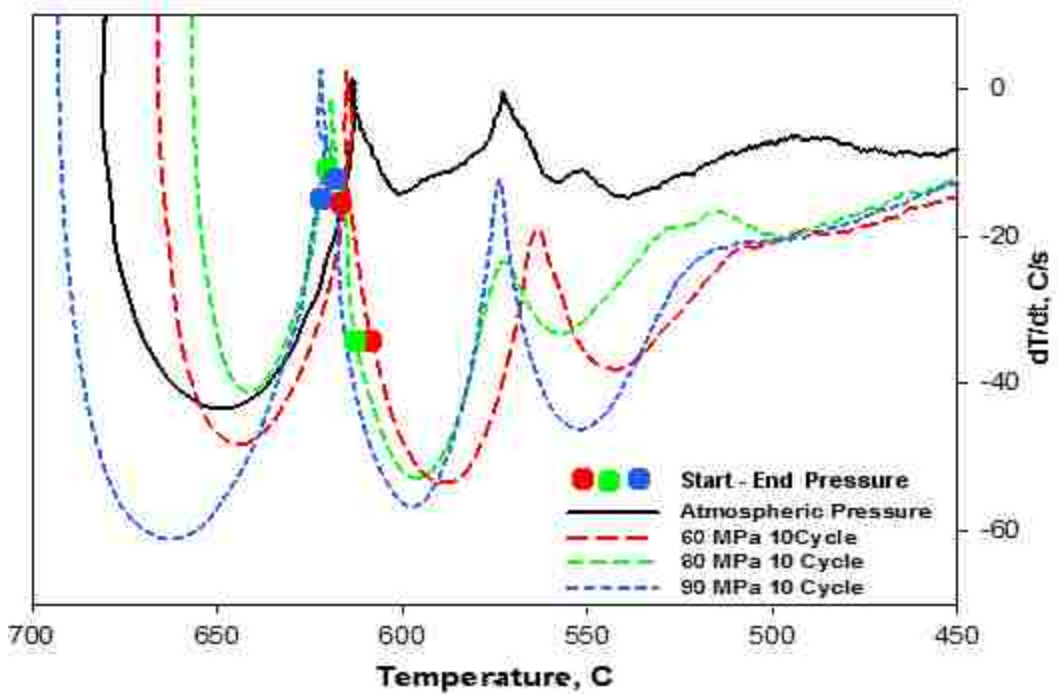

Figure 46 – Comparison of first derivatives of cooling curves of unmodified A356 at different pressure profiles.

The above experiments revealed that the increase and decrease in the $T^{\alpha DEN}{}_{G}$ and $T^{AlSi}{}_{E,G}$ varied based on the start and end points of the pressure applied region. As can be seen in Figures 116, 120 and 124 in Appendix A, whenever pressure was applied in the region between the end of α-Al Dendrite Growth and beginning of nucleation of Al-Si Eutectic, the $T^{\alpha DEN}{}_{G}$ was found to be increased and the $T^{AlSi}{}_{E,G}$ was found to be decreased.

By contrast, when the pressure was applied between the start and end point of α-Al Dendrite Growth region as shown in Figures 128 and 132 in Appendix A, both the $T^{\alpha DEN}{}_{G}$ and $T^{AlSi}{}_{E,G}$ were found to be increased simultaneously.

On the other hand, when pressure is applied between the start of α-Al Dendrite Growth and the end of Al-Si Eutectic growth region as shown in Figure 136 in Appendix A, the $T^{\alpha DEN}{}_{G}$ was found to be increased with a decrease in the $T^{AlSi}{}_{E,G}$. Lastly, as shown in Figures 140 and 144 in Appendix A, when pressure was applied from the start of α-Al

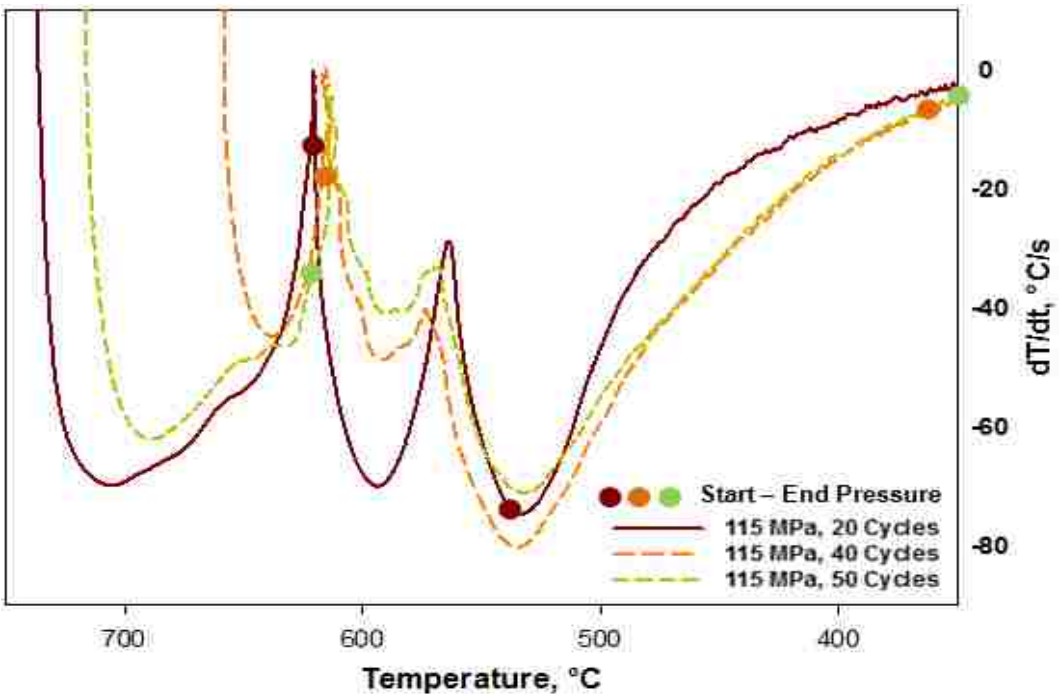

Figure 47 - Comparison of first derivatives of cooling curves of unmodified A356 at 115 MPa pressure profiles

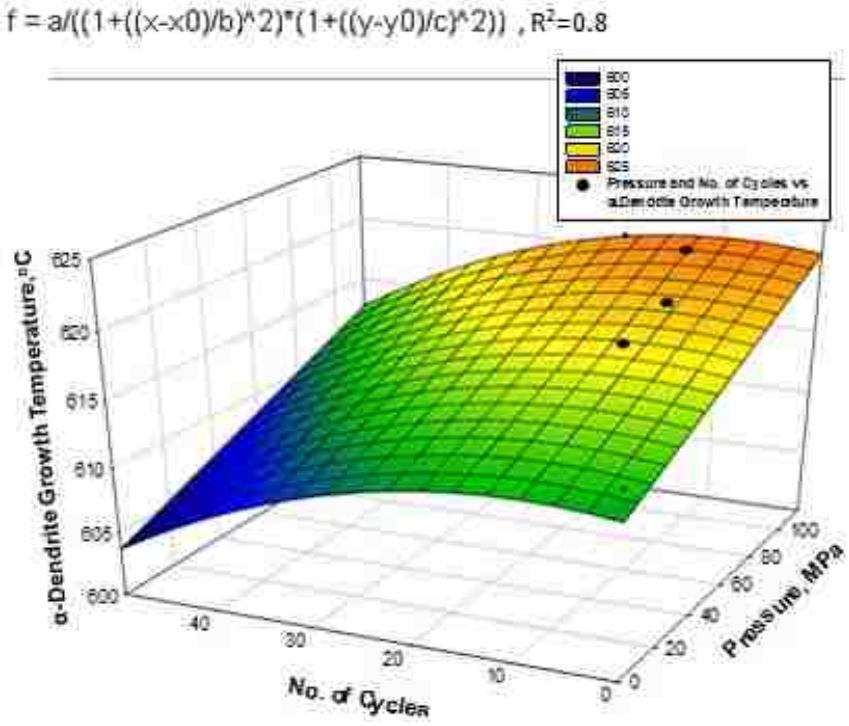

Figure 48 - Correlation between α-dendrite growth temperature and cyclic pressure of unmodified A356 alloy at different pressure profiles (Appendix E)

Dendrite Growth and beyond the end of Al-Si Eutectic growth region, the $T^{\alpha DEN}_{G}$ was found to be decreased with increasing of $T^{AlSi}_{E,G.}$ Most importantly, the behavior of the alloy, as relating to those changes on the transformation temperatures appear to have a significant impact on the silicon modification that will be discussed in a later section.

The apparent Solidification Temperature (T_S) was found to increase inconsistently with the increase of pressure in the range of 50-90 MPa and for increasing number of cycles from 1-10. However, at 115 MPa pressure, T_S reduced substantially to 532^{o}C for increasing number of cycles up to 50. The total time of solidification range has been abruptly reduced from 11.2 s at atmospheric pressure to 2.2 s at 115 MPa pressure for 20 numbers of cycles

4.3.2. Changes in the Internal Energy of the 356 Alloy System

Energy input by the servo hydraulic ram can be expressed as the product of load and stroke. During the squeeze casting experiments, the movement of the plunger and the increase in load or pressure as applied on the solidifying melt, added thermal energy to the melt system. For instance, Fig. 49 shows in red the load- stroke curve during the pressure load cycling. The enclosed area (integral of pressure and stroke difference) in green is the total energy imparted by the movement and load of the plunger. Hence the internal energy of the melt system was increased. As can be seen in Table 16 and Fig. 50, the cumulative energy increased from 8.6 J to 67.5 J after increasing squeeze pressure from 50 MPa to 115 MPa for increasing number of pressure cycles of 1-50. Basically applied pressure has been converted into thermal energy and has increased the overall

internal energy of the melt system, which is responsible for all thermal and metallurgical changes in the alloy.

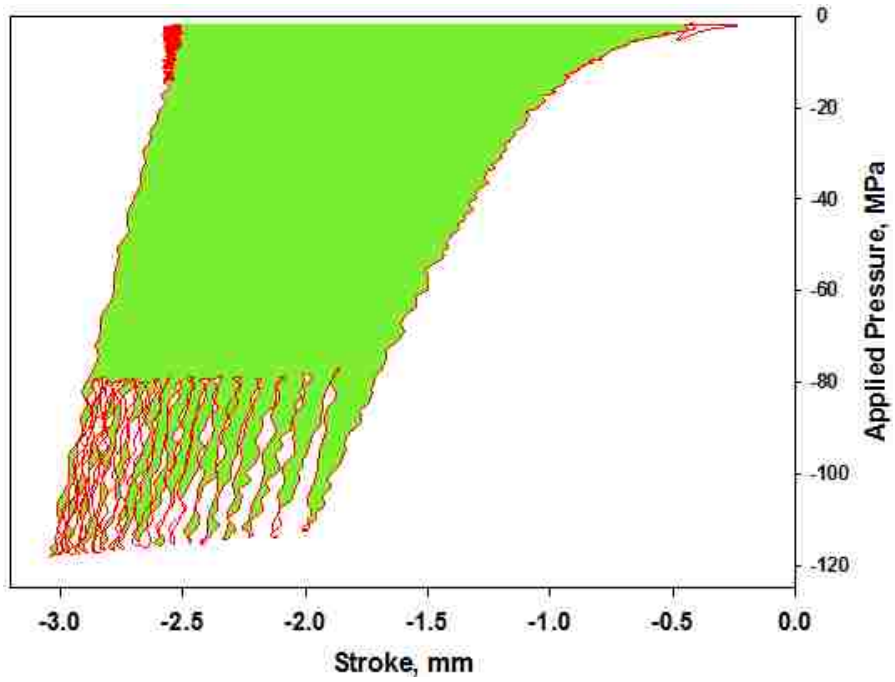

Figure 49 – Cumulative energy of unmodified A356 alloy under 115 MPa with 20 pressure cycles.

4.3.3. Changes in the Solidification Rate of Unmodified A356 Alloy

Generally SR increases with cyclic pressure. When the melt was solidified in the SC UMSA Platform at atmospheric pressure, the SR was only 6.5°C/s. However, when the melt was solidified at high pressure of 50 MPa, the SR increased to 23.2°C/s. With the further increment of pressure from 55 MPa to 115 MPa, the SR increased up to maximum of 40.1°C/s. Fig. 51 shows that solidification rate is varied with the cumulative energy. As cumulative energy increased the solidification rate increased to some extent and one would expect a corresponding effect on the microstructural changes. As can be seen from Fig. 52, SDAS or dendrite cell size has been reduced to a great extend as SR is increased.

When SR was 6.5°C/s, the dendrite cell size was 23.8 µm. However, it drastically changed to 8.1 µm, when SR increased to 40.1°C/s. Similarly, most of the finest dendrite cells were observed in the range of SR 30-40°C/s.

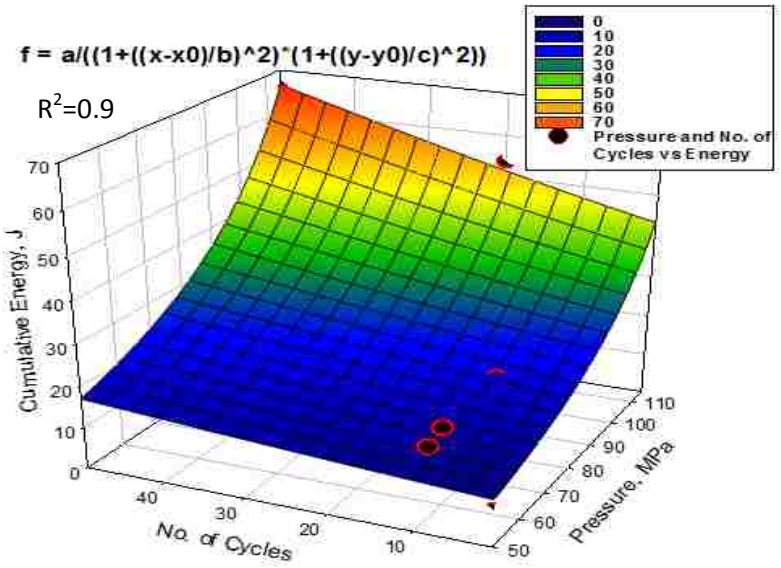

Figure 50 - Correlation between cumulative energy and cyclic pressure of unmodified A356 alloy at different pressure profiles (Appendix F)

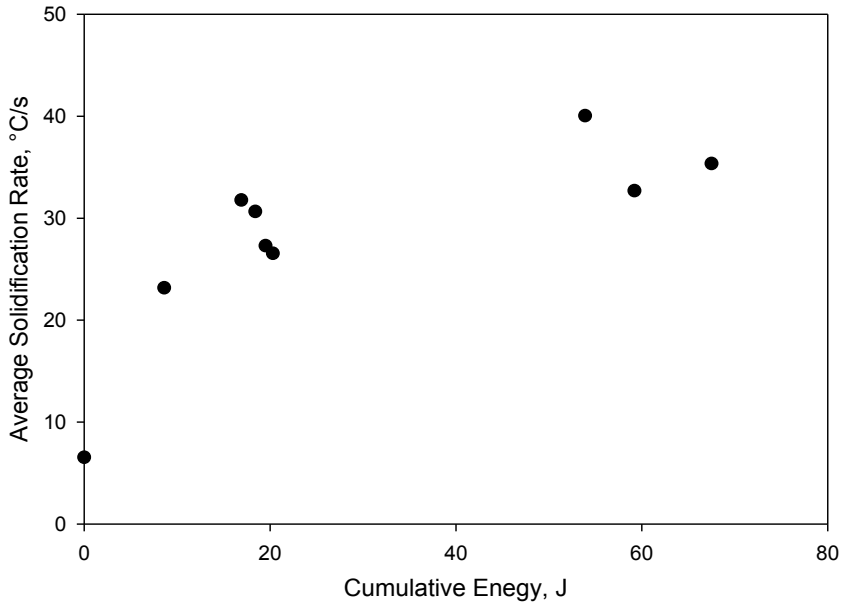

Figure 51 - Correlation between solidification rate and cyclic pressure of unmodified A356 alloy at different pressure profiles.

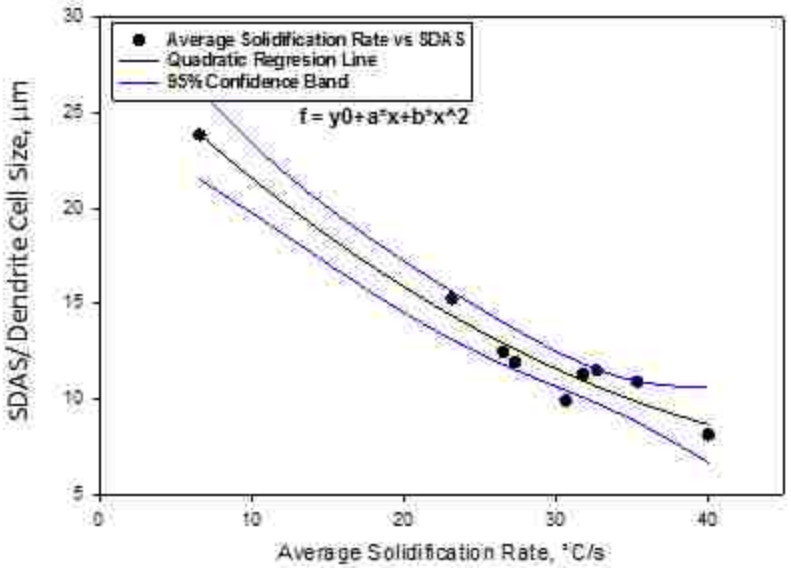

Figure 52 - Correlation between SDAS or dendrite cell size and average solidification rate of unmodified A356 alloy at different pressure profiles.

4.4. Effect of Cyclic Pressure on the Sr Modified A356 Alloy in SC UMSA Platform

4.4.1. Changes in the Thermal Characteristics of Sr Modified Alloy

As can be seen in Table 17 as well as observed in Figures 53-54 and Figures 146-163 in Appendix B, the cyclic pressure didn't change the α--Al Dendrite Growth Temperature ($T^{\alpha DEN}{}_{G}$) much while it has great impact on the Al-Si Eutectic Growth temperature ($T^{AlSi}{}_{E,G}$) in Sr modified A356 alloy. The α-Al Dendrite Growth Temperature ($T^{\alpha DEN}{}_{G}$) at atmospheric pressure has been found decreased from 613.9°C (unmodified) to 612.3°C after modifying with Sr, which is a general characteristic trend for unmodified and Sr modified A356 alloy proven from the literature. Interestingly $T^{\alpha DEN}{}_{G}$ was decreased further to 610°C after applying pressure of 100 MPa for single cycle and then it increased to 613.9°C at 100 MPa applied pressure for 10 numbers of cycles. It increased further with increasing the pressure to 115 MPa for a pressure cycles of 7.

Table 17 - Summary of Results and Thermal Characteristics of Modified A356 at Variable Pressure with Variable Cycles.

Ref. #	Melt Drop Temp. °C	Applied Pressure MPa		No. of Cycles	Temp. of Applied Press.°C		Cum. Energy Joule	$T^{\alpha DEN}{}_{G}$ °C	$t^{\alpha DEN}{}_{G}$ s	Ts °C	t_s s	$T^{ALS}{}_{E,G}$ °C	Sol. Time s	SR °C/s	SDAS (D.Cell) µm
		Min.	Max.		Start	End									
A356+Sr															
72413	756	0	0	0	-	-	0	612.3	2.0	548.7	8.8	561.0	6.7	9.4	13.0
51313	740	0	100	1	591	568	25	610.5	1.1	-	-	-	-	-	10.8
51513	682	80	100	10	614	593	31	613.9	1.4	534.4	3.3	559.0	2.0	40.3	10.8
61913	714	20	115	7	619	565	51	616.1	0.9	535.7	3.2	571.0	2.3	34.5	9.4
71613	691	20	115	50	619	360	54	615.0	1.6	526.7	3.6	558.0	2.0	43.4	9.3
A356 + Alumina															
72413	740	0	0	0	-	-	0	607.5	3.0	532.0	12.8	555.7	9.8	7.7	16.1
61213	709	20	115	2	615	602	35	617.5	1.1	544.3	3.6	566.0	2.5	29.6	7.8
62013	735	80	115	20	615	538	50	614.7	0.7	534.7	3.1	557.0	2.4	33.1	11.3
71513	720	20	115	50	614	430	52	612.7	1.1	518.2	4.2	541.0	3.1	30.4	9.2
A356+Sr + Alumina															
72413	699	0	0	0	-	-	0	606.7	2.3	530.4	12	545.0	9.7	7.9	15.2
81413	700	20	115	12	623	534	67	612.4	1.2	512.8	4.3	540.6	3.1	32.6	9.2
62413	704	80	115	20	617	523	45	616.7	1.1	519.9	3.5	547.2	2.4	40.4	9.9
61713	699	20	115	50	623	366	60	613.0	1.1	518.1	3.8	556.8	2.7	35.0	7.6

However, the $T^{\alpha DEN}{}_{G}$ was reduced to 615°C for the further increasing of pressure cycles to 50. On the other hand, the Al-Si Eutectic Growth temperature, $T^{AlSi}{}_{E,G}$ was decreased from 573°C to 561°C after addition of Sr at atmospheric pressure. Surprisingly, no peak was found for the $T^{AlSi}{}_{E,G}$ when 100MPa pressure was applied in the first occurrence. Then the same pressure was applied for 10 number of cycles and it reduced $T^{AlSi}{}_{E,G}$ to 659°C. However, $T^{AlSi}{}_{E,G}$ was decreased further to 558°C after applying a high pressure of 115 MPa for 50 pressure cycles despite an increase to 57 °C for 7 pressure cycles.

Some underlying information has been revealed from the above experiments. The tendency of those increases and decreases in the $T^{\alpha DEN}{}_{G}$ and $T^{AlSi}{}_{E,G}$ were found to be varied based on the start and end of pressure applied region.

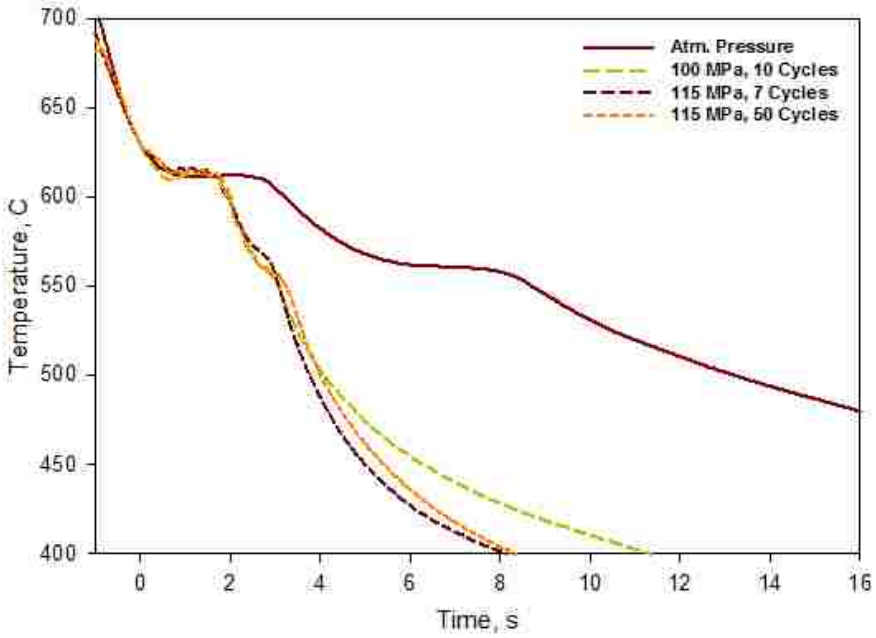

Figure 53 - Cooling curves of Sr modified A356 at variable pressure with variable cycles.

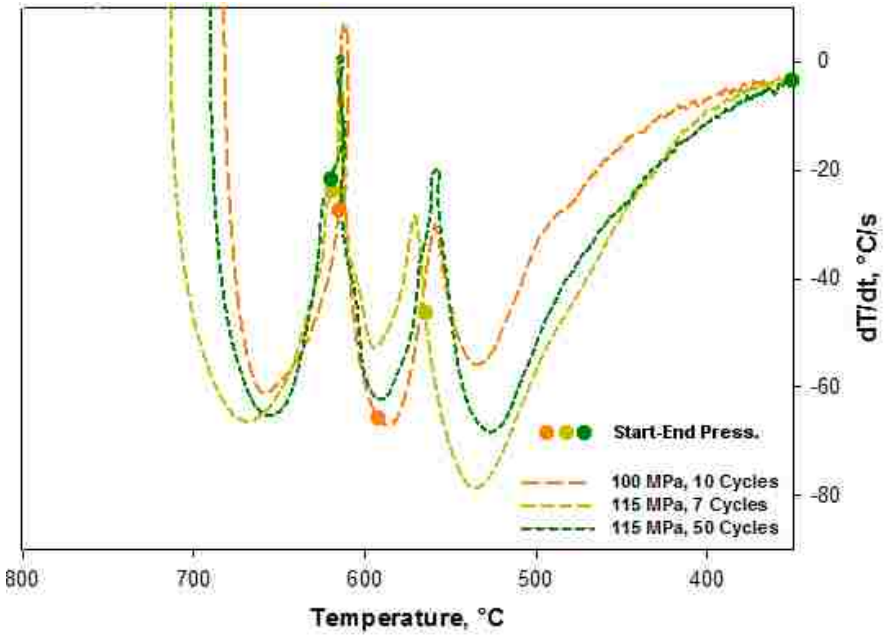

Figure 54 - First derivatives of cooling curves of Sr modified A356 at variable pressure with variable cycles.

In the first occurrence as shown in Figures 150 in Appendix B, pressure was applied at 586°C and ended at 565°C in the region between the start of nucleation of Al-Si Eutectic and the end of Al-Si Eutectic growth. This incident had a great impact on the transformation temperature. Surprisingly no peak was found for the $T^{AlSi}{}_{E,G}$ while the $T^{\alpha DEN}{}_{G}$ decreased to 610°C.

By contrast, when the pressure was applied between the start and end point of α-Al Dendrite Growth region as shown in Figure 154 in Appendix B, both the $T^{\alpha DEN}{}_{G}$ and the $T^{AlSi}{}_{E,G}$ were found to be increased simultaneously. On the contrary, as can be seen in Figure 158, when pressure was applied between the nucleation of α-Al Dendrite and the nucleation of Al-Si Eutectic region, the both $T^{\alpha DEN}{}_{G}$ and $T^{AlSi}{}_{E,G}$ were found to be increased again. Lastly, as shown in Figure 162, when pressure was applied at the nucleation of α-Al Dendrite and beyond the end of Al-Si Eutectic growth region, the $T^{\alpha DEN}{}_{G}$ and $T^{AlSi}{}_{E,G}$ were both decreased. Most importantly, these behaviors of alloy relating to those changes on the transformation temperatures appeared to have a great impact on the silicon modification that will be discussed in section 4.7.

On the other side, the apparent Solidification Temperature (T_S) have been decreased for the variable pressure cycles at the pressure range of 100-115 MPa. The total time of solidification range has also been reduced from 6.7 s at atmospheric pressure to 2 s at max. 115 MPa pressure for 50 numbers of cycles.

4.4.2. Changes in the Solidification Rate of Sr Modified Alloy

Solidification rate has been increased from 6.5°C/s to 9.4°C/s at atmospheric pressure in unmodified alloy to Sr modified alloy. Since the Al-Si eutectic growth and solidification

peak temperature were unable to be identified after applying pressure of 100 MPa for a single cycle, solidification rate was unable to be calculated for this pressure. By contrast, SR was found to be 40.3°C/s at the same pressure level for 10 pressure cycles. SR has been further increased to 43.4°C/s at 115 MPa for 50 pressure cycles.

4.5. Effect of Cyclic Pressure on the Nano Alumina Modified A356 Alloys in the SC UMSA Platform

4.5.1 Changes in the Thermal Characteristics of Nano Alumina Modified A356 Alloy

As can be seen from Table 16-17 as well as Figures 55-56 and Figures 164-177 in Appendix C, the addition of Nano alumina to A356 alloy decreased the $T^{\alpha DEN}{}_{G}$ from 613.9°C to 607.5°C at atmospheric pressure and it increased to 617.5°C at 115 MPa for 2 pressure cycles and then it reduced to 614.7°C and 612.7°C after increasing the number of pressure cycles from 20 to 50 respectively keeping the level of pressure same as max. 115 MPa. Similarly the $T^{AlSi}{}_{E,G}$ decreased from 573°C to 555.7°C after addition of Nano alumina at atmospheric pressure and then it increased to 566°C at 115 MPa for 2 pressure cycles. However, it decreased again for increasing number of cycles from 20 to 50 at the same level of pressure.

On the other hand, the apparent Ts decreased from 540°C to 532°C at atmospheric pressure with the modification of Nano alumina and then increased to 544.3°C at 115 MPa for 2 pressure cycles and decreased again to 534°C and 518°C with the increase of pressure cycles from 20-50. Conversely, SR increased from 7.7°C/s at atmospheric pressure to 29.1°C/s at 115 MPa for 2 pressure cycles and then increased to 33.1°C/s after

increasing the pressure cycles to 20. However, it decreased to 30.4°C/s again with further increasing of pressure cycles to 50.

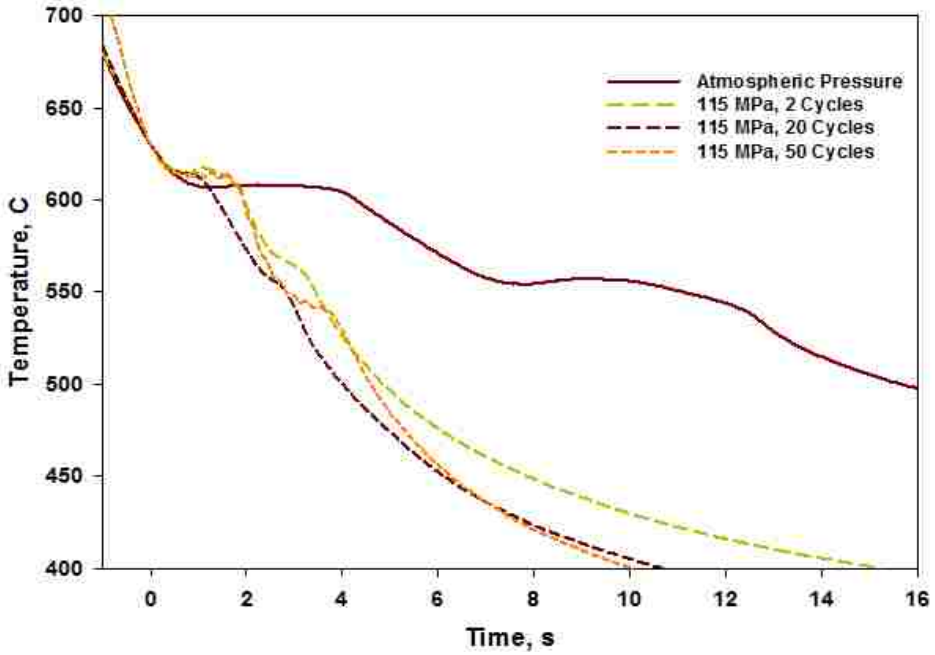

Figure 55 - Cooling curves of Nano alumina modified A356 at 115 MPa pressure with variable cycles.

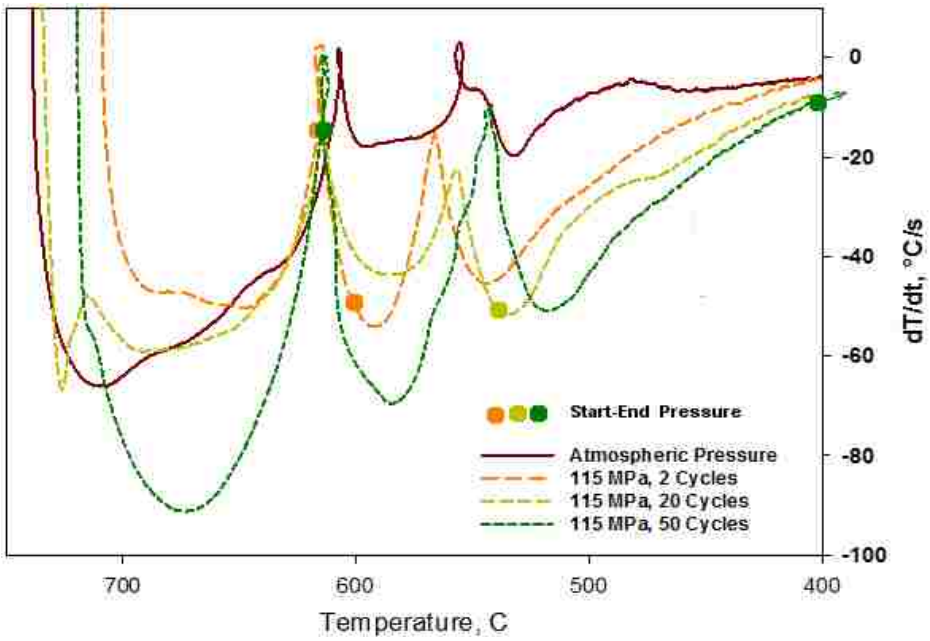

Figure 56 - First derivatives of cooling curves of Nano alumina modified A356 at 115 MPa pressure with variable cycles.

4.6. Effect of Cyclic Pressure on the Sr and Nano Alumina Combined Modified A356 Alloy in the SC UMSA Platform

4.6.1. Changes in the Thermal Characteristics of Strontium & Nano Alumina Combined Modified A356 Alloy

As can seen in Figures 57-58, the α--Al Dendrite Growth Temperature ($T^{\alpha DEN}_{G}$) was not much affected by the cyclic pressure while the Al-Si Eutectic Growth temperature ($T^{AlSi}_{E,G)}$ was abruptly shifted 16°C higher temperature, in the Sr and Nano Alumina combined modified A356 alloy.

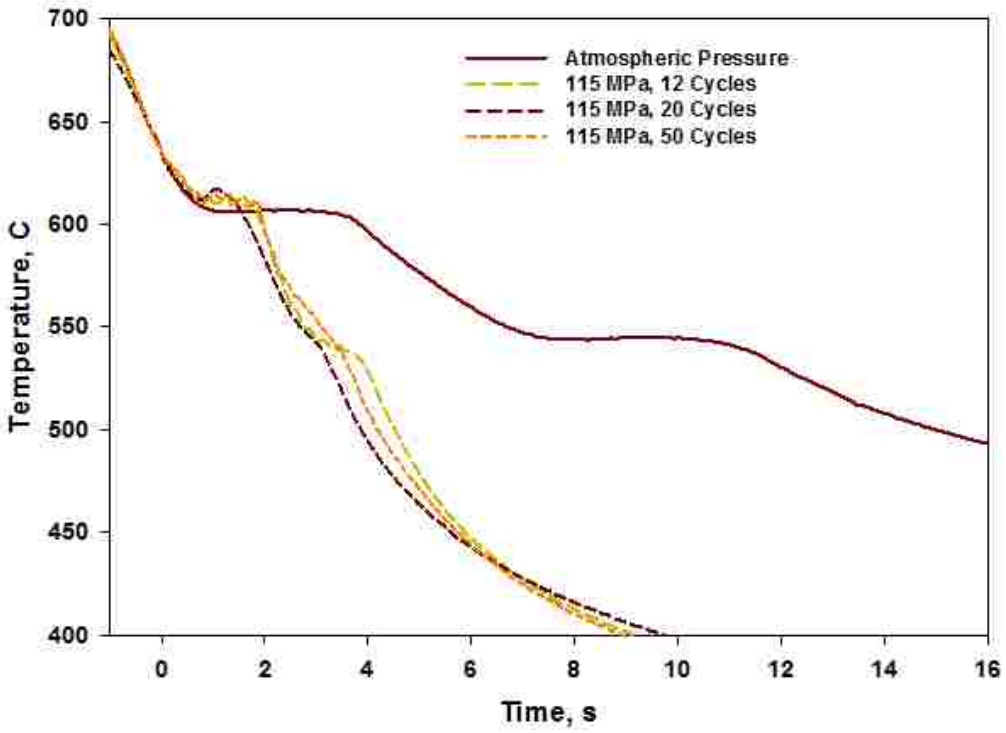

Figure 57 - Cooling curves of Sr & Nano alumina modified A356 alloy at 115 MPa pressure with variable cycles.

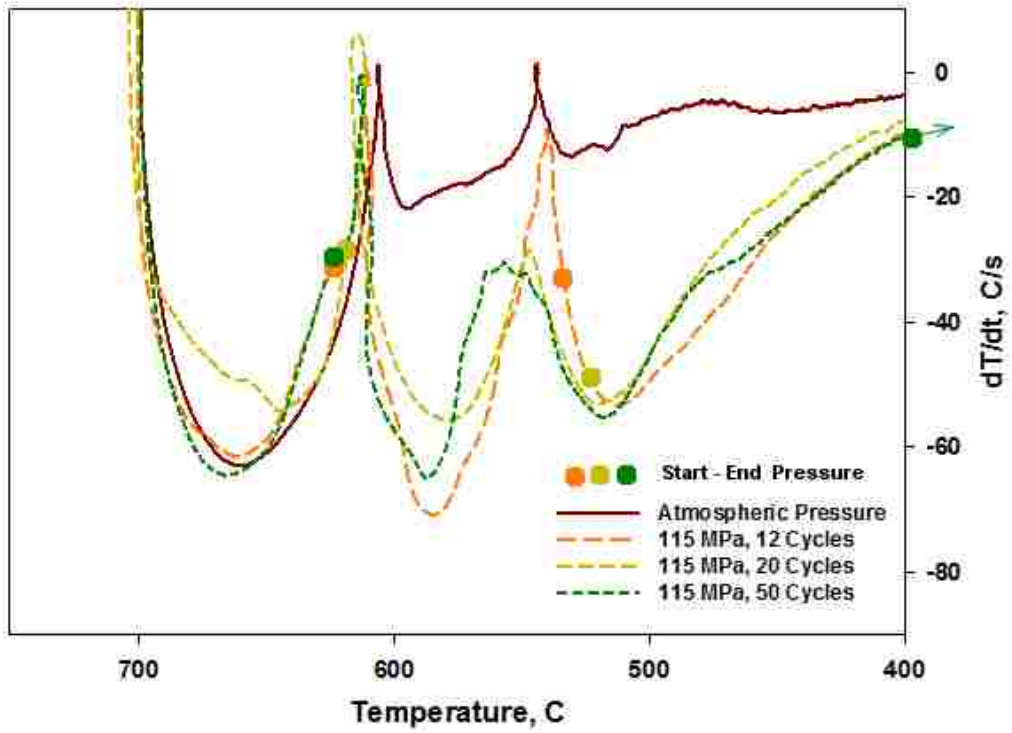

Figure 58 - First derivatives of cooling curves of Sr & Nano alumina modified A356 alloy at 115 MPa pressure with variable cycles.

As shown in Figures 178-191 in Appendix D and Table 17, the α-Al Dendrite Growth Temperature ($T^{\alpha DEN}{}_{G}$) at atmospheric pressure has been found decreased from 613.9°C (unmodified) to 606.7°C after modifying with both Sr and Nano alumina combined Master Alloys compare to 612.3°C and 607°C individually in Sr modified and Nano Alumina MA modified alloy. The $T^{\alpha DEN}{}_{G}$ was increased to 612.4°C at 115 MPa for 12 pressure cycles and then it increased further to 616.7°C at the same level of pressure but for 20 cycles. However, at further increase of pressure cycles to 50, the $T^{\alpha DEN}{}_{G}$ was decreased to 613°C.

On the other hand, at atmospheric pressure the Al-Si Eutectic Growth Temperature, $T^{AlSi}{}_{E,G}$ was decreased from 573°C to 545°C after addition of Sr & Nano Alumina MA. The $T^{AlSi}{}_{E,G}$ was further decreased to 540°C after applying 115 MPa pressure for 12 cycles.

However, at the same level of pressure, it has been increased to 547.2°C and 556.8°C at 20 and 50 pressure cycles respectively.

Pressure has also an effect on the apparent solidus temperature as it was substantially reduced from 530°C at atmospheric pressure to 512.8°C at 115 MPa pressure for 12 cycles. However, it increased to 519.9°C and 518.1°C at the same level of pressure when pressure cycles were increased to 20 and 50 respectively.

The Solidification Rate was drastically increased from 7.9°C/s at atmospheric pressure to 40.4°C/s at 115 MPa with a variation with respect to number of pressure cycles. Surprisingly, pressure has a great effect on the cumulative energy that increases up to 67 Joule at 115 MPa pressure compare to Sr or NAM modified alloy individually.

4.7. Microstructural Analysis

The LOM micrographs are primarily used to identify the main phases and measurement of dendrite cell size or secondary dendrite arm spacing (SDAS). The SEM micrographs are used to see those phases in high resolution and to confirm the LOM findings. SEM micrographs are also used to do EDS analysis and calculations of the volume of those main phases. The main phases are identified as primary α-Al dendrite and Al-Si eutectic phase. The intermetallic phases are Fe or Mg rich phases. A very small fraction of Mg_2Si phase appeared. Two types of Fe phases were found, namely script type and plate type phases. The script type phases could have been π or α-AlFeSi. However, the presence of magnesium in almost all of the particles examined in SEM/EDS analysis showed that they are a π-AlSiMgFe phase. The plate type Fe phase is most likely to be β-phase of

AlFeSi. But SEM/EDS analysis confirmed that it is π-AlSiMgFe phase as well. In almost all microstructures, all of those phases are commonly found, although the morphology of those phases is varied with respect to various pressure profiles. A few MgO, SiO_2 oxide phases have also been found in some microstructures. The α-Al dendrite is the first phase that solidified followed by AlSiMgFe and Al-Si eutectic phase. Eutectic Si and AlSiMgFe eutectic phases are solidified in the interdendritic region.

4.7.1. Microstructural Analysis of the Unmodified A356 Alloy

Cyclic pressure application have significantly affected the eutectic Si and dendrite cell size or dendrite arm spacing (SDAS) without the addition of any chemical modifiers or grain refiners. In some squeeze casting experiments, eutectic Si was modified so ultra finely that it was impossible to do image analysis of those modified microstructure even at 1000x of LOM micrographs. Compare to acicular type Si (dia. 2-3 μm) formed at atmospheric pressure (Figures 59-60), eutectic Si were transformed into a combination of acicular and lamellar structure at 50 MPa (Fig. 61) with a dia. of 0.8-1.0 μm. At an increasing pressure, the eutectic Si modified into ultra fine fibrous Si dendrite at 55-60 MPa pressure for 10 pressure cycles (Figures 63-64) that achieved a Si dia. between 0.5-0.6 μm. By contrast, Si remains in acicular shape (dia. 1-3 μm) at 80-90 MPa for 10 pressure cycles (Figures 65-66) though the length of acicular Si is comparatively reduced at these high pressure ranges. At high pressure like 115 MPa, Si modification behaved differently for different numbers of pressure cycles. At 115 MPa for 20 cycles, the eutectic Si fully converted into a ultra fine fibrous Si (dia. 0.15-0.25 μm) dendritic structure (Fig. 67), which is confirmed by SEM micrographs (Fig.68) of a deep etched sample (etching done by 10% NaOH solution). However, Si didn't show much

modification after increasing the number of cycles in the range of 40-50 as shown in Figures 69-72, and the Si dia. observed was 1.0-1.5 µm

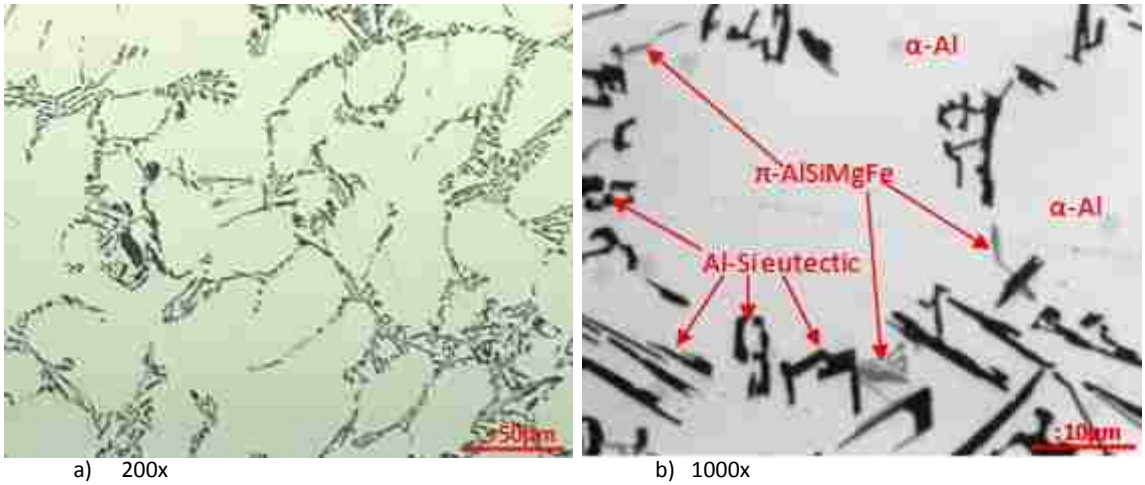

a) 200x b) 1000x

Figure 59 - LOM Microstructure of UM A356 alloy (Ref. # 31513) solidified in SC die at atmospheric pressure a) Morphology of α-Al Dendrite and Al-Si eutectics, dendrite cell size 23.8 µm b) Main phases are identified , acicular eutectic Si.

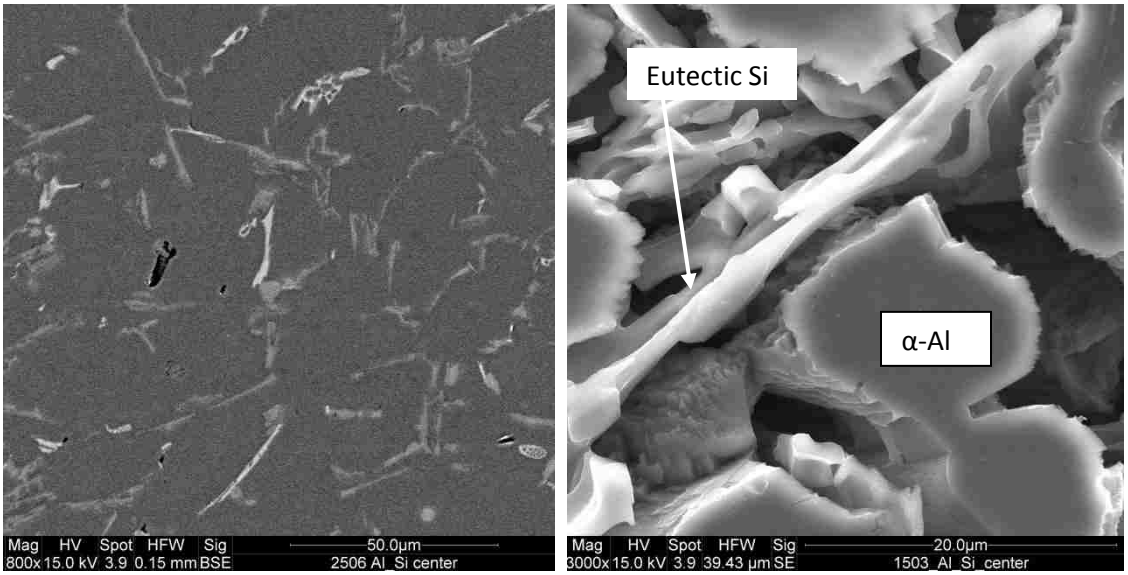

a) Polished sample 800x a) Etched sample 3000x

Figure 60 - SEM Microstructure of UM A356 alloy (Ref. # 31513) solidified in SC die at atmospheric pressure a) Morphology of α-Al Dendrite, Si eutectics, AlSiMgFe size is 30x2 µm b) eutectic Si and α-Al in deep etched sample, , Si size 40x1 µm.

On the other hand, as shown in Fig. 62, the secondary dendrite arm spacing (SDAS) or dendrite cell size has been reduced substantially with the increasing cyclic pressure during solidification. It is found that the dendrite cell size has been reduced from 24 µm

at atmospheric pressure (Fig. 59) to 15 µm at 50MPa Pressure (Fig. 61). It was further reduced from 15 µm to 8 µm at the increase of pressure up to 115 MPa despite some minor variations (Figures 63-68). The dendrite cell size greatly reduced at the 20 numbers of pressure cycles (Fig. 67). However, when the number of pressure cycles increased up to 50, the dendrite cell didn't get refined but became coarser (Figures 69-72) than the earlier (Fig. 67). It was also observed that the traditional dendrite arms were broken in most of the cases and transformed into semi solid equiaxed cells as shown in Figures 63-64 and 67.

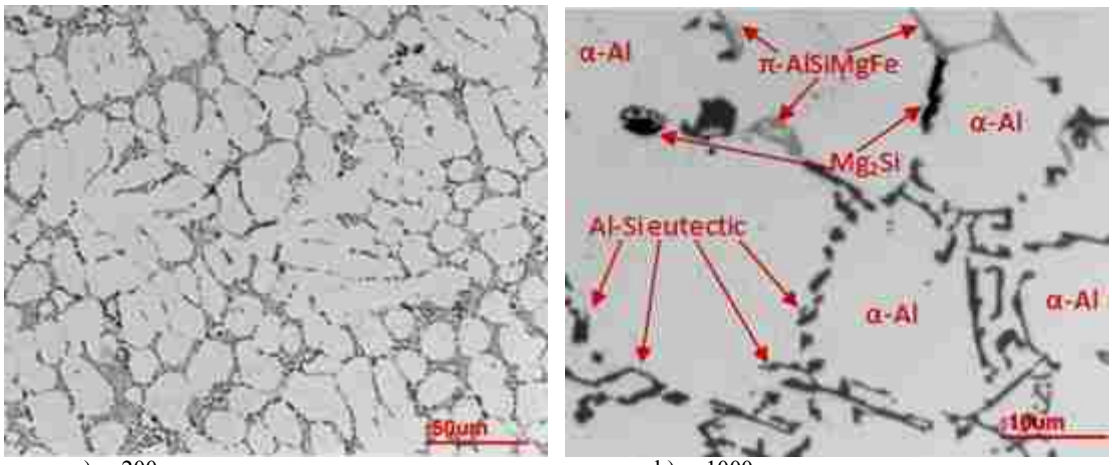

a) 200x b) 1000x

Figure 61 - LOM Microstructure of UM A356 alloy (Ref. # 32813) solidified in SC die at 50 MPa/1 pressure a) Morphology of α-Al Dendrite and Al-Si eutectics, dendrite cell size 15.2 µm, b) Main phases are identified , lamellar eutectic Si.

Cyclic pressure also has a significant effect on the Intermetallic phases like AlSiMgFe and Mg_2Si. It has been observed that the highest length of AlSiMgFe is reduced from 30µm at atmospheric pressure to 8 µm at 115 MPa for 20 pressure cycles and most intermetallics are broken into small pieces. Mg_2Si phase is almost absent in the microstructure at the high pressure solidification.

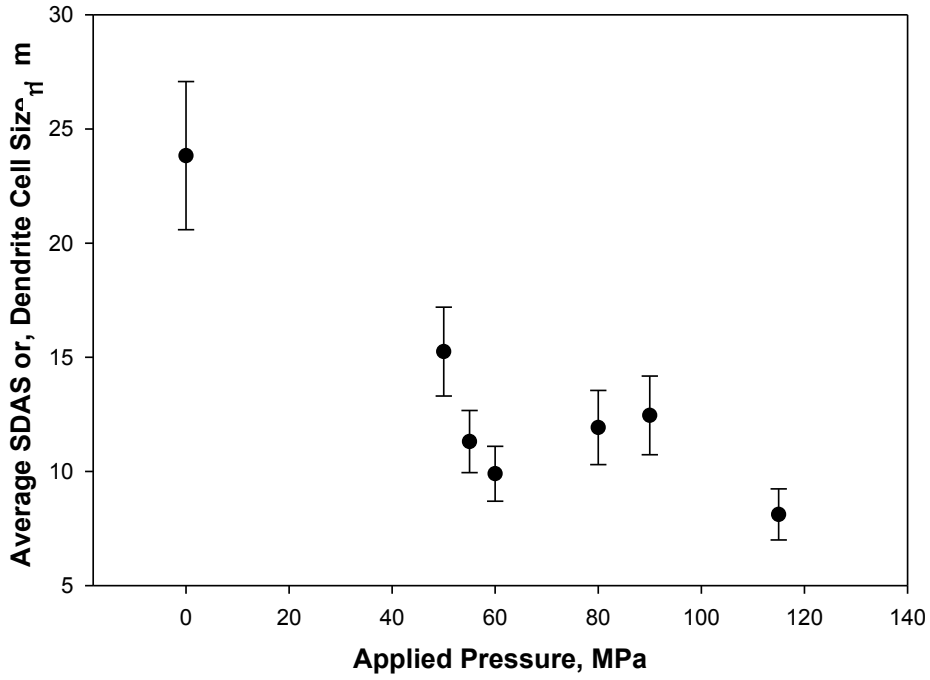

Figure 62 – Average SDAS or Dendrite Cell Size relationship with Pressure.

In this investigation, two levels of pressure profiles, 10 cycles @ 50 MPa and 20 cycles @ 115 MPa, were found to have successfully modified the eutectic Si and to refine the dendrite cell size. A good correlation was found between the thermal analysis and the microstructural characterization and the mode of pressure application in those test samples. Details will be discussed in section 4.9.

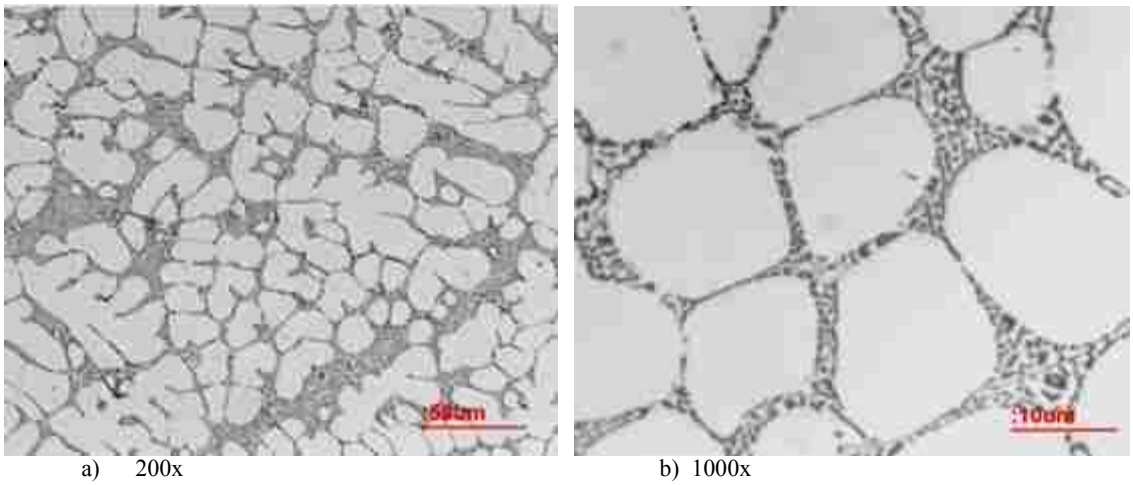

a) 200x b) 1000x

Figure 63 - LOM Microstructure of UM A356 alloy(Ref. # 40113) solidified in SC die at 55 MPa/10 pressure a) Morphology of α-Al cells and Al-Si eutectics, dendrite cell size 11.3 µm, b) Fibrous eutectic Si.

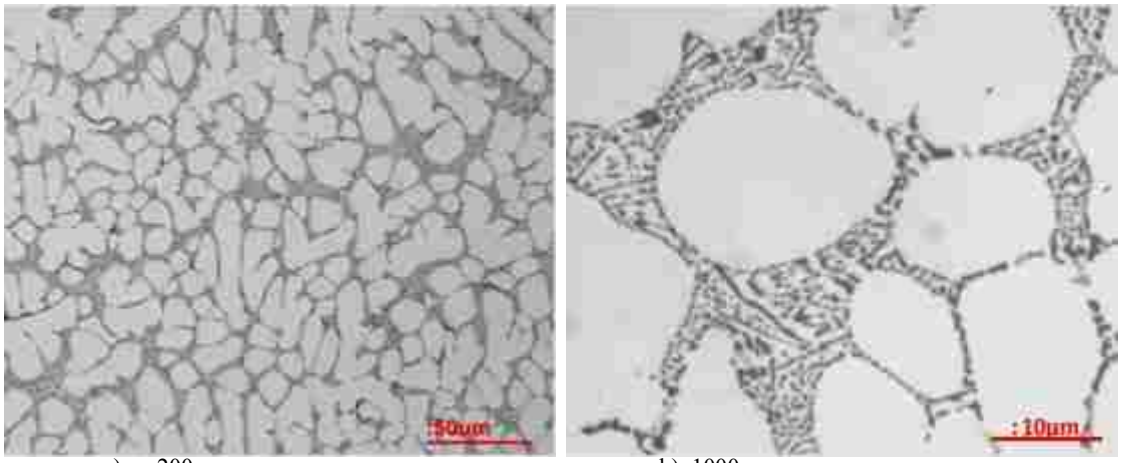

a) 200x b) 1000x

Figure 64 - LOM Microstructure of UM A356 alloy (Ref. # 40213) solidified in SC die at 60 MPa/10 pressure, a) Morphology of α-Al cells and Al-Si eutectics, dendrite cell size 9.9 µm, b) Fibrous eutectic Si.

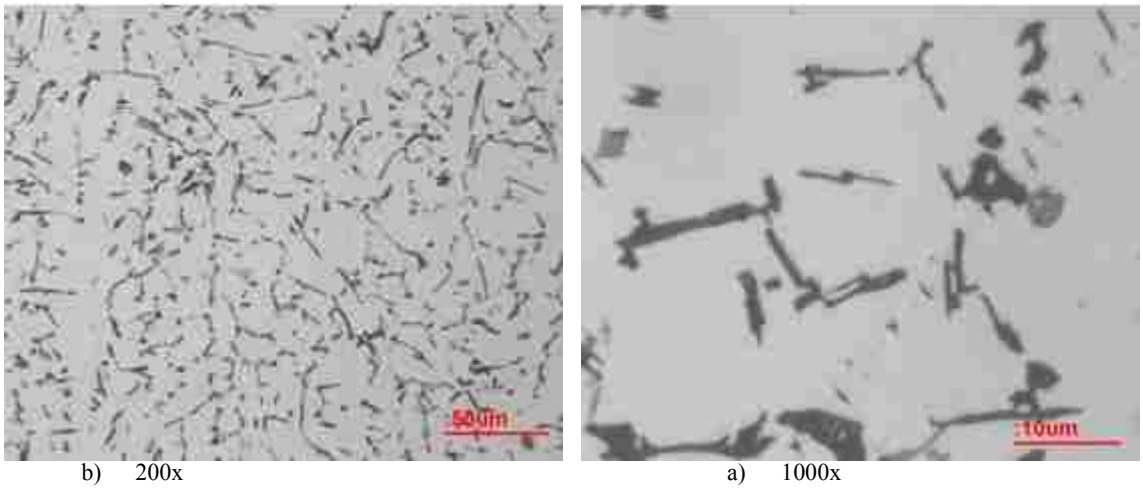

b) 200x a) 1000x

Figure 65 - LOM Microstructure of UM A356 alloy (Ref. # 41913) solidified in SC die at 80 MPa/10 pressure a) Morphology of α-Al Dendrite and Al-Si eutectics, dendrite cell size 11.9 µm, b) Acicular eutectic Si.

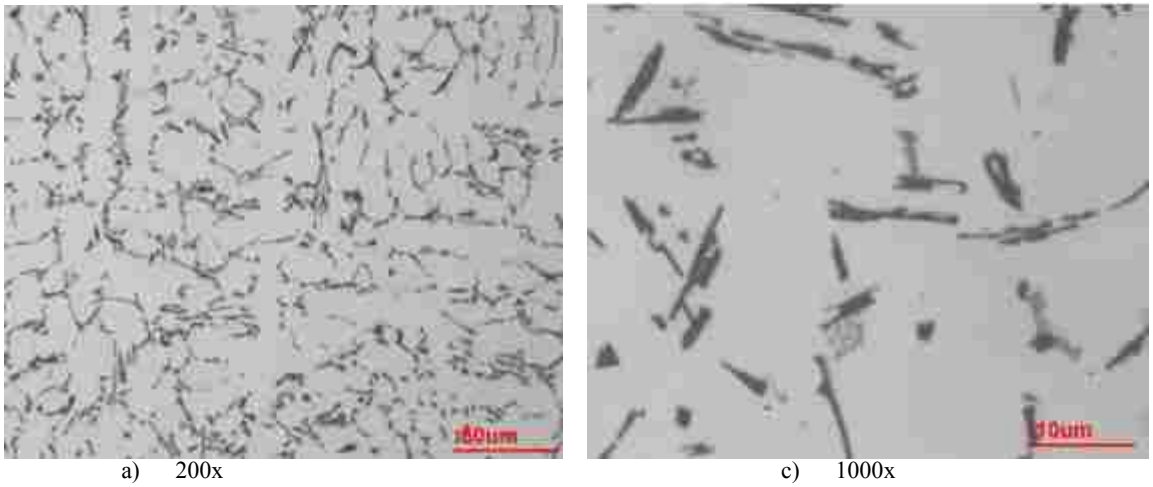

a) 200x c) 1000x

Figure 66 - LOM Microstructure of UM A356 alloy (Ref. # 41713) solidified in SC die at 90 MPa/10 pressure a) Morphology of α-Al Dendrite and Al-Si eutectics, dendrite cell size 12.5 µm, b) Acicular eutectic Si.

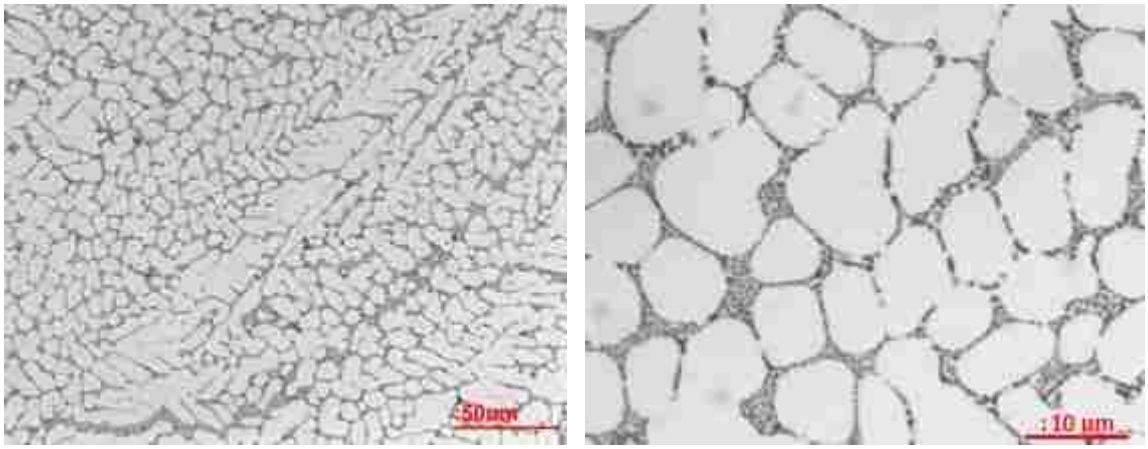

a) 200x b) 1000x

Figure 67 - LOM Microstructure of UM A356 alloy (Ref. # 62513) solidified in SC die at 115 MPa/20 cycles pressure a) Morphology of α-Al cells and Al-Si eutectics, dendrite cell size 8.1 µm, b) Fibrous eutectic Si.

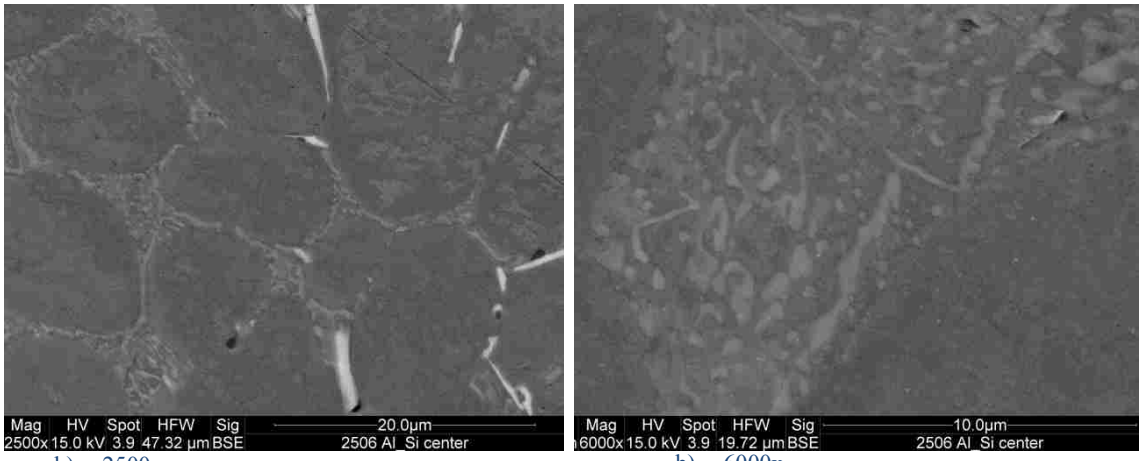

b) 2500x b) 6000x

Figure 68 - SEM Microstructure of UM A356 alloy (Ref. # 62513) solidified in SC die at 115 MPa/20 cycles pressure a) Morphology of α-Al cells and Al-Si eutectics, dendrite cell size 8.1 µm, b) Fibrous eutectic Si.

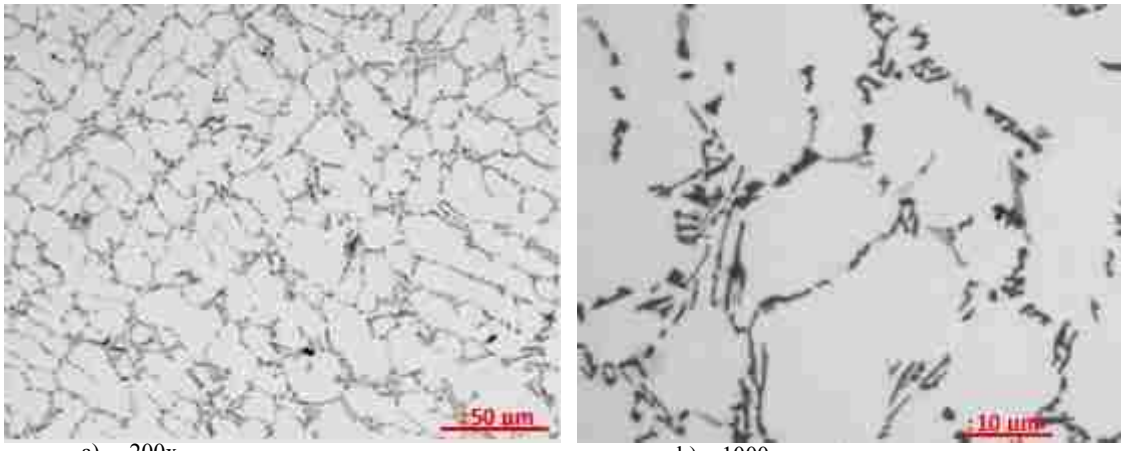

a) 200x b) 1000x

Figure 69 - LOM Microstructure of UM A356 alloy (Ref. # 61013) solidified in SC die at 115 MPa/40 pressure a) Morphology of α-Al Dendrite and Al-Si eutectics, dendrite cell size 11.5 µm b) Lamellar eutectic Si.

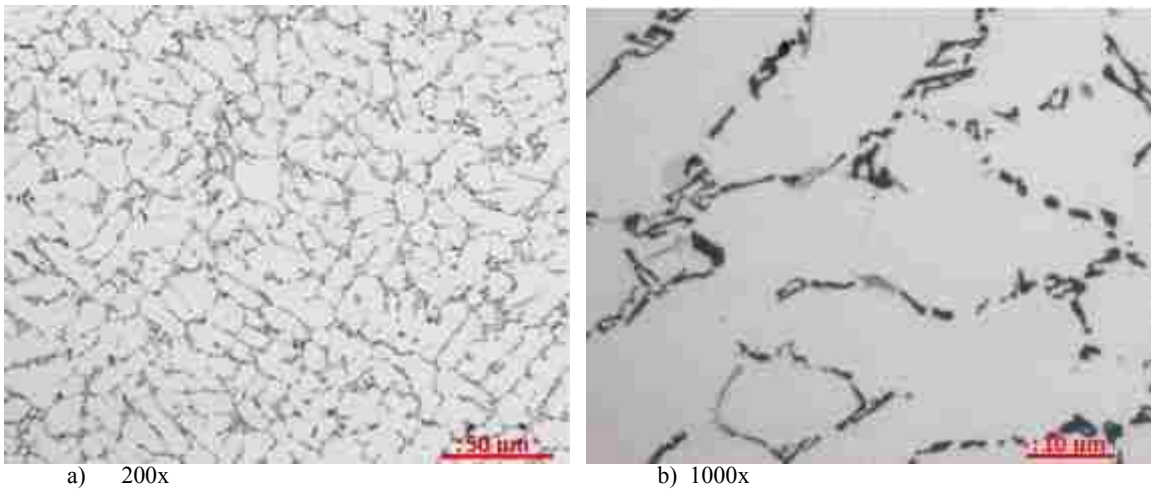

a) 200x b) 1000x

Figure 70 - LOM Microstructure of UM A356 alloy (Ref. # 61213A) solidified in SC die at 115 MPa/50 pressure a) Morphology of α-Al Dendrite and Al-Si eutectics, dendrite cell size 10.9 µm b) Lamellar eutectic Si.

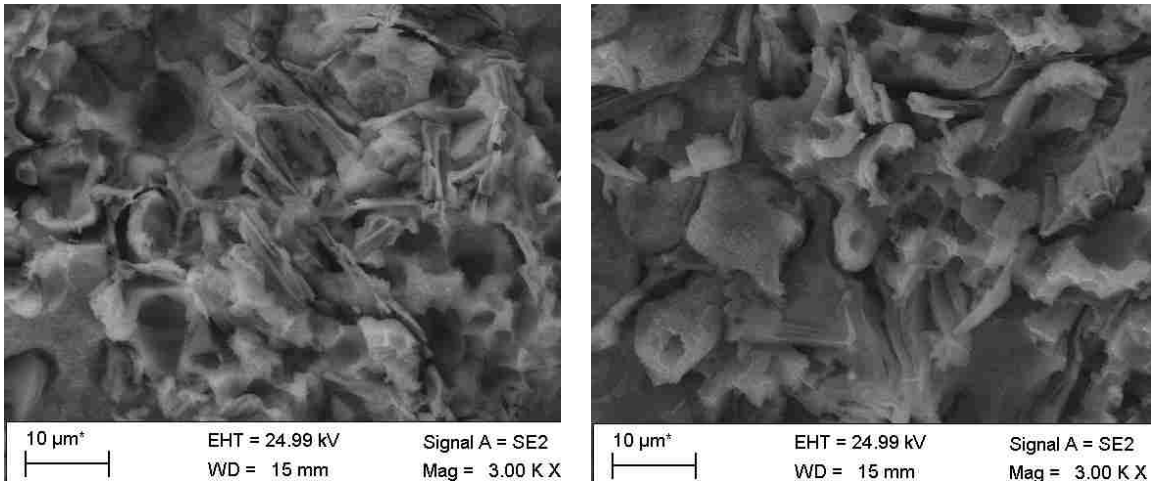

Figure 71 - SEM Microstructure of UM A356 alloy solidified in SC die at 115 MPa, α-Al and Al-Si eutectics in deep etched sample, acicular eutectic Si, a) at 40 cycles (Ref. # 61013) b) at 50 cycles pressure (Ref. # 61213A).

*4.7.1.1. SEM/EDS Analysis of Unmodified A356 Alloy**

Out of the eight unmodified test samples, one best sample (Ref. # 62513, 20 cycles @ 115 MPa) was selected for SEM/EDS analysis in an "as polished" condition. Four distinct phases were identified namely α-Al, Eutctic Al, Eutectic Si and AlSiMgFe intermetallic phases through EDS/SEM analysis. Their compositions were deconvoluted and phase distribution quantities were determined and results are tabulated in Table 18 and summarized as below:

*This work was done in collaboration with Dr. Adam Gesing.

1. The α-Al phase was solidified first constituting 71 wt% as large dendrite colonies with an average dendrite cell size of 8.1 μm. The α-Al solid solution consists of 97.84 wt% Al, 1.33 wt %Si, 0.58 wt% Mg and 0.49 wt% Fe
2. The residual liquid was then pushed into the Interdendritic region that constitutes 29 wt%. The interdendritic region consists of 21 wt% eutectic Al, 5.4 wt% eutectic Si dendrites, 2 wt% AlSiMgFe intermetallic phase and 0.1 wt% AlSiMg oxide.
3. The AlSiMgFe intermetallic phase appeared to be solidified as a second phase in the interdendritic region, where it was found in the narrow gaps between the α-Al dendrite arms and appeared as plates 1 micron thick and 1-10 microns long. It nucleated on the surface of α -Al dendrite arms and grew without interacting with Si. AlSiMgFe was also found in a script structure. It didn't nucleate new α-Al grains. The solid solution of this eutectic phase consists of 66.77 wt % Al, 19.52 wt% Si, 8.07 wt% Mg and 5.64 wt% Fe
4. The eutectic Si dendrites solidified in the interdendritic region with 0.1-1 μm thick arms spaced at between 1-2 μm. No evidence was found that Si nucleates on the AlFeSiMg intermetallic as claimed by Shankar et al [108]. Si is present in the narrow gaps as both plates and as classic geometrically repeating eutectic structure of fine plates and rods. The composition of the eutectic solid solution was composed of 0.2 wt% Al, 99.62 wt% Si and 0.17 wt% Fe.
5. Subsequently the eutectic Al solidified with a phase composition similar to the primary α-Al dendrites.

Table 18 - Summary of EDS Analysis for UM A356 at 115 MPa with 20 pressure cycles.

Alloy Area Average	Phase				Alloy	
	α- Al	Al (Eutectic)	Si (Eutectic)	AlSiMgFe	Calculated	Measured
Phase Distribution (wt %)	71.36%	21.09%	5.35%	2.1%		
Element						
Al	97.84%	97.61%	0.20%	66.77%	91.90%	89.50%
Si	1.33%	1.44%	99.62%	19.52%	9.13%	9.13%
Mg	0.58%	0.57%	0.00%	8.07%	0.80%	0.78%
Fe	0.25%	0.39%	0.17%	5.64%	0.59%	0.59%
Interdendritic Area	Phase				Alloy	
	α- Al	Al (Eutectic)	Si (Eutectic)	AlSiMgFe	Calculated	Measured
Phase Distribution (wt %)	0.00%	79.78%	20.22%	0.00%		
Element						
Al	97.84%	97.61%	0.20%	66.77%	77.91%	77.84%
Si	1.33%	1.44%	99.62%	19.52%	21.29%	21.29%
Mg	0.58%	0.57%	0.00%	8.07%	0.46%	0.36%
Fe	0.25%	0.39%	0.17%	5.64%	0.34%	0.50%

4.7.2. Microstructural Analysis of the Sr Modified A356 Alloy

Strontium is known as a strong modifier of Si that can modify the eutectic Si at atmospheric pressure (Fig. 72) as well as at high pressure (100-115MPa) in the SC UMSA platform. In a 0.004wt% Sr modified A356 alloy at 100 MPa for a single pressure cycle, Si was found modified ultra finely (dia. 0.25-0.35 μm) as shown in LOM micrograph in Fig.73. SEM micrographs confirmed that Si transformed into a tree like dendritic structure (Figures 75-78). This kind of structure was not found in the literature. It is a new structure observed in this investigation. Similar structures were observed at the same level of pressure with an increasing number of pressure cycles to 10 (Fig. 74). Eutectic Si was found to be modified (dia. 0.3-0.5 μm) even when the amount of

strontium was decreased to 0.015 wt. % at atmospheric pressure as shown in Fig.72. When the same level of Strontium was added in two more experiments subjected to 115 MPa pressure for different pressure cycles, it was found that Si was fully modified and transformed into fibrous structure (dia. 0.25-0.35µm) at 115 MPa for 50 pressure cycles, as shown in LOM microstructure in Fig. 80 and confirmed in SEM micrograph in Figures 81-82. However, surprisingly it was found that Si was not modified at the same level of pressure for only 7 cycles (Fig. 79). The result may be due to the improper melting or mixing of Sr with base alloy during solidification.

On the other hand, dendrite cell size or SDAS have been reduced from 13 µm at atmospheric pressure to 9 µm at 115 MPa due to simultaneous effect of cyclic pressure and increased solidification rate.

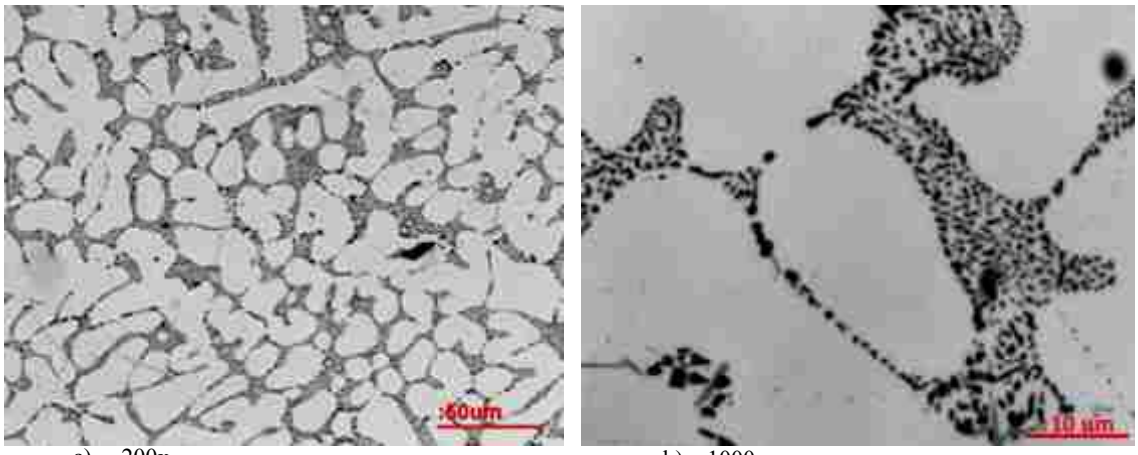

a) 200x b) 1000x

Figure 72 - LOM Microstructure of 0.015 wt% Sr M A356 alloy (Ref. # 72413) solidified in SC die at atmospheric pressure, a) Morphology of α-Al cell and Al-Si eutectics, dendrite cell size 13 µm, b) Fibrous eutectic Si.

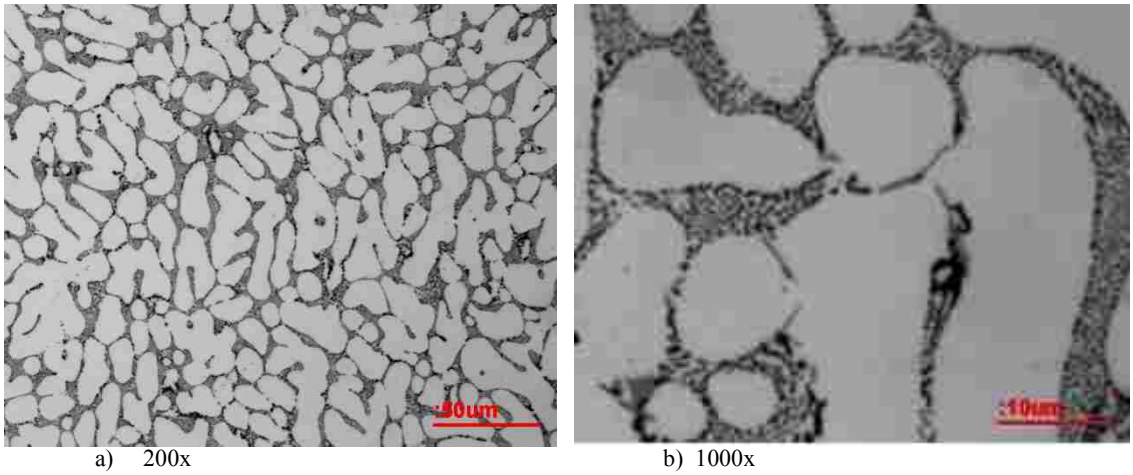

a) 200x b) 1000x

Figure 73 - LOM Microstructure of 0.04 wt% Sr M A356 alloy (Ref. # 51313) solidified in SC die at 100 MPa, 1 cycle pressure a) Morphology of α-Al cells and Al-Si eutectics, dendrite cell size 10.8 µm, b) Fibrous eutectic Si.

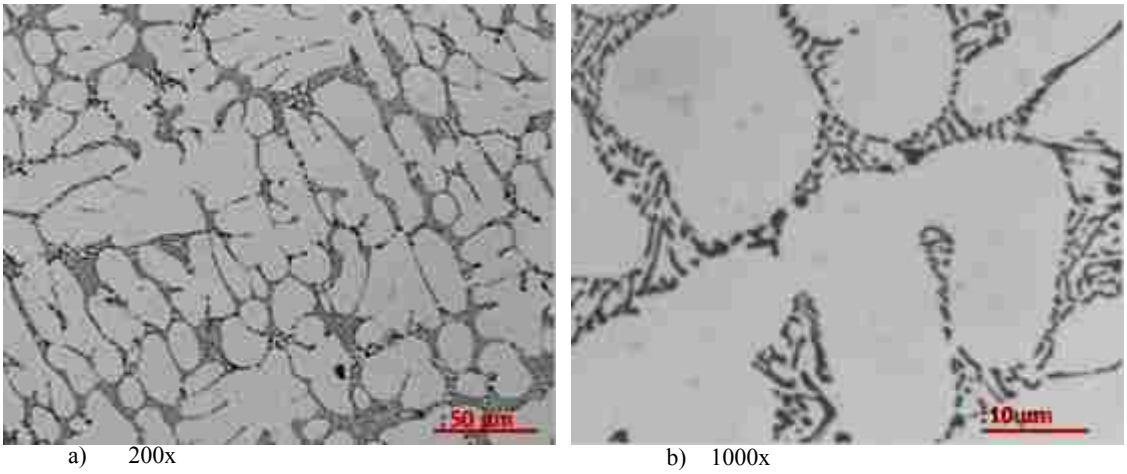

a) 200x b) 1000x

Figure 74 - LOM Microstructure of 0.04 wt% Sr M A356 alloy (Ref. # 51513) solidified in SC die at 100 MPa 10 cycle pressure, a) Morphology of α-Al cells and Al-Si eutectics, dendrite cell size 10.8 µm, b) Fibrous eutectic Si.

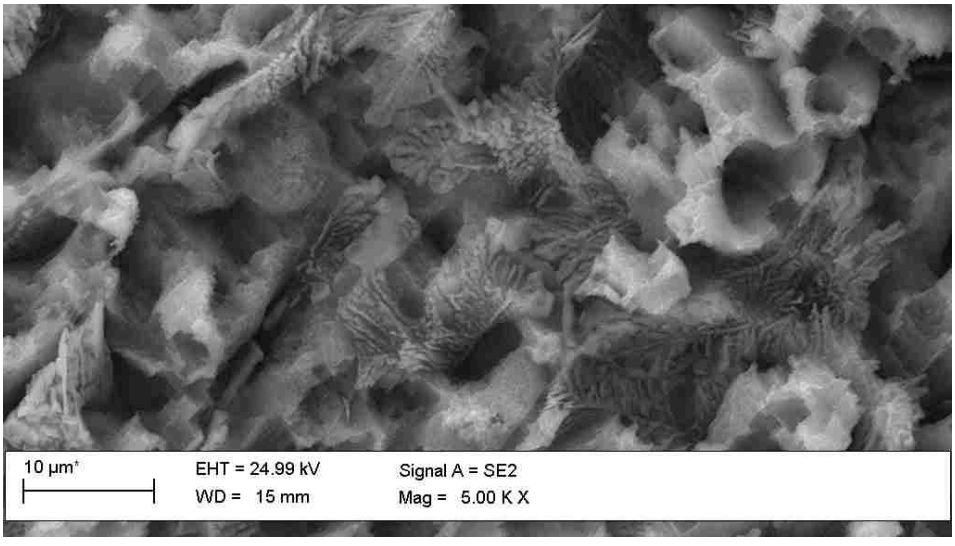

Figure 75 - SEM ultrafine as-cast microstructure of 0.04 wt% Sr M A356 alloy (Ref. # 51313) solidified in SC die at 100 MPa/1 cycle pressure, Morphology of α-Al cells and Al-Si eutectics in etched sample, Fibrous dendritic Si.

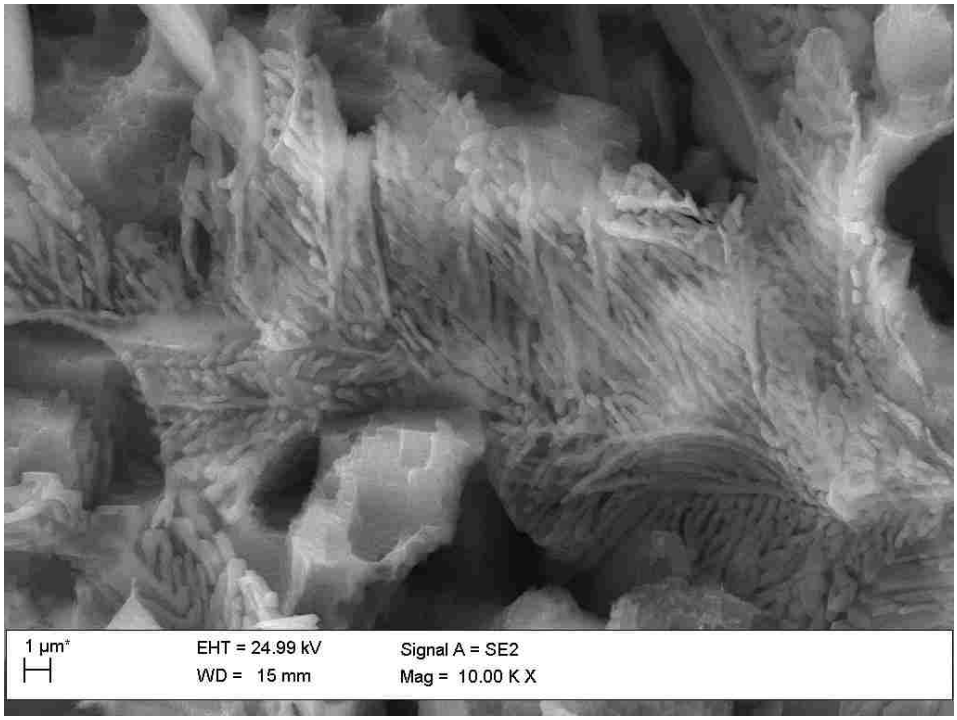

Figure 76 - SEM ultrafine as-cast microstructure of 0.04 wt% Sr M A356 alloy (Ref. # 51313) solidified in SC die at 100 MPa/1 cycle pressure, Morphology of α-Al cells and Al-Si eutectics in etched sample, Fibrous dendritic Si.

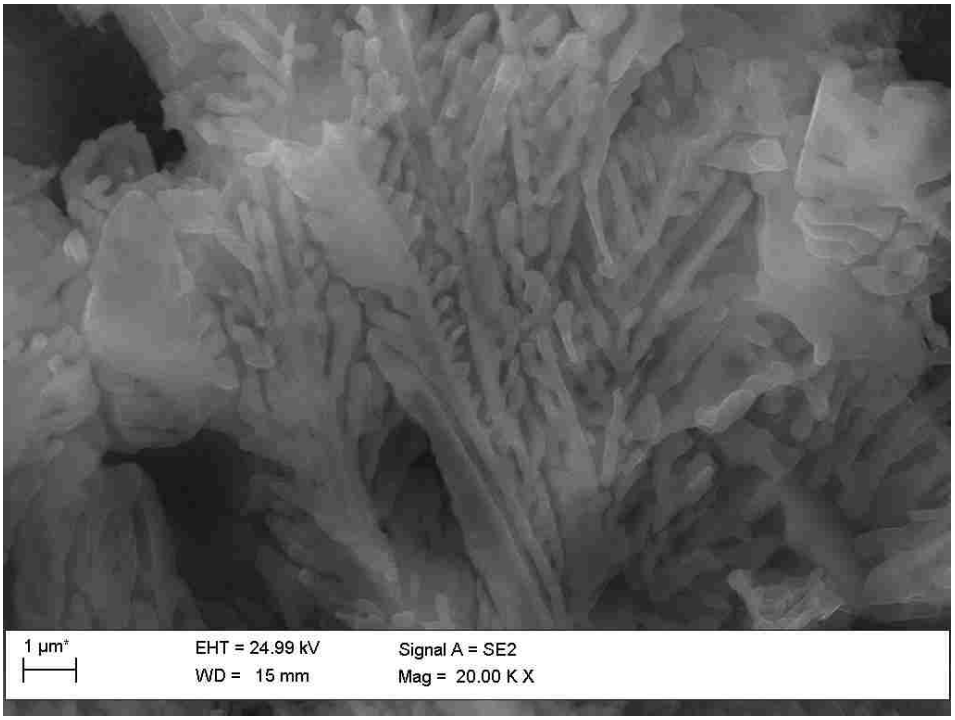

Figure 77 – SEM ultrafine as-cast microstructure of 0.04 wt% Sr M A356 alloy (Ref. # 51313) solidified in SC die at 100 MPa/1 cycle pressure, Morphology of α-Al cells and Al-Si eutectics in etched sample, Fibrous dendritic Si.

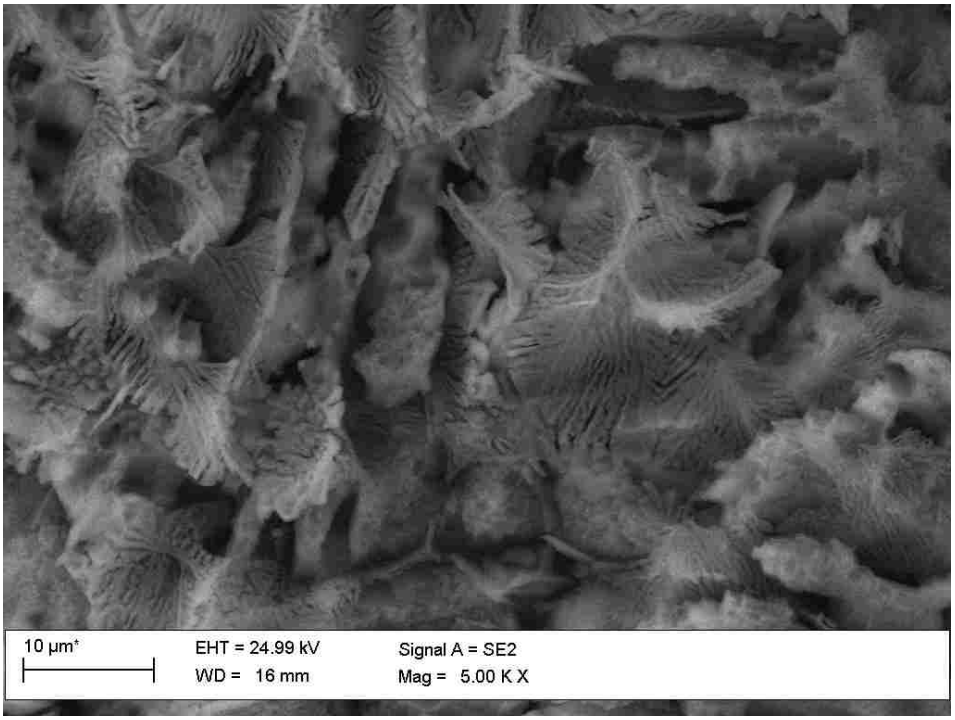

Figure 78 - SEM ultrafine as-cast microstructure of 0.04 wt% Sr M A356 alloy (Ref. # 51513) solidified in SC die at 100 MPa/10 cycles pressure, Morphology of α-Al cells and Al-Si eutectics in etched sample, Fibrous dendritic Si.

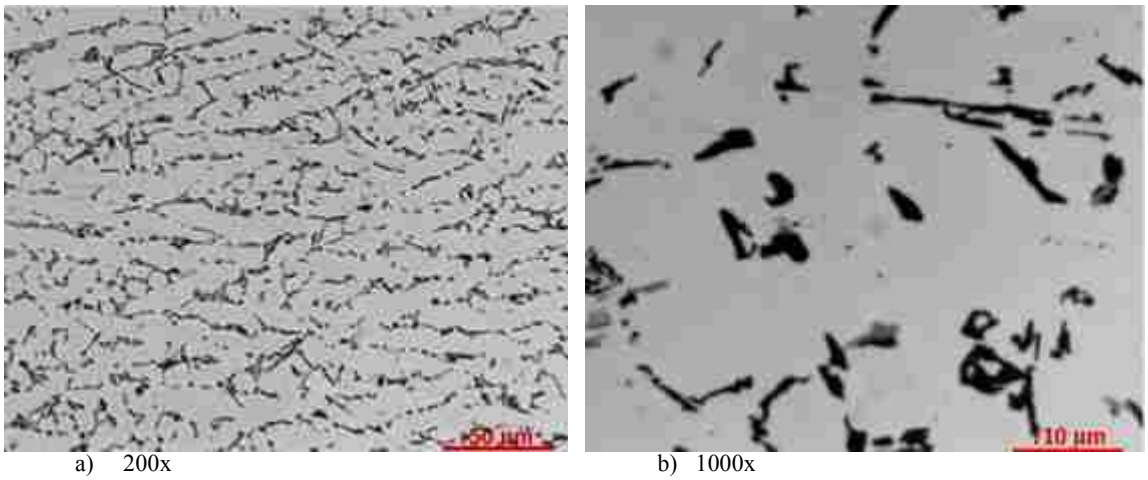

a) 200x b) 1000x

Figure 79 - LOM Microstructure of 0.015 wt% Sr M A356 alloy (Ref. # 61913) solidified in SC die at 115 MPa 7 cycle pressure a) Morphology of α-Al elongated cells and Al-Si eutectics, dendrite cell size 9.4 µm b) Acicular eutectic Si.

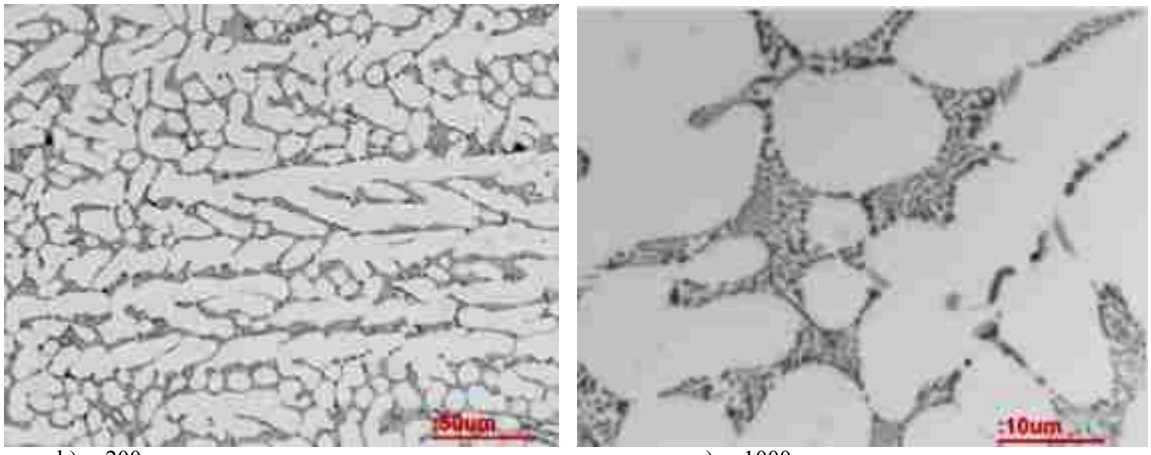

b) 200x a) 1000x

Figure 80 - LOM Microstructure of 0.015 wt% Sr M A356 alloy (Ref. # 71613) solidified in SC die at 115 MPa 50 cycles pressure a) Morphology of α-Al fragmented cells and Al-Si eutectics, dendrite cell size 9.3 µm b) Fibrous eutectic Si.

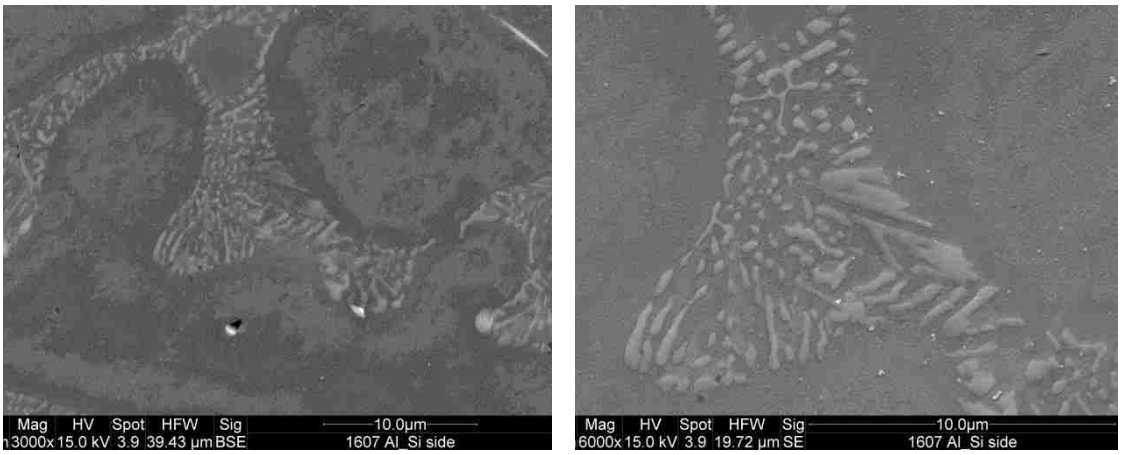

a) 3000x b) 6000x

Figure 81 - SEM Microstructure of 0.015 wt% Sr M A356 alloy (Ref. # 71613) solidified in SC die at 115 MPa/50 cycles pressure a) Morphology of α-Al cells and Al-Si eutectics in polished sample, Fibrous dendritic Si.

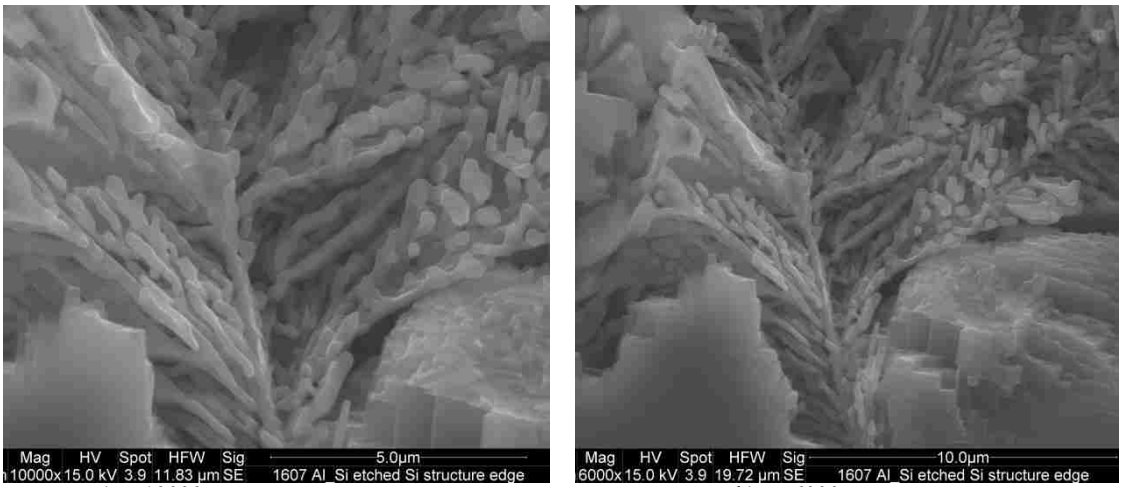

a) 10000x b) 6000x

Figure 82 - SEM Microstructure of 0.015 wt% Sr M A356 alloy (Ref. # 71613) solidified in SC die at 115 MPa/50 cycles pressure a-b) Morphology of Si eutectics in etched sample, Fibrous dendritic Si.

*4.7.2.1. SEM/EDS Analysis of Sr Modified Alloy**

One of the best samples (Ref. 71613) modified with 0.015 wt% Strontium and solidified at 115 MPa with 50 pressure cycles was selected for SEM/EDS analysis. Similar to unmodified A356 alloy, four distinct phases were identified namely α-Al, Eutctic Al, Eutectic Si and AlSiMgFe intermetallic phases through EDS/SEM analysis. Their compositions were deconvoluted and phase distribution quantities were determined and results are tabulated in Table 19 and summarized as below:

1. The α-Al phase was solidified first constituting 65.73 wt% as dendrite cells with an average cell size of 9.3 µm. The α-Al solid solution consists of 98 wt% Al, 1.38 wt %Si and 0.62 wt% Mg.
2. The residual liquid was then pushed into the Interdendritic region. The interdendritic region consists of: 29.06 wt% eutectic Al, 5.13 wt% eutectic Si and 0.08 wt% AlSiMgFe intermetallic phases.
3. The AlSiMgFe intermetallic was appeared to be the second phase that solidified in the narrow gaps before Si and between the -Al dendrite cells. It is appeared as plates 1 micron thick and 1-10 microns long. It nucleates on the surface of α -Al dendrite arms and grows without interacting with Si. AlSiMgFe also found in the form of script structure. It didn't nucleate new α-Al grains. This eutectic phase consists of 2.88 wt % Al, 32 wt% Si, 34.1 wt% Mg and 31.02 wt% Fe.
4. The third phase that solidified in the interdendritic region is eutectic Si dendrites with 0.1-.5 µm thick arms spaced at between 0.5-1.0 µm. No evidence was found that Si nucleates on the AlFeSiMg intermetallic as claimed by Shankar et al [108]. Si was present in the form of a classic tree shaped branched dendrite,

*This work was done in collaboration with Dr. Adam Gesing

which indicated Si solidification occurred in the residual liquid rather than simultaneous formation of Al-Si solid eutectic structure The composition of eutectic solid solution of dendritic Si composed of 0.10 wt% Al, 99.86 wt% Si and 0.04 wt% Mg.

5. Residual Al liquid solidified at the end in the interdendritic region. It has a phase composition similar to the primary α-Al dendrites.

Table 19 - Summary of EDS Analysis for 0.015 wt% Sr M A356 at 115 MPa with 50 pressure cycles.

Alloy Area Average	Phase				Alloy	
	α- Al	Al (Interdendritic)	Si (Dendritic)	AlSiMgFe	Calculated	Measured
Phase Distribution (wt %)	65.73%	29.06%	5.13%	0.08%		
Element						
Al	98.00%	98.18%	0.10%	2.88%	92.96%	91.35%
Si	1.38%	1.38%	99.86%	32.00%	6.45%	8.07%
Mg	0.62%	0.44%	0.04%	34.10%	0.56%	0.58%
Fe	0.00%	0.00%	0.00%	31.02%	0.03%	0.00%
Interdendritic Area	Phase				Alloy	
	α- Al	Al (Interdendritic)	Si (Dendritic)	AlSiMgFe	Calculated	Measured
Phase Distribution (wt %)	0.00%	79.36%	20.64%	0.00%		
Element						
Al	98.00%	98.18%	0.10%	2.88%	77.93%	77.78%
Si	1.38%	1.38%	99.86%	32.00%	21.71%	21.71%
Mg	0.62%	0.44%	0.04%	34.10%	0.36%	0.51%
Fe	0.00%	0.00%	0.00%	31.02%	0.00%	0.00%

4.7.3. Microstructural Analysis of the Nano Alumina Modified A356 Alloy

Apart from Al-Sr master alloy, in this investigation 1wt% Nano Alumina Master Alloy was found to be a good Si modifier for A356 alloy as well as grain refiner. In almost all micrographs, α-Al Dendrite cells converted to a semi dendritic structure. The LOM

micrographs (Figures 86-87) show a significant modification in Eutectic Si at 115 MPa with some exceptions. Compare to atmospheric pressure samples (Fig. 83), Si showed full modification at 115 MPa with increasing pressure cycles 20 and 50. The SEM micrographs (Figures 88-89) confirmed that Si was converted to fibrous structure (Si. dia. 0.3-0.4 µm) with the presence of shrinkage cavity full of MgO. Details will be discussed in EDS analysis section. However, no modification was observed at 2 pressure cycles despite having the same pressure during solidification (Figures 84-85) due to unknown reasons.

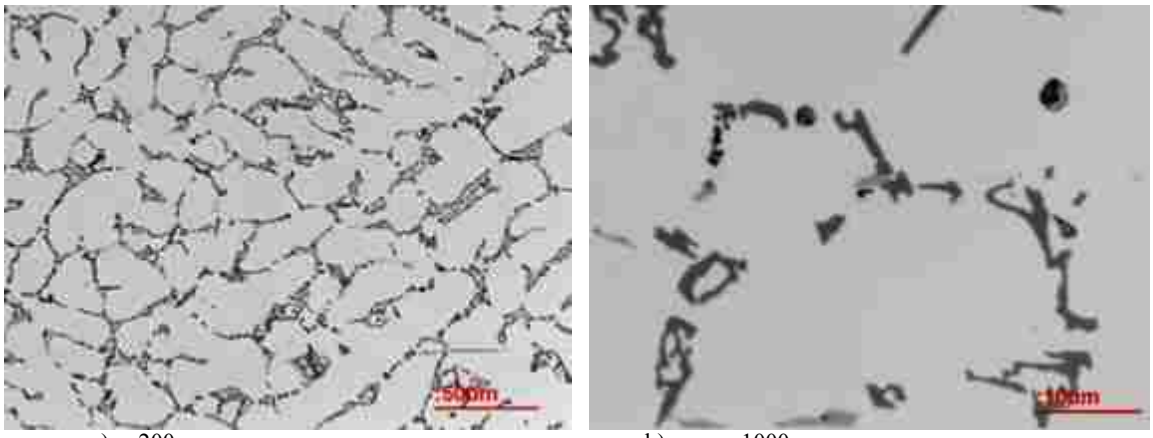

a) 200x b) 1000x

Figure 83 - LOM Microstructure of 1 wt% NAMA M A356 alloy (Ref. # 72413) solidified in SC die at atmospheric pressure a) Morphology of α-Al cells and Al-Si eutectics, dendrite cell size 16.1 µm, b) Acicular eutectic Si.

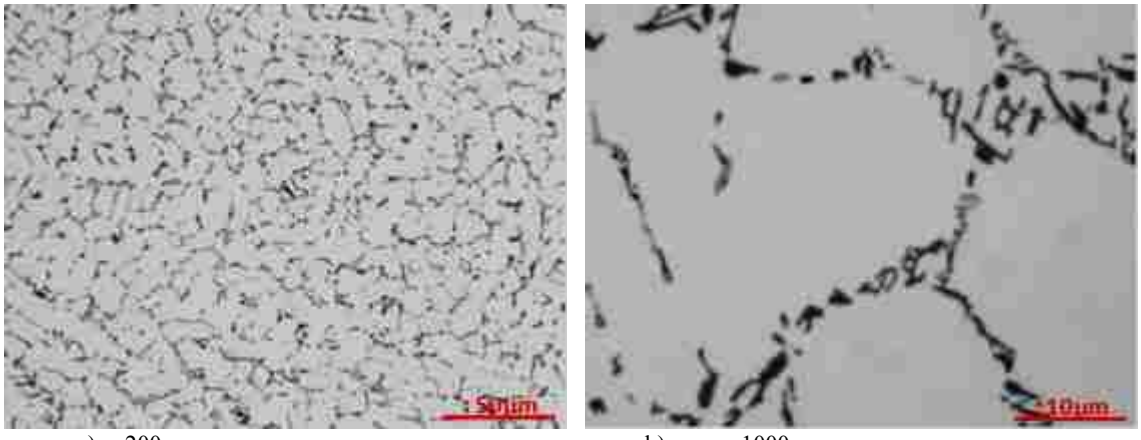

a) 200x b) 1000x

Figure 84 - LOM Microstructure of 1 wt% NAMA M A356 alloy (Ref. # 61213B) solidified in SC die at 115 MPa 2 cycles pressure a) Morphology of α-Al cells and Al-Si eutectics, dendrite cell size 7.8 µm, b) Acicular eutectic Si.

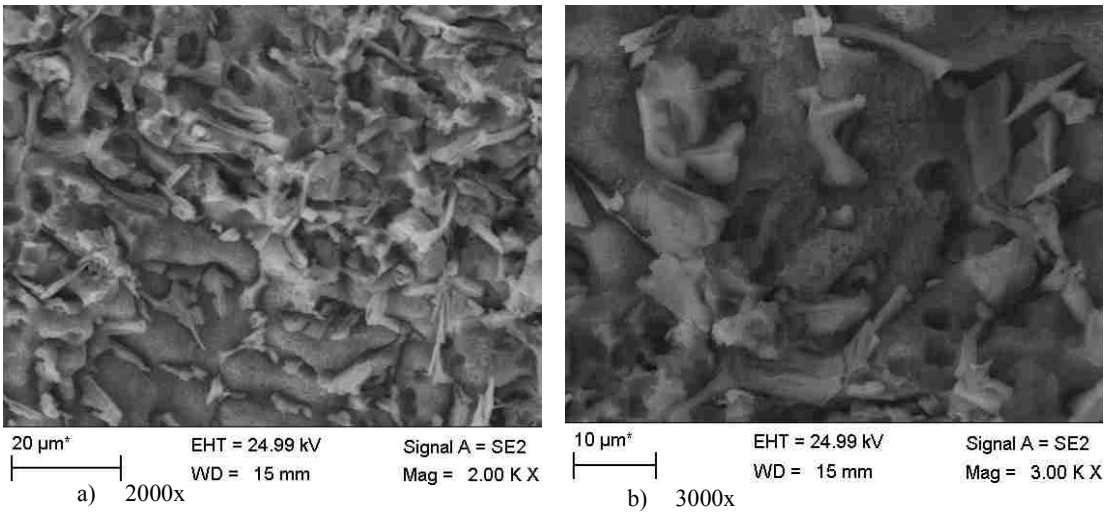

a) 2000x b) 3000x

Figure 85 - SEM Microstructure of 1 wt% NAMA M A356 alloy (Ref. # 61213B) solidified in SC die at 115 MPa 2 cycles pressure, Morphology of α-Al cells and Al-Si eutectics in an etched sample, acicular eutectic Si.

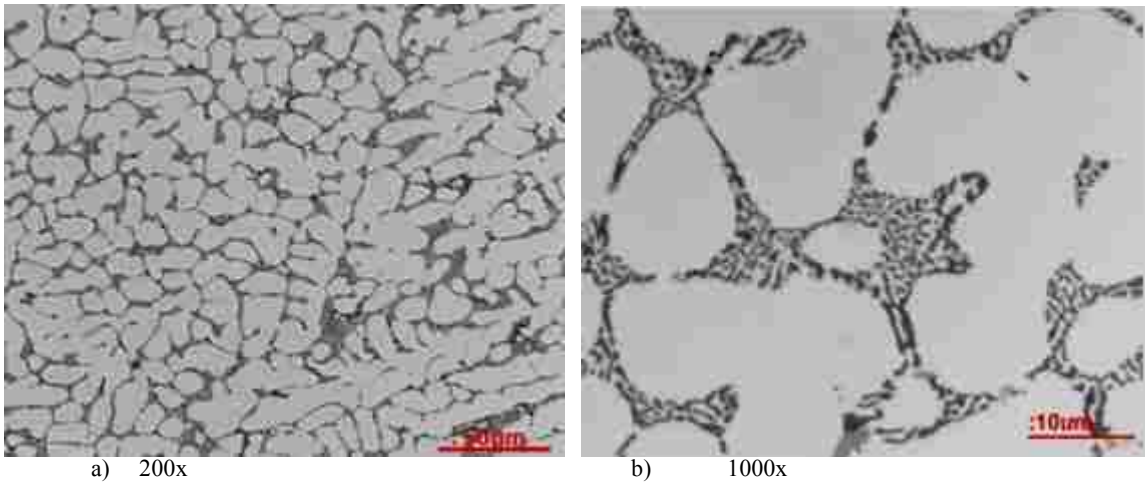

a) 200x b) 1000x

Figure 86 - LOM Microstructure of 1 wt% NAMA M A356 alloy (Ref. # 62013) solidified in SC die at 115 MPa 20 cycles pressure a) Morphology of fragmented and semi-solid α-Al dendrites and Al-Si eutectics, dendrite cell size 11.3 µm, b) Fibrous eutectic Si.

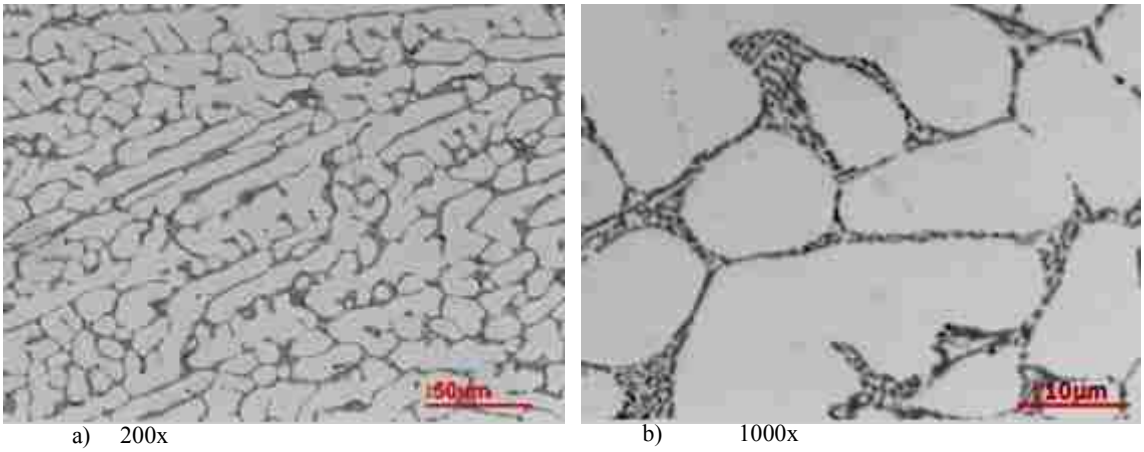

a) 200x b) 1000x

Figure 87 - LOM Microstructure of 1 wt% NAMA M A356 alloy (Ref. # 71513) solidified in SC die at 115 MPa 50 cycles pressure a) Morphology of α-Al cells and Al-Si eutectics, dendrite cell size 9.2 µm b) Fibrous eutectic Si.

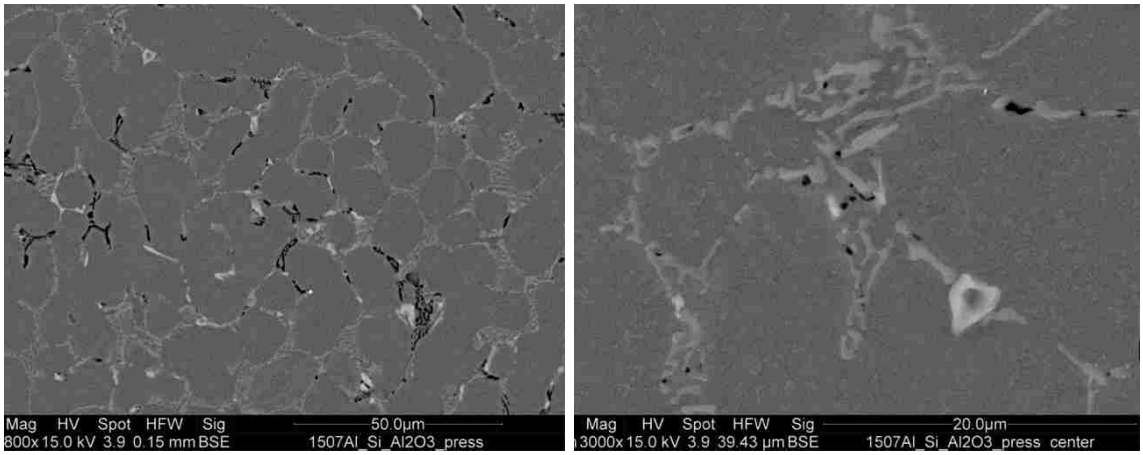

a) 800x a) 3000x

Figure 88 - SEM Microstructure of 1 wt% NAMA M A356 alloy (Ref. # 71513) solidified in SC die at 115 MPa 50 cycles pressure a) Morphology of α-Al Cells and Al-Si eutectics in polished sample, b) Ultrafine Si.

The dendrite cell size is reduced from 16 µm at atmospheric pressure to 9 µm at 115 MPa with 50 pressure cycles and it refined to 8 µm with 2 pressure cycles (Fig.84). Most of the dendrites converted into equiaxed and semi-solid morphology (Figures 87-88).

a) 3000x a) 6000x

Figure 89 - SEM Microstructure of 1 wt% NAMA M A356 alloy (Ref. # 71513) solidified in SC die at 115 MPa 50 cycles pressure a) Morphology of α-Al equiaxed cells and Al-Si eutectics in polished sample, b) shrinkage porosity filled with MgO.

*4.7.3.1. SEM/EDS Analysis of Nano Alumina Modified A356 Alloy**

One of the best samples (Ref. 71513) modified with 1 wt% Nano Alumina Master Alloy and solidified at 115 MPa with 50 pressure cycles was selected for SEM/EDS analysis.

*This work was done in collaboration with Dr. Adam Gesing

Similar to unmodified and strontium modified A356 alloy, four distinct phases were identified in this alloy. Their compositions are deconvoluted and phase distribution quantities are determined. Results are shown in Table 20 and an observational summary is presented below.

1. The α-Al phase was solidified first and constituted 75.47 wt% dendrite cells with an average dendrite cell size of 9.2 μm. The α-Al solid solution consists of 97.18 wt.% Al, 1.28 wt. %Si and 0.75 wt.% Mg, 0.79wt.% Fe.
2. The residual liquid was then pushed into the interdendritic regions that account for 24.53wt.% of the alloy. The interdendritic region consists of 17.64 wt% eutectic Al, 6.89wt.% eutectic Si and a negligible amount of AlSiMgFe intermetallic phase.
3. AlSiMgFe intermetallics were appeared to be solidified first in the interdendritic region and found in the narrow gaps between the α-Al dendrite arms as plates. The plates are less than 1 micron thick and 1-10 microns long. It is found to be nucleated on the surface of α -Al dendrite arms and grew without interacting with Si. Hence it can be concluded that it solidified before Si. Moreover, AlSiMgFe intermetallics didn't show any tendency on nucleating any new α -Al grains.
4. Subsequently Eutectic Si was found to have solidified in dendritic structure just after AlSiMgFe phase solidification. No evidence was found that Si nucleates on the AlFeSiMg intermetallics. Si appeared as dendritic trees growing in the gaps in between α-Al dendrite arms. Si dendrite arms are around 0.3-0.4 microns in diameter and are spaced approximately 1.5 microns apart. The shape of the eutectic Si dendrites suggested that it grew in the residual melt, rater than

simultaneous eutectic solidification. The composition of Si eutectic solid solution composed of 0.04 wt% Al, 99.68 wt% Si and 0.15 wt% Mg.

5. 17.64 wt% of α-Al matrix were found in the Al-Si "eutectic region". It was composed of a phase that is actually purer than that of the primary α-Al dendrite. Calculation suggested that no Si was available in the matrix solid solution and Mg content of 0.8% was almost similar in the both Al matrix. Fe was also low, but it did not show its concentration in the EDX results.
6. AlSiMg oxide were found to be present as a glass layer in the solidification shrinkage cavities formed as secondary dendritic arms in the interdendritic region (Fig. 89). Associated with interdendritic Si, these secondary dendrites have 0.5-1 micron arm spacing, Oxides are found at the location which was locally last to solidify in the interdendritic region. In this case it is clear that there is oxide liquid in the microstructure at the location that solidified last. The calculated composition should be solid at 550^{o}C. The observations suggest that the oxide liquid is under cooled and deformable by the solidifying secondary Al dendrite.
7. Alumina nano-particles are very non-uniformly distributed in the interdendritic space. They did not nucleate the primary α-Al dendrites. There are also no rosette structures in the secondary interdendritic structure that radiate from a central Alumina nanoparticle in the Si, rather the individual alumina nano particles are located in the secondary Al phase and the structure of the Si dendrites appear not to be affected by them. Many nano-particles probably reacted to form the oxide glass that was observed to coat the solidification shrinkage cavities in the interdendritic space.

Table 20 - Summary of EDS Analysis for 1 wt% Nano Alumina Modified A356 at 115 MPa with 50 Pressure cycles.

Alloy Area Average	Phases				Alloy	
	α- Al	Al (Eutectic)	Si (Eutectic)	AlSiMgFe	Calculated	Measured
Phase Distribution (wt %)	75.47%	17.64%	6.89%	0.00%		
Element						
Al	97.18%	99.17%	0.04%	31.75%	90.84%	90.95%
Si	1.28%	0.00%	99.68%	42.42%	7.83%	8.05%
Mg	0.75%	0.83%	0.15%	17.76%	0.72%	0.99%
Fe	0.79%			8.06%	0.61%	0.00%
Interdendtitic Area	Phases				Alloy	
	α- Al	Al (Eutectic)	Si (Eutectic)	AlSiMgFe	Calculated	Measured
Phase Distribution (wt %)	00.00%	71.92%	28.08%	2.36%		
Element						
Al	97.18%	99.17%	0.04%	31.75%	72.27%	72.27%
Si	1.28%	0.00%	99.68%	42.42%	27.06%	27.06%
Mg	0.75%	0.83%	0.15%	17.76%	0.65%	0.67%
Fe	0.79%			8.06%	0.03%	0.00%

4.7.4. Microstructural Analysis of the Sr and Nano Alumina Combined Modified A356 Alloy

As discussed in the previous sections, it was found that Sr and NAM master alloy played an important role on the modification of Si. In this investigation, the combined effects of both Sr and NAMA have been revealed quite significantly over their individual role on the microstructure of A356 Alloy along with the simultaneous effect of pressure. The eutectic Si is fully modified at both atmospheric pressure (Fig. 90) and 115 MPa pressure with various cycles. Three experiments were done at the same pressure level with varying pressure cycles. The SEM micrograph (Fig.94) confirmed that the eutectic Si (dia. 0.15-0.3 µm) was super modified (Fig. 91) for 12 cycles of pressure at 115 MPa, compared to at 20 (Fig. 92) and 50 pressure cycles (Fig. 93). Also, the dendrite cell size (9.2 µm) was

found to be comparatively refined and transformed into equiaxed structure (Fig. 91) than those pressure cycles (Figures 92-93).

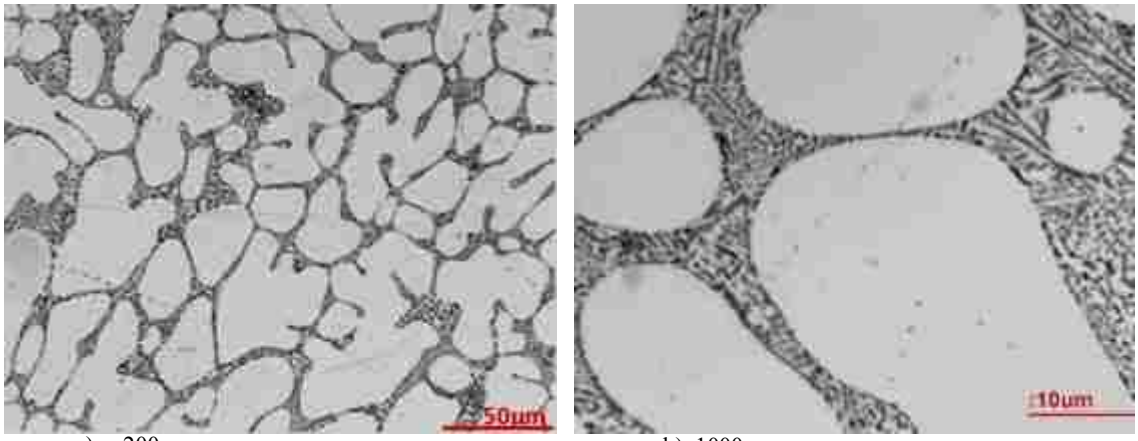

a) 200x b) 1000x

Figure 90 - LOM Microstructure of both 0.015 wt% Sr & 1 wt% NAMA M A356 alloy (Ref. # 72413C) solidified in SC die at atmospheric pressure a) Morphology of α-Al cells & Al-Si eutectics, dendrite cell size 15.2 µm b) Fibrous eutectic Si.

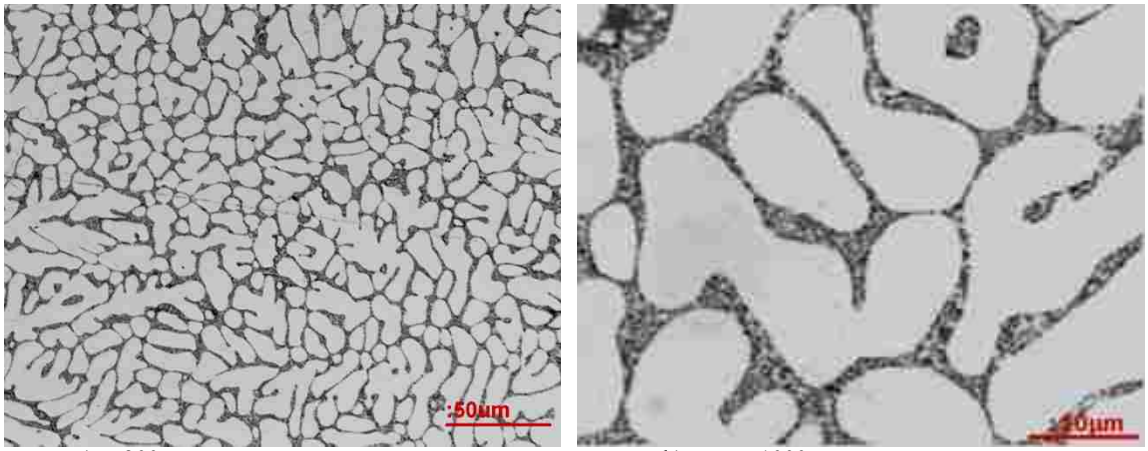

a) 200x b) 1000x

Figure 91 - LOM Microstructure of both 0.015 wt% Sr & 1 wt% NAMA M A356 alloy (Ref. # 81413) solidified in SC die at 115 MPa 12 cycles pressure a) Morphology of α-Al cells & Al-Si eutectics, dendrite cell size 9.2 µm b) Fibrous eutectic Si.

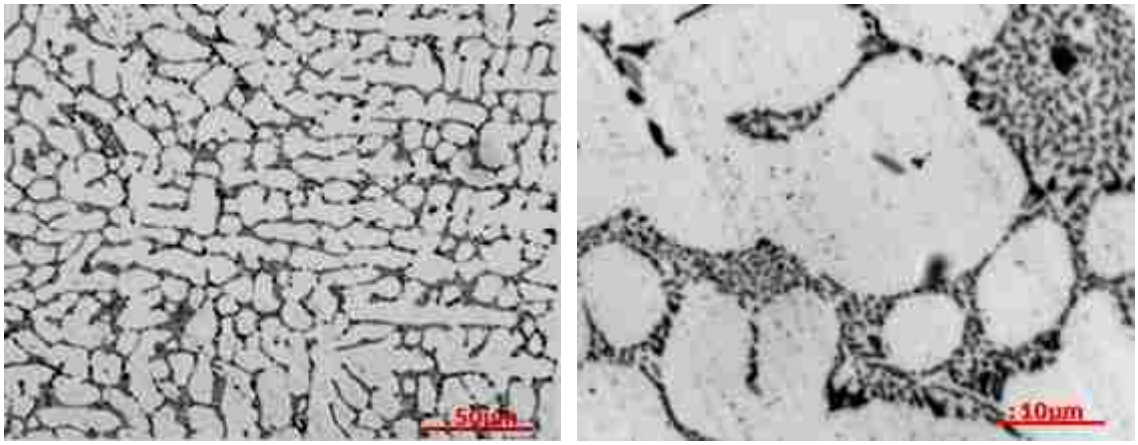

a) 200x b) 1000x

Figure 92 - LOM Microstructure of both 0.015 wt% Sr & 1 wt% NAMA M A356 alloy (Ref. # 62413) solidified in SC die at 115 MPa 20 cycles pressure a) Morphology of α-Al cells and Al-Si eutectics, dendrite cell size 9.9 µm b) Fibrous eutectic Si.

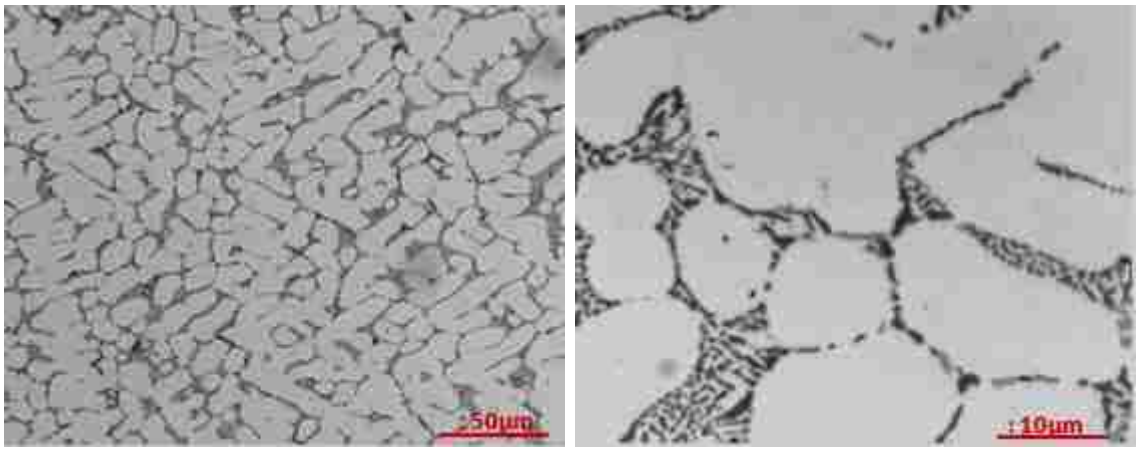

a) 200x b) 1000x

Figure 93 - LOM Microstructure of both 0.015 wt% Sr & 1 wt% NAMA M A356 alloy (Ref. # 61713) solidified in SC die at 115 MPa 50 cycles pressure a) Morphology of α-Al cells and Al-Si eutectics, dendrite cell size 7.6 µm b) Fibrous eutectic Si.

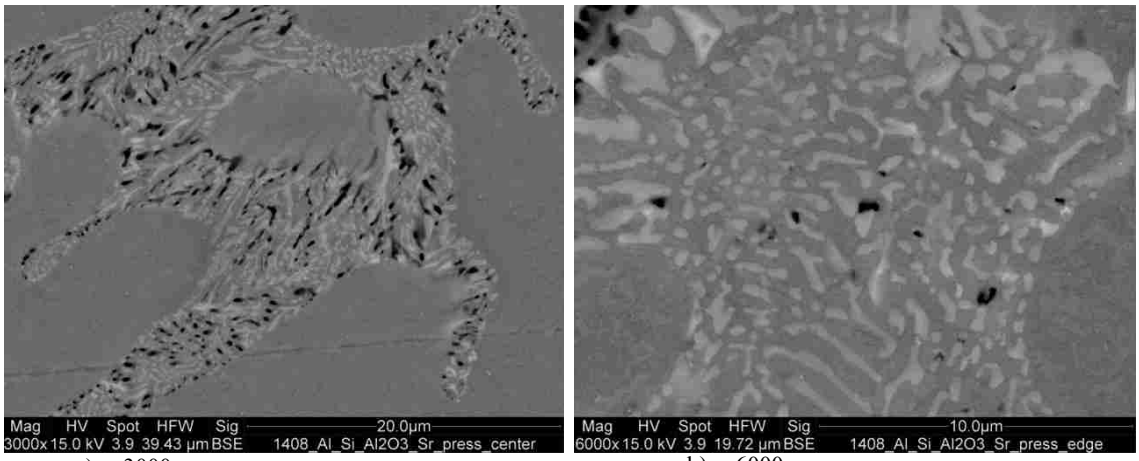

a) 3000x b) 6000x

Figure 94 - SEM Microstructure of both 0.015 wt% Sr & 1 wt% NAMA M A356 alloy (Ref. # 81413) solidified in SC die at 115 MPa 12 cycles pressure a) Morphology of α-Al cells and Al-Si eutectics in polished sample b) Fibrous eutectic Si.

4.8. Solution Treatment

The main purpose of the solution treatment was to change the morphology of silicon from lamellar and fibrous structure to globular structure within a very short period of soaking time. In the industrial practice of the Alcoa Wheel, it used to take 5 hours at 540°C. In this investigation, the same temperature was used for the solution treatment. However, the target was to determine the shortest time in order to achieve complete spheroidization of Si. Two types of test samples were chosen for the solution treatment, namely unmodified A356 alloy (Ref. # 62513, Figures 67-68) and Strontium modified A356 alloy (Ref. # 71613, Figures 80-82). Both test samples were solidified at 115 MPa pressure, one with 20 and the other with 50 cycles respectively in the SC UMSA platform. From each type of alloy two test samples were cut and subjected to two different soaking times. The first unmodified test sample was tried for 30min and the second one for 15min. The strontium modified test samples were soaked similarly.

LOM micrographs (Figures 95-98) indicated that both unmodified and Sr modified alloy showed very rapid spheroidization within 15 min and the eutectic silicon transformed into ultra fine globular type Si with an average diameter of 1.12-1.16 μm. The silicon spheroids were homogenously distributed all over the microstructure in both alloys. SEM micrographs (Figures 99-100) confirmed the result and also identified the main phases very clearly. Most of the AlSiMgFe intermetallic compound was broken into small pieces of average 1-2 μm in length, except a few that remained at 5 μm.

Image Analysis (Figures 101-105) of the Si spheroids showed that the perimeter, area and diameter of the Si spheroids increased if the soaking time increased from 15 to 30 min in

both Sr modified and unmodified alloy, that is, with increasing soaking time, silicon particles become larger in terms of three characteristic size (perimeter, area and mean diameter), which is not desirable. However, compare to unmodified samples, Si spheroids were found relatively smaller in Sr modified samples at both soaking times. It is expected that with lesser soaking time Si spheroids could have been smallest in size. However, Vanko et al. [25] didn't observe complete spheroidization of Si within 5-10 minutes soaking time at 540°C for the same alloy cast at 100Mpa squeeze pressure.

Roundness of Si spheroids was calculated through image analysis, where roundness is a dimensionless shape factor describing the circularity of Si spheroids. A Si particle having roundness 1 means it is truly circular. It is observed that the silicon spheroids in both modified and unmodified samples were almost round and didn't have a significant difference between them at varying soaking time. The Sr modified samples was found to be comparatively more round with a smaller aspect ratio than the unmodified samples.

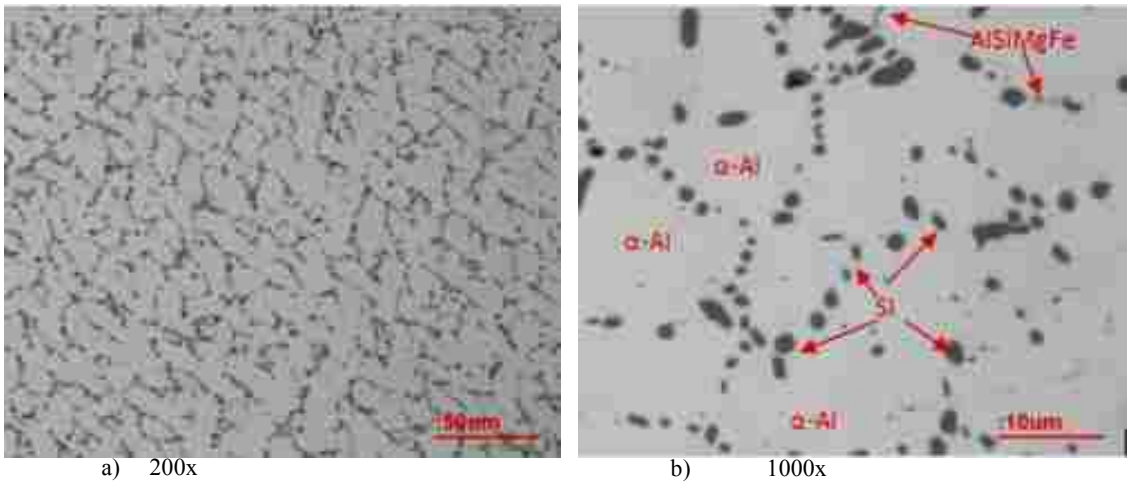

a) 200x b) 1000x

Figure 95 - LOM Microstructure of UM A356 alloy (Ref. # 62513) solidified in SC die at 115 MPa 20 cycles pressure and Solution Treated at 540°C for 15 min a) Morphology of α-Al & Al-Si eutectics, b) Spheroids of eutectic Si and other phases.

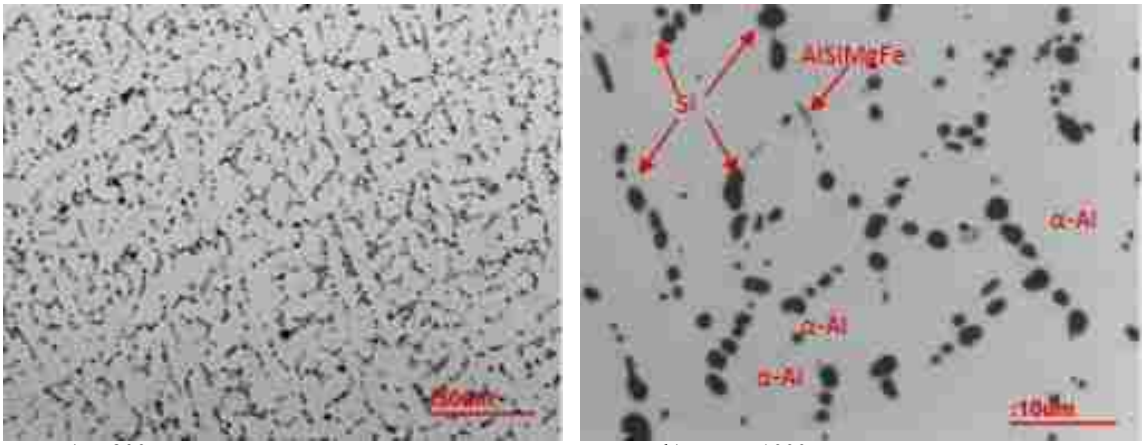

a) 200x b) 1000x

Figure 96 - LOM Microstructure of UM A356 alloy (Ref. # 62513) solidified in SC die at 115 MPa 20 cycles pressure and Solution Treated at 540°C for 30 min a) Morphology of α-Al & Al-Si eutectics, b) Spheroids of eutectic Si and other phases.

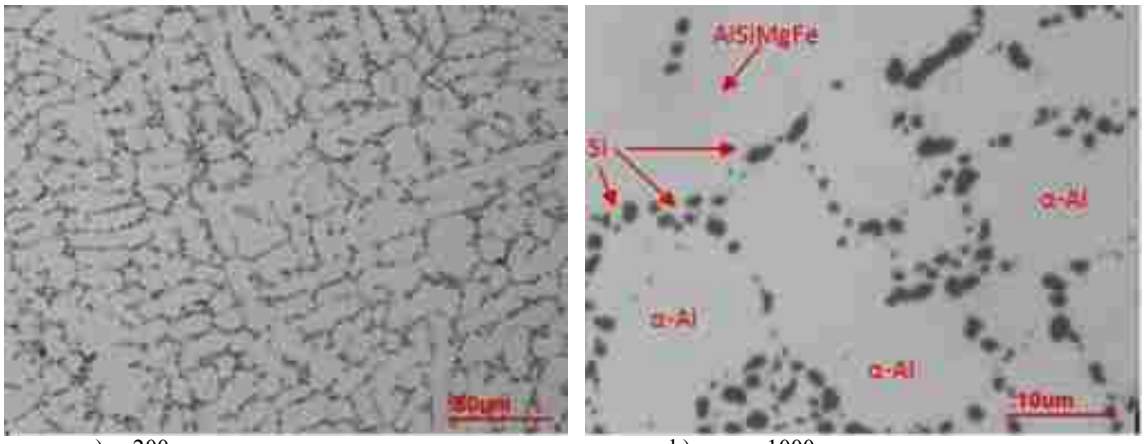

a) 200x b) 1000x

Figure 97 - LOM Microstructure of 0.015 wt% Sr M A356 alloy (Ref. # 71613) solidified in SC die at 115 MPa 50 cycles pressure and Solution Treated at 540°C for 15 min a) Morphology of α-Al Dendrite & Al-Si eutectics, b) Spheroids of eutectic Si and other phases.

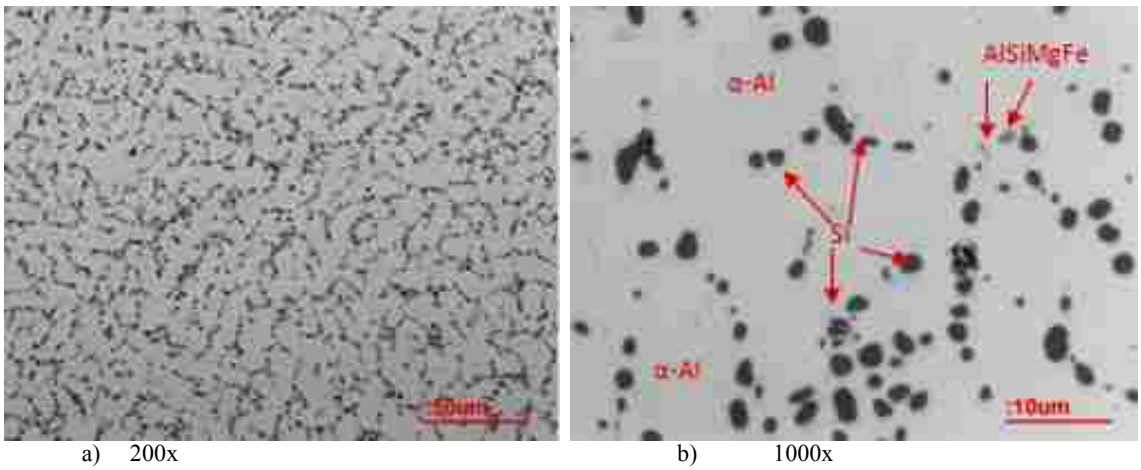

a) 200x b) 1000x

Figure 98 - LOM Microstructure of 0.015 wt% Sr M A356 alloy (Ref. # 71613) solidified in SC die at 115 MPa 50 cycles pressure and Solution Treated at 540°C for 30 min a) Morphology of α-Al & Al-Si eutectics, b) Spheroids of eutectic Si and other phases.

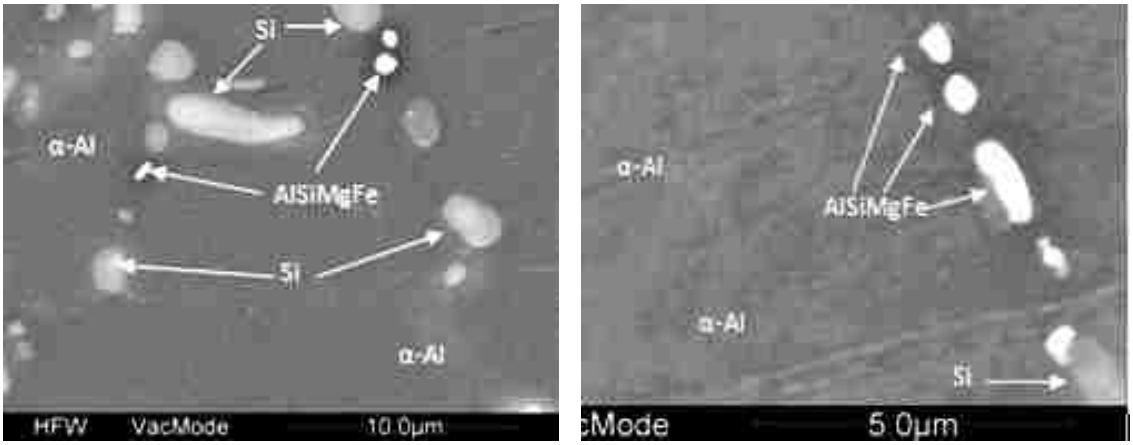

b) 3000x a) 6000x

Figure 99 - SEM Microstructure of UM A356 alloy (Ref. # 62513) solidified in SC die at 115 MPa 20 cycles pressure and Solution Treated at 540°C for 30 min a) Morphology of α-Al & Al-Si eutectics, b) Spheroids of eutectic Si and other phases.

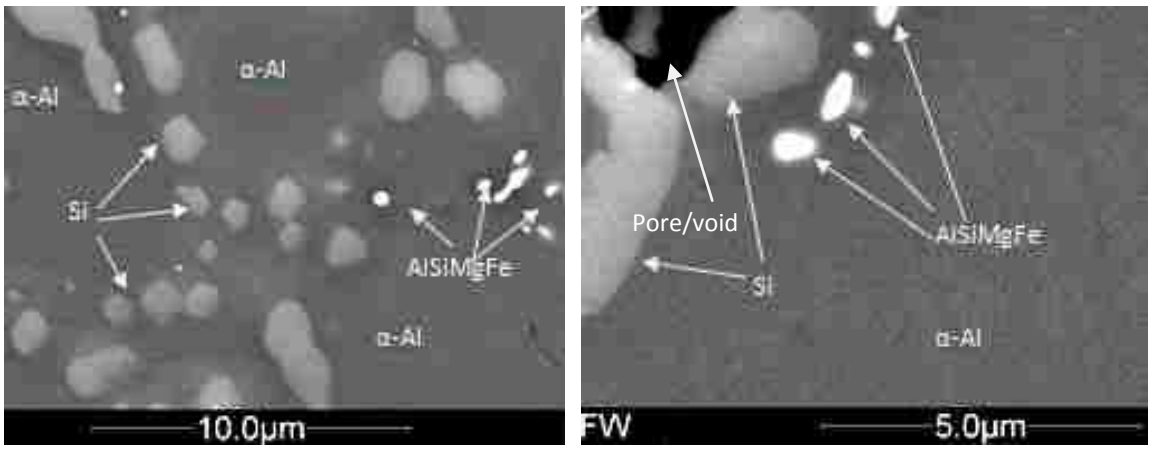

b) 3000x a) 6000x

Figure 100 - SEM Microstructure of 0.015 wt% Sr M A356 alloy (Ref. # 71613) solidified in SC die at 115 MPa 50 cycles pressure and Solution Treated at 540 °C for 30 min a) Morphology of α-Al & Al-Si eutectics, b) Spheroids of eutectic Si and other phases.

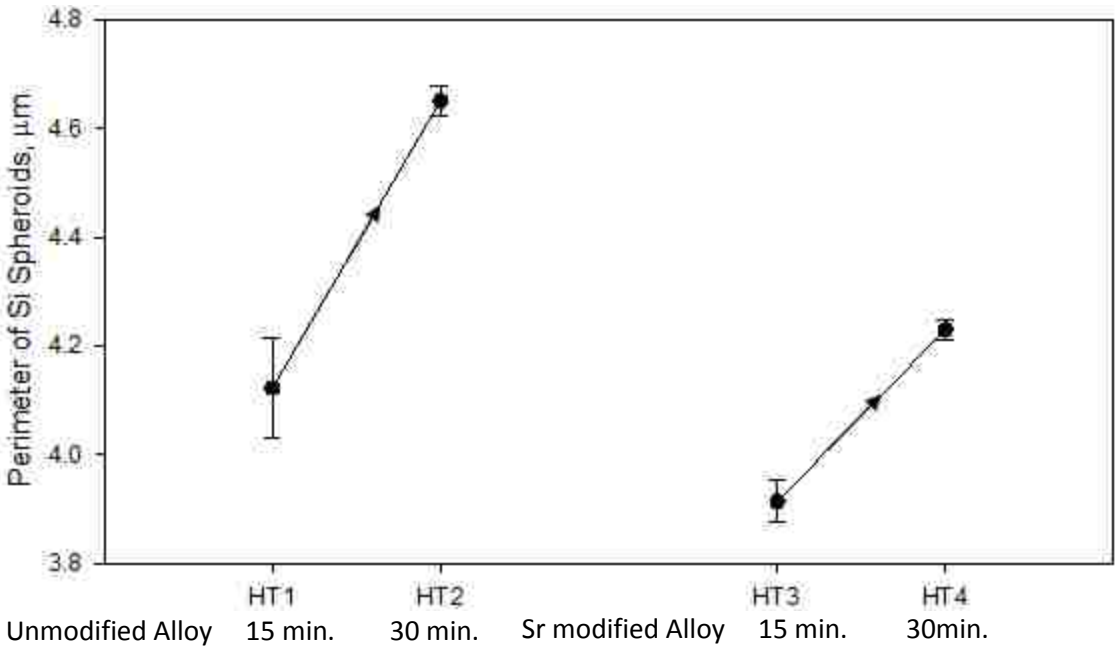

Figure 101 - Image Analysis of Si Spheroids in Solution Treatment for UM and Strontium modified alloy at 540°C for 15-30 min, Comparison of Perimeter of Si spheroids at different soaking time and alloy.

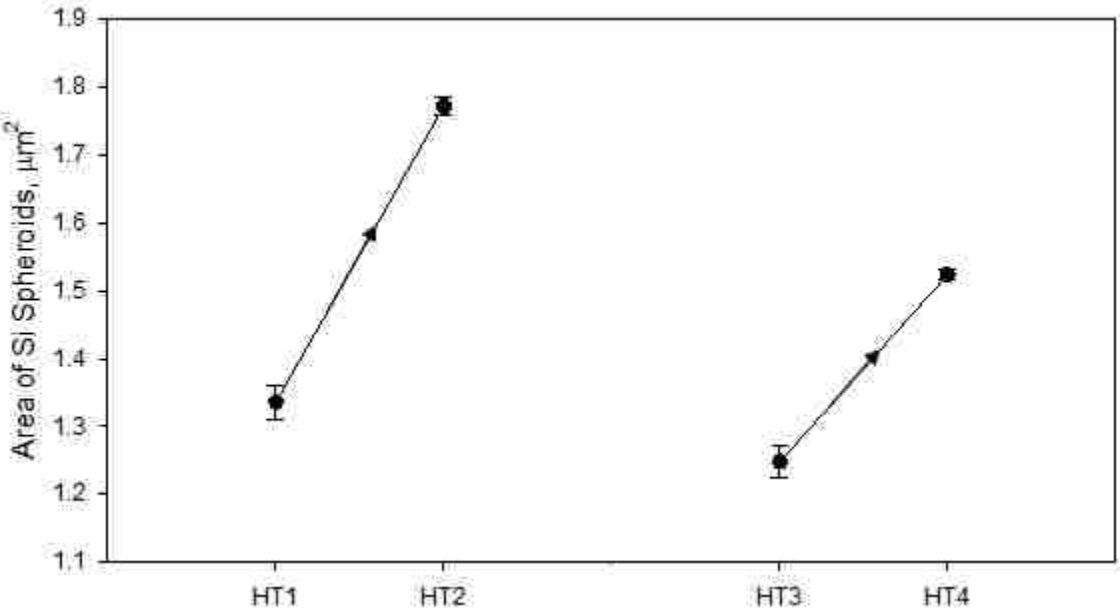

Figure 102 - Image Analysis of Si Spheroids in Solution Treatment for UM and Strontium modified alloy at 540°C for 15-30 min, Comparison of Area of Si spheroids at different soaking time and alloy.

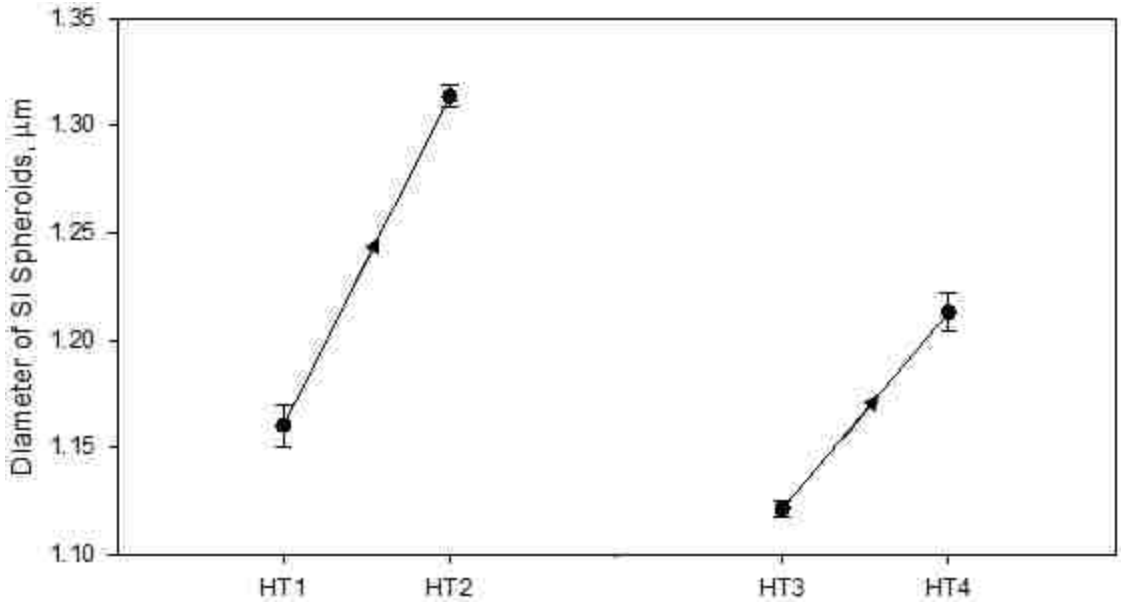

Figure 103 - Image Analysis of Si Spheroids in Solution Treatment for UM and Strontium modified alloy at 540°C for 15-30 min, Comparison of Diameter of Si spheroids at different soaking time and alloy.

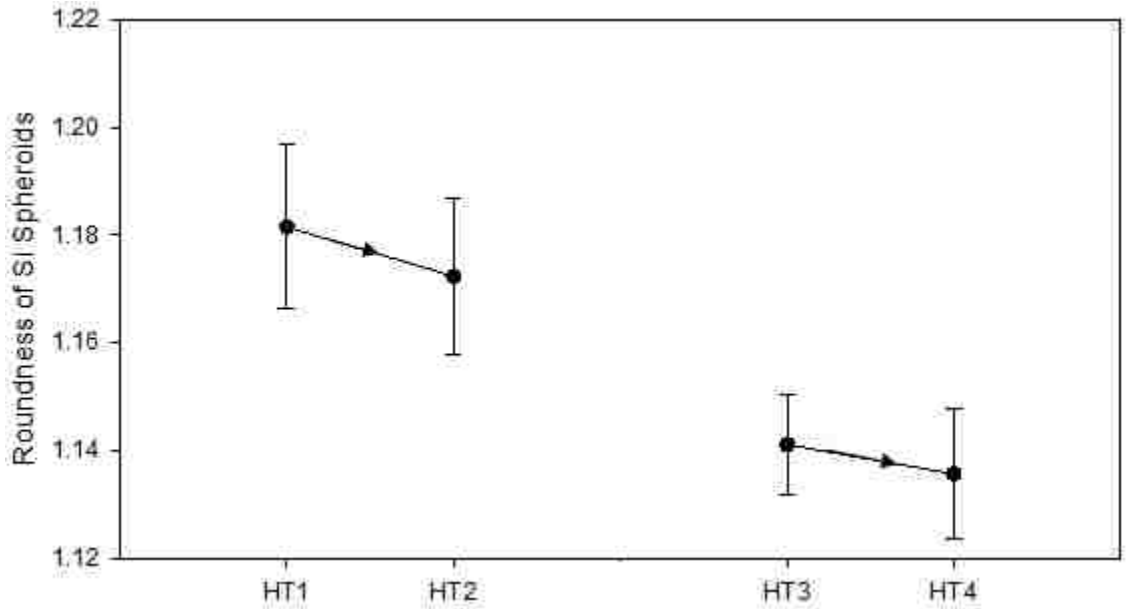

Figure 104 - Image Analysis of Si Spheroids in Solution Treatment for UM and Strontium modified alloy at 540°C for 15-30 min, Comparison of Roundness of Si spheroids at different soaking time and alloy.

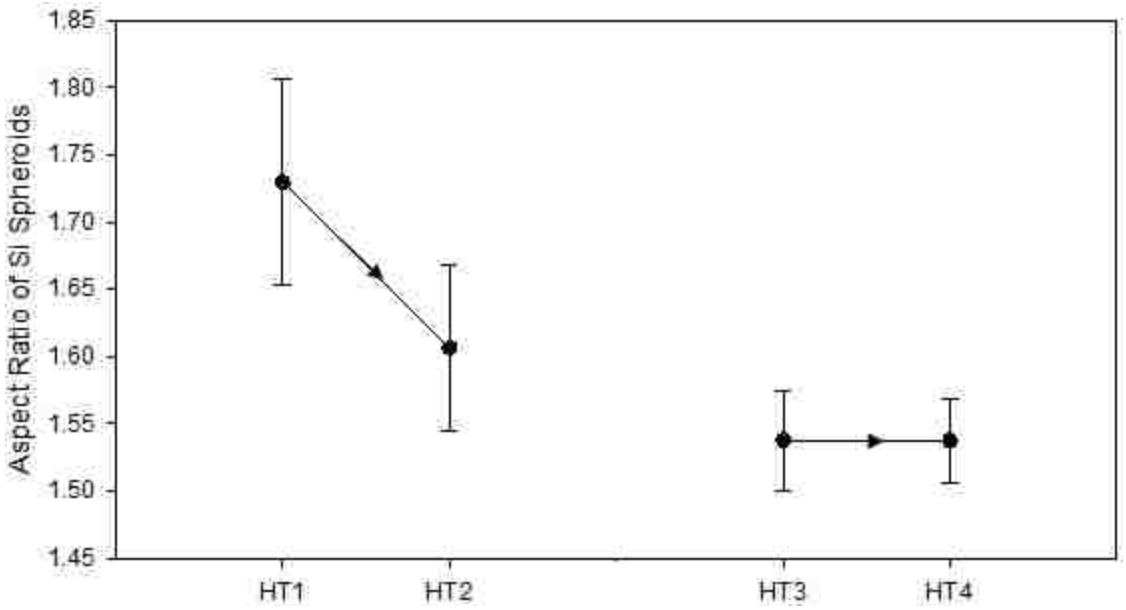

Figure 105 - Image analysis of Si spheroids in solution treatment for UM and Strontium modified alloy at 540°C for 15-30 min, Comparison of aspect ratio of Si spheroids at different soaking time and alloy.

4.8.1. SEM/EDS Analysis for Solution Treated UM A356 Alloy*

As can be seen in Table 22, after the solution treatment at 540°C for 30 min, the alloy area average composition was found to be almost the same as the as-cast sample. There was no observed change in the percentage of Si, Mg and Fe except the availability of a new element Ni. Ni was available only in the trace level in the as-cast alloy composition. Its presence could be due to contamination of Ni during re-melting or solution treatments of the sample. However, there was a significant change in the percentage of phases that appeared after the solution treatment. Eutectic Si phase (average dia. of 1.12 - 1.16 µm) was found homogenously distributed throughout the α-Al matrix. The AlSiMgFe phase which was originally present as plates had also been in the process of breakup and spheroidization during solution treatment. Additionally, a new phase AlSiFeNi appeared in the alloy pushing the Mg element to go into the solid solution of α-Al matrix and eutectic Si. Hence, it was found that Mg was increased in both solid solutions.

Round voids were also found around 2 microns in diameter scattered randomly, but associated with Si and/or AlFeSiMg particles, and located in the original interdendritic regions. This could be either shrinkage porosity that was spheroidized by solution treatment or of H_2 bubbles that came out of solution during heat treatment.

4.8.2. SEM/EDS Analysis for Solution Treated Sr Modified Alloy*

There was a significant change in the alloy composition, percentage of phases and phase composition of as-cast and solution treated strontium modified A356 alloy at 540°C for 30 min.

Table 21 - Summary of EDS Analysis for Solution Treated UM Squeezed Cast A356 Alloy.

Alloy Area Average	Phase				Alloy	
	α- Al	Si (Eutectic)	AlSiMgFe	AlSiFeNi	Calculated	Measured
Phase Distribution (wt %)	90.94%	7.9%	0.12%	1.04%		
Element						
Al	97.01%	0.20%	80.88%	74.35%	89.11%	89.50%
Si	1.34%	99.30%	6.45%	6.09%	9.13%	9.13%
Mg	0.87%	0.03%	0.54%	0.18%	0.80%	0.78%
Fe	0.44%	0.47%	12.14%	13.27%	0.59%	0.59%
Ni	0.34%	0.00%		6.10%	0.37%	

Table 22 - Summary of EDS Analysis for Solution Treated Sr M Squeezed Cast A356 Alloy.

Alloy Area Average	Phase				Alloy	
	α- Al	Si (Eutectic)	AlFeSi	AlSiFeMg	Calculated	Measured
Phase Distribution (wt %)	91.33%	8.67%	0.39%	0.03%		
Element						
Al	97.43%	0.76%	55.31%	83.05%	89.05%	89.51%
Si	1.20%	98.79%	5.75%	6.94%	9.66%	9.66%
Mg	0.94%	0.00%	0.00%	0.64%	0.86%	0.57%
Fe	0.43%	0.44%	38.94%	9.38%	0.43%	0.26%

*This work was done in collaboration with Dr. Adam Gesing

On the other hand, Si spheroids particles (0.1-1.5 micron) were homogenously distributed in the α-Al matrix decorating the original interdendritic locations. The Sr containing sample had larger volume fraction of interdendritic liquid, the Si particle containing bands were wider, in places higher than 5 micron wide, with few particles distributed across the band.

It was found that the percentage of AlSiMgFe had been reduced. The AlSiFe phase showed up in three shapes. Firstly, oval shaped AlSiFe particles (0.1 μm) often arranged in strings associated with the original as-cast AlSiFeMg phase plate or needle. They also appeared in the original interdendritic locations. Secondly, plate or needle shaped AlSiFe (size 2-5 x 0.1μm) particles that did not appear to fragment and recrystalized under the 540^{o}C heat treatment conditions. Thirdly, more irregularly shaped recrystalized AlSiFe (less than 2 μm) particles recrystalizing in close contact with Si. Total content of the AlSiFe phases was even less than 1 wt%.

Round voids/bubbles were indentified with a size less than 3 microns in the original interdendritic locations. Sr containing phases were not detected, and Sr content of the Al matrix was below the EDX detection limit. After heat treatment the effect of Sr addition on A356 alloy microstructure is significantly diminished. The microstructures of modified and unmodified differ principally in the distribution of the Si particles in the α-Al grains. The slightly higher proportion of Si particles in modified microstructure is likely due to a lower contamination by Fe and the absence of Ni, and consequently less Si is trapped in the AlSiFeX phases

4.9. Comparison and Correlation between Thermal and Microstructural Analysis of Unmodified and Modified Alloys

Most of the squeeze casting experiments was done using unmodified A356 alloy to determine the suitable pressure profiles. In this investigation, it was found that 115 MPa is the highest pressure that can produce desirable microstructure at varying pressure cycles. Keeping the same pressure, cycles were varied as 10, 20 and 50 number cycles. However, due to the complexity of the experiments it was sometimes difficult to get the desired number of cycles. Despite repeating some experiments, certain numbers of cycles were not being imposed in some experiments. Given these reservations, modified and unmodified alloys were compared based on the achieved pressure profiles. Moreover, other parameters like melt temperature and die temperature were tried to keep constant at 750˚C and 250˚C, though it was difficult to keep the same temperatures sometimes, which may slightly affect the outputs.

Generally it was observed that cumulative energy, a product of pressure and stroke, increased with increasing number of cycles. As can be seen in Fig. 106, unmodified alloy achieved the highest energy at the same level of pressure and for 20 and 50 cycles compared to Sr and NAMA modified alloys, despite an abnormal increase of energy in combined modified (Sr and NAMA) alloy at 12 cycles pressure. Having higher cumulative energy and higher α-dendrite growth temperature appeared to be an indication of higher effect of pressure and resulted in better microstructures. The α-dendrite growth temperature also has a higher increase in unmodified alloy compared to any other modified alloys at the same pressure for 20 numbers of cycles (Fig. 107).

On the other hand, eutectic growth temperature was the lowest in the combined (Sr and NAMA) modified alloy compared to individually modified alloy and unmodified alloy in all instances of pressure cycles at 115 MPa. It was concluded that having lower eutectic growth temperature is the best for fully modified ultrafine eutectic silicon (Fig. 108). Compare to unmodified alloy, modified alloys either Sr modified or NAMA modified or combined modified alloy showed lower Al-Si eutectic growth temperature for their eutectic Si modification.

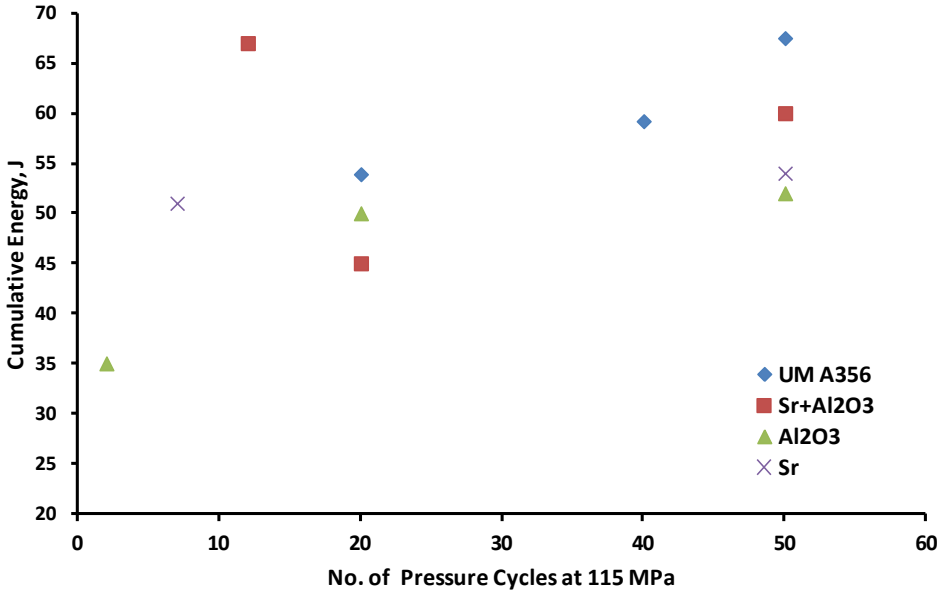

Figure 106 – Correlation between cumulative energy and pressure cycles for modified and unmodified alloys at 115MPa.

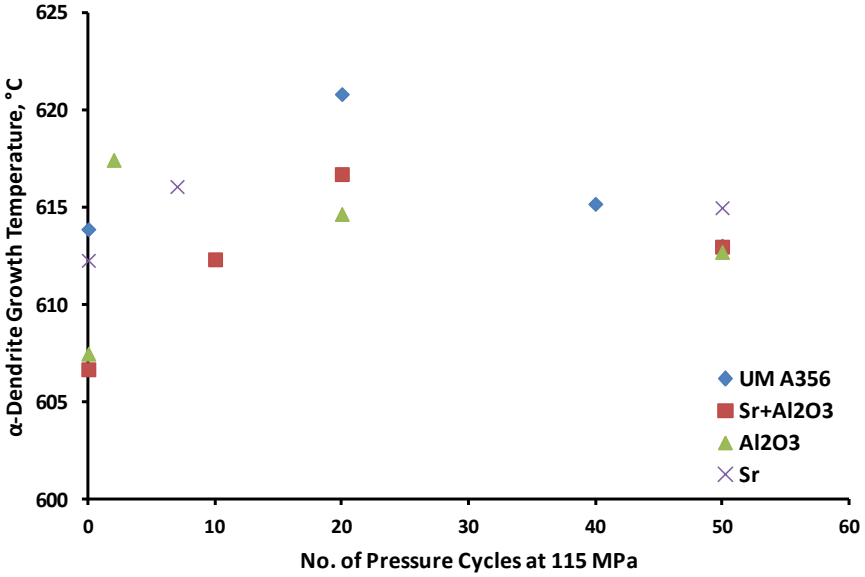

Figure 107 – Correlation between α dendrite growth temperature and pressure cycles for modified and unmodified alloys at 115 MPa.

It was observed that unmodified alloys showed eutectic modification in the range of 563-564°C of Al-Si eutectic temperature, while Sr modified alloys showed within the range of 558-561°C, NAMA modified alloys showed within the range of 541-557°C and combined modified showed within the range of 540 -556°C of Al-Si eutectic temperature.

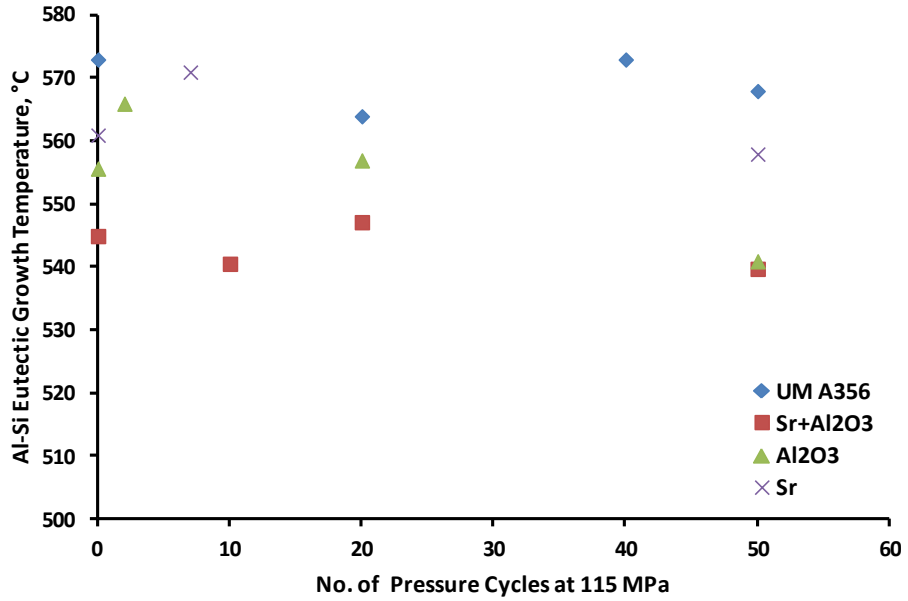

Figure 108 – Correlation between Al-Si eutectic growth temperature and pressure cycles for modified and unmodified alloys at 115 MPa.

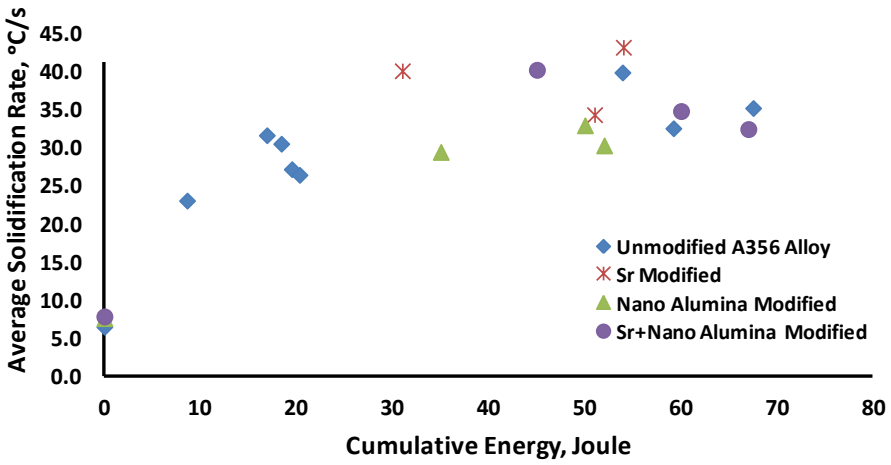

Figure 109 – Correlation between average SR and cumulative energy for modified and unmodified alloys.

As shown in Fig. 109, there is a good correlation between the average solidification rate and cumulative energy for all modified and unmodified alloys. Generally average solidification rate increased with the increase of cumulative energy and then decreased to some extent. In contrast, average SDAS or dendrite cell size decreased as cumulative energy increased (Fig. 110) in a weak correlation. However, a strong correlation was found between the average SR and average SDAS or dendrite cell size. As shown in Fig.

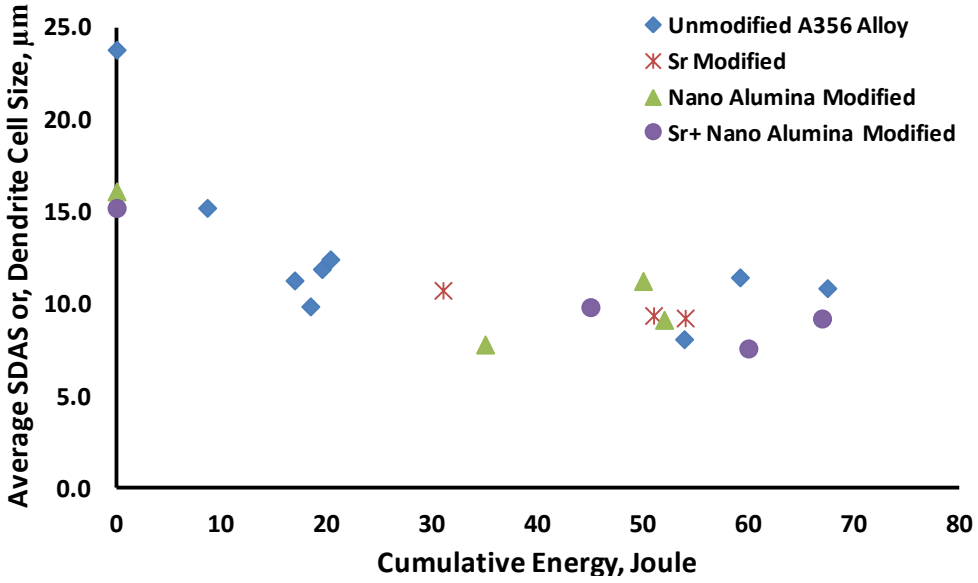

Figure 110 - Correlation between average SDAS or dendrite cell size and cumulative energy for modified and unmodified alloys.

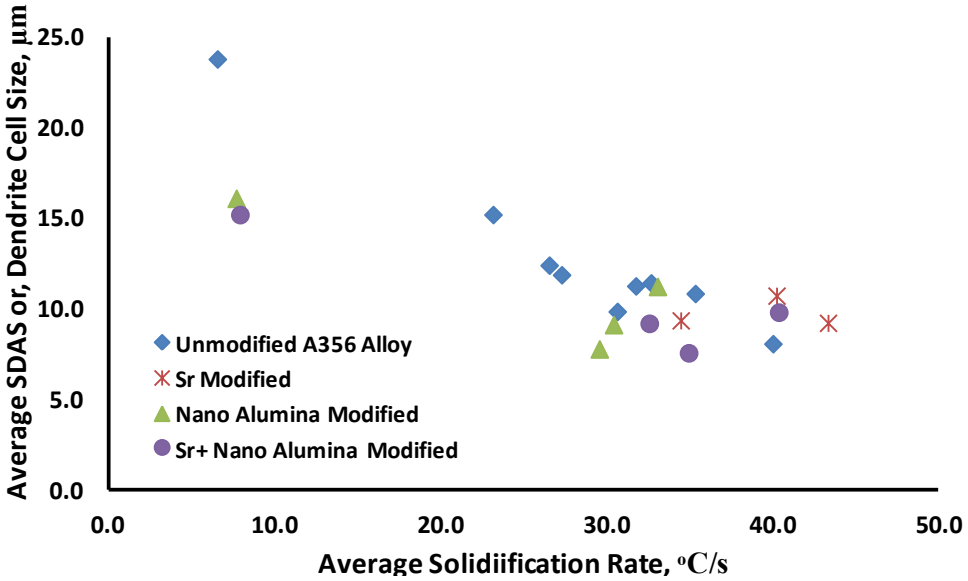

Figure 111 – Correlation between average SDAS or dendrite cell size and average solidification rate for modified and unmodified alloys.

Fig.111, average SDAS or dendrite cell size decreased with increasing the average SR. The unmodified alloys showed better correlation compared to the modified alloys. Previous research in the literature indicated that the higher the SR, the better the refined microstructure, was confirmed for the refinement of dendrite cell size or small SDAS as shown in Fig. 111. However, there was found no strong correlation between the average SDAS or dendrite cell size and the pressure cycles (Fig. 112).

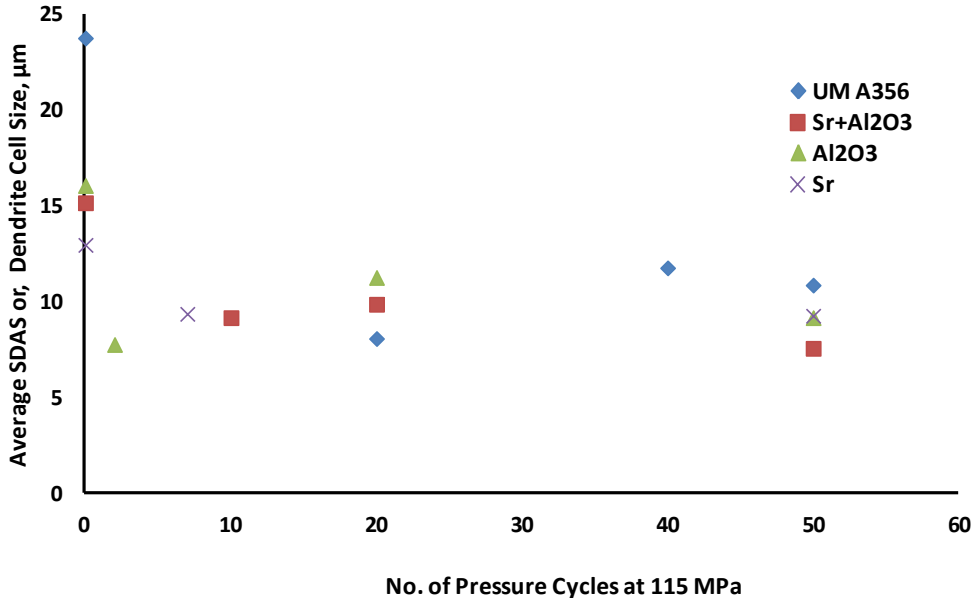

Figure 112 – Correlation between SDAS or dendrite cell size and pressure cycles at 115 MPa for modified and unmodified alloys.

4.10. Comparison with the Alcoa A356 Alloy Wheel

As discussed in the preceding sections, unmodified and modified A356 alloys showed a high degree of microstructural improvement in terms of very fine dendrite cells and ultrafine eutectic silicon compare to Alcoa A356 wheel material as shown in Figure 113. Average dendrite cell size or SDAS of the Alcoa wheel material is found to be 17.31± 2.5 µm which is comparatively higher than that of squeezed cast unmodified A356 (8.1 ±1.1 µm), Sr modified (9.3±1.2 µm), Nano Alumina modified (9.2±1.2 µm) and combined modified A356 alloy (7.6±0.8 µm). Moreover, in squeeze cast samples, eutectic Si was super modified having ultra fine Si particles as shown in Figures 67, 80, 87 and 91-93 when compared to Alcoa wheel Si morphology. Squeeze cast samples also showed full spheroidization of Si within 15 minutes of soaking time, as compared to 5 hours in LPDC produced Alcoa wheel at 540 °C followed by water quenching at 70 °C. It is expected that

the solution treatment time could be further shorten to 5-10 minutes to produce smaller Si spheroids.

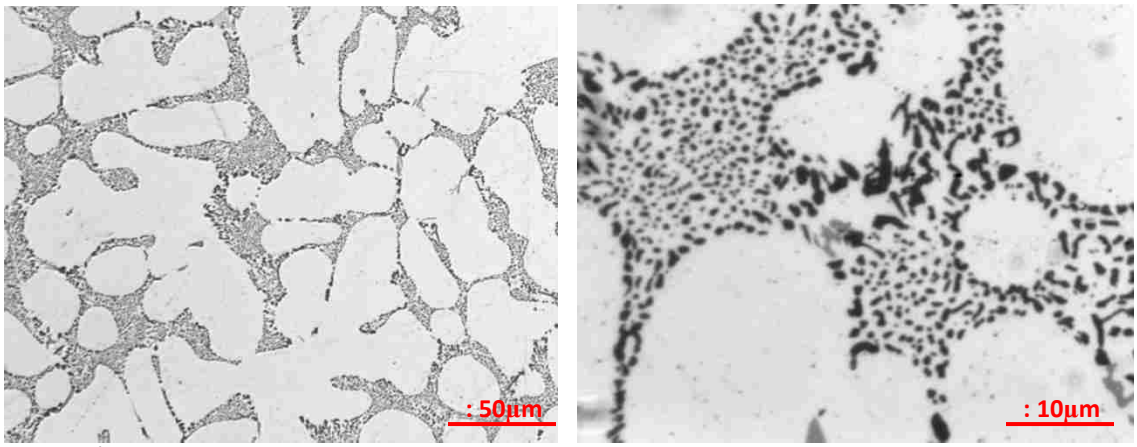

a) 200x b) 1000x

Figure 113 – LOM Microstructure of Alcoa wheel part with 0.015 wt% Sr M A356 alloy solidified at atmospheric pressure in LPDC process and Solution Treated at 540 °C for 5 hours a) Morphology of α-Al Dendrite & Al-Si eutectics, b) Eutectic Si and other phases.

CHAPTER FIVE – SUMMARY AND CONCLUSIONS

5.1. Summary

The motivation of this research was to improve the microstructure of A356 alloy as well as to introduce a new squeeze casting (SC) UMSA process compared to the LPDC process. By introducing for the first time a unique cycling of pressure on the solidifying melt and analyzing its effect on the thermal and microstructural behavior of A356 alloy, it was revealed that cyclic pressure significantly improved the microstructure of unmodified and modified A356 alloy in terms of finest equiaxed dendrite cell size and ultrafine modified fibrous eutectic Si. The SEM analysis on the deep etched samples revealed a 3D tree like ultrafine (0.15 micron width) dendritic structure which is not found in the literature. For squeeze cast unmodified and Sr modified alloy, very rapid Si spheroidization was achieved in a solution treatment at 540^{o}C within a very short 15 minute soaking time. Moreover, melt treatment by Sr and Nano Alumina Master Alloy showed that their individual and combined effect along with effect of cyclic pressure were able to produce a super modified microstructure of A356 alloy.

Cyclic pressure changed the thermal characteristics of A356 alloy. Compared to atmospheric pressure, alloy solidified at high pressure showed a significant shifting of the α-dendrite growth temperature with some exceptions.

1. The α-dendrite growth temperature of unmodified alloy increased 2-8°C at the range of 50-115 MPa pressure with 10-20 pressure cycles. In one experiment there was a 1°C decrease.

2. There was 2-4°C increase in the α-dendrite growth temperature for Sr modified alloy at 115 MPa pressure with 10-50 cycles. One experiment showed a 2°C decrease.
3. Solidified at the same pressure level, Nano alumina modified alloyed showed 5-10°C increase in the α-dendrite growth temperature with varying pressure cycles of 2-50.
4. Combined (Sr and Nano Alumina) modified alloy also showed 5-10°C increase in the α-dendrite growth temperature at 115 MPa pressure within 12-50 pressure cycles.

Cyclic pressure application caused significant changes in the Al-Si eutectic growth temperature compared to alloy solidified at atmospheric pressure. Depending on the start and end point of pressure applied region during solidification, the Al-Si eutectic growth temperature increased or decreased. A decrease of eutectic temperature to values between 540-565°C showed significant modifications in the eutectic silicon of the alloy microstructure while increasing eutectic temperature above 565°C didn't show any modification on the eutectic Si. Some highlights stated below:

1. For untreated A356 alloy, the Al-Si eutectic growth temperature decreased 1-10°C within the range of 50-115 MPa pressure for 10-50 cycles. One experiment showed a 1°C increase and another showed no change.
2. There was 2-3°C decrease in Sr treated alloy solidified at 115 MPa pressure for 10-50 pressure cycles although one experiment gave a 10°C increase.

3. Nano Alumina treated alloy experiments showed 1 -15°C decrease in Al-Si eutectic temperature. One experiment showed a 10°C increase.
4. Combined (Sr and Nano Alumina) modified alloy experiments showed a 5°C decrease in one experiment while 2-11°C increase in other two experiments at the same pressure for 20-50 pressure cycles. However, despite this increase in Al-Si eutectic temperature, the eutectic Si was fully modified as the resulted eutectic temperature was well below 560°C.

With regard to α-Al dendrite cell, the best results are achieved at 115 MPa pressure for varying pressure cycles 10-50. Microstructural analysis of some as-cast samples solidified at 115 MPa revealed that

1. The SDAS or α-dendrite cell size reduced from 23.84 μm at atmospheric pressure to 8.12 μm at 115 MPa, which is very significant compared to 17.3 μm at atmospheric pressure in LPDC made AlCOA wheel.
2. Sr modified test samples showed a dendrite cell size of 9.3 μm at 115 MPa pressure for 50 cycles compared to 13 μm found at atmospheric pressure for the same alloy.
3. Nano Alumina modified alloy showed a similar improvement in dendrite cell size having 9.2 μm compared to 16.1 μm at atmospheric pressure.
4. The super refined dendrite cell size of 7.6 μm was achieved in a combined modified (Sr and Nano Alumina) alloy at the same pressure profiles.

Increasing the number of pressure cycle causes a slight improvement in cell size.

With respect to silicon modification of as-cast samples solidified at the 115 MPa pressure profiles revealed that

1. Untreated as-cast A356 sample solidified at 115 MPa with 20 pressure cycles showed super modified Si (dia. 0.15-0.25 μm) compared to acicular Si (dia. 2-3μm) at atmospheric pressure.
2. Without any chemical modifiers, cyclic pressure seems to modify eutectic Si if pressure is applied at a certain range of solidification process between the starting of α-dendrite growth temperature and the ending of Al-Si eutectic growth temperature.
3. Sr treated and Nano alumina master alloy treated alloy also showed similar eutectic modification having super modified Si (dia. 0.25-0.35 and 0.3-0.4 μm respectively) at the range of 100-115 MPa pressure.
4. Cyclic pressure also produced super modified Si (dia. 0.15-0.3 μm) in combined (Sr and Nano alumina) melt treated alloy.

It is not clear if number of pressure cycles influence the Si modification.

In both Sr modified and unmodified alloy solution treatments, the percentage of Mg and Fe has been increased in the solid solution of α-Al matrix, whereby most of the Mg_2Si and part of AlSiMgFe phases went into solid solution of α-Al matrix, which is an indication of precipitation of Mg_2Si in the solid solution of the matrix.

Cyclic pressure appeared to generate cumulative energy that increased from 8.6 J to 67.5 J as pressure increased from 50 MPa to 115 MPa 0 increasing pressure cycles 1-50 in the solidification of unmodified alloy. Experiments also showed a similar energy input

increment in the Sr and Nano Alumina modified alloy solidified at 115 MPa pressure. It is not clear whether pressure alone or this energy is the deciding factor for the metallurgical changes. However, cyclic pressure appeared to be one of the main factors for the thermal and microstructural changes in the A356 alloy.

5.2. Conclusions

1. A comprehensive literature review was carried out and did not provide any information on the cyclic mechanical pressure utilized during solidification of castable alloys.

2. Limited calibration of the thermocouples and the Data Acquisition System was carried out at high Solidification Rates using pure Al and Zn, however, due to the time constraints, and complexity of high cyclic mechanical pressure further calibration needs to be carried out for future determination of the unbiased TA characteristics.

3. Extensive experimentation was carried out on the A356 alloy leading to the development of a novel processing technology rendering an ultra fine dendritic Si structure and semi-solid α-Al cell structure.

3.1. The unmodified alloy solidified at 115 MPa for 20 cycles showed the best microstructure. The Sr modified alloy solidified at the range of 100 -115 MPa pressure for 10-50 cycles, the Nano Alumina modified alloy solidified at 115 MPa pressure for 20-50 cycles and the combined modified alloy solidified at

115 MPa pressure for 12-50 cycles showed the best microstructures in terms of ultra fine dendritic Si and semi-solid equiaxed α-Al cells.

3.2. Limited Solution Treatment experiments with the A356 alloy using processing parameters (540°C, 15-30minutes, water quenching at 70°C) rendered spherical Si particles having an average diameter range of 1.12-1.16 μm. It is expected that a 15 minute Solution Treatment time could be further shortened to 5-10 minutes to produce a smaller Si dia. Sr modified alloy showed smaller and round Si spheroids compared to unmodified alloy. Significant industrial cost savings will be feasible in comparison with a 5 hrs Solution Treatment of the ALCOA Wheel.

4. In order to understand the effect of the experimental conditions on the as-cast thermal and microstructural data as well as in depth characterization of 3D Si morphology, it will be necessary to continue SEM/TEM comprehensive analysis based on TA and squeeze casting UMSA processing data available to-date.

CHAPTER SIX - RECOMMENDATIONS FOR FUTURE WORK

1. Perform calibration at different pressure profiles to determine the effect of pressure on the thermocouple materials at high temperature and high pressure.
2. Perform squeeze casting experiments considering wide range of variables including superheat temperature, melt pouring temperature and die temperature at different pressure profiles to analyze effect of pressure at different thermal conditions.
3. Design a new die to produce a single cylindrical test sample with 60mm length and 20 mm diameter in order to perform mechanical testing to determine the fatigue behaviour of A356 alloy as well as to determine the yield strength, ultimate tensile strength, elongation and hardness of the alloy subjected to high pressure.

REFERENCES/BIBLIOGRAPHY

[1] Alcoa, "Alcoa Introduces New Lighter, Stronger High-Load Aluminum Wheels Unavailable in Steel," *International Motor Show (IAA) Commercial Vehicles conference*, 2012. [Online]. Available: http://www.alcoa.com/global/en/news/news_detail.asp?pageID=20120919005844en&newsYear=2012. [Accessed: 02-Jan-2014].

[2] J. H. Sokolowski, and W. Kasprzak, B. Hernandez, "Novel Cost Effective Structure Refinement and Modification Technologies for ALCOA Wheel Production, Collingwood, Ontario, Canada, MMO Project #40636," Windsor, Ontario, 2006.

[3] A.L. Kearney, "Properties of Cast Aluminum Alloys, Properties and Selection: Nonferrous Alloys and Special-Purpose Materials," in the *ASM Handbook , Vol 2*, ASM International, 1990, pp. 152–177.

[4] Elwin L. Rooy, "Introduction to Aluminum and Aluminum Alloys, Properties and Selection: Nonferrous Alloys and Special-Purpose Materials," in in *ASM Handbook , Vol 2*, ASM International, 1990, pp. 3–14.

[5] D. S. Mackenzie, *Handbook of Aluminum*. New York: Marcel Dekker, 2003.

[6] Robert. E. Sanders. Jr., "Aluminum and Aluminum Alloys," in *Kirk-Othmer Encyclopedia of Chemical Technology*, Online., vol. 2, John Wiley & Sons, Inc., 2012.

[7] C. Grard, *Aluminium and Its Alloys*. Warrington: Constable and Company Ltd., 1920, pp. 1–5.

[8] R. T. Alcan, "Foundry Alloys," *Online*, 2013. [Online]. Available: https://www.rtapublicsales.riotinto.com/En/OurGlobalNetwork/Americas/Pages/FoundryAlloys.aspx. [Accessed: 10-Feb-2013].

[9] L. F. Mondolfo, *Aluminum Alloys: Structure and Properties*. London, UK: Butterworths, 1976, p. 369.

[10] J. Bäckerud, Lennart; Chai, Guocai ;Tamminen, *Solidification Characteristics of Aluminum Alloys Vol. 2: Foundry Alloys*. American Foundry Society, 1990.

[11] J. G. Kaufman and E. L. Rooy, *Aluminum Alloy Castings: Properties, Processes, and Applications*. Materials Park, OH: ASM International., 2004.

[12] J. F. Major and R. T. Alcan, "Aluminum and Aluminum Alloy Castings," in *Nonferrous Alloy Castings,*, ASM, 2008.

[13] D. Apelian, “Enabling Tools for Improved Performance Aluminum Cast Alloys :,” *Optimization*, 2009.

[14] J. R. Davis, Ed., *ASM Specialty Handbook: Aluminium and Aluminium Alloys*. ASM International, 1993.

[15] M. Smillie, “Casting and Analysis of Squeeze Cast Aluminium Silicon Eutectic Alloy - Doctoral Thesis, Mechanical Engineering,” University of Canterbury, 2006.

[16] W. D. Shilvock, “The Effect of Alloy and Impurity Variation on the Treatment, Casting and Physical Properties of Aluminium-Silicon Eutectic Alloys - Doctoral Thesis, Mechanical Engineering,” University of Canterbury, 1995.

[17] X. Jian, T. T. Meek, and Q. Han, “Refinement of eutectic silicon phase of aluminum A356 alloy using high-intensity ultrasonic vibration,” *Scripta Materialia*, vol. 54, no. 5, pp. 893–896, Mar. 2006.

[18] L. Wang, D. Apelian and S. Shivkumar, “Molten Metal Processing of Advanced Cast Aluminum Alloys,” *Journal of the Minerals, Metals and Materials Society*, pp. 26–32.

[19] G. K. Sigworth, “Theoretical and Practical Aspects of the Modification of Al-Si Alloys,” *AFS Transactions*, vol. 83–66, pp. 7–16.

[20] W. G. Lidman, “Master Alloys Improve Aluminum Casting Properties,” *Foundry M&T*, pp. 46–47, 1994.

[21] S. Shivkumar, L. Wang, and B. Steenhoff, “Metallurgical Quality of Aluminum Castings produced by the Lost Foam Process,” *AFS Transactions*, vol. 89–140, pp. 825–836, 1989.

[22] Shouxun. Ji, Y. Wang, D. Watson, and Z. Fan, “Microstructural Evolution and Solidification Behavior of Al-Mg-Si Alloy in High-Pressure Die Casting,” *Metallurgical and Materials Transactions A*, vol. 44, no. 7, pp. 3185–3197, Feb. 2013.

[23] B. Closset, and J.E.Gruzleski, “Structure and Properties of Hypoeutectic Al-Si-Mg Alloys Modified with Pure Strontium,” *Metallurgical Transactions*, vol. 13A, pp. 945–951, 1982.

[24] M. Fatahalla, N., Hafiz, “Effect of microstructure on the mechanical properties and fracture of commercial hypoeutectic Al-Si alloy modified with Na, Sb, and Sr,” *Journal of Materials Science*, vol. 34, pp. 3555–3564, 1999.

[25] B. Vanko, “Effect of Silicon Spheroidization Treatment on Mechanical Properties of Unmodified Al-Si Alloy Squeeze Castings,” *Die Casting Engineer, NADCA*, November, pp. 22–25, 2013.

[26] D. G. Mallapur, K. R. Udupa, S. A. Kori, and R. S. Kadadevarmath, “Influence of Grain Refining and Modification on Microstructure and Mechanical Properties of Cast and Forged A356 Alloy – A Comparative Study.” pp. 21–25, 2012.

[27] S. Lu and A. Hellawell, “The Mechanism of Silicon Modification in Aluminum-Silicon Alloys : Impurity Induced Twinning,” *Metallurgical Transactions A*, vol. 18, October, pp. 1721–1733, 1987.

[28] M. D. Hanna, S. Lu, and A. Hellawell, “Modification in the Aluminum Silicon System,” *Metallurgical Transactions A*, vol. 15, March, pp. 459–469, 1984.

[29] H. V. Guthy, “Evolution of the Eutectic Microstructure in Chemically Modified and Unmodified Aluminum Silicon Alloys - Master Thesis, Material Science and Engineering,” Worcester Politechnique Institute, 2002.

[30] M. Zarif, B. Mckay, and P. Schumacher, “Study of Heterogeneous Nucleation of Eutectic Si in High-Purity Al-Si Alloys with Sr Addition,” *Metallurgical and Materials Transactions A*, vol. 42, no. 6, pp. 1684–1691, Dec. 2010.

[31] K. Nogita and A. Dahle, “Effects of boron on eutectic modification of hypoeutectic Al–Si alloys,” *Scripta Materialia*, vol. 48, no. 3, pp. 307–313, Feb. 2003.

[32] C. Zhongwei, “Effect of strontium on primary dendrite and eutectic temperature of A357 aluminum alloy,” *China Foundary*, May, pp. 149–152, 2010.

[33] M. Dudyk, “The Influence of Modification, Using Strontium and Antimony on the Properties of AlSi6CuMg and AlSi8CuMgMn Aluminum Alloys Used for Automobile Castings,” *Cast Metals*, vol. 3, pp. 157–162, 1990.

[34] A. Shabestari, S. G. Miresmaeili, S. M., Boutorabi, “Effects of Sr-modification and melt cleanliness on melt hydrogen absorption of 319 aluminium alloy,” *Journal of Materials Science*, vol. 38, pp. 1901–1907, 2003.

[35] Hess, P. D.; Blackmun, E. V. “Strontium as a Modifying Agent for Hypoeutectic Aluminum-Silicon Alloys,” *AFS Transactions*, vol. 83, pp. 87–90, 1975.

[36] Martínez, E. J., Cisneros M. A., Valtierra, S., Lacaze, J. “Effect of strontium and cooling rate upon eutectic temperatures of A319 aluminum alloy,” *Scripta Materialia*, vol. 52, pp. 439–443., 2005.

[37] S. Khan and R. Elliott, “Quench modification of aluminium-silicon eutectic alloys,” *Journal of Materials Science*, vol. 31, no. 14, pp. 3731–3737, 1996.

[38] Kang, H.G; H, Miyahara; Ogi, K. “Influence of cooling rate and additions of Sr and Ti-B on solidification structures of AC4B type alloy,” in *the 3rd Asian Foundry Congress*, 1995, pp. 108–115.

[39] Chadwick, T. M.; Thomas A.“The Effects of Chemistry, Grain Refiner, Modifier, and Cooling Rate on the Microstructure of 356,” in *Molten Aluminum Processing (AFS)*, 1995.

[40] W. Jie, Z. Chen, W. Reif, and K. Müller, “Superheat Treatment of Al-7Si-0 . 55Mg Melt and Its Influences on the Solidification Structures and the Mechanical Properties,” vol. 34, March, 2003.

[41] S. A. Al Kahtani, “Effect of Melt Thermal Treatment on Eutectic Silicon Particles Characteristics in Cast Al-Si-Mg Alloys,” vol. 2, pp. 144–153, 2013.

[42] N. Abu-Dheir, M. Khraisheh, K. Saito, and A. Male, “Silicon morphology modification in the eutectic Al–Si alloy using mechanical mold vibration,” *Materials Science and Engineering: A*, vol. 393, no. 1–2, pp. 109–117, Feb. 2005.

[43] A. K. Dahle, K. Nogita, J. W. Zindel, S. D. Mcdonald, and L. M. Hogan, “Eutectic Nucleation and Growth in Hypoeutectic Al-Si Alloys at Different Strontium Levels,” vol. 32, no. April, pp. 949–960, 2001.

[44] A. K. Dahle, K. Nogita, S. D. McDonald, C. Dinnis, and L. Lu, “Eutectic modification and microstructure development in Al–Si Alloys,” *Materials Science and Engineering: A*, vol. 413–414, pp. 243–248, Dec. 2005.

[45] V. Heusser, Peter; Pocajt, “Modification and Refinement of Aluminum-Silicon Alloys,” *Key to Metals AG, Total Materia*, 2003. [Online]. Available: http://www.keytometals.com/page.aspx?ID=CheckArticle&site=ktn&NM=85. [Accessed: 13-Apr-2013].

[46] Gruzleski, J. E.; Closset B. M. E, “The Treatment of Liquid Aluminum-Silicon Alloys,” *American Foundrymen’s Society, Inc*, pp. 1–105, 1990.

[47] *ASM Handbook, Vol. 15, Casting*, vol. 15. ASM International, 2008, pp. 220–224.

[48] Beumler, R.D; Hammerstad, H; DasGupta, “Analysis of Modified 319 Aluminum Alloy,” *AFS Transactions*, vol. 88, no. 54, pp. 1–12.

[49] Apelian, D; Cheng, J.A.“Effect of Processing Variables on the Grain Refinement and Eutectic Modification of Al-Si Foundry Alloys,” *International Molten Aluminum Processing Conference*, 1986.

[50] Chai, G; Backerud, L. “Factors Affecting Modification of Al-Si Alloys by Adding Sr-Containing Master Alloys,” *AFS Transactions*, vol. 92–194, pp. 847–854.

[51] Emadi, D. and Gruzleski, J.E. “The Effects of Casting and Melt Variables on Porosity in Directionally Solidified Al-Si Alloys,” *AFS Casting Congress*, vol. 98, 1994.

[52] Mcdonald, S. D.; Zindel, J.W. and Dahle, A.K; Nogita Kazuhiro, “Eutectic Solidification Mode in Sodium Modified Al- 7 mass%Si-3.5 mass%Cu-0.2 mass%Mg Casting Alloys,” *The Japan Institutes of Metals, Materials Transactions*, vol. 42, no. 9, pp. 1981–1986, 2001.

[53] J. Brown, “Aluminium casting alloys,” pp. 23–45, 1999.

[54] U. Feurer, “Influence of Alloy Composition and Solidification Conditions on Dendrite Arm Spacing, Feeding, and Hot Tearing Properties of Aluminum Alloys,” pp. 131–145.

[55] M. Djurdjevic, H. Jiang, and J. Sokolowski, “On-line prediction of aluminum–silicon eutectic modification level using thermal analysis,” *Materials Characterization*, vol. 46, no. 1, pp. 31–38, Jan. 2001.

[56] Gruzleski, J. E., “Thermal Analysis Studies of the Effect of Cooling Rate on the Microstructure of 319 Aluminum Alloy,” *AFS Transactions*, vol. 92-¬141, pp. 383–391, 1992.

[57] S. Bhowmik, “Simultaneous Modification and Grain Refinement of the Al-Si-Cu Alloy using a Magnesium Matrix Alumina Composite as the Master Alloy-Masters Thesis” University of Windsor, 2007.

[58] M. A. Alam, “Simultaneous Si Modification and Grain Refinement of A356 Al-Si Alloy using a Magnesium Matrix Alumina Composite (MgAl2O3) as a Master Alloy - Masters Thesis” University of Windsor, 2010.

[59] Radhakrishna, K., Seshan, S. “Dendrite Arm Spacing in Aluminum Alloy Castings,” *AFS Transactions*, vol. 80–87, pp. 695–702.

[60] Paray, F., and Gruzleski, J.E. “Some Factors to Consider in Modification,” *AFS Casting Congress*, vol. 98, 1994.

[61] J. E. Gruzleski, *Microstructure Development During Metal Casting*. AFS, American Foundry Society Inc, 2000.

[62] Helmut Kaufmann & Peter J. Uggowitzer, *Metallurgy and Processing of High Integrity Light Metal Pressure Castings*. Schiele & Schon GmbH, Berlin, 2007.

[63] T. M. Yue, G. A. Chadwick, “Squeeze casting of light alloys and their composites,” *Journal of Materials Processing Technology*, vol. 58, pp. 302–307, 1996.

[64] J. C. Benedy K, “Aluminum Alloys for Lightweight Automotive Structures,” in the *ASM Hanbook*, ASM International., 2010, pp. 79–113.

[65] M. R. Ghomashchi and A. Vikhrov, “Squeeze Casting : An Overview,” *Journal of Materials Processing Technology*, vol. 101, May 1998, pp. 1–9, 2000.

[66] K. M. Lyer, “Selecting Steel for High Pressure Die Casting Dies,” *Metalworld*, January, pp. 8–13, 2008.

[67] J. J. Sobczak, L. Drenchev, and R. Asthana, “Effect of pressure on solidification of metallic materials,” *International Journal of Cast Metals Research*, vol. 25, no. 1, pp. 1–14, Jan. 2012.

[68] Han, Y.S.; Lee, H.I.; Kim, D.H.; Kim, Y.G. “Effect of applied pressure during solidification on the microstructural refinement in an Al-Cu alloy,” *Scripta Metallurgica et Materialia*, vol. 31:12, pp. 1623–1628, 1994.

[69] B. Denise, B. Alberto, C. Girolamo, T. M. Elisa, Q. Fabrizio, and S. Loredana, “Squeeze Casting of Al-Si Alloys,” in *Recent Researches in Metallurgical Engineering - From Extraction to Forming*, Online., Mohammad Nusheh, Horacio Garza Ahuett and Alejandro Arrambide, Ed. InTechopen.com, 2012.

[70] G.Smith, “Squeeze Casting of Pure Al/Si Alloys, Ph.D.Project,” University of Southampton,UK, 1986.

[71] O.G. Epanchistov, “Structure and Properties of Metals Solidified Under High Pressure,” *Russian Casting Prod.*, pp. 34–37, 1972.

[72] J. A. Aniyi and M. B. Adeyemi, “Effects of Squeeze Casting Parameters on Temperature Distribution During Casting of Aluminum,” *Journal of Applied Science and Technology (JAST)*, vol. 14, no. 1 & 2, pp. 67–73, 2009.

[73] J. A. Aniyi and M. B. Adeyemi, “Effects of Pressure , Die , and Stress-Relief Temperatures on the Residual Stresses and Mechanical Properties of Squeeze-Cast Aluminum Rods,” *Journal of Materials Engineering and Performance*, vol. 5, no. June, pp. 399–404, 1996.

[74] J. O. Aweda, “Improving the electrical properties of aluminium metal through squeeze casting process.” Ilorin, pp. 1–13, 2009.

[75] M. Gallerneault, G. Durrant, and B. Cantor, "The Squeeze Casting of Hypoeutectic Binary Al-Cu," *Metallurgical and Materials Transactions A*, vol. 27A, December, pp. 4121–4132, 1996.

[76] E. . Kim, K. . Lee, and Y. . Moon, "A feasibility study of the partial squeeze and vacuum die casting process," *Journal of Materials Processing Technology*, vol. 105, no. 1–2, pp. 42–48, Sep. 2000.

[77] R. R. Li and Y. Bai, "Effect of specific pressure on microstructure and mechanical properties of squeeze casting ZA27 alloy," *Transactions of Nonferrous Metals Society of China*, vol. 20, no. 1, pp. 59–63, Jan. 2010.

[78] D. Y. Maeng, J. H. Lee, C. W. Won, S. S. Cho, and B. S. Chun, "The effects of processing parameters on the microstructure and mechanical properties of modi ® ed B390 alloy in direct squeeze casting," *Journal of Materials Processing Technology*, vol. 105, pp. 196–203, 2000.

[79] A. Maleki, B. Niroumand, and A. Shafyei, "Effects of squeeze casting parameters on density, macrostructure and hardness of LM13 alloy," *Materials Science and Engineering: A*, vol. 428, no. 1–2, pp. 135–140, Jul. 2006.

[80] M. Masoumi and H. Hu, "Influence of applied pressure on microstructure and tensile properties of squeeze cast magnesium Mg–Al–Ca alloy," *Materials Science and Engineering: A*, vol. 528, no. 10–11, pp. 3589–3593, Apr. 2011.

[81] S. Rajagopal, "Squeeze Casting: A Review and Update," *J. Applied Metal Working, American Society for Metals*, vol. 1, no. 4, pp. 3–14, 1981.

[82] G. K. Stefanos, M. Skolianos, "Effect of applied pressure on the microstructure and mechanical properties of squeeze-cast aluminum AA6061 alloy," *Materials Science and Engineering*, vol. A231, pp. 17–24, 1997.

[83] J. F. Wallace, "Optimization of the Squeeze Casting Process for Aluminum Alloy Parts, Final Report for U.S. Department of Energy, Case Western reserve University," 2002.

[84] Y. Yang, L. Peng, P. Fu, B. Hu, W. Ding, and B. Yu, "Effects of Process Parameters on the Macrostructure of a Squeeze-Cast Mg-2.5 mass%Nd Alloy," *Materials Transactions*, vol. 50, no. 12, pp. 2820–2825, 2009.

[85] M. Zhang, W. Zhang, H. Zhao, D. Zhang, and Y. Li, "Effect of pressure on microstructures and mechanical properties of Al-Cu-based alloy prepared by squeeze casting," *Transactions of Nonferrous Metals Society of China*, vol. 17, no. 3, pp. 496–501, Jun. 2007.

[86] A. A. Moosa, “Microstructure and Some Properties of Aluminum-Silicon Matrix Composites Reinforced by Alumina or Chromia,” *Al-Khwarizmi Engineering Journal*, vol. 6, no. 1, pp. 57–68, 2010.

[87] A. Yu, S. Wang, N. Li, and H. Hu, “Pressurized solidification of magnesium alloy AM50A,” *Journal of Materials Processing Technology*, vol. 191, no. 1–3, pp. 247–250, Aug. 2007.

[88] M. T. Abou El-khair, “Microstructure characterization and tensile properties of squeeze-cast AlSiMg alloys,” *Materials Letters*, vol. 59, no. 8–9, pp. 894–900, Apr. 2005.

[89] W. Kasprzak, J. H. Sokolowski, M. Kasprzak, and W.T. Kierkus “Method and Apparatus for Universal Metallurgical Simulation and Analysis (UMSA)” Canada Patent No. PCT/CA2002/0019032002, US Patent No., US20050151306 A1

[90] P. C. Marchwica, “Microstructual and Thermal Analysis of AlSi and MgAl Alloys Subjected to High Cooling Rates - Masters Thesis” University of Windsor, 2012.

[91] R. Maniara, J. H. Sokolowski, “The effect of cast Al-Si-Cu alloy solidification rate on alloy thermal characteristics,” Journal of Achievements in Materials and Manufacturing Engineering, vol. 17, Issue 1-2, pp. 217–220, 2006.

[92] L. A. Dobrzañski, R. Maniara, and J. H. Sokolowski, “The effect of cooling rate on microstructure and mechanical properties of AC AlSi9Cu alloy,” Archives of Materials Science and Engineering, vol. 28, no. 2, pp. 105–112, 2007.

[93] W. Kasprzak, J. H. Sokolowski, M. Sahoo, L. Metals, C. Technology, and C. Techniques, “Thermal characteristics of the AM50 magnesium alloy,” Journal of Achievements in Materials and Manufacturing Engineering, vol. 29, no. 2, pp. 15–18, 2008.

[94] L. A. Dobrzański, M. Król, T. Tański, and R. Maniara, “Effect of cooling rate on the solidification behavior of magnesium alloys,” ARCHIVES of Computational Materials Science and Surface Engineering, International Scientific Journal published quarterly by the Association of Computational Materials Science and Surface Engineering, 2009, vol. 1, no. 1, pp. 21–24, 2009.

[95] W. Kasprzak, M. Sahoo, J. Sokolowski, H. Yamagata, and H. Kurita, “The Effect of the Melt Temperature and the Cooling Rate on the Microstructure of the Al-20 % Si Alloy Used for Monolithic Engine Blocks,” *American Foundry Society*, pp. 55–72, 2009.

[96] L. A. Dobrzañski, M. Król, T. Tañski, and R. Maniara, “Thermal analysis of the MCMgAl9Zn1 magnesium alloy,” ARCHIVES of Computational Materials Science and Surface Engineering, International Scientific Journal published

quarterly by the Association of Computational Materials Science and Surface Engineering, vol. 34, no. 2, pp. 113–116, 2008.

[97] P. Marchwica, J. H. Sokolowski, and W. T. Kierkus, "Fraction solid evolution characteristics of AlSiCu alloys - dynamic baseline approach," Achievements in Materials and Manufacturing Engineering, vol. 47, no. 2, pp. 115–136, 2011.

[98] S. Thompson, "Effect of Cooling rate on Soldification Characteristics of Aluminum Alloys A356 and AA5182 - Masters Thesis" University of British Columbia, 2003.

[99] L. A. Dobrzanski, W. Kasprzak, and J. H. Sokolowski, "Analysis of the Al-Si Alloy Structure Development using Thermal Analysis and Rapid Quenching Techniques," Achievements in Mechanical and Materials Engineering, 12th International Scientific Conference Proceedings, pp. 225–228.

[100] L. A. Dobrza, W. Kasprzak, J. Sokołowski, R. Maniara, and M. Krupi, "Applications of the derivation analysis for assessment of the ACAlSi7Cu alloy crystallization process cooled with different cooling rate," *Achievements in Mechanical and Materials Engineering*, 2005.

[101] Djurdjevic, M.B., J.H. Sokolowski, "Modelling of Casting Processes Parameters for the 3XX Series of Aluminum Alloys Using The Silicon Equivalency Algorithm," *Association of Metallurgical Engineers Serbia and Montenegro (AME)*, 2003.

[102] F. C. R. Hernandez, M. B. Djurdjevic, W. T. Kierkus, and J. H. Sokolowski, "Calculation of the liquidus temperature for hypo and hypereutectic aluminum silicon alloys," *Materials Science and Engineering: A*, vol. 396, no. 1–2, pp. 271–276, Apr. 2005.

[103] Omega Engineering Inc., "Thermocouples," *Omega Engineering Inc.*, 2013. [Online]. Available: (http://www.omega.com/thermocouples.html. [Accessed: 03-Dec-2013].

[104] "RDC Control. Thermocouples." [Online]. Available: http://www.rdccontrol.com/en/thermocouple/thermocouple-junctions-and-response-time.html#q9. [Accessed: 09-Apr-2014].

[105] Calibration Guide, "Calibration of Thermocouples," by European Association of National Metrology Institutes, EURAMET cg-8, Version 2.1 (10/2011)

[106] E. C. Lloyd, "Accurate Characterization of the High Pressure Environments," in *National Bureau of Standards*, Conference Proceedings, 1968.

[107] G. W. Burns and M. G. Scroger, “NIST Measurement Services: Calibration of Thermocouples and Thermocouples Materials.” National Institute of Stadards and Technology, NIST Special Publication 250-35, 1989.

[108] S. Shankar, Y. W. Riddle, and M. M. Makhlouf, “Eutectic solidification of aluminum-silicon alloys,” *Metallurgical and Materials Transactions A*, vol. 35, no. 9, pp. 3038–3043, Sep. 2004.

APPENDICES

Appendix A – UM A356 at Different Pressure Profiles (Cooling Curve, First Derivative Curve, Pressure Curve, Stroke and Cumulative Energy Curve)

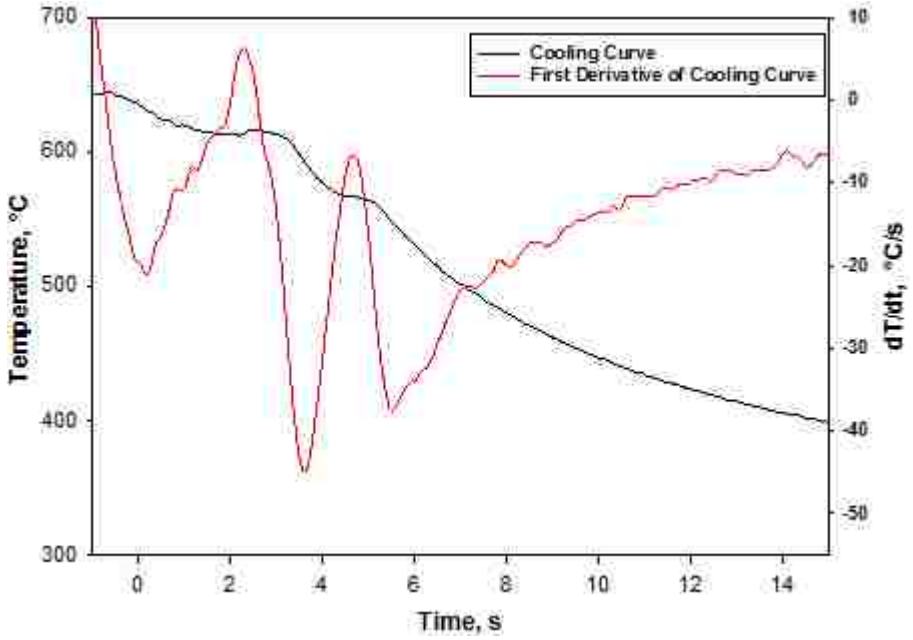

Figure 114 - Cooling curve and its first derivative of unmodified A356 at 50 MPa with 1 pressure cycle.

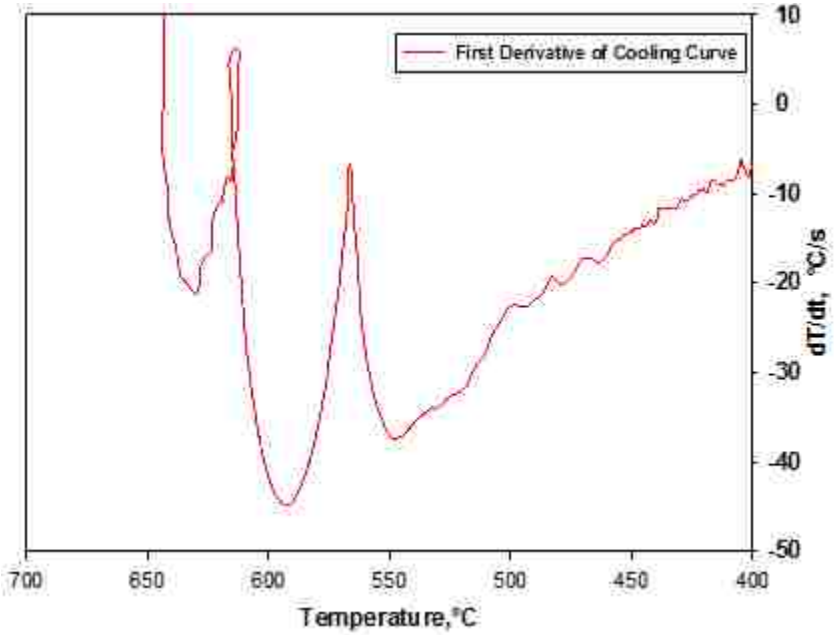

Figure 115 - First derivative of the cooling curve of unmodified A356 at 50 MPa 1 pressure cycle.

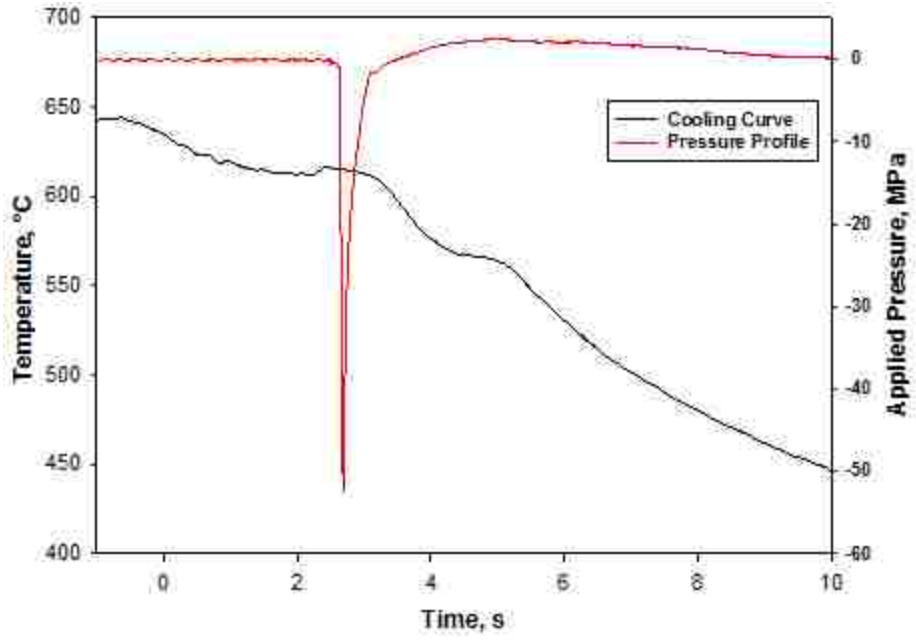

Figure 116 - Cooling curve and pressure profile of unmodified A356 at 50 MPa with 1 pressure cycle showing pressure applied location on the cooling cuve.

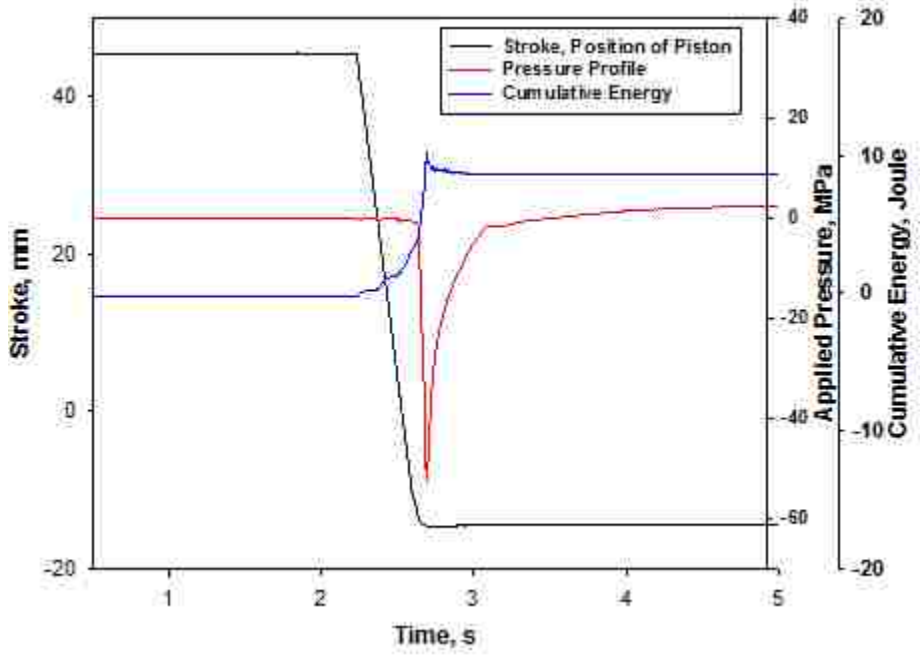

Figure 117 - Stroke and pressure curve of unmodified A356 at 50 MPa with 1 pressure cycle.

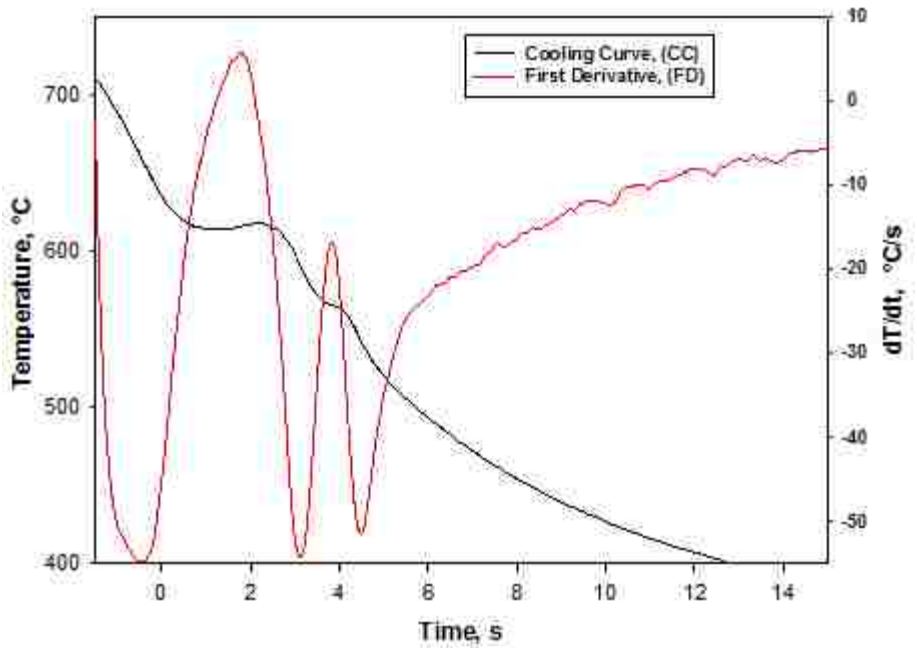

Figure 118 - Cooling curve and first derivative of unmodified A356 at 55 MPa with 10 pressure cycles.

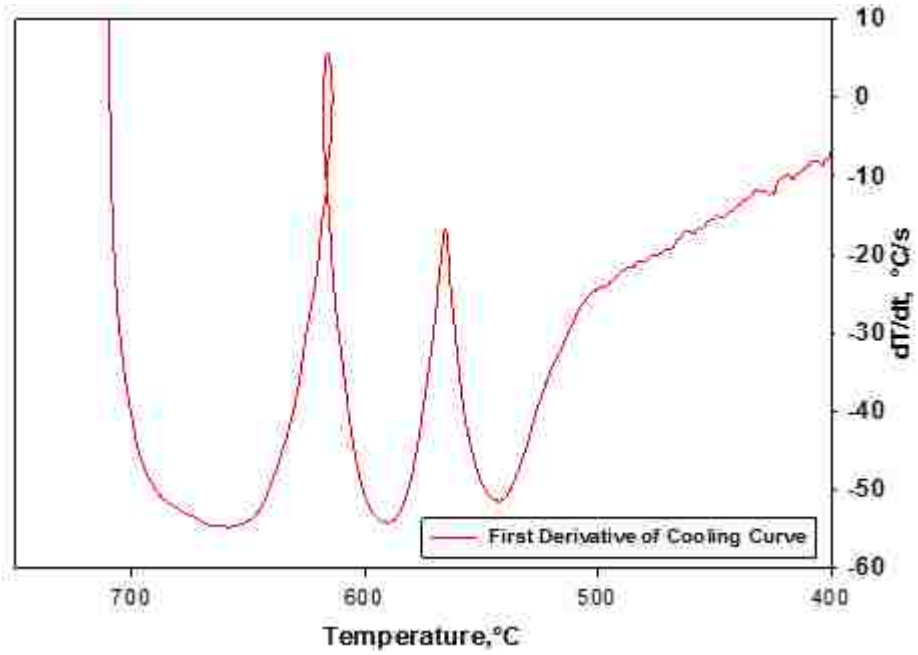

Figure 119 - First derivative of cooling curve of unmodified A356 at 55 MPa with 10 pressure cycles.

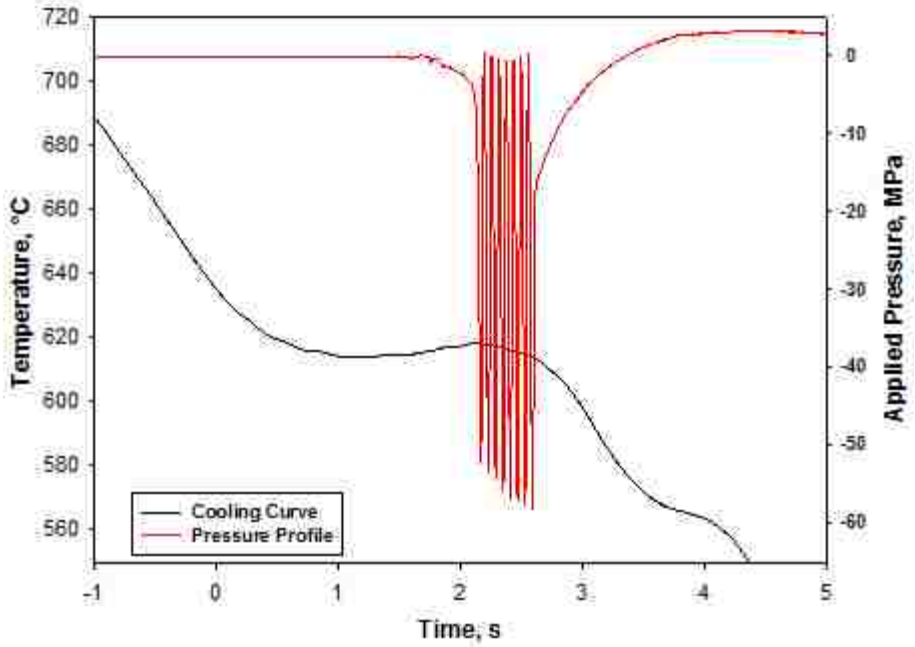

Figure 120 - Cooling curve and pressure profile unmodified A356 at 55 MPa with 10 pressure cycles.

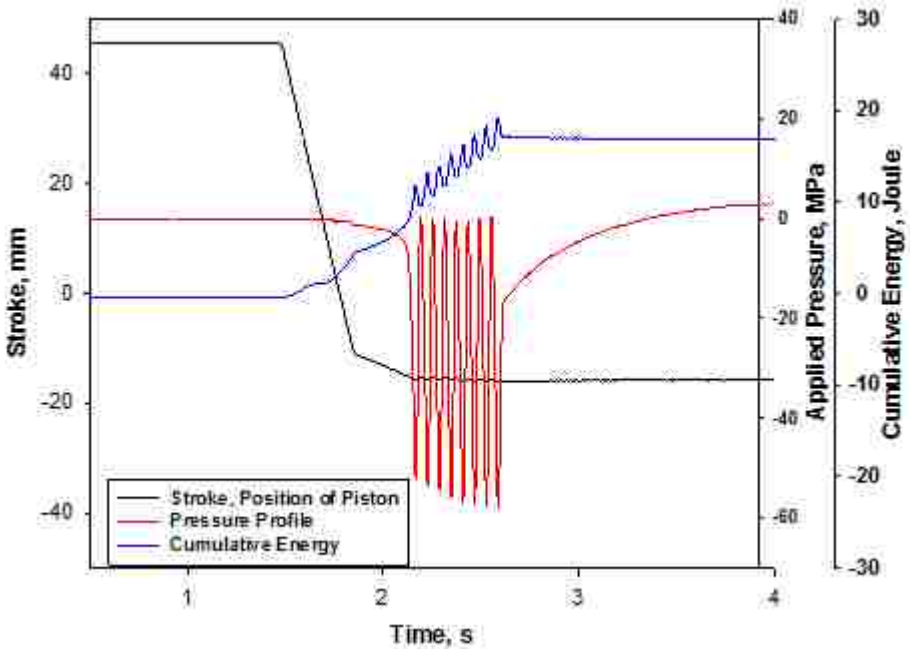

Figure 121 - Stroke, pressure and cumulative energy of unmodified A356 at 55 MPa with 10 pressure cycles.

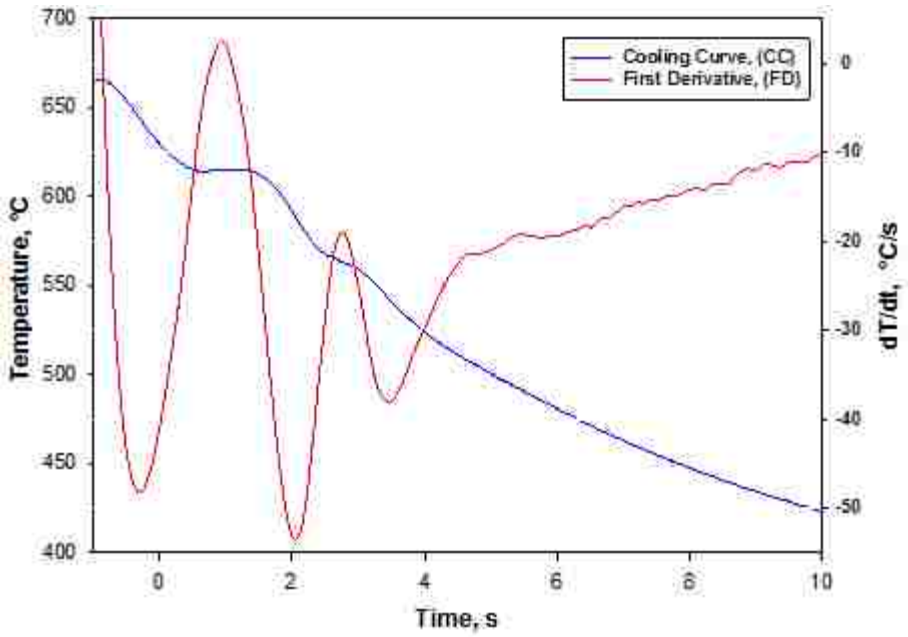

Figure 122 - Cooling curve and its first derivative of unmodified A356 at 60 MPa with 10 pressure cycles.

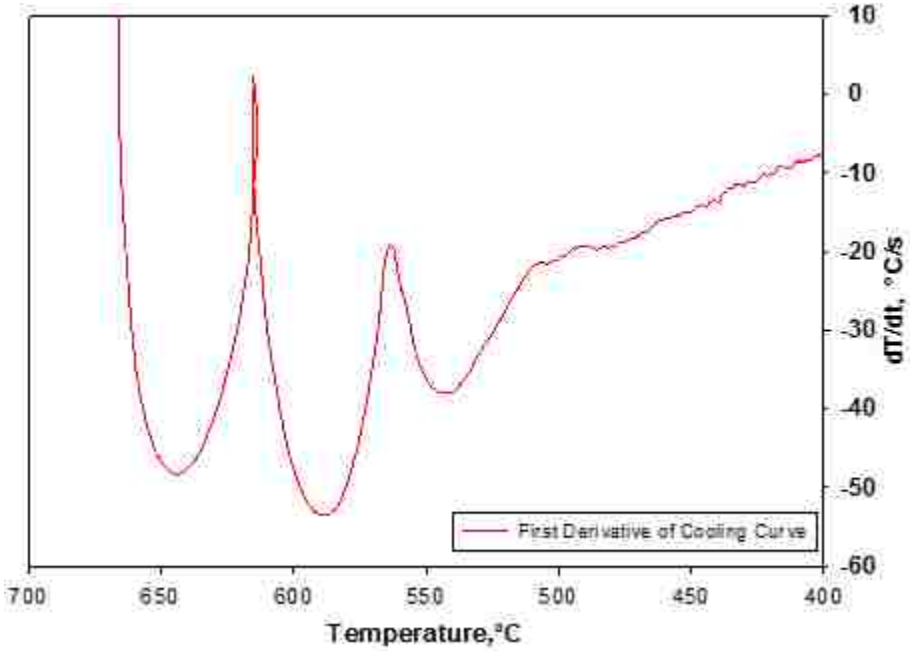

Figure 123 - First derivative of cooling curve of unmodified A356 at 60 MPa with 10 pressure cycles.

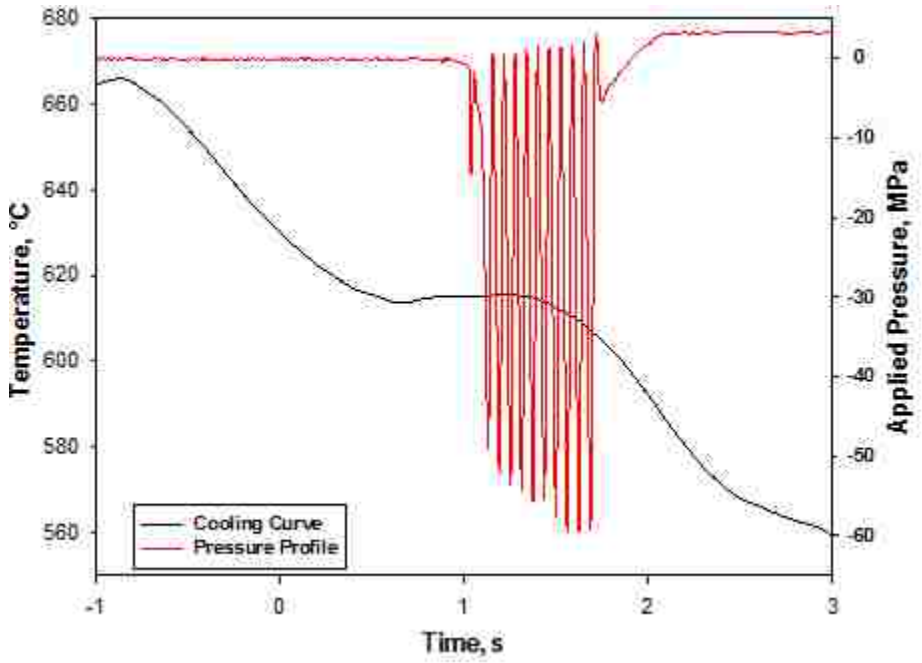

Figure 124 - Cooling curve and pressure profile of unmodified A356 at 60 MPa with 10 pressure cycles.

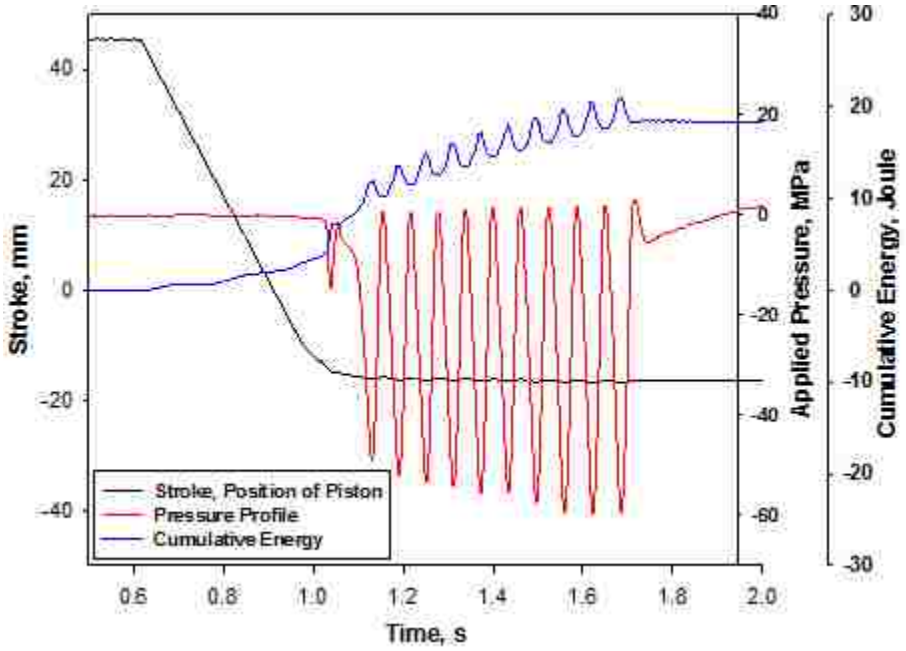

Figure 125 - Stroke, pressure profile and cumulative energy of unmodified A356 at 60 MPa with 10 pressure cycles.

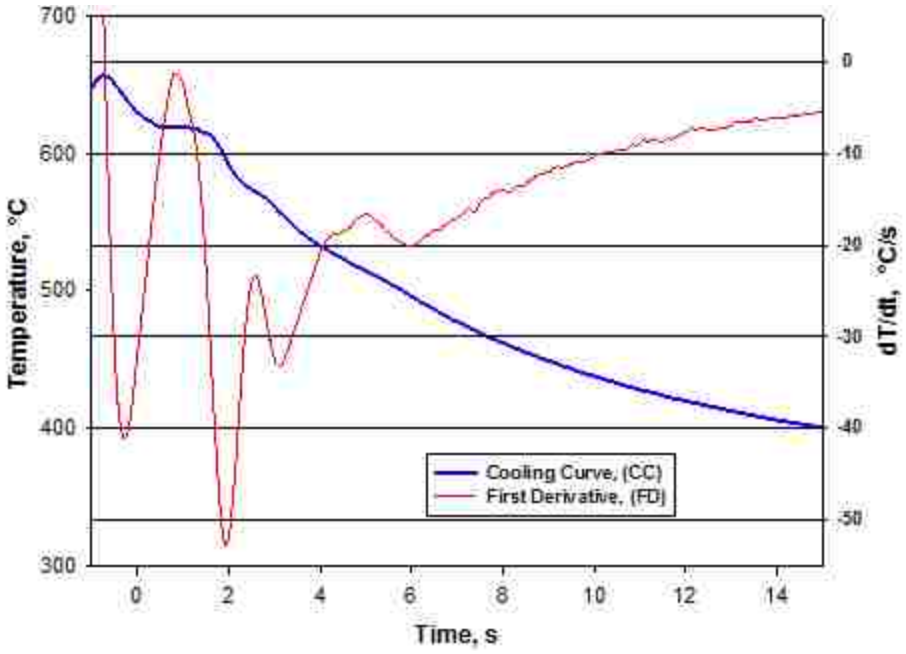

Figure 126 - Cooling curve and its first derivative of unmodified A356 at 80 MPa with 10 pressure cycles.

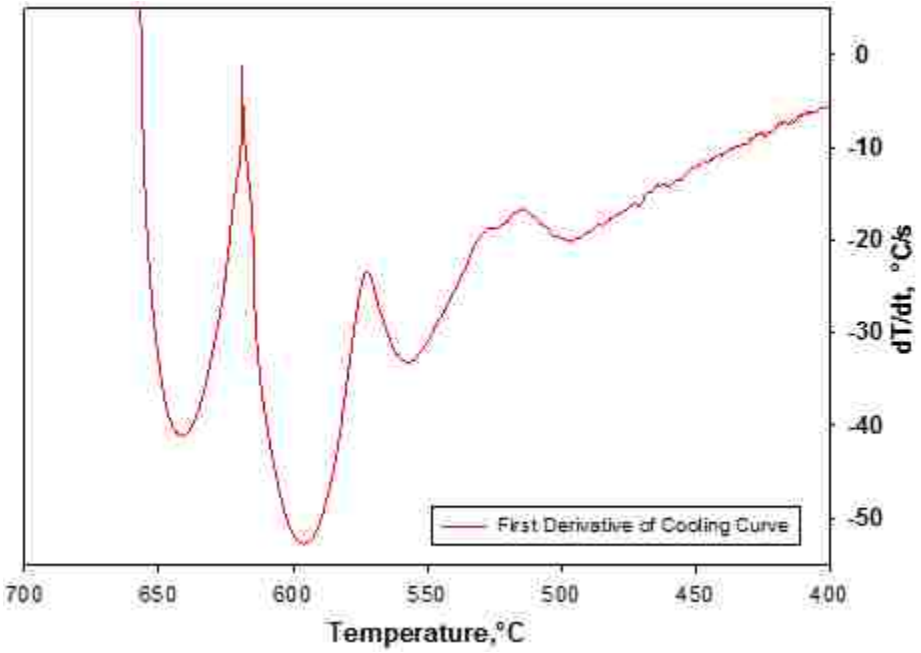

Figure 127 - First derivative of cooling curve of unmodified A356 at 80 MPa with 10 pressure cycles.

.

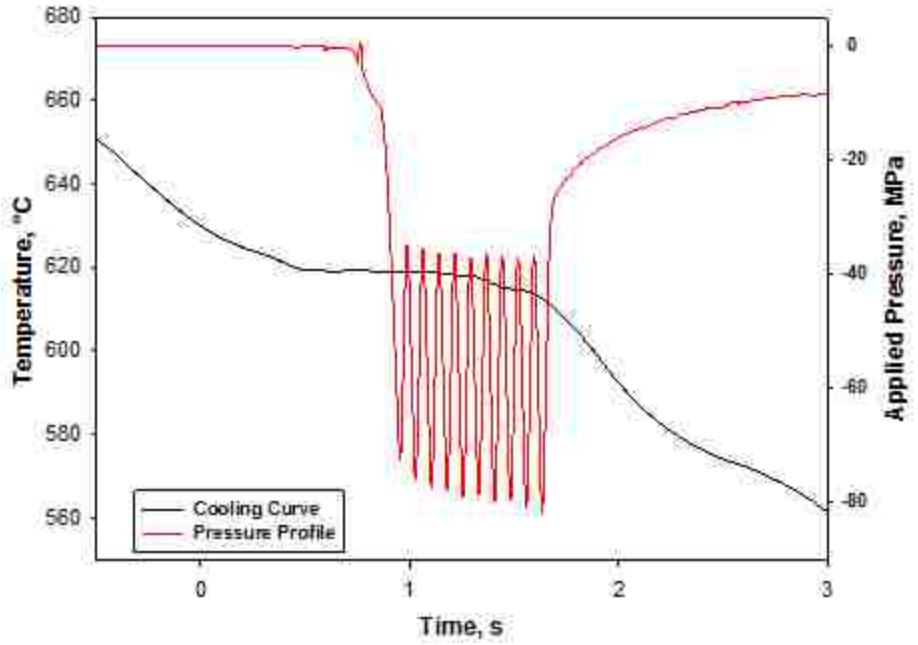

Figure 128 - Cooling curve and pressure profile of unmodified A356 at 80 MPa with 10 pressure cycles.

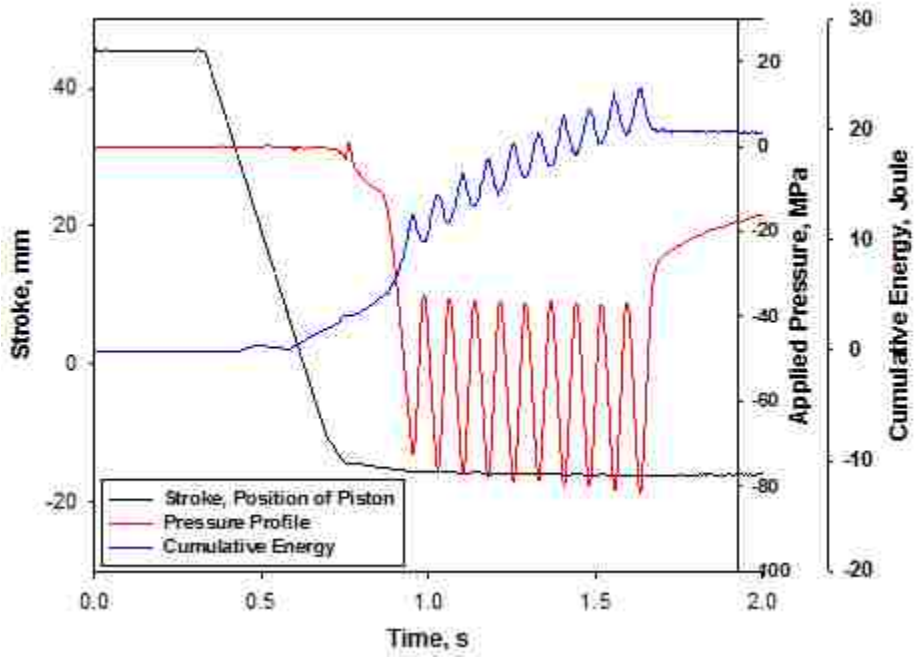

Figure 129 - Stroke, Pressure profile and cumulative energy unmodified A356 at 80 MPa with 10 pressure cycles.

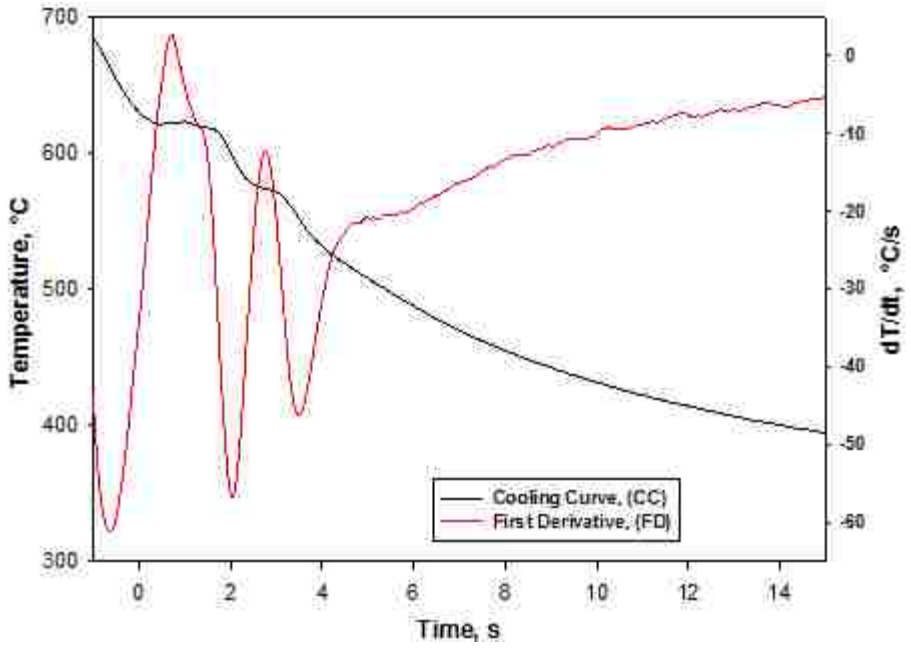

Figure 130 - Cooling curve and its first derivative of unmodified A356 at 90 MPa with 10 pressure cycles.

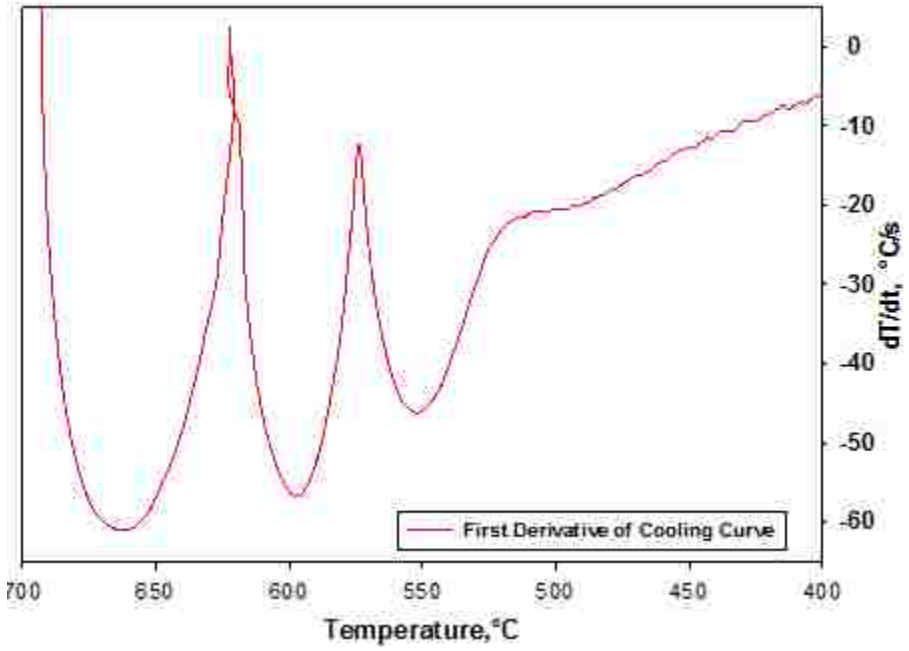

Figure 131 - First derivative of cooling curve of unmodified A356 at 90 MPa with 10 pressure cycles.

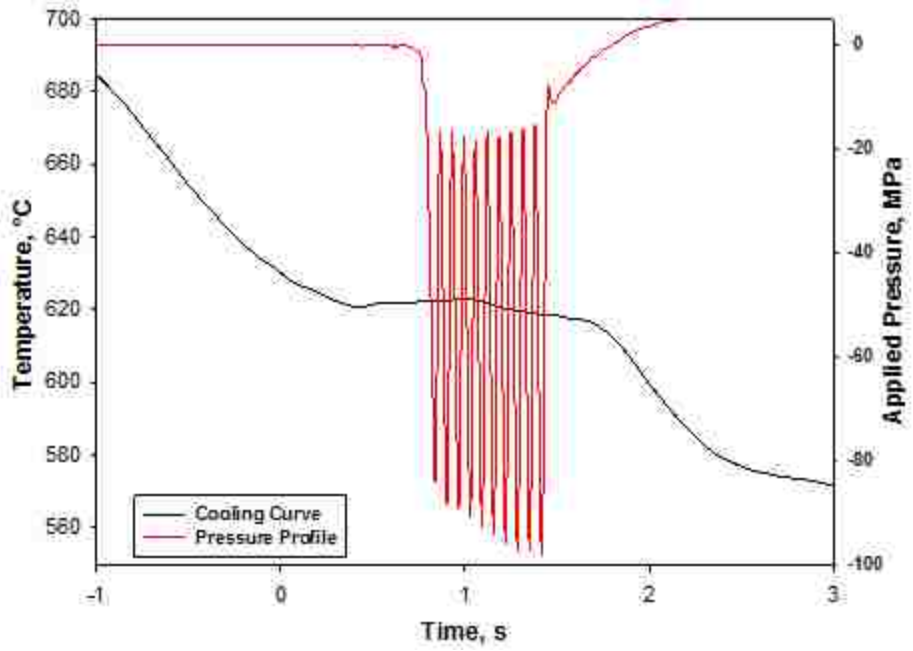

Figure 132 - Cooling curve and pressure profile of unmodified A356 at 90 MPa with 10 pressure cycles.

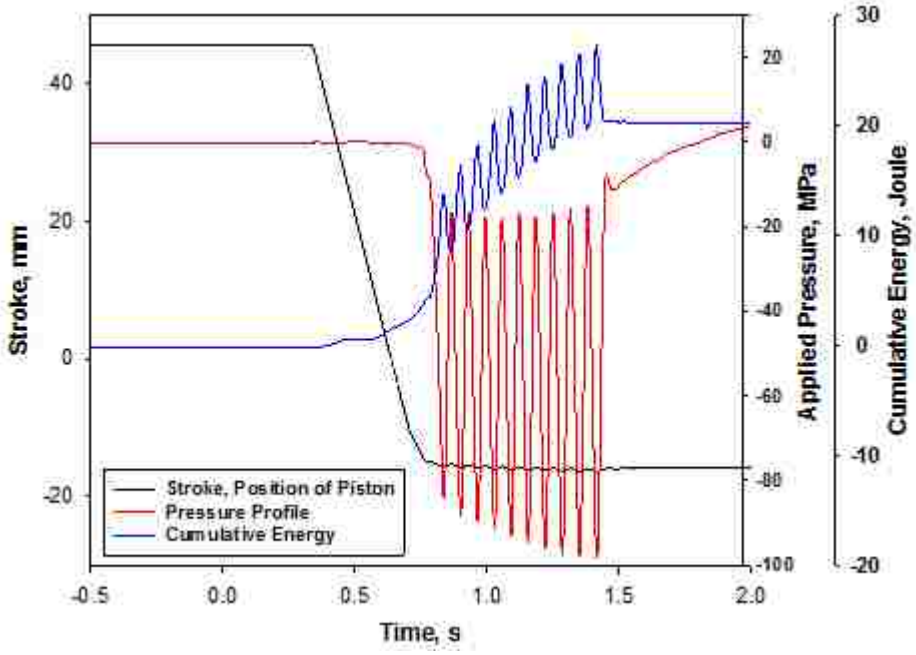

Figure 133 - Stroke, pressure profiles and cumulative energy of unmodified A356 at 90 MPa with 10 pressure cycles.

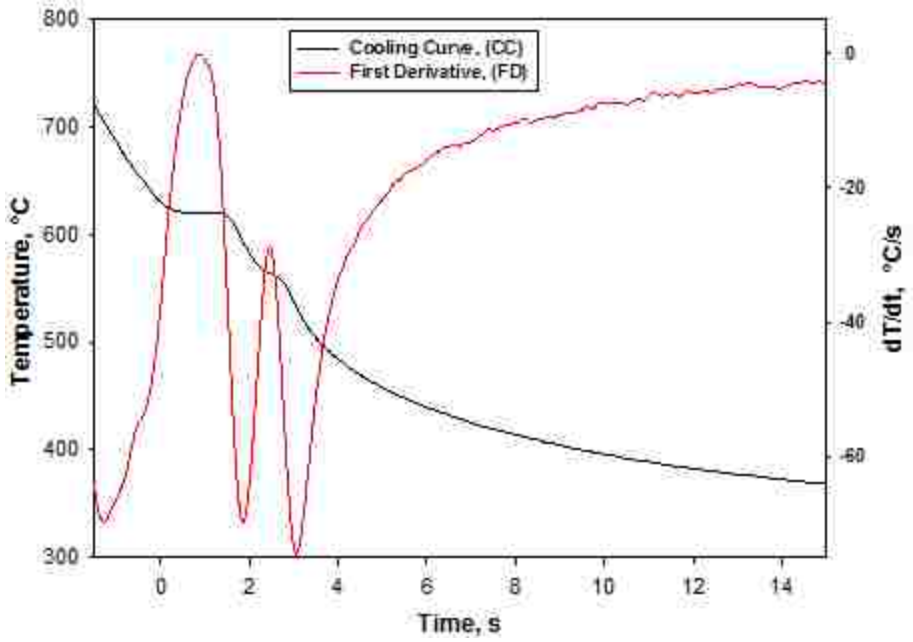

Figure 134 - Cooling curve and its first derivative of unmodified A356 at 115 MPa with 20 pressure cycles.

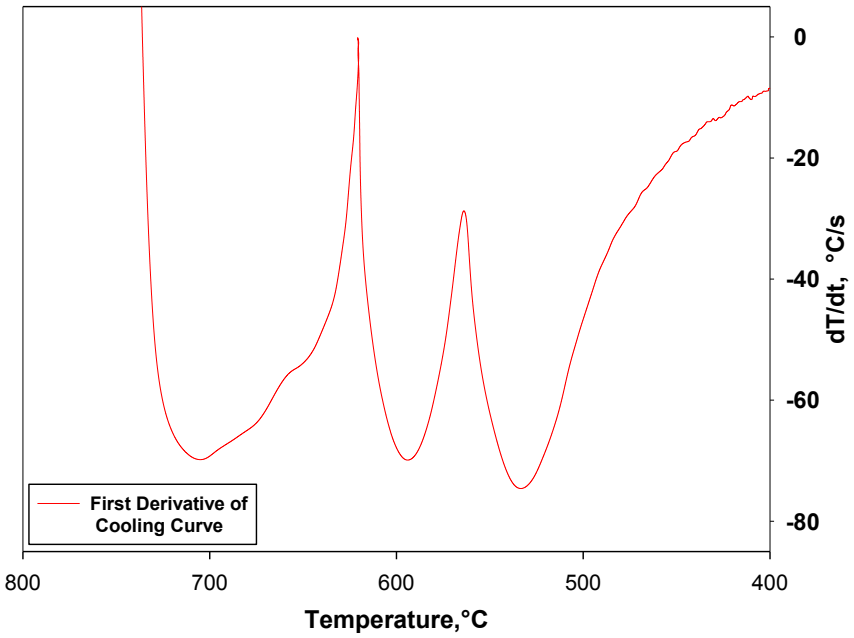

Figure 135 - First derivative of cooling curve of unmodified A356 at 115 MPa with 20 pressure cycles.

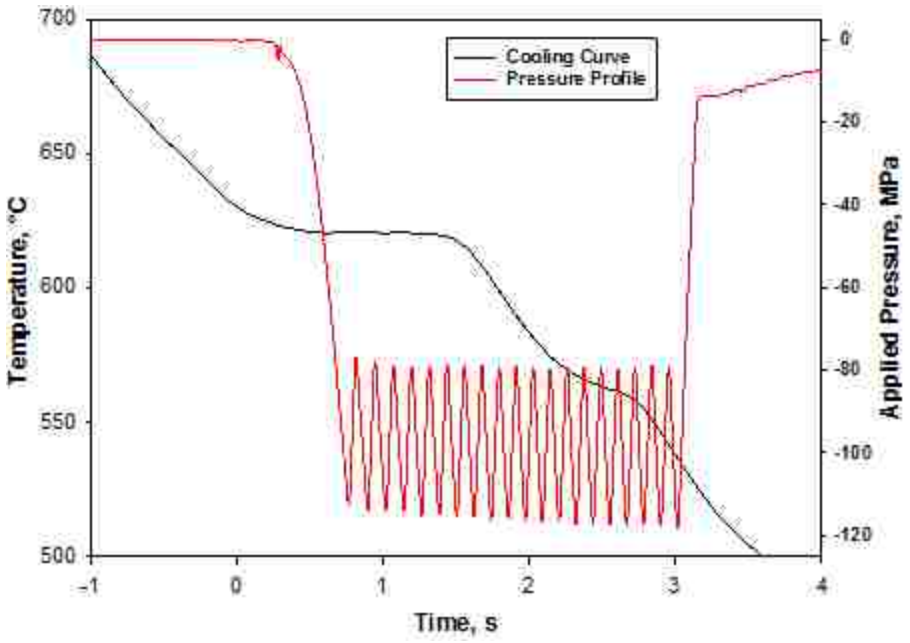

Figure 136 - Cooling curve and pressure profile of unmodified A356 at 115 MPa with 20 pressure cycles.

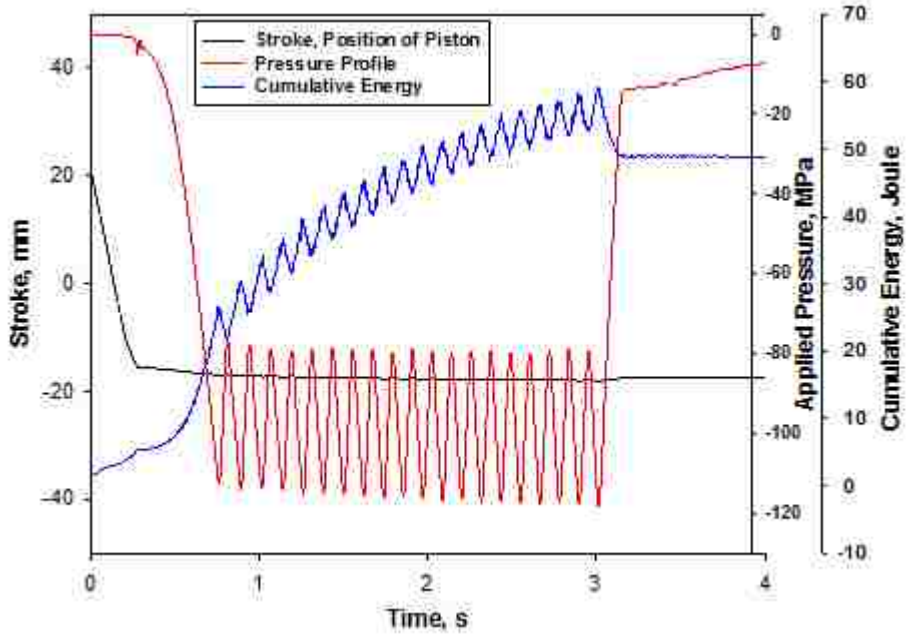

Figure 137 - Stroke, pressure profile and cumulative energy of unmodified A356 at 115 MPa with 20 pressure cycles.

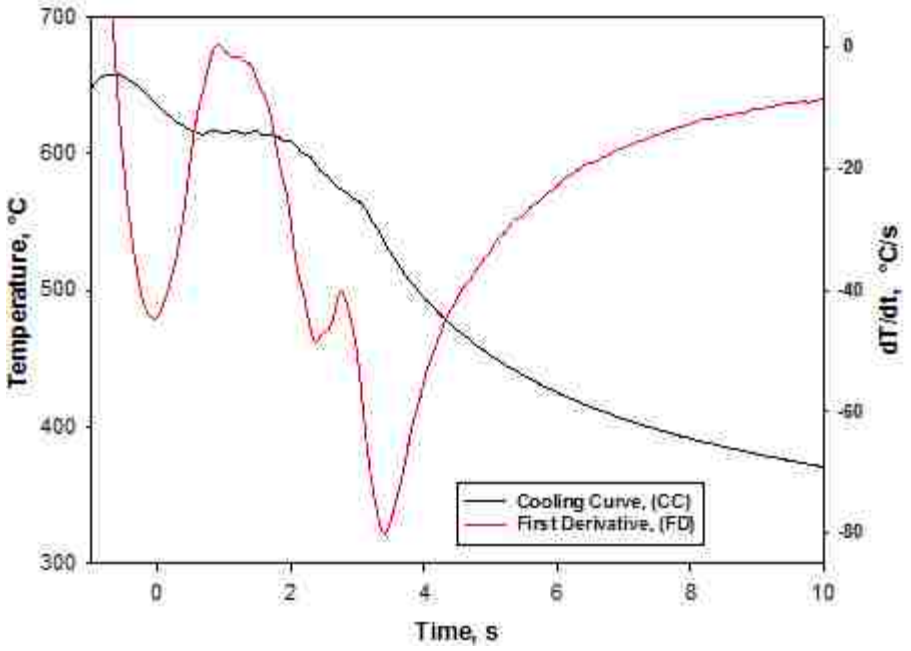

Figure 138 - Cooling curve and first derivative of unmodified A356 at 115 MPa with 40 pressure cycles.

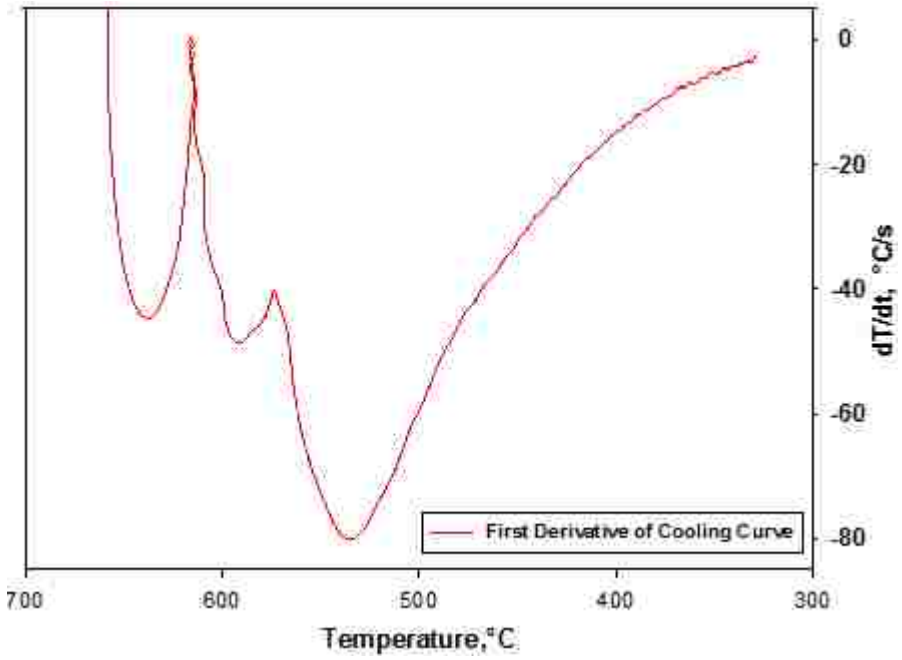

Figure 139 - First derivative of cooling curve of unmodified A356 at 115 MPa with 40 pressure cycles.

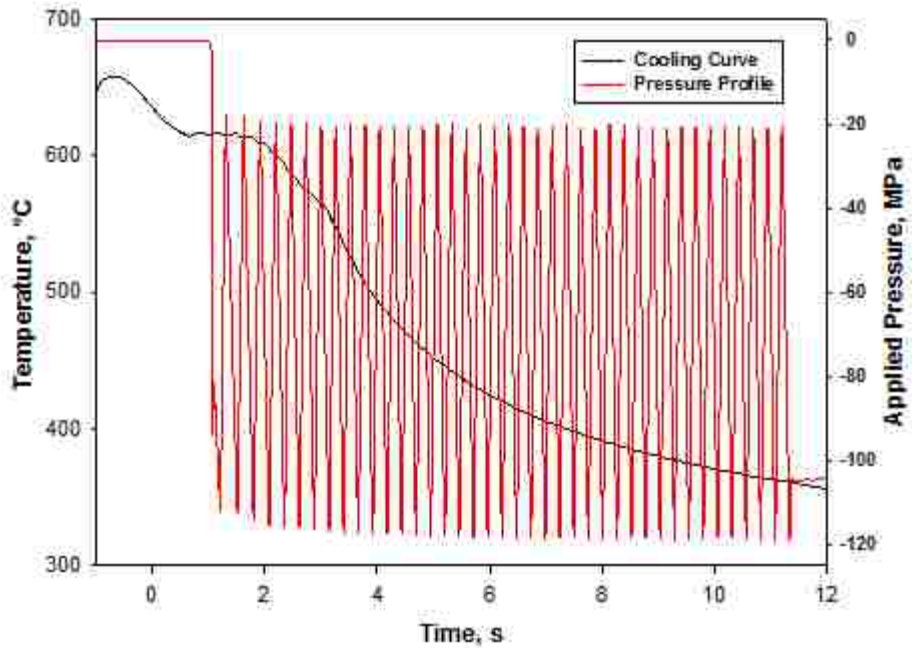

Figure 140 - Cooling curve and pressure profile of unmodified A356 at 115 MPa with 40 pressure cycles.

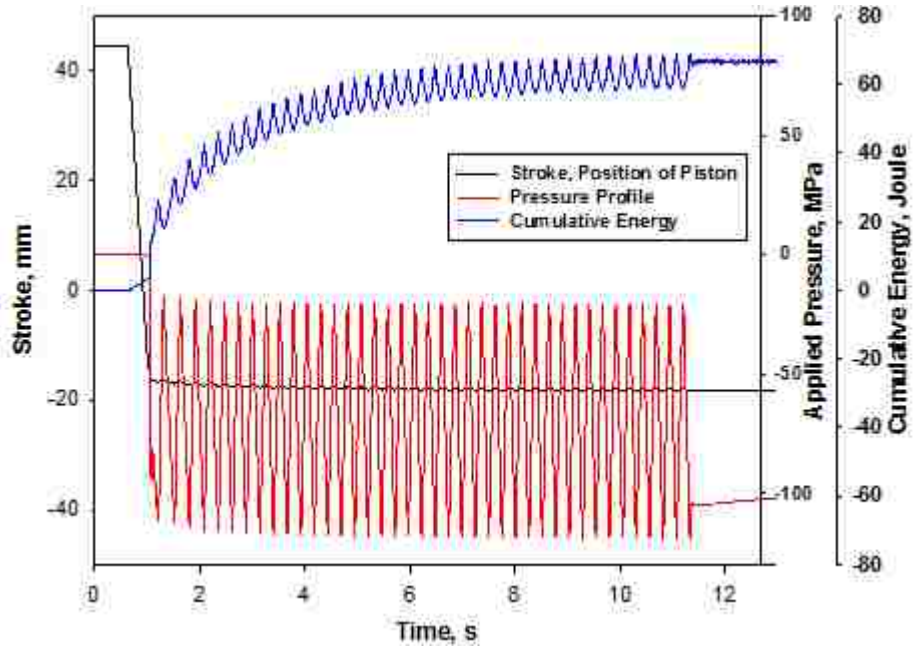

Figure 141 - Stroke, pressure and cumulative energy of unmodified A356 at 115 MPa with 40 pressure cycles.

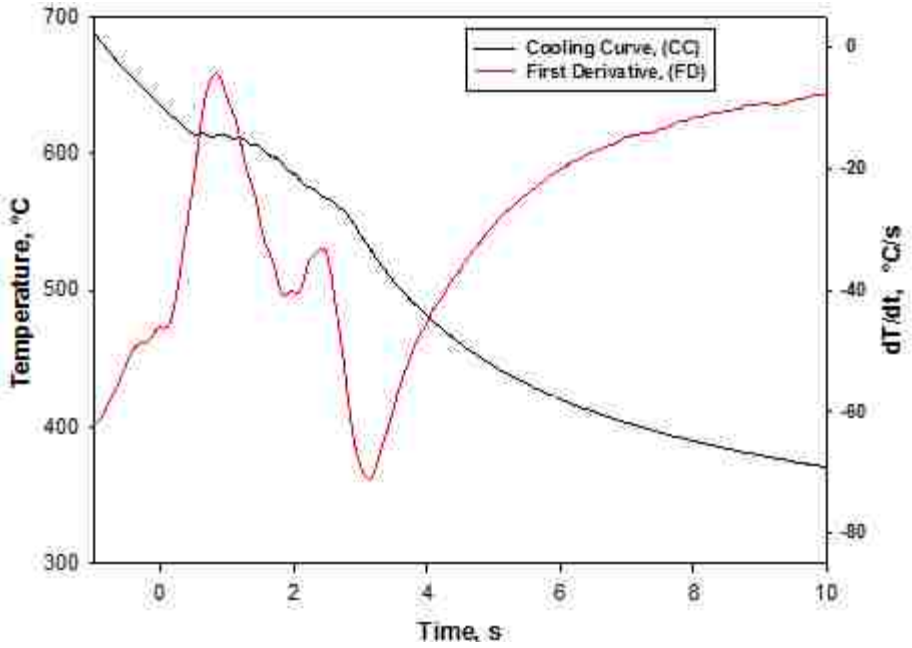

Figure 142 – Cooling curve and its first derivative of unmodified A356 at 115 MPa with 50 pressure cycles.

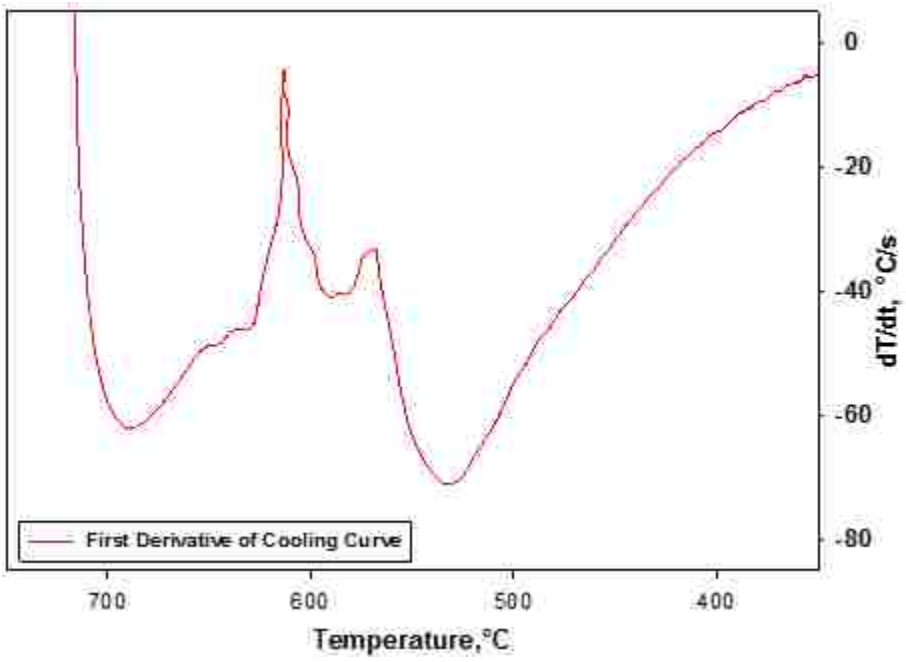

Figure 143 - First derivative of cooling curve of unmodified A356 at 115 MPa with 50 pressure cycles

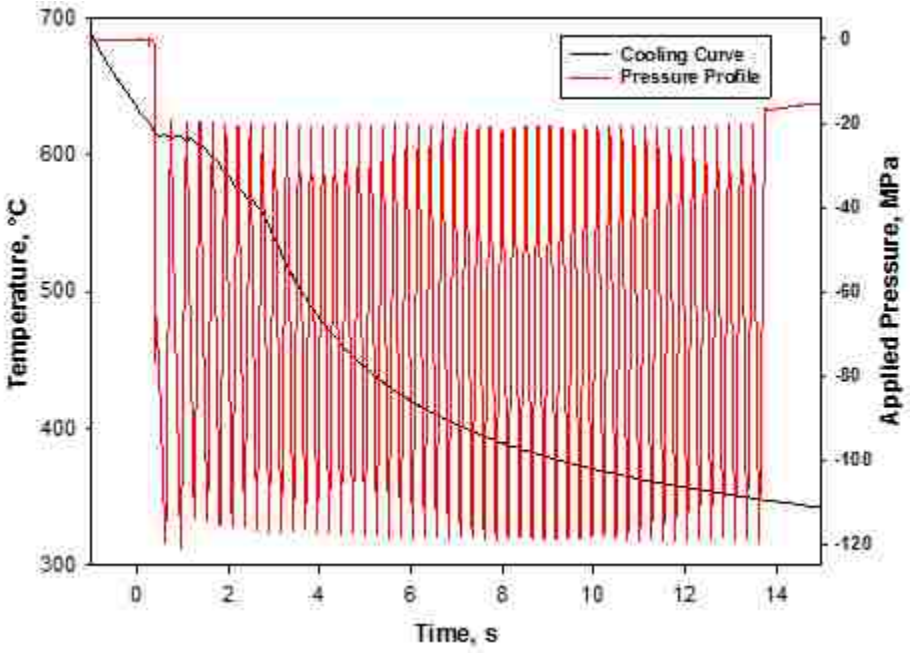

Figure 144 - Cooling curve and pressure profile of unmodified A356 at 115 MPa with 50 pressure cycles.

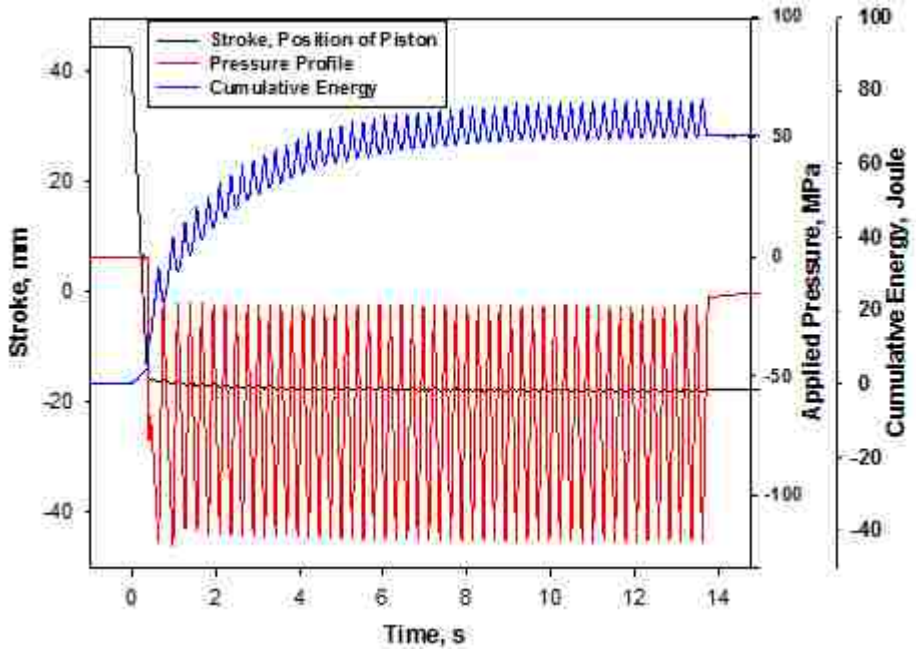

Figure 145 - Stroke, pressure and cumulative energy of unmodified A356 at 115 MPa with 50 pressure cycles.

Appendix B – Sr Modified A356 Alloy at Different Pressure Profiles (Cooling Curve, First Derivative Curve, Pressure Curve, Stroke and Cumulative Energy Curve)

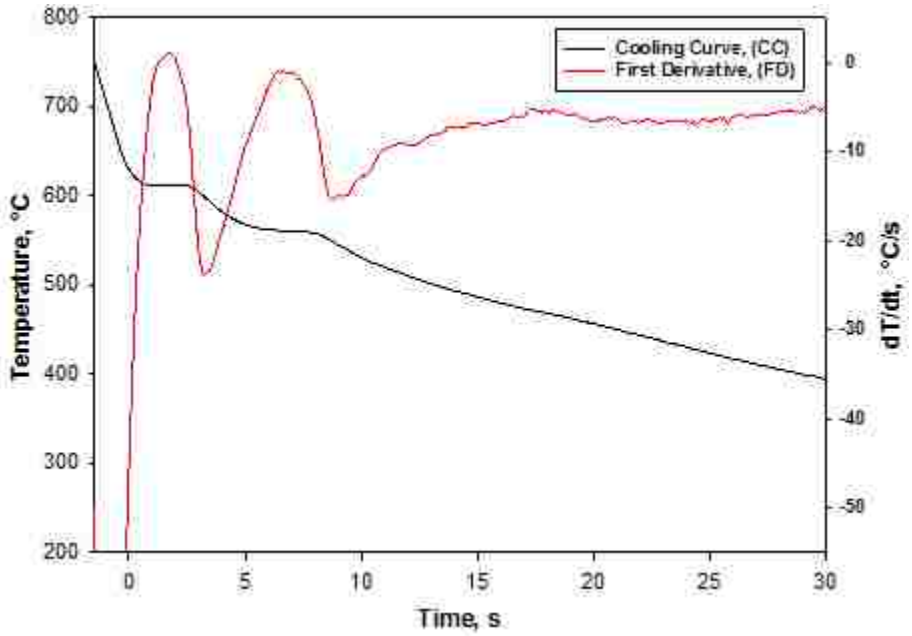

Figure 146 - Cooling curve and first derivative of Sr modified A356 at atmospheric pressure.

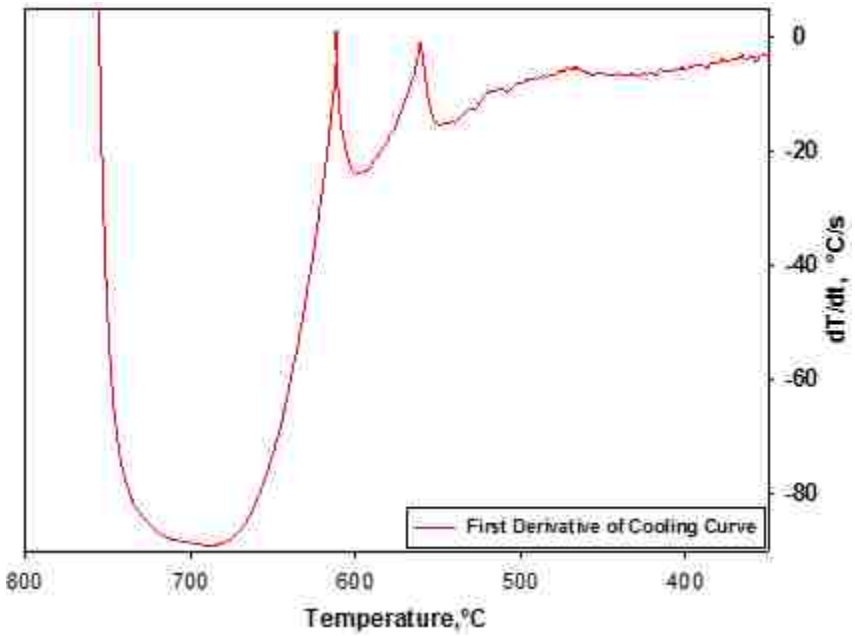

Figure 147 - First derivative of cooling curve of Sr modified A356 at atmospheric pressure.

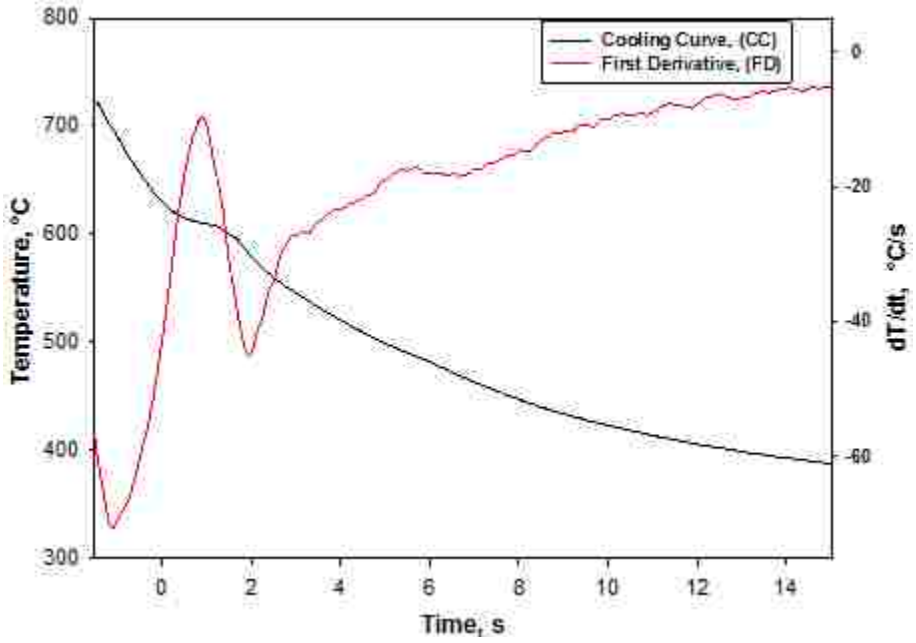

Figure 148 - Cooling curve and first derivative of Sr modified A356 at 100 MPa with 1 pressure cycle.

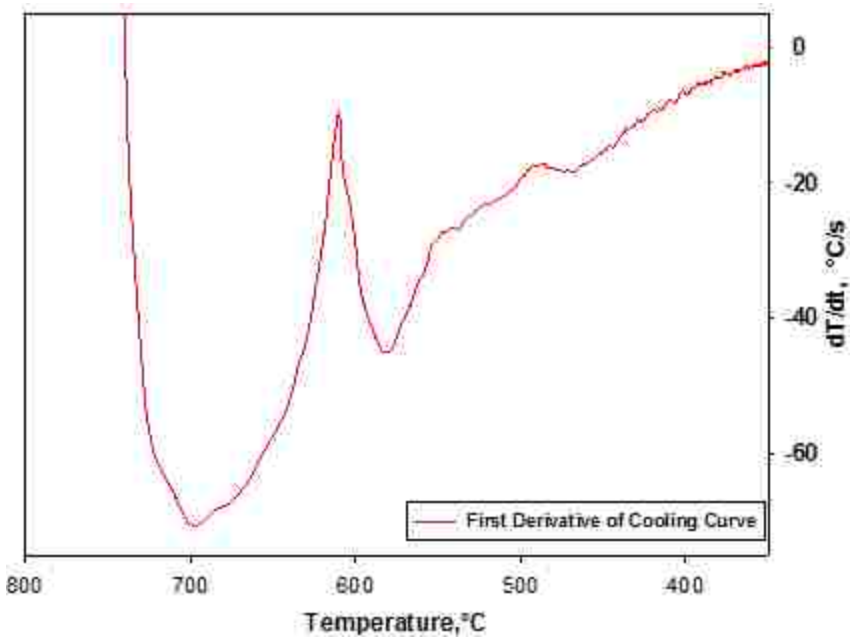

Figure 149 - First derivative of cooling curve of Sr modified A356 at 100 MPa with 1 pressure cycle.

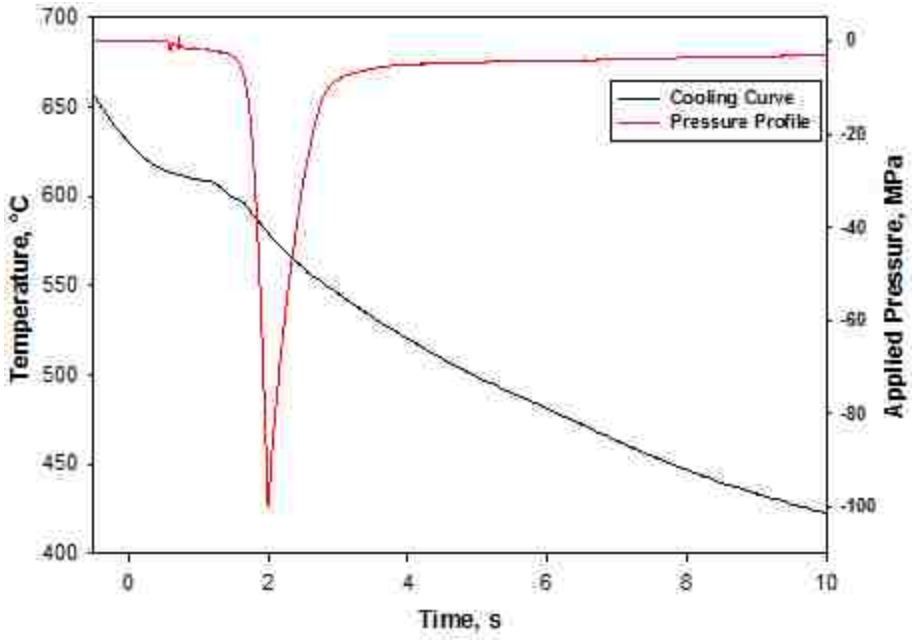

Figure 150 - Cooling curve and pressure profile of Sr modified A356 at 100 MPa with 1 pressure cycles.

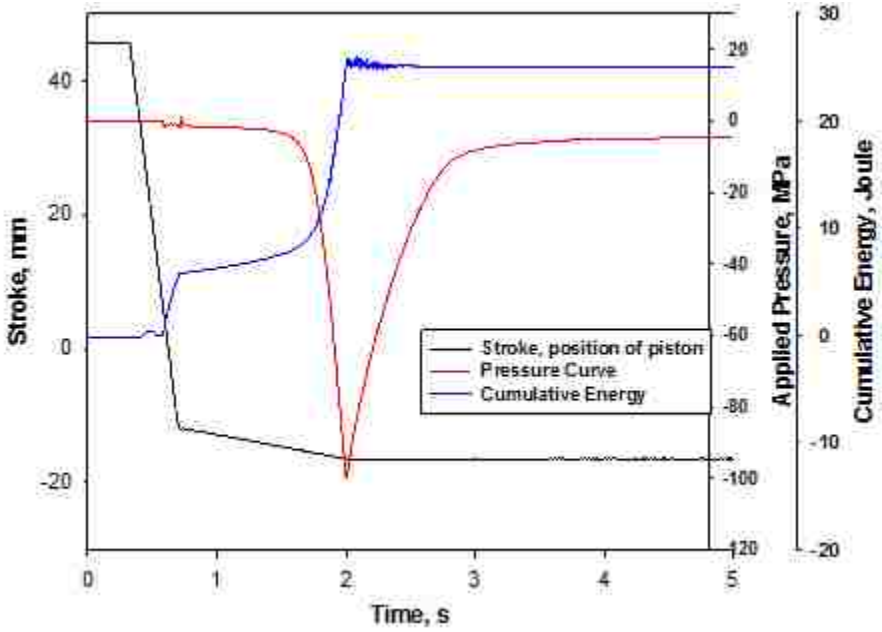

Figure 151 - Stroke, pressure profiles and cumulative energy of Sr modified A356 at 100 MPa with 1 pressure cycle.

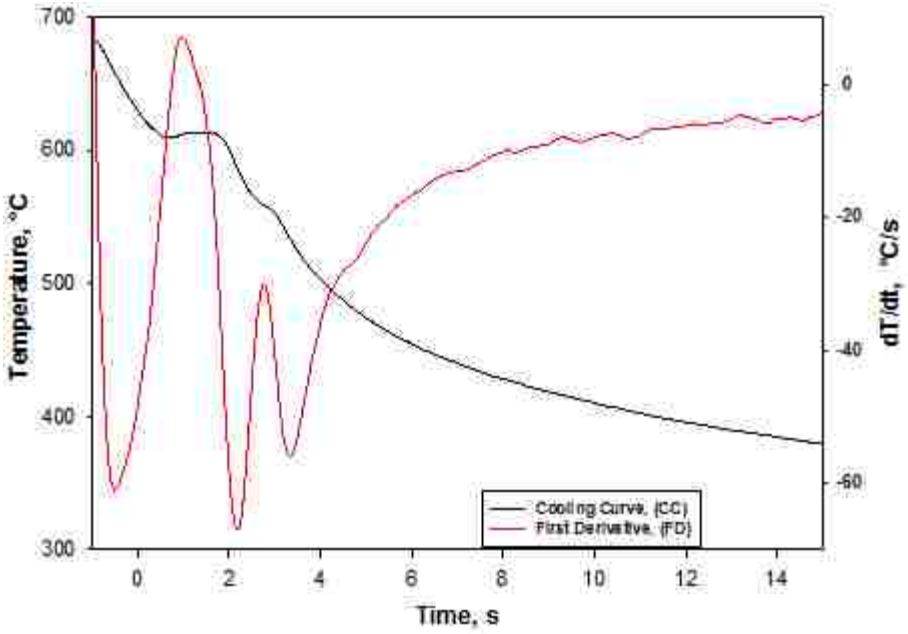

Figure 152 - Cooling curve and first derivative of Sr modified A356 at 100 MPa with 10 pressure cycles.

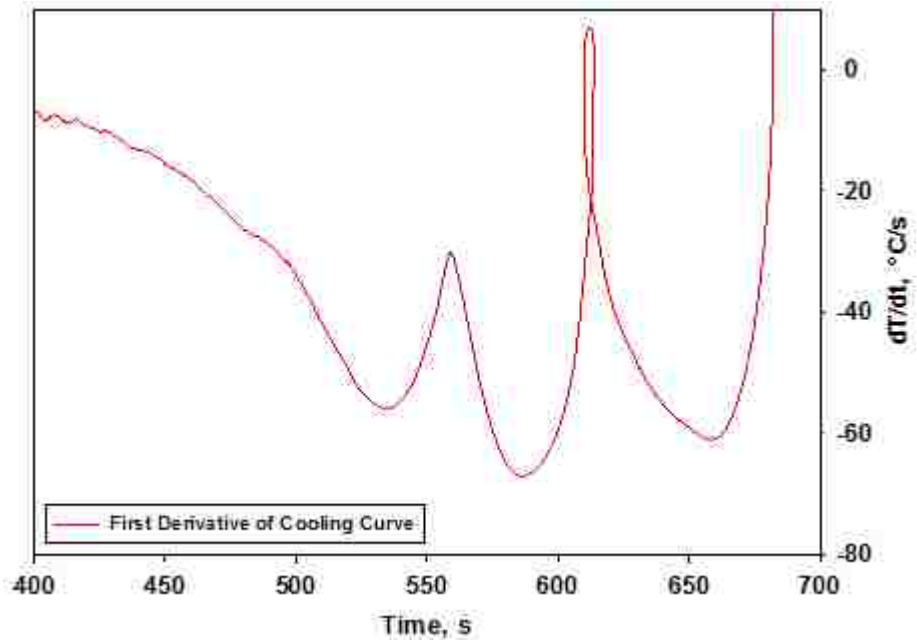

Figure 153 - First derivative of cooling curve of Sr modified A356 at 100 MPa with 10 pressure cycles.

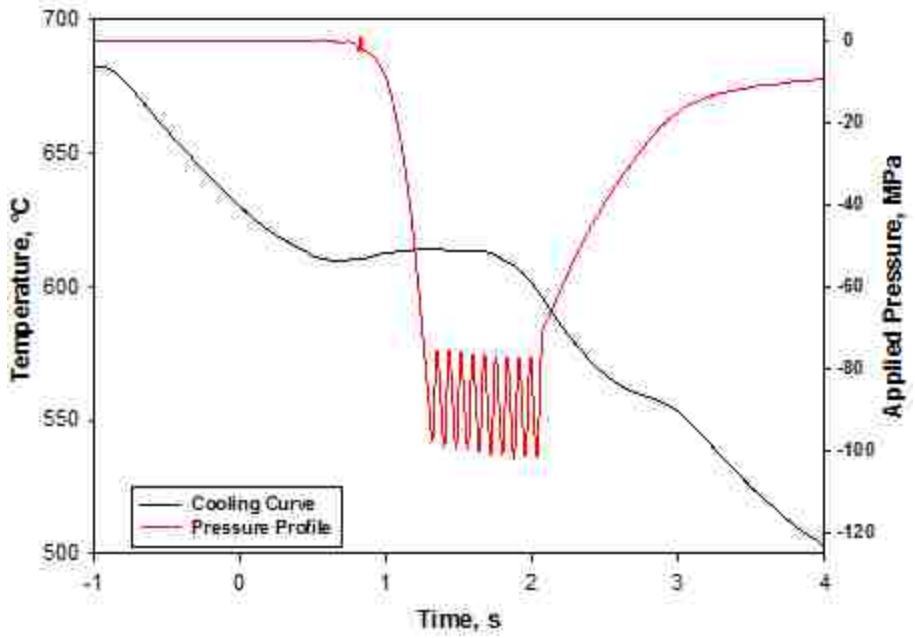

Figure 154 - Cooling curve and pressure profile of Sr modified A356 at 100 MPa with 10 pressure cycles.

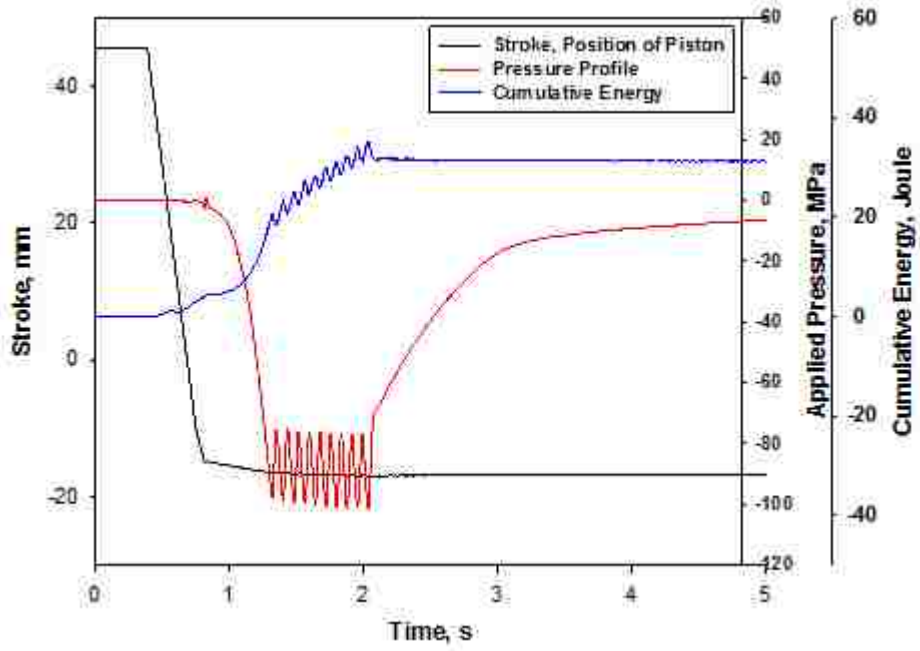

Figure 155 - Stroke, pressure profiles and cumulative energy of Sr modified A356 at 100 MPa with 10 pressure cycles.

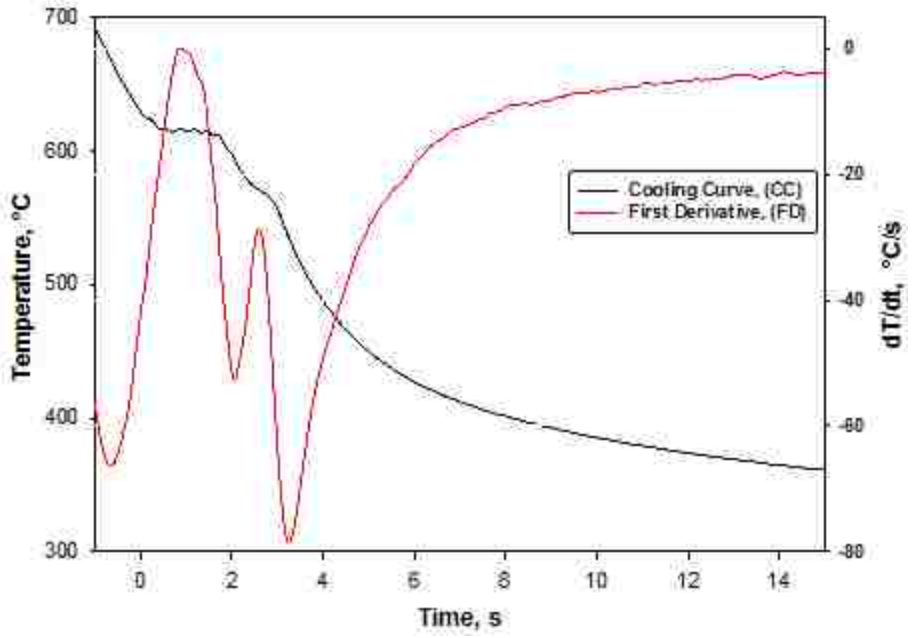

Figure 156 – Cooling curve and its first derivative of Sr modified A356 at 115 MPa with 7 pressure cycles.

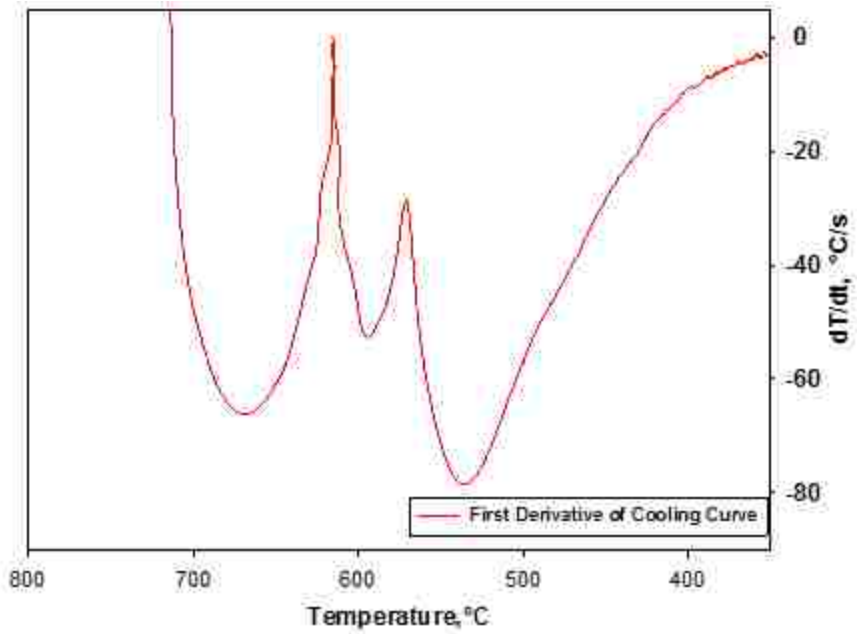

Figure 157 - First derivative of cooling curve of Sr modified A356 at 115 MPa with 7 pressure cycles.

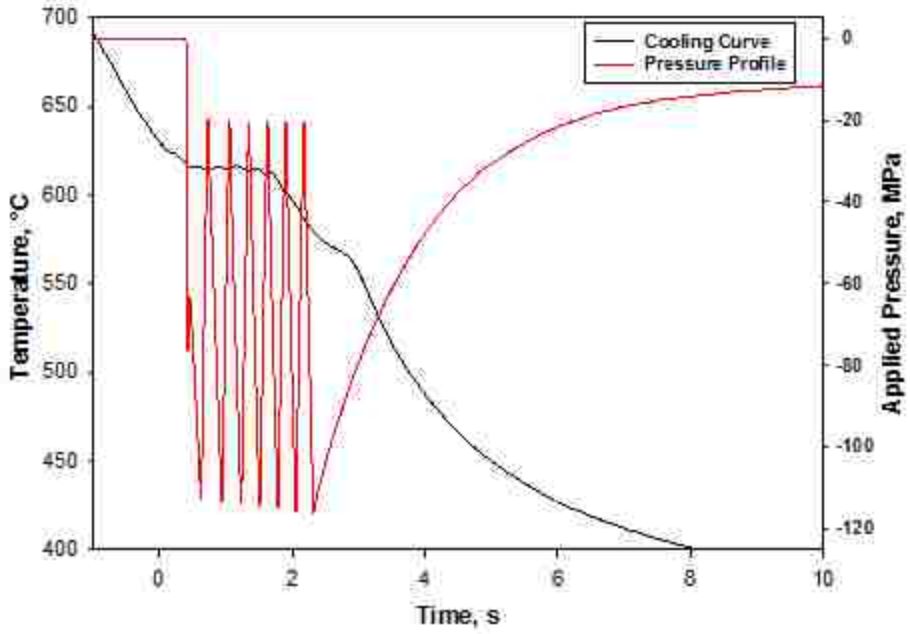

Figure 158 - Cooling curve and pressure profile of Sr modified A356 at 115 MPa with 7 pressure cycles.

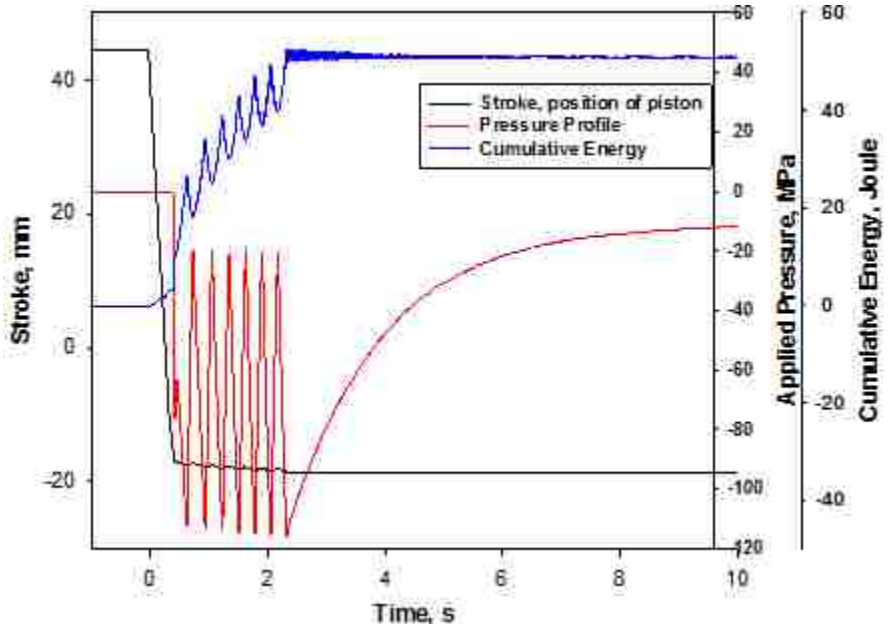

Figure 159 - Stroke, pressure profile and cumulative energy of Sr modified A356 at 115 MPa with 7 pressure cycles.

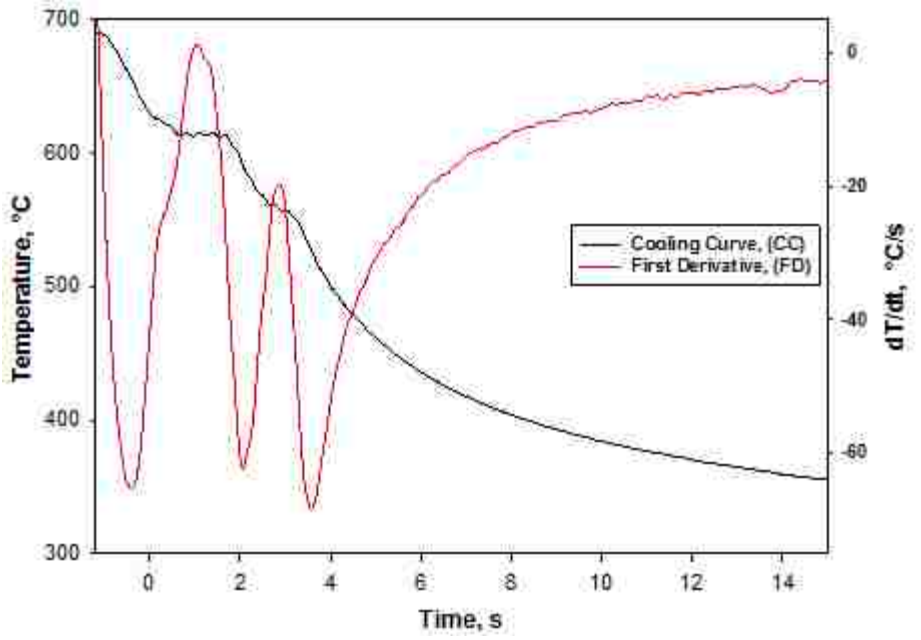

Figure 160 – Cooling curve and its first derivative of Sr modified A356 at 115 MPa with 50 pressure cycles.

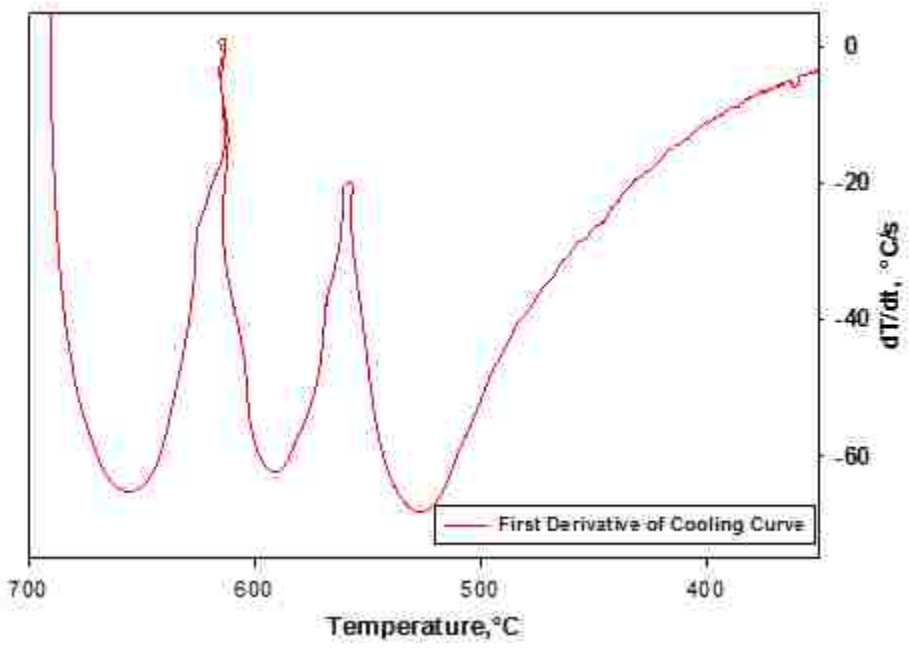

Figure 161 - First derivative of cooling curve of Sr modified A356 at 115 MPa with 50 pressure cycles.

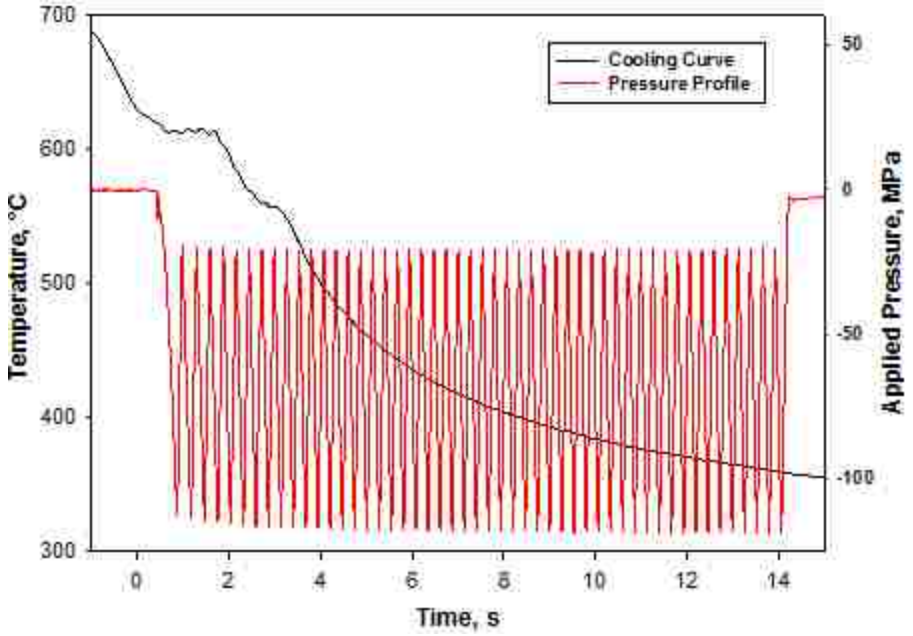

Figure 162 - Cooling curve and pressure profile of Sr modified A356 at 115 MPa with 50 pressure cycles.

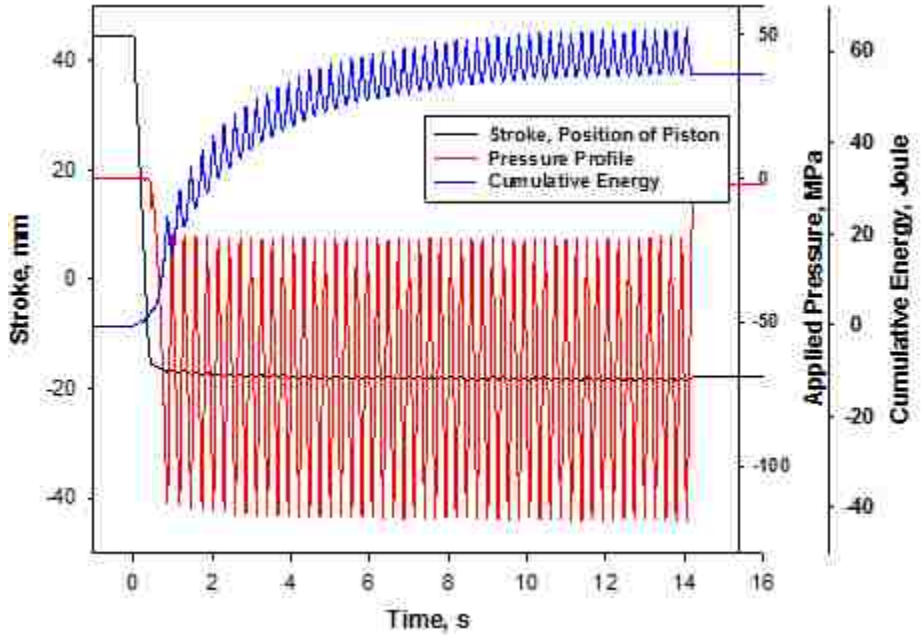

Figure 163 - Stroke, pressure profile and cumulative energy of Sr modified A356 at 115 MPa with 50 pressure cycles.

Appendix C – Nano Alumina Modified A356 at Different Pressure Profiles (Cooling Curve, First Derivative Curve, Pressure Curve, Stroke and Cumulative Energy Curve)

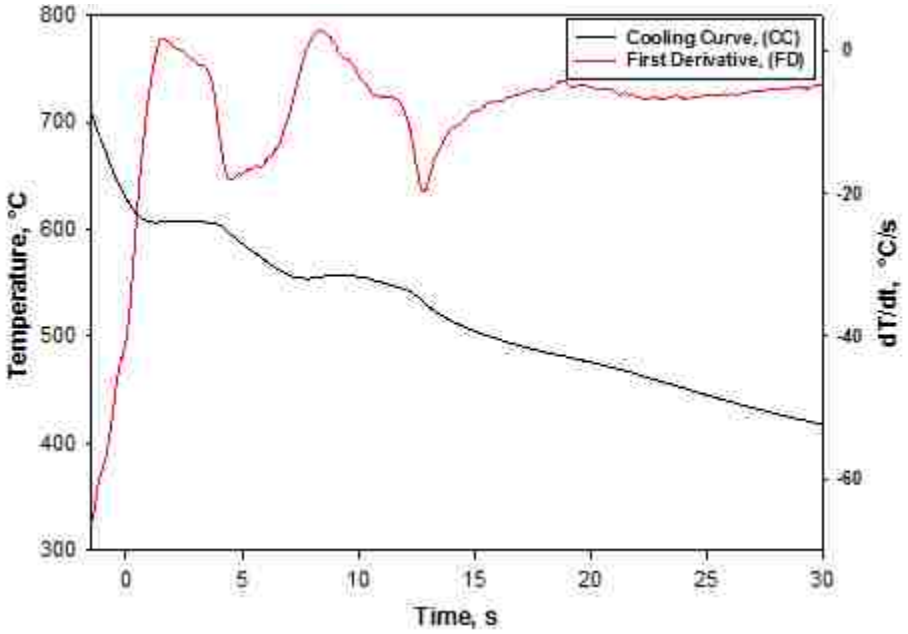

Figure 164 - Cooling curve and its first derivative of Nano alumina modified A356 at atmospheric pressure.

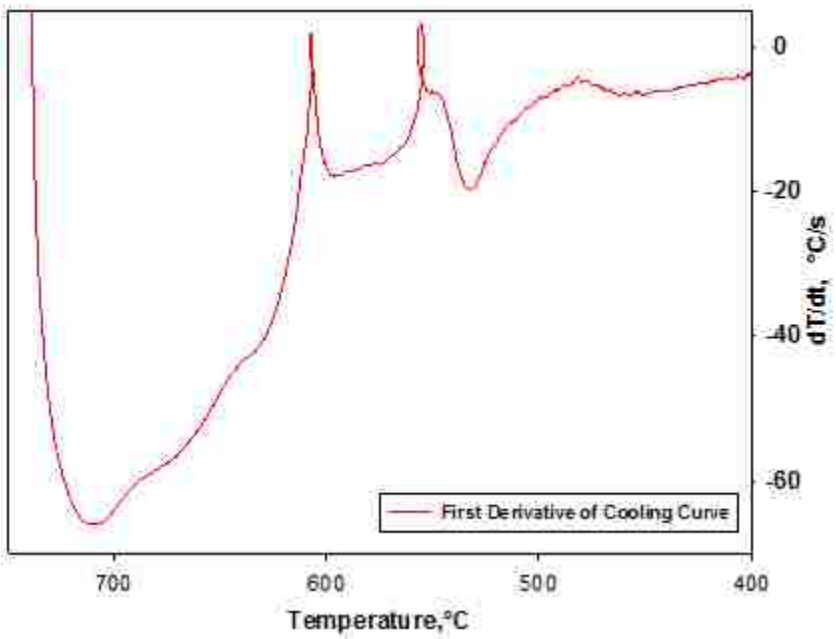

Figure 165 - First derivative of cooling curve of Nano alumina modified A356 at atmospheric pressure.

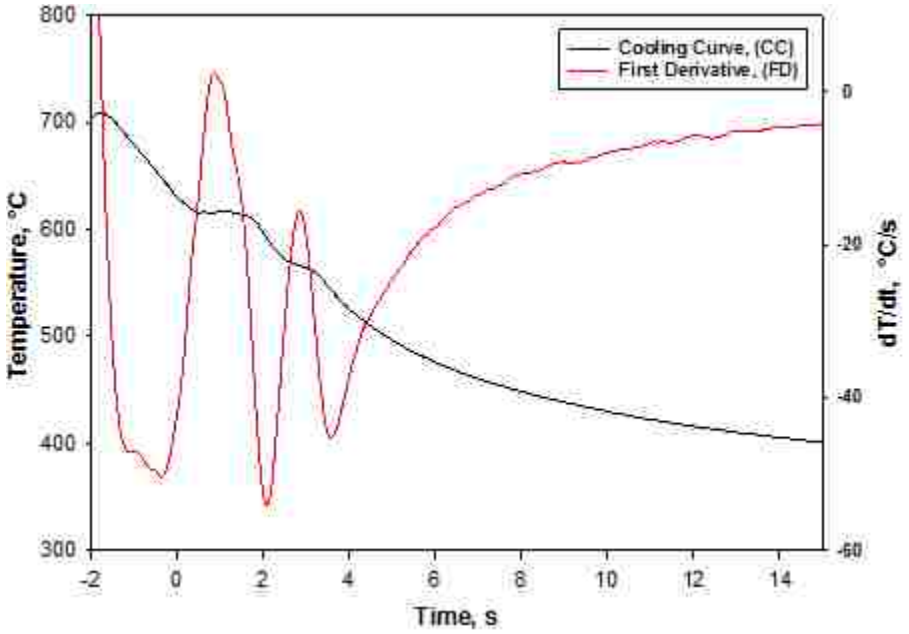

Figure 166 - Cooling curve and its first derivative Nano alumina modified A356 at 115 MPa with 2 pressures cycles.

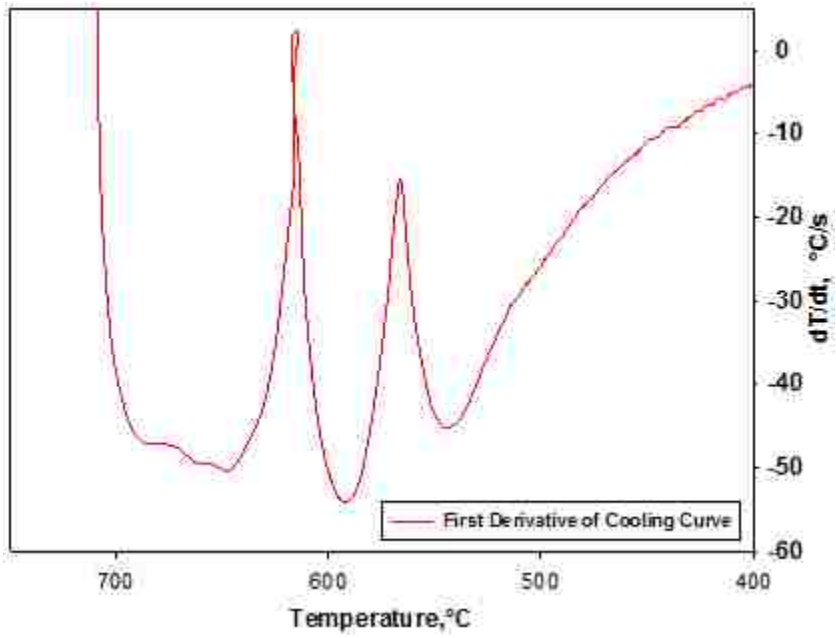

Figure 167 - First derivative of cooling curve of Nano alumina modified A356 at 115 MPa with 2 pressures cycles.

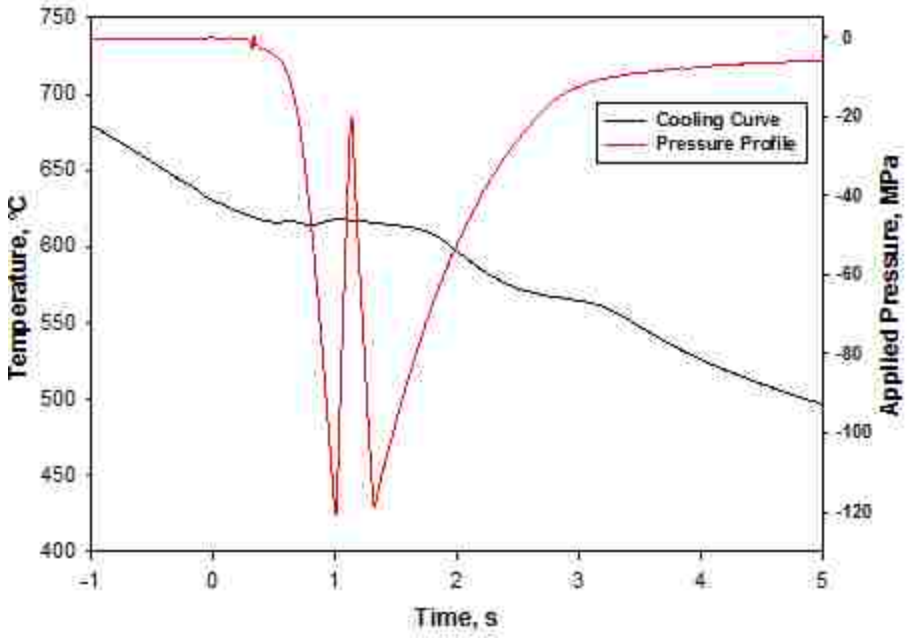

Figure 168 - Cooling curve and pressure profile of Nano alumina modified A356 at 115 MPa with 2 pressures cycles

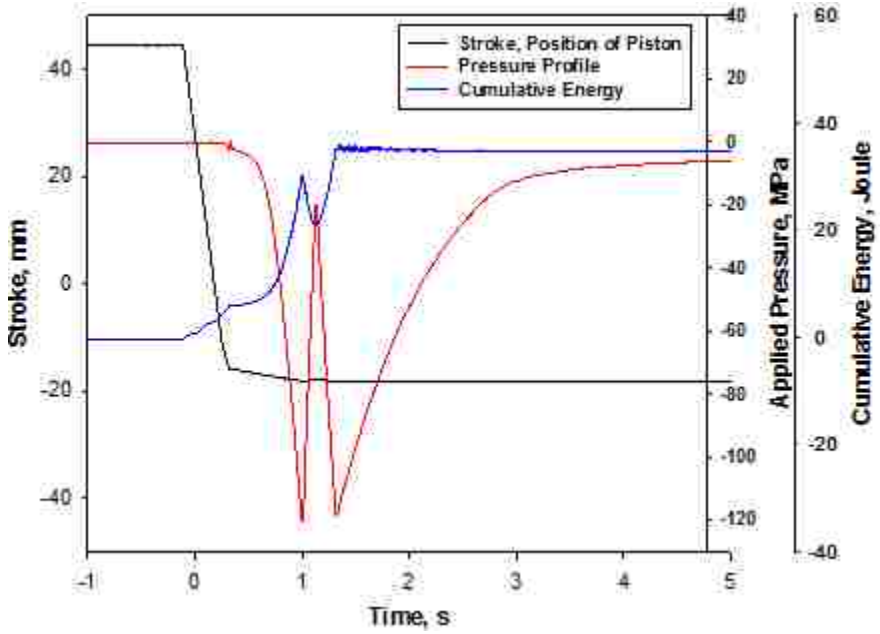

Figure 169 - Stroke, pressure profile and cumulative energy of Nano alumina modified A356 at 115 MPa with 2 pressures cycles.

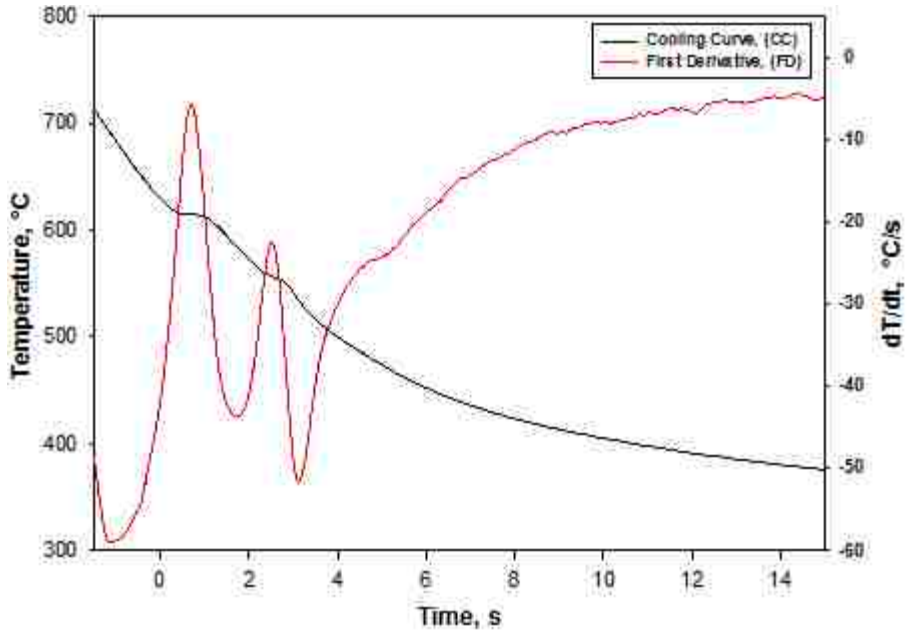

Figure 170 - Cooling curve and its first derivative Nano alumina modified A356 at 115 MPa with 20 pressures cycles.

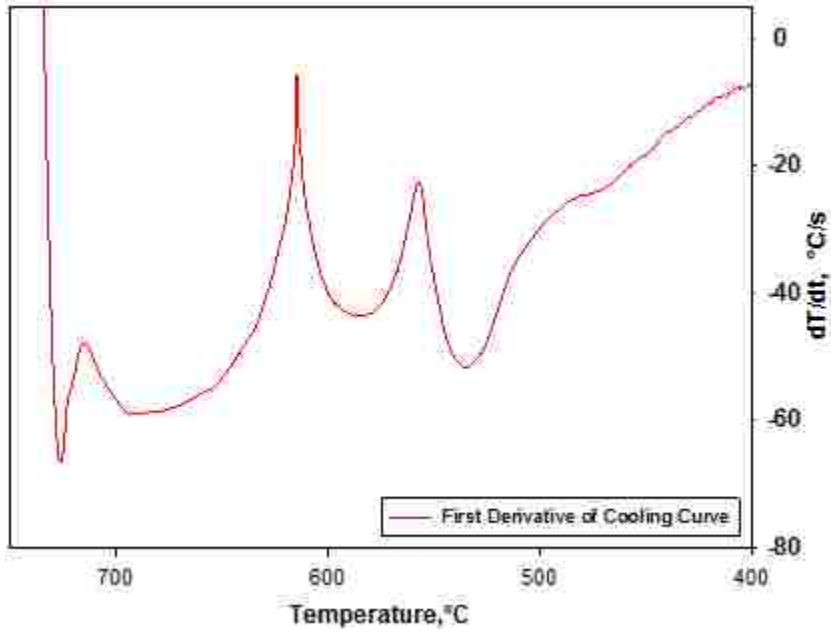

Figure 171 - First derivative of cooling curve of Nano alumina modified A356 at 115 MPa with 20 pressures cycles.

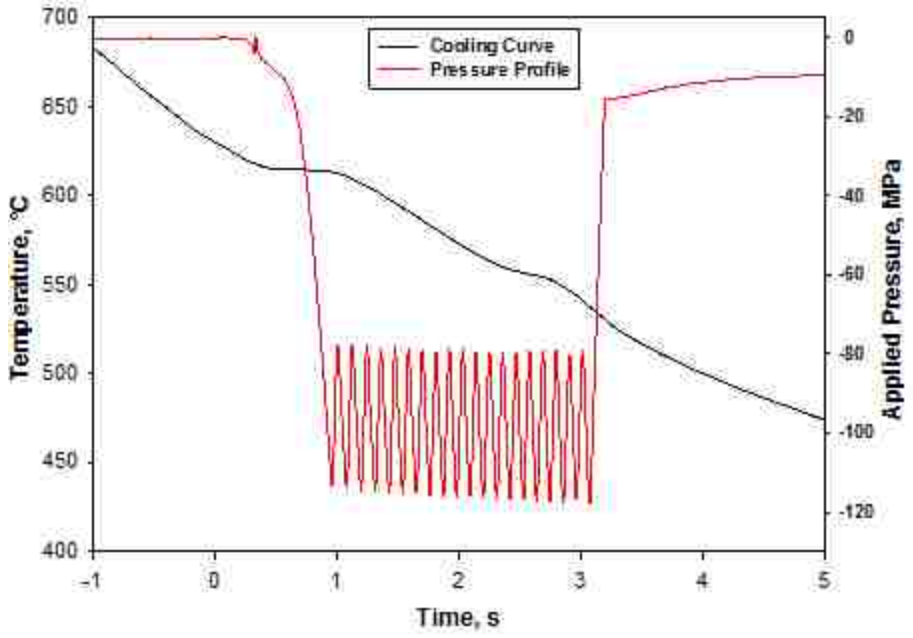

Figure 172 - Cooling curve and pressure profile of Nano alumina modified A356 at 115 MPa with 20 pressures cycles.

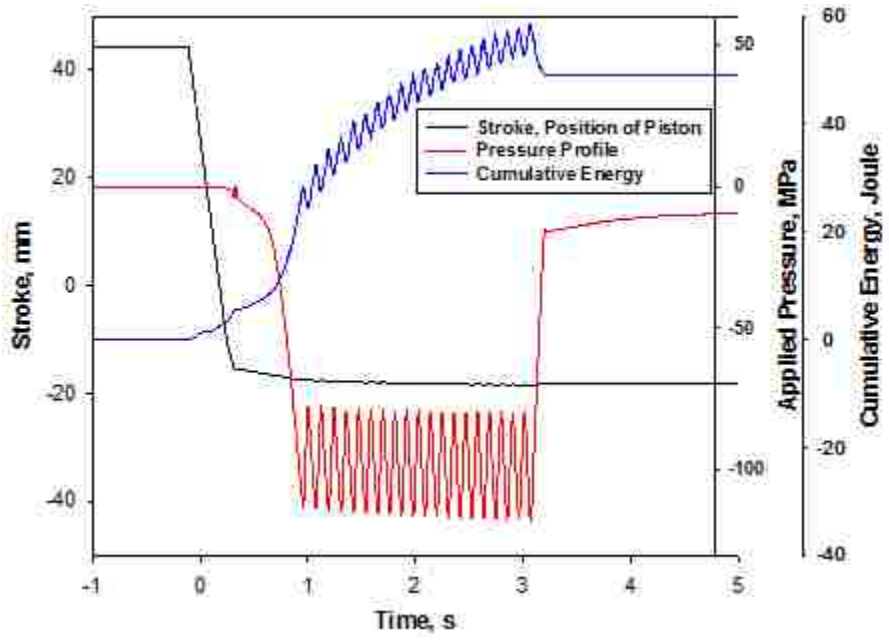

Figure 173 - Stroke, pressure profile and cumulative energy of Nano alumina modified A356 at 115 MPa with 50 pressures cycles.

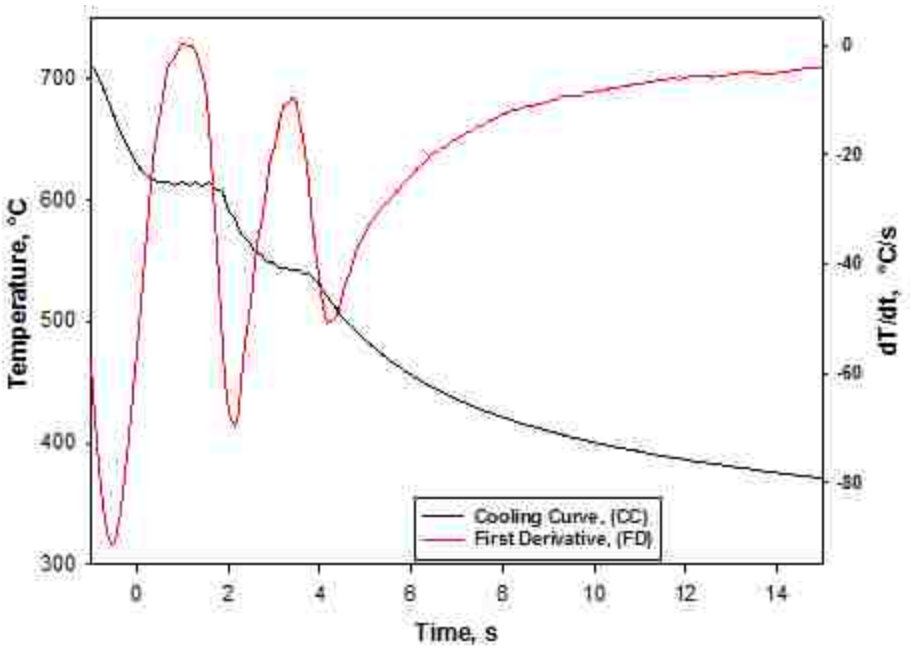

Figure 174 - Cooling curve and its first derivative Nano alumina modified A356 at 115 MPa with 50 pressures cycles.

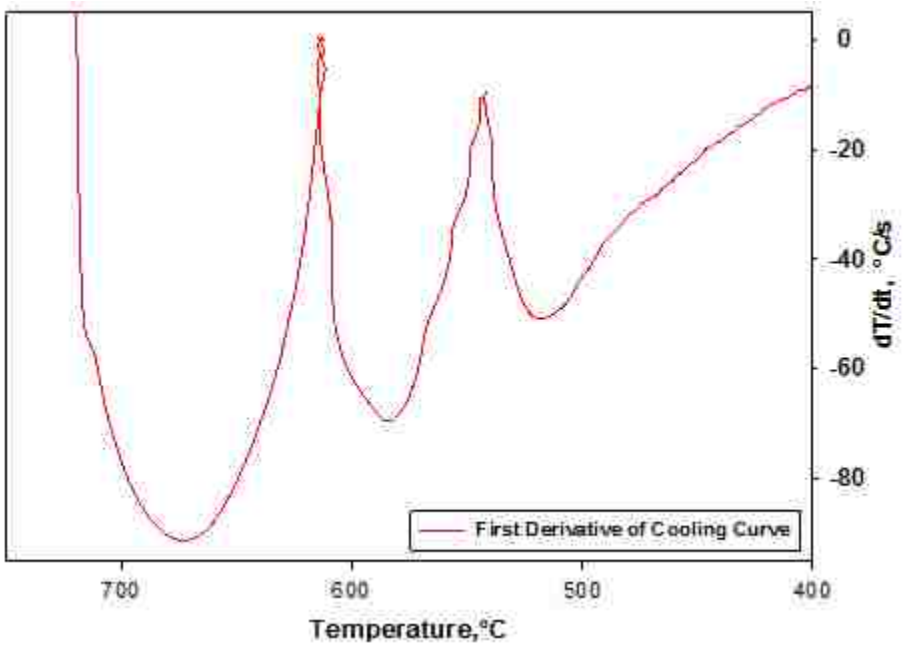

Figure 175 - First derivative of cooling curve of Nano alumina modified A356 at 115 MPa with 50 pressures cycles.

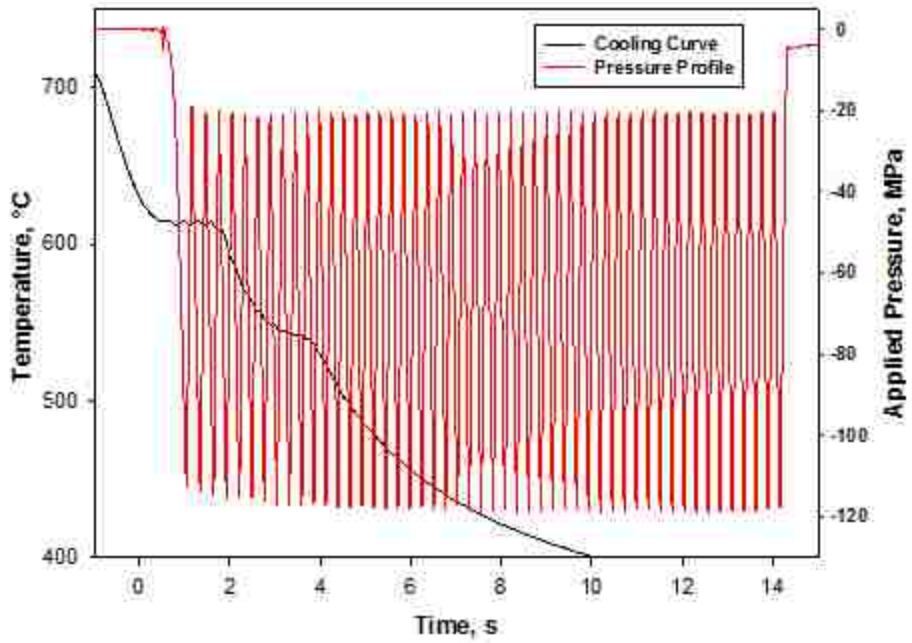

Figure 176 - Cooling curve and pressure profile of Nano alumina modified A356 at 115 MPa with 50 pressures cycles.

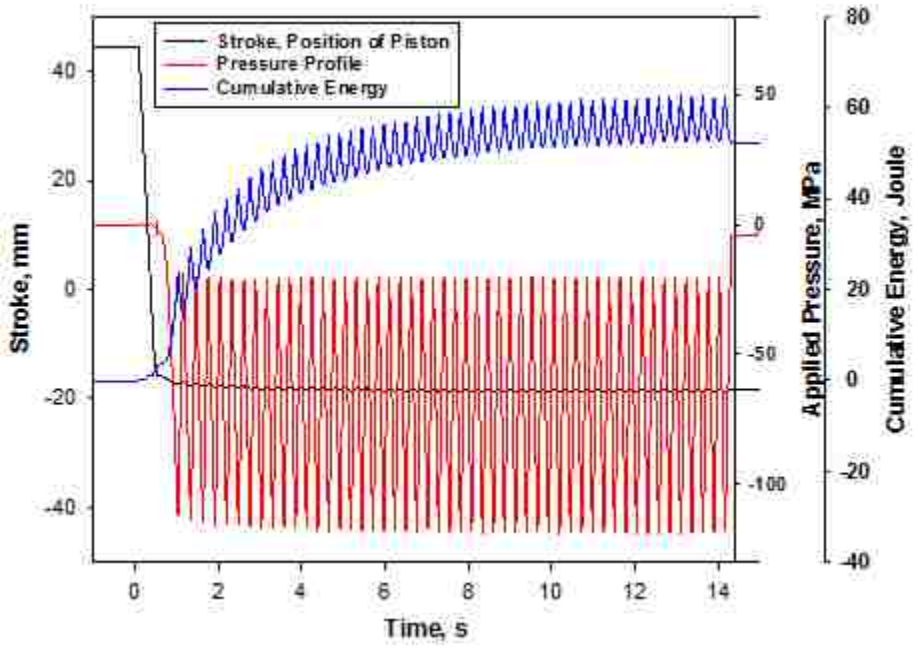

Figure 177 - Stroke, pressure profile and cumulative energy of Nano alumina modified A356 at 115 MPa with 50 pressures cycles.

Appendix D – Sr and Nano Alumina Combinedly Modified A356 at Different Pressure Profiles (Cooling Curve, First Derivative Curve, Pressure Curve, Stroke and Cumulative Energy Curve)

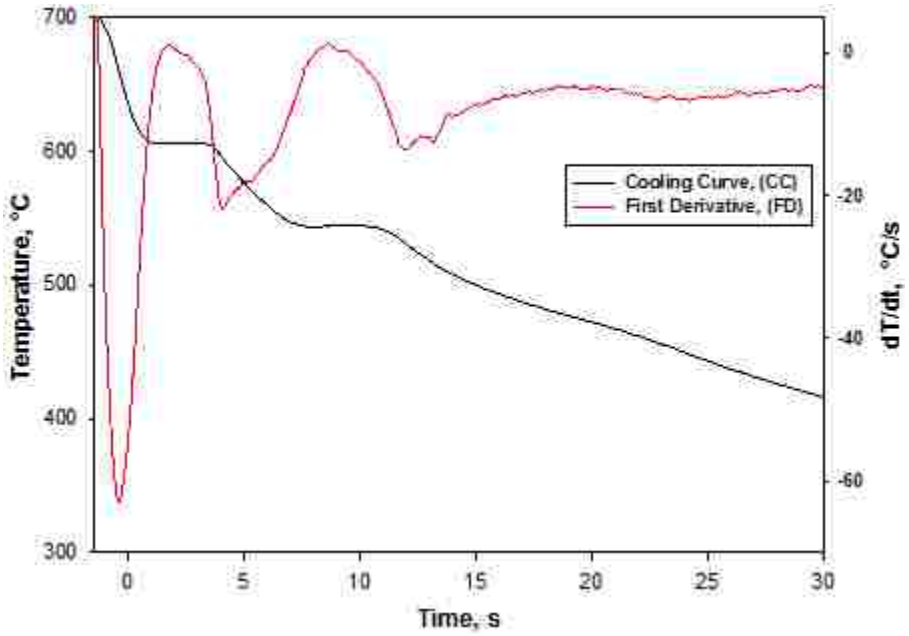

Figure 178 - Cooling Curve and its first derivative of Sr and Nano alumina modified A356 at atmospheric pressure.

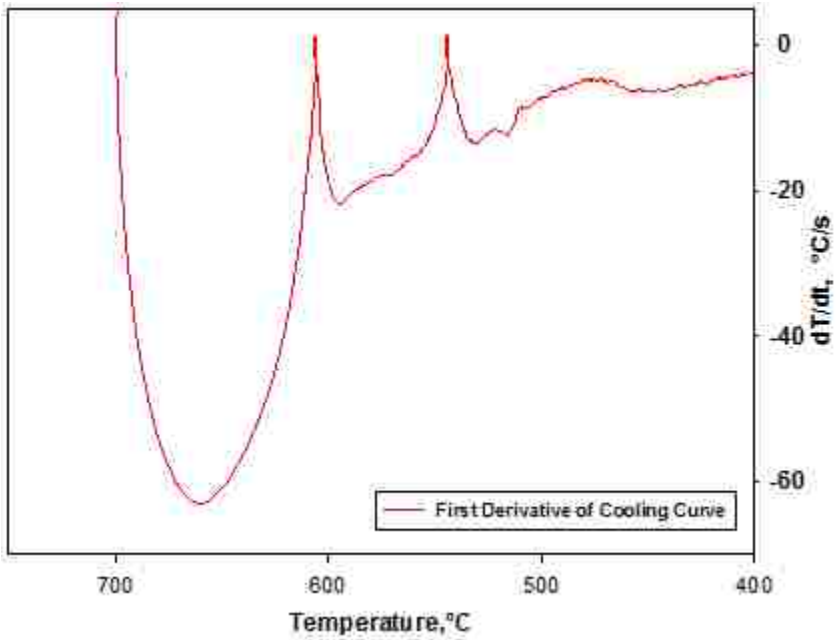

Figure 179 - First derivative of cooling curve of Sr and Nano alumina modified A356 at atmospheric pressure.

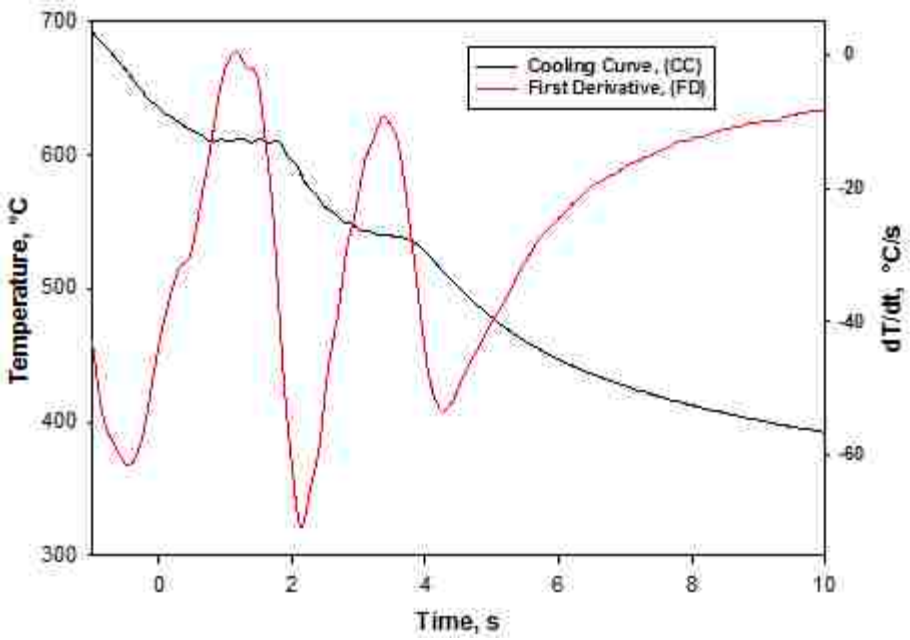

Figure 180 - Cooling Curve and its first derivative of Sr and Nano alumina modified A356 at 115 MPa with 12 pressures cycles.

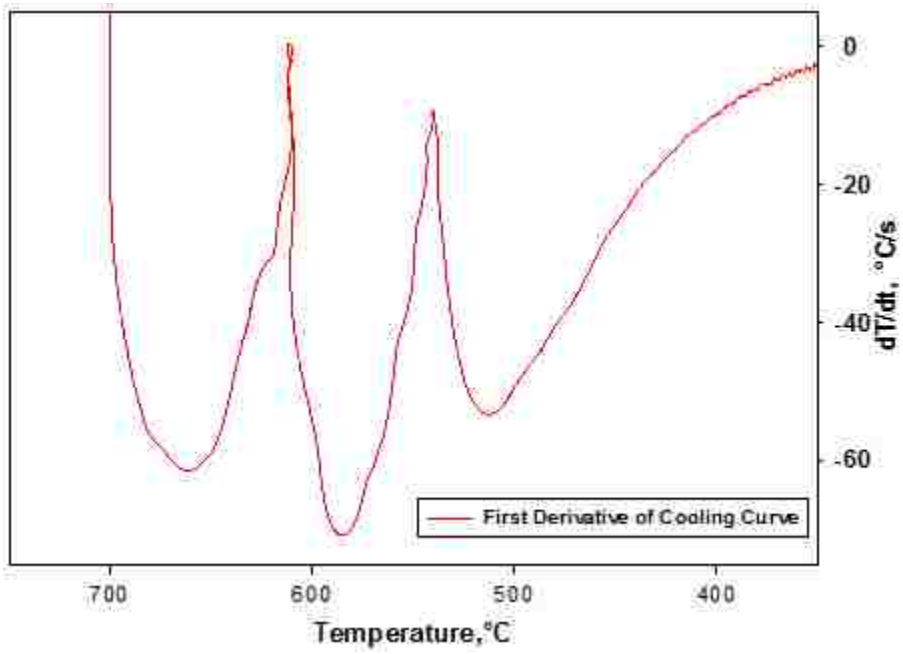

Figure 181 - First derivative of cooling curve of Sr and Nano alumina modified A356 at 115 MPa with 12 pressures cycles.

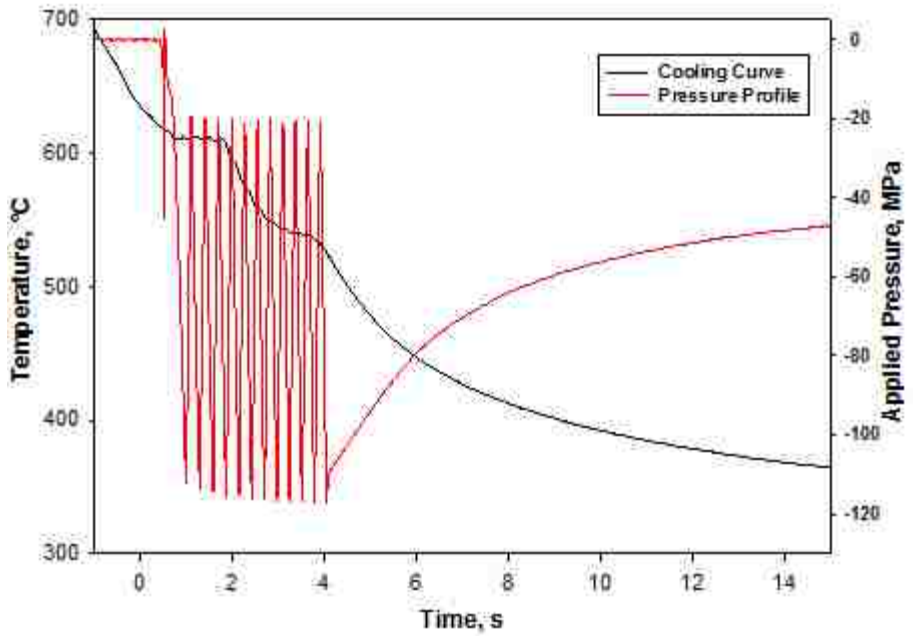

Figure 182 - Cooling curve and pressure profile of Sr and Nano alumina modified A356 at 115 MPa with 12 pressures cycles.

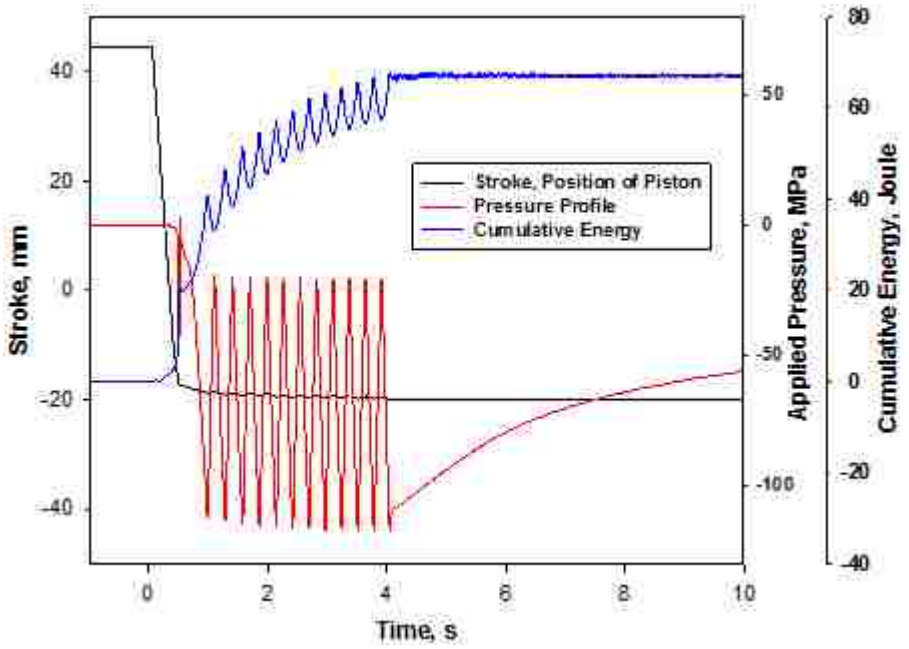

Figure 183 - Stroke, Pressure profile and cumulative energy of Sr and Nano alumina modified A356 at 115 MPa with 12 pressures cycles.

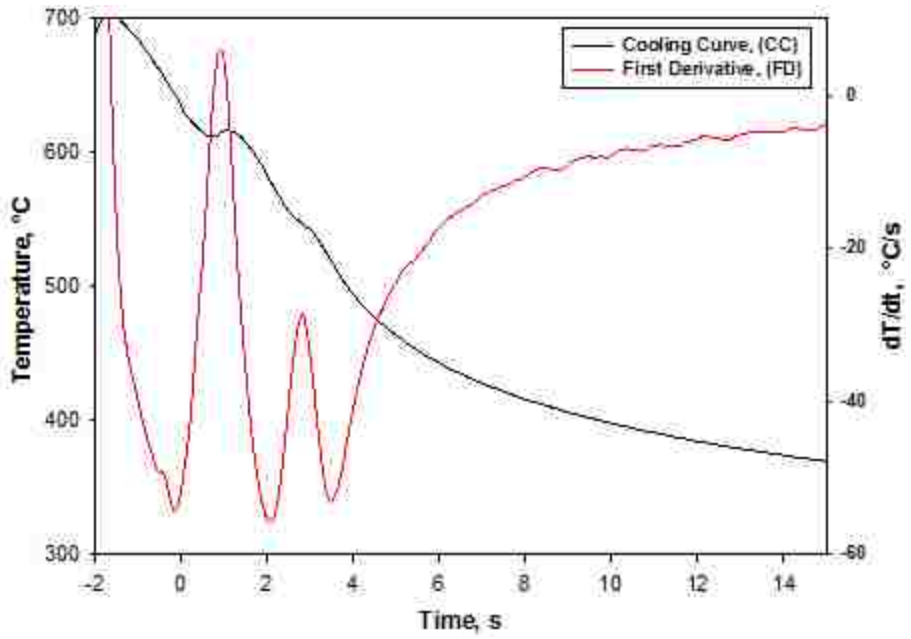

Figure 184 - Cooling Curve and its first derivative of Sr and Nano alumina modified A356 at 115 MPa with 20 pressures cycles.

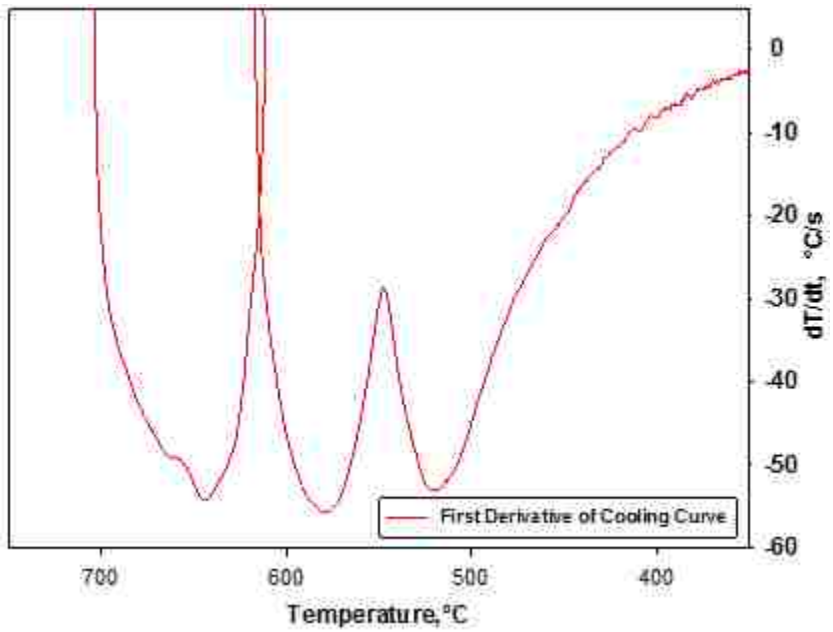

Figure 185 - First derivative of cooling curve of Sr and Nano alumina modified A356 at 115 MPa with 20 pressures cycles.

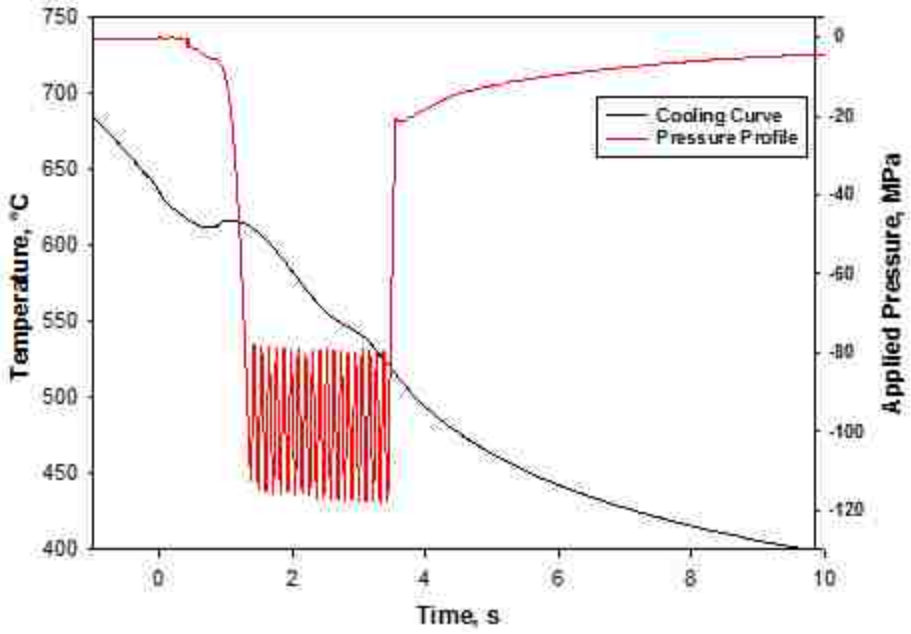

Figure 186 - Cooling curve and pressure profile of Sr and Nano alumina modified A356 at 115 MPa with 20 pressures cycles.

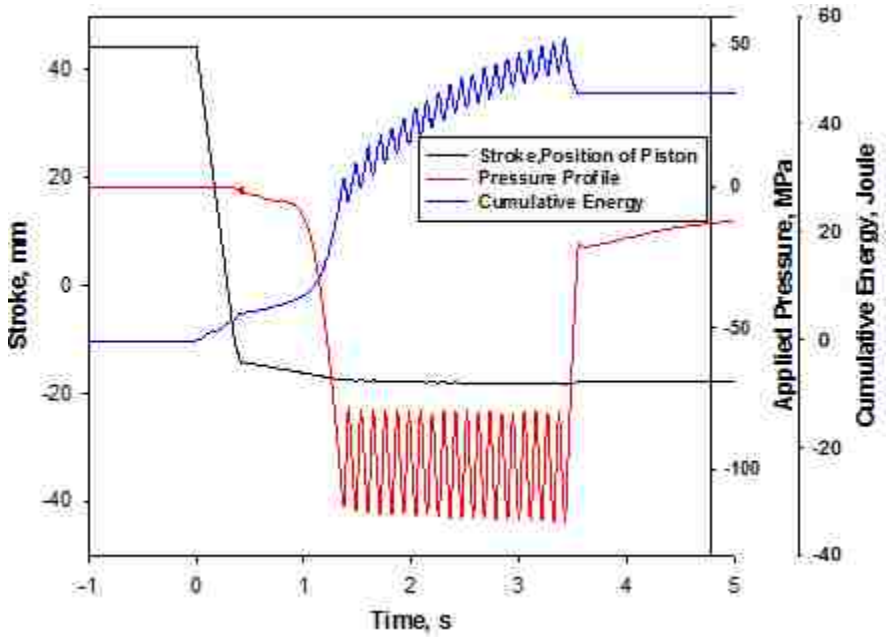

Figure 187 - Stroke, Pressure profile and cumulative energy of Sr and Nano alumina modified A356 at 115 MPa with 20 pressures cycles.

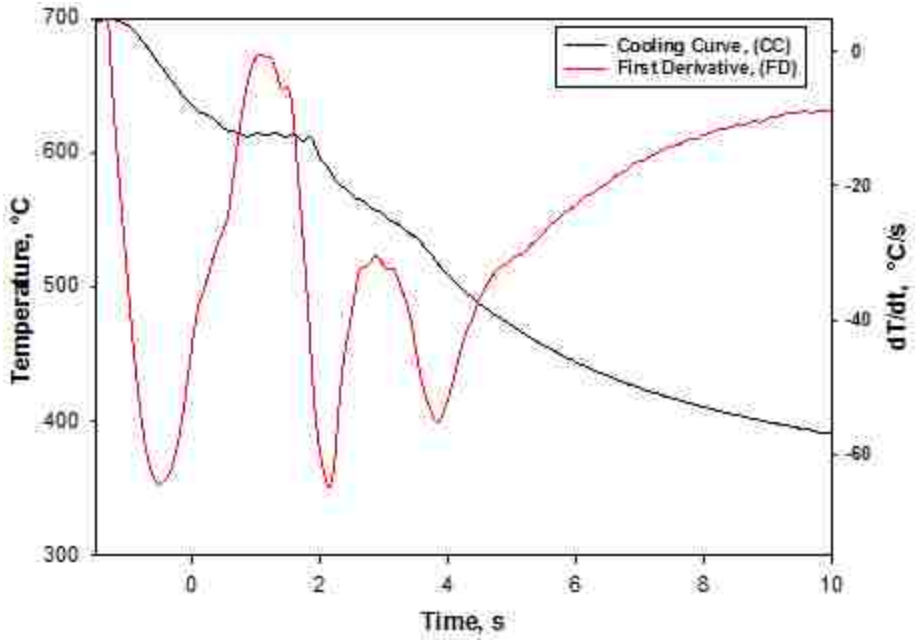

Figure 188 - Cooling Curve and its first derivative of Sr and Nano alumina modified A356 at 115 MPa with 50 pressures cycles.

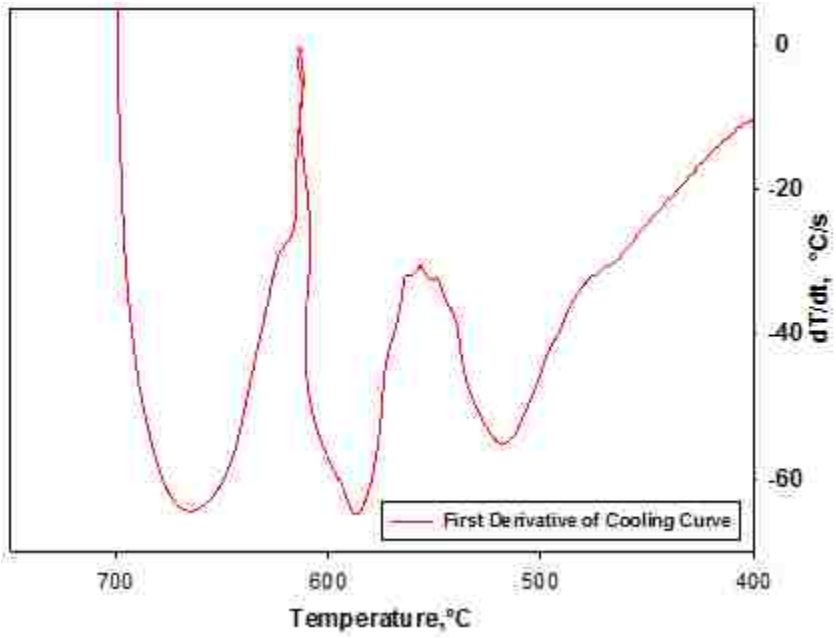

Figure 189 - First derivative of cooling curve of Sr and Nano alumina modified A356 at 115 MPa with 50 pressures cycles.

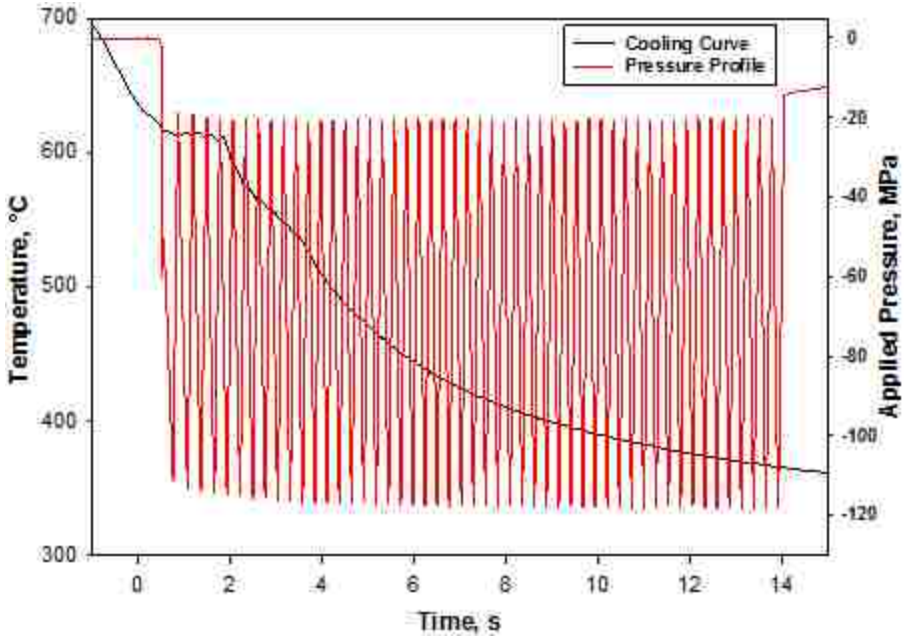

Figure 190 - Cooling curve and pressure profile of Sr and Nano alumina modified A356 at 115 MPa with 50 pressures cycles.

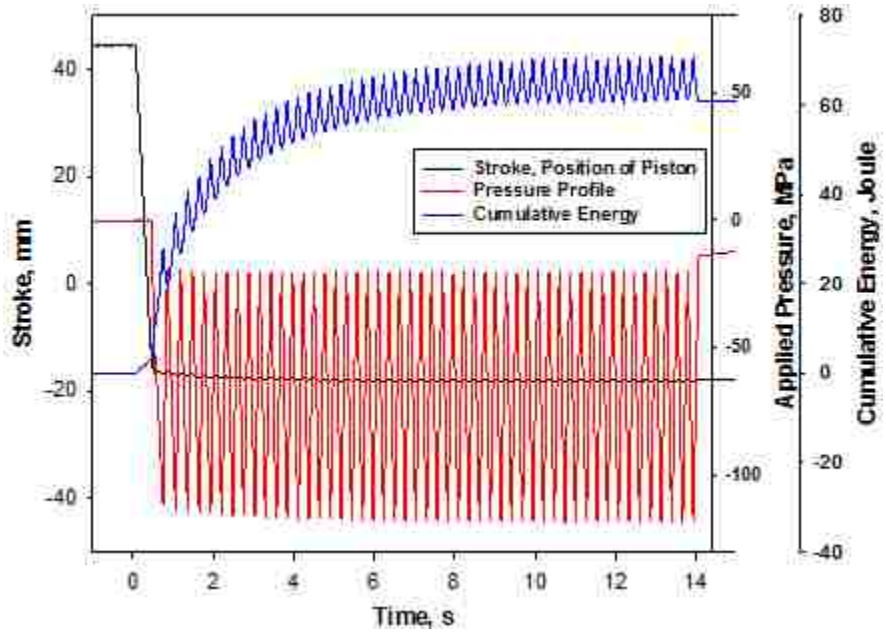

Figure 191 - Stroke, Pressure profile and cumulative energy of Sr and Nano alumina modified A356 at 115 MPa with 50 pressures cycles.

Appendix E - Non Linear Regression for the Correlation between the α-Dendrite Growth Peak Temperature and the Cyclic Pressure of UM A356 alloy at Different Pressure Profiles.

Nonlinear Regression **Saturday, January 04, 2014, 12:23:31 PM**

Data Source: Squeeze casting A356 UM (α-dendrite growth peak temperature and cyclic pressure of UM A356 alloy at different pressure profiles)

Equation: 3D, Lorentzian
f = a/((1+((x-x0)/b)2)*(1+((y-y0)/c)2))

R	Rsqr	Adj Rsqr	Standard Error of Estimate
0.8814	0.7769	0.5537	2.2248

	Coefficient	Std. Error	t	P
x0	11821.4713	2189821.8988	0.0054	0.9960
y0	9.5026	24.0970	0.3943	0.7134
a	2612.8240	1575095.8419	0.0017	0.9988
b	6539.3980	1362891.6004	0.0048	0.9964
c	340.3248	176.2774	1.9306	0.1257

Analysis of Variance:

	DF	SS	MS
Regression	5	3421520.6737	684304.1347
Residual	4	19.7988	4.9497
Total	9	3421540.4725	380171.1636

Corrected for the mean of the observations:

	DF	SS	MS	F	P
Regression	4	68.9268	17.2317	3.4814	0.1272
Residual	4	19.7988	4.9497		
Total	8	88.7256	11.0907		

Statistical Tests:

Normality Test (Shapiro-Wilk) Passed (P = 0.8448)

W Statistic= 0.9646 Significance Level = 0.0500

Constant Variance Test Passed (P = 0.6116)

Fit Equation Description:
[Variables]
x = col(1)
y = col(2)
z = col(3)
reciprocal_z = 1/abs(z)

reciprocal_zsquare = 1/z^2
reciprocal_pred = 1/abs(f)
reciprocal_predsqr = 1/f^2
[Parameters]
x0 = xatymax(x,z) "Auto {{previous: 11821.5}}
y0 = xatymax(y,z) "Auto {{previous: 9.50265}}
a = max(z) "Auto {{previous: 2612.82}}
b = if(fwhm(x,z)<>0, fwhm(x,z)/2, (max(x)-min(x))/4) "Auto {{previous: 6539.4}}
c = if(fwhm(y,z)<>0, fwhm(y,z)/2, (max(y)-min(y))/4) "Auto {{previous: 340.325}}
[Equation]
f = a/((1+((x-x0)/b)^2)*(1+((y-y0)/c)^2))
fit f to z
"fit f to z with weight reciprocal_pred
"fit f to z with weight reciprocal_predsqr
"fit f to z with weight reciprocal_z
"fit f to z with weight reciprocal_zsquare
[Constraints]
[Options]
tolerance=1e-8
"tolerance=0.0000000001
"tolerance=1e-7
"tolerance=1e-9
stepsize=1
iterations=2000
"iterations=1000
"iterations=1500
"iterations=200

Number of Iterations Performed = 822

Appendix F - Non Linear Regression for the Correlation between the Cumulative Energy and the Cyclic Pressure of UM A356 alloy at Different Pressure Profiles.

Nonlinear Regression **Saturday, January 04, 2014, 11:50:41 AM**

Data Source: Squeeze casting A356 UM (cumulative energy and cyclic pressure of UM A356 alloy at different pressure profiles)

Equation: 3D, Lorentzian
f = a/((1+((x-x0)/b)2)*(1+((y-y0)/c)2))

R	Rsqr	Adj Rsqr	Standard Error of Estimate
0.9889	0.9779	0.9558	5.0906

	Coefficient	Std. Error	t	P
x0	177.1338	169.5315	1.0448	0.3551
y0	114.0800	707.6268	0.1612	0.8797
a	12411.0116	6124343.1051	0.0020	0.9985
b	5.2335	1285.3275	0.0041	0.9969
c	113.9836	273.8228	0.4163	0.6986

Analysis of Variance:

	DF	SS	MS
Regression	5	12352.9137	2470.5827
Residual	4	103.6563	25.9141
Total	9	12456.5700	1384.0633

Corrected for the mean of the observations:

	DF	SS	MS	F	P
Regression	4	4591.3037	1147.8259	44.2935	0.0014
Residual	4	103.6563	25.9141		
Total	8	4694.9600	586.8700		

Statistical Tests:

Normality Test (Shapiro-Wilk) Passed (P = 0.7808)

W Statistic= 0.9583 Significance Level = 0.0500

Constant Variance Test Passed (P = 0.0874)

Fit Equation Description:
[Variables]
x = col(1)
y = col(2)
z = col(3)
reciprocal_z = 1/abs(z)

reciprocal_zsquare = 1/z^2
reciprocal_pred = 1/abs(f)
reciprocal_predsqr = 1/f^2
[Parameters]
x0 = xatymax(x,z) "Auto {{previous: 177.134}}
y0 = xatymax(y,z) "Auto {{previous: 114.08}}
a = max(z) "Auto {{previous: 12411}}
b = if(fwhm(x,z)<>0, fwhm(x,z)/2, (max(x)-min(x))/4) "Auto {{previous: 5.23346}}
c = if(fwhm(y,z)<>0, fwhm(y,z)/2, (max(y)-min(y))/4) "Auto {{previous: 113.984}}
[Equation]
f = a/((1+((x-x0)/b)^2)*(1+((y-y0)/c)^2))
fit f to z
"fit f to z with weight reciprocal_pred
"fit f to z with weight reciprocal_predsqr
"fit f to z with weight reciprocal_z
"fit f to z with weight reciprocal_zsquare
[Constraints]
[Options]
tolerance=1e-7
"tolerance=0.0000000001
stepsize=1
iterations=1000
"iterations=200

Number of Iterations Performed = 368

Appendix G – Permission from Co-Author

University of Windsor

Mohammad Alam <alam117@uwindsor.ca>

Permission for using the EDS calculations in my thesis

Mohammad Alam <alam117@uwindsor.ca> Thu, Mar 27, 2014 at 1:01 PM
To: Adam Gesing <gesingconsultants@gmail.com>
Cc: Jerry Sokolowski <jerry@uwindsor.ca>

Dear Dr. Adam
I am almost done with my thesis. Despite our mutual understanding on the collaborative work for publication of papers based on the findings on my research and thesis, now i need your official permission to include those calculations in my thesis.
Please confirm me that i can use those calculations in my thesis.

Best regards,
Mohammad Alam

Research Assistant
Metal Casting and Post-Processing Technology Group
Room 1178, Center for Engineering Innovation (CEI)
(519) 253-3000 ext.: 5727
Department of Mechanical, Automotive and Materials Engineering
University of Windsor,
401 Sunset Avenue,
Windsor, Ontario, Canada,
N9B 3P4.

University of Windsor

Mohammad Alam <alam117@uwindsor.ca>

Permission for using the EDS calculations in my thesis

Adam Gesing <gesingconsultants@gmail.com> Mon, Mar 31, 2014 at 9:40 AM
To: Mohammad Alam <alam117@uwindsor.ca>, "Dr. Jerry H. Sokolowski" <jerry@uwindsor.ca>

Mohammad,

You certainly may use our elemental composition calculations in your thesis. Is this email enough documentation for you, or will you need a signed letter in .pdf format?

Best Regards,

Adam

Adam J Gesing, President,

Gesing Consultants Inc; *13160 Amanda Court, Tecumseh, Ontario, Canada N8N 4J1*

Tel: 1.519.979.6398, **Email:** <adam@gesingconsultants.com; <gesingconsultants@gmail.com>; www.gesingconsultants.com

University of Windsor

Mohammad Alam <alam117@uwindsor.ca>

Permission for using the EDS calculations in my thesis

Mohammad Alam <alam117@uwindsor.ca> Mon, Mar 31, 2014 at 11:34 AM
To: Adam Gesing <gesingconsultants@gmail.com>
Cc: "Dr. Jerry H. Sokolowski" <jerry@uwindsor.ca>

Dear Dr. Adam
Thank you so much much for your email. I think this email is okay as permission.

Best regards,
Mohammad

VITA AUCTORIS

NAME:	Mohammad Khurshed-Ul Alam	
PLACE OF BIRTH:	Chittagong, Bangladesh	
YEAR OF BIRTH:	1974	
EDUCATION:	Notre Dame College, Dhaka, Bangladesh,	
	Higher Secondary Certificate, Science	1991
	Bangladesh University of Engineering & Technology, Dhaka	
	B.A.Sc., Materials and Metallurgical Engineering,	1998
	University of Windsor, Windsor, Ontario, Canada	
	M.A.Sc., Mechanical, Automotive & Materials Engineering,	2014